

**TAKE-OFF AND LANDING  
CRITICAL ATMOSPHERIC TURBULENCE (TOLCAT)—  
EXPERIMENTS AND ANALYSIS**

*C. E. ELDERKIN, D. C. POWELL, A. G. DUNBAR AND T. W. HORST*

Approved for public release; distribution unlimited.

## FOREWORD

This report was prepared by Battelle, Pacific Northwest Laboratories, Richland, Washington, in partial fulfillment of United States Air Force Contract No. F33615-68-M-5009, "Take-Off and Landing Critical Atmospheric Turbulence (TOLCAT)."


The work was administered under the direction of the Air Force Flight Dynamics Laboratory, Air Force Systems Command, United States Air Force, Wright-Patterson Air Force Base, Ohio, with Mr. William P. Johnson (FBE-A) as Project Engineer.

The research reported was conducted by the scientific and technical personnel of the Atmospheric Physics Section, Atmospheric Sciences Department of Battelle, Pacific Northwest Laboratories. Dr. C. E. Elderkin was the Project Director and the principal investigators were Messrs. D. C. Powell and A. G. Dunbar. The work was accomplished during the period from November 1969 to October 1971.

Acknowledgment is made for the assistance of the following Battelle personnel: Messrs. O. B. Abbey, J. C. Draper, V. T. Henderson, and F. D. Lloyd, all of the Atmospheric Sciences Department, for their contributions to the development and operation of the TOLCAT measuring system and to the processing of data produced by it; Mr. R. L. Conley, Miss L. L. Carratt, and Mrs. Lois Lee, also of the Atmospheric Sciences Department, for their assistance in preparing and editing reports; and to Messrs. M. D. Erickson and K. M. Busness, Systems Engineering Department, for evaluating the capabilities of the CARDS trailer equipment to TOLCAT application.

This report was submitted by the authors in November 1971.

This technical report has been reviewed and is approved.

  
GORDON R. NEGARD, Major, USAF  
Chief, Design Criteria Branch  
Structures Division

## ABSTRACT

Measurements of turbulence were made from various arrays of tower mounted sensors to demonstrate methods of describing the temporal and spatial character of turbulence pertinent to Take-Off and Landing Critical Atmospheric Turbulence (TOLCAT) problems of the Air Force.

Measurement and data reduction techniques for sonic and three-propeller anemometers were optimized to assure true and accurate measurements of the vertical and two horizontal wind components from sensors remotely mounted on towers. Both analog and digital magnetic tape field recording options were demonstrated to provide flexibility in measurement array configurations and to optimize recording capabilities for a variety of measurement requirements. Data played back from field recordings in both analog and digital form underwent preliminary processing on an SEL 840A medium-size computer and were re-recorded on industry standard digital computer tapes for detailed analyses performed later on a UNIVAC 1108 computer. The preliminary processing incorporated selectable digitizing and averaging rates to provide smoothed basic data samples at various time intervals appropriate to a variety of applications.

Probability density functions, both individual and joint, were calculated for any pair of wind component variables, oriented in a preselected coordinate system and optionally high pass filtered for various aircraft response applications. Spectral analyses are provided through fast Fourier transform calculations. Power spectra of each of the time series and cross spectra for different wind components at the same point and for the same component at different points were calculated for time series optionally tapered or detrended. The auto- and cross-correlation functions can, in turn, be transformed from the spectral functions when required. Also, the first four moments for each of the wind components were computed. Finally, bispectral estimates are available from the fast Fourier calculated coefficients.

# *Contrails*

Results were obtained from analyzing measurements made from several arrays utilizing both 62-meter fixed towers and 30-meter expandable portable towers. Power spectra from 15, 30, and 58-meter heights show characteristics at frequencies above those where the micrometeorological peak energies occur, or the region of greatest interest for aircraft applications. These are reasonably predictable from a knowledge of the near-surface stress, wind speed, and stability.

The spatial aspects of turbulence structure and the relationship between temporal and spatial aspects were also studied. Plots of the space-time dependence of the correlation functions were obtained from turbulence measurements taken from a logarithmically spaced line of towers, offering a means of determining the turbulence spectrum for a given wind component encountered by an aircraft flying through a field of turbulence at a given wind speed. Such analyses were obtained for each wind component with the mean wind along the line of towers and with the wind normal to the line of towers. The apparent usefulness of Taylor's hypothesis for determining correlation functions from fixed point data for aircraft moving upwind at any speed can be seen. The deviation from a frozen turbulence field hypothesis when moving with the mean wind was also demonstrated in the alongwind tower-line tests. Taylor's hypothesis and the shear induced limitations of its applicability, relative to eddy size, were studied more thoroughly with cross-spectral analyses for parallel components at two points along the direction of the mean wind. Phase spectra demonstrated that eddy sizes smaller than approximately ten times the height of measurement were advected coherently with an eddy translation speed slightly greater than the mean wind speed.

TABLE OF CONTENTS

TAKE-OFF AND LANDING CRITICAL ATMOSPHERIC  
TURBULENCE (TOLCAT) - EXPERIMENTS AND ANALYSIS

		<u>Page</u>
SECTION I	INTRODUCTION	1
SECTION II	THEORY	4
	BASIC MATHEMATICAL DESCRIPTION OF TURBULENCE	6
	CHARACTERISTIC VELOCITIES AND LENGTHS	9
	THE FUNDAMENTAL TOLCAT INVESTIGATION	11
	THE MINIMUM AND MAXIMUM TURBULENCE SCALES TO WHICH AIRCRAFT RESPOND	20
	THIRD MOMENT ANALYSIS	20
SECTION III	SENSOR DESCRIPTION AND EVALUATION	22
	WIND COMPONENT METER	22
	VECTORVANE	24
	SONIC ANEMOMETER	25
	GILL UVW ANEMOMETER	28
	Cosine Response	29
	Frequency Response	30
	Threshold Response	35
	CONCLUSIONS	40
SECTION IV	MEASUREMENT SYSTEMS AND FIELD ARRAYS	42
	SENSORS	43
	INSTRUMENT LEVEL DETECTORS	47
	INSTRUMENT REORIENTING EQUIPMENT	53
	MOUNTING CONFIGURATIONS	60
	Boom Configurations	60
	Tower Top Mountings	64
	DATA ACQUISITION SYSTEM	64
	FIELD ARRAYS	67
SECTION V	DATA CONVERSION SYSTEM	79
	HARDWARE	79
	SOFTWARE	83
	The Main Program	83
	The Subroutines	84
	Program Verification and Equipment Testing	86

# Contrails

	<u>Page</u>
SECTION VI	COMPUTER PROGRAMMING FOR ANALYSIS 87
	INITIAL UNIVAC 1108 TAPE PROGRAM 87
	FINAL MASTER TAPE PROGRAM 88
	Editing 88
	Correction of Gill Data for Noncosine Response 89
	Reorientation of all Data with Respect to an Arbitrary X-Axis 90
	ANALYSIS PROGRAM 91
SECTION VII	EXPERIMENTS AND ANALYSIS 98
	THE EXPERIMENTS 98
	SPECTRAL GAP ANALYSIS 102
	Heuristic Arguments 102
	Analytical Results 105
	Aspects of Weak Spectral Gap Verification 111
	TAYLOR'S HYPOTHESIS VERIFICATION 114
	Analysis of Space and Time Correlations 115
	Phase Spectral Analysis 133
	VARIANCES AND COVARIANCES 147
	Problems in Modeling the Variances 147
	Magnitude Correlations 153
	POWER SPECTRAL ANALYSIS 155
	Vertical Component Models 155
	Universal Values Proposed for Spectral Forms 157
	Horizontal Component Models 159
	CORRELATION ANALYSIS 177
	Correlation Forms 177
	Effect of Nonstationarity on Correlation Values 180
	Autocorrelation Analysis of Time Series $R_{\alpha\alpha}(\tau)$ 181
	Correlation in Space and Time 185
	SHEAR INTENSITIES 193
	BISPECTRAL ANALYSIS 195
	PROBABILITY DENSITIES 204
	Individual Probability Distributions 206
	Joint Probability Densities 207
SECTION VIII	SUMMARY AND CONCLUSIONS 213
	RESULTS 213
	RECOMMENDED MEASUREMENTS AND OPTIMIZED ARRAY 221
	Dual System Operation 222
	Sensor Array Description 223
	Data Acquisition 227

# Contrails

	<u>Page</u>	
APPENDIX I	PHASE SPECTRUM IN RELATION TO TAYLOR'S HYPOTHESIS	237
APPENDIX II	BISPECTRAL ANALYSIS	240
	DEFINITIONS	240
	PROPERTIES OF $Q_1(\tau_1, \tau_2)$	241
	Comparisons with Second-Order Covariance Function	241
	Redundancy in the Third-Order Covariance Function	243
	COMPUTATION OF $B_1(\omega_1, \omega_2)$ FOR FAST FOURIER TECHNIQUES	245
	PROPERTIES OF $B_1(\omega_1, \omega_2)$	247
APPENDIX III	SENSOR LEVELING AND ORIENTATION DETAILS	252
APPENDIX IV	SUPPLEMENTARY ANALYSIS FIGURES	260
REFERENCES		281



## LIST OF FIGURES

<u>FIGURE</u>	<u>TITLE</u>	<u>PAGE</u>
2.1	Turbulence as seen by an Anemometer and by an Aircraft	11
2.2	Isopleths of $R(\tau, \xi)$	19
3.1	Sensors used in TOLCAT Measurement System	23
3.2	Power Spectra Measured by Adjacent Sonic Anemometers	31
3.3	Alongwind Power Spectra Measured by Adjacent Gill UVW and Sonic Anemometers	32
3.4	Vertical Power Spectra Measured by Adjacent Gill UVW and Sonic Anemometers	33
3.5	Probability Distributions of the Vertical Wind Measured by Adjacent UVW Gill and Sonic Anemometers	36
3.6	Probability Distributions of the Vertical Wind Measured by Adjacent UVR Gill and Sonic Anemometers	38
3.7	Vertical Power Spectra Measured by Adjacent Sonic, UVR Gill and UVW Gill Anemometers	39
4.1	The 125-Meter Hanford Meteorology Tower	44
4.2	Four 62-Meter Towers on the 1600-Meter Arc	45
4.3	125-Meter Meteorology Tower Data Recording Center	46
4.4	Sonic Anemometer with Electrolytic Levelers	48
4.5	Gill Anemometer with Electrolytic Levelers	49
4.6	Electrolytic Leveler Location Relative to Sensor Axes	50
4.7	Sensor Alignment Check and Calibration Relative to Standard Level Surface Plate	51
4.8	Electrolytic Leveler Monitor and Readout	52
4.9	Two-Axis Level Deviation Monitor	54
4.10	Sensor and Rotor Adaptation to Tower Top Mounting	55



# Contracts

<u>FIGURE</u>	<u>TITLE</u>	<u>PAGE</u>
4.11	Sensor and Rotor Adaptation to Instrument Booms	56
4.12	Sensor and Rotor with Direction Sensing and Control Cables	58
4.13	Rotor Power Junction Box	59
4.14	Single Rotor Control and Direction Heading Controller	61
4.15	Multiple Channel (10) Rotor Control and Direction Heading Controller	62
4.16	Sonic and Gill Anemometers with Rotor Adaptation to Tower Top Mountings	65
4.17	Typical Instrumentation System for TOLCAT Experiments	66
4.18	TOLCAT Grid Tower and Equipment Layout for First Phase Experiments	68
4.19	TOLCAT Grid Tower and Equipment Layout for Second Phase Experiments	69
4.20	TOLCAT Tower "T" Configuration at the 58-Meter Level	71
4.21	Sensor Array for Comparison Tests	73
4.22	Vertical Logarithmic Sensor Spacing for Single Tower Array	74
4.23	Logarithmically-Spaced "L" Configuration of Portable Collapsible Towers at 32-Meter Height	75
4.24	Logarithmically-Spaced "L" Array Including Tower 106 with Instrument Boom and Collapsible Towers at 32-Meter Height	77
4.25	Single Sensor - Sonic Anemometer - On Top of a Collapsible Tower Utilizing the 125-Meter Meteorology Tower	78
5.1	Diagram of the Data Conversion and Processing System	80
7.1	Hypothetical Spectrum, $S(n)$ , with Two Energy Sources (After Roth, Reference 7.2)	103
7.2	Van der Hoven's Spectrum of Horizontal Wind Speed, $S(n)$	104
7.3	Power Spectral Density, $S(n)$ , at 60 Meters, Test E508	107
7.4	Power Spectral Density, $S(n)$ , at 15 Meters, Test T603	108

# Contrails

<u>FIGURE</u>	<u>TITLE</u>	<u>PAGE</u>
7.5	HICAT Power Spectrum of Lateral Gust Velocity, Test T107, Run 18, 500 Lags	109
7.6	HICAT Power Spectrum of Longitudinal Gust Velocity, Test T107, Run 18, 500 Lags	110
7.7	Van der Hoven's Spectrum, nS(n)	112
7.8	Time and Space Correlations for $u'_a$ , Test T603	118
7.9	Time and Space Correlations for $v'_a$ , Test T603	119
7.10	Time and Space Correlations for $w'$ , Test T603	120
7.11	Time and Space Correlations for $u'_a$ , Test T704	123
7.12	Time and Space Correlations for $v'_a$ , Test T704	124
7.13	Time and Space Correlations for $w'$ , Test T704	125
7.14	Time and Space Correlations for $u'_a$ , Test T703	127
7.15	Time and Space Correlations for $v'_a$ , Test T703	128
7.16	Time and Space Correlations for $w'$ , Test T703	129
7.17	Phase Spectra - Separation Distance 4 Meters, Test T603	134
7.18	Phase Spectra - Separation Distance 8 Meters, Test T603	135
7.19	Phase Spectra - Separation Distance 12 Meters, Test T603	136
7.20	Phase Spectra - Separation Distance 16 Meters, Test T603	137
7.21	Phase Spectra - Separation Distance 24 Meters, Test T603	138
7.22	Phase Spectra - Separation Distance 32 Meters, Test T603	139
7.23	Phase Spectra - Separation Distance 48 Meters, Test T603	140
7.24	Phase Spectra - Separation Distance 64 Meters, Test T603	141
7.25	Nondimensional $w'$ Spectra for 3 Heights - Neutral Case	158
7.26	Dimensional $u'$ Spectra for 4 Heights - Neutral Case	161

# Contrails

<u>FIGURE</u>	<u>TITLE</u>	<u>PAGE</u>
7.27	Nondimensional $u'$ Spectra for 3 Heights - Neutral Case	162
7.28	Nondimensional $u'$ and $w'$ Spectra, Test T603	164
7.29	Nondimensional $u'$ and $w'$ Spectra, Test T701	165
7.30	Nondimensional $u'$ and $w'$ Spectra, Test T703	166
7.31	Nondimensional $u'$ and $w'$ Spectra, Test T704	167
7.32	Power Spectra from Two Tests at 131 Meters	169
7.33	Cospectra for $u'_a$ , Test T603	171
7.34	Quadrature Spectra for $u'_a$ , Test T603	172
7.35	Cospectra for $v'_a$ , Test T603	173
7.36	Quadrature Spectra for $v'_a$ , Test T603	174
7.37	Cospectra for $w'$ , Test T603	175
7.38	Quadrature Spectra for $w'$ , Test T603	176
7.39	Autocorrelation Functions for $u'_a$ , Test T603	182
7.40	Autocorrelation Functions for $v'_a$ , Test T603	183
7.41	Autocorrelation Functions for $w'$ , Test T603	184
7.42	Two-Argument Autocorrelation Function of $u'_a$ in Time and Space, Test T603	187
7.43	Two-Argument Autocorrelation Function of $v'_a$ in Time and Space, Test T603	188
7.44	Two-Argument Autocorrelation Function of $w'$ in Time and Space, Test T603	189
7.45	Two-Argument Autocorrelation Function of $u'_a$ in Time and Space, Test T704	190
7.46	Two-Argument Autocorrelation Function of $v'_a$ in Time and Space, Test T704	191
7.47	Two Argument Autocorrelation Function of $w'$ in Time and Space, Test T704	192

<u>FIGURE</u>	<u>TITLE</u>	<u>PAGE</u>
7.48	Display of 2nd Octant of Bispectral Computations	196
7.49	Positive and Negative Areas for Real and Imaginary Parts of $B_w(n_1, n_2)$ for T804	198
7.50	Vertical Component, W, Test T805	200
7.51	Equivalent Path of Integration for Horizontal Line when Mapped into First Octant	201
7.52	Bispectrum of One Argument - Integration of $B_i(n_1, n_2)$ over One Quadrant	203
7.53	Bispectrum of One Argument - Integration of $B_i(n_1, n_2)$ over One Octant	205
7.54	Joint Probability Density Function for $u'$ - No Filter, Test T704	208
7.55	Joint Probability Density Function for $u'$ - 300-Second High-Pass Filter, Test T704	209
7.56	Joint Probability Density Function for $u'$ - 60-Second High-Pass Filter, Test T704	210
7.57	Joint Probability Density Function for $u'$ - 12-Second High-Pass Filter, Test T704	211
8.1	Optimized TOLCAT Array	224
8.2	Traveling Instrument Boom	225
8.3	Micrometeorological Profile System Utilizing Gill Anemometers	228
8.4	Field Digital Recorder, Metrodata DL-620 in TOLCAT System	229
8.5	CARDS Trailer	231
8.6	CARDS Equipment	232
8.7	CARDS Digital Data Processing System - Major Assemblies	233
8.8	Optimized Configuration for Portable Wind Turbulence Data Acquisition System	234

# Contrails

FIGURE	TITLE	PAGE
II.1	Even Function, Skewed with Respect to Horizontal Axis	241
II.2	Odd Function, Skewed with Respect to Vertical Axis	242
II.3	Mapping of $Q_1(\tau_1, \tau_2)$ from First Octant into Remainder of $\tau_1, \tau_2$ Plane	244
II.4	Direct Mapping of $B_1(\omega_1, \omega_2)$ from First Octant into Third, Fourth, Seventh, and Eighth Octant	248
II.5	Complete Mapping of $B_1(\omega_1, \omega_2)$ from First Octant into Remainder of $\omega_1, \omega_2$ Plane	249
III.1	Two Dimensional X-Axis and Y-Axis Leveler Schematic	253
III.2	Level Monitor Calibration — X-Axis Versus Meter Indication	254
III.3	Level Monitor Calibration — Y-Axis Versus Meter Indication	255
III.4	Remote Long Line Rotor Control Junction Box	256
III.5	Rotor Control and Direction Heading System Schematic	257
III.6	Rotor and Instrument Direction Heading Calibration — Duo-Dial and Null Indicator Readout Versus Direction Heading	258
III.7	Rotor Control — Direction Heading — Level Monitor System Diagram	259
IV.1	Phase Spectra — Separation Distance 32 Meters, Test T703	261
IV.2	Phase Spectra — Separation Distance 64 Meters, Test T703	262
IV.3	Phase Spectra — Separation Distance 7.5 Meters, Test T202	263
IV.4	Phase Spectra — Separation Distance 223 Meters, Test T105	264
IV.5	Probability Density Function for $u', v', w'$ , Test T701, No Filter	265
IV.6	Probability Density Function for $u', v', w'$ , Test T701, 300-Second High-Pass Filter	266
IV.7	Probability Density Function for $u', v', w'$ , Test T701, 60-Second High-Pass Filter	267
IV.8	Probability Density Function for $u', v', w'$ , Test T701, 12-Second High-Pass Filter	268

# Contrails

<u>FIGURE</u>	<u>TITLE</u>	<u>PAGE</u>
IV.9	Probability Density Function for $u'$ , $v'$ , $w'$ , Test T704, No Filter	269
IV.10	Probability Density Function for $u'$ , $v'$ , $w'$ , Test T704, 300-Second High-Pass Filter	270
IV.11	Probability Density Function for $u'$ , $v'$ , $w'$ , Test T704, 60-Second High-Pass Filter	271
IV.12	Probability Density Function for $u'$ , $v'$ , $w'$ , Test T704, 12-Second High-Pass Filter	272
IV.13	Joint Probability Density Function for $u'$ , Test T704, Separation Distance 4 Meters	273
IV.14	Joint Probability Density Function for $v'$ , Test T704, Separation Distance 4 Meters	274
IV.15	Joint Probability Density Function for $w'$ , Test T704, Separation Distance 4 Meters	275
IV.16	Joint Probability Density Function for $v'$ , Test T704, Separation Distance 8 Meters	276
IV.17	Joint Probability Density Function for $w'$ , Test T704, Separation Distance 8 Meters	277
IV.18	Joint Probability Density Function for $u'$ , Test T704, Separation Distance 12 Meters	278
IV.19	Joint Probability Density Function for $v'$ , Test T704, Separation Distance 12 Meters	279
IV.20	Joint Probability Density Function for $w'$ , Test T704, Separation Distance 12 Meters	280

## LIST OF TABLES

<u>TABLE</u>	<u>TITLE</u>	<u>PAGE</u>
3.1	Fraction of Cosine Response for Gill Anemometer	29
7.1	Experimental Arrays for Meteorological Analysis	98
7.2	Tests Analyzed for TOLCAT	101
7.3	Parameters for TOLCAT Tests	116
7.4	Correlation From Test T202	132
7.5	Comparable Phase Spectral and Coherency Analyses for Seven-Minute Data	145
7.6	Summary of Phase Spectral and Coherency Analyses	146
7.7	Ratios of Variance ( $\sigma_u^2$ , $\sigma_v^2$ , $\sigma_w^2$ ) to $-\overline{u'w'}(z)$ and to $\bar{U}^2(15)$	149
7.8	Effects of High Frequency Truncation on Variances and $\overline{u'w'}$	152
7.9	Magnitude Correlations for 15, 30, and 60-Meter Data	154
7.10	Magnitude Correlations for 131-Meter Data	154
7.11	Normalizing Parameters for Four TOLCAT Tests	163
7.12	Characteristic Time and Length Values from Autocorrelation Functions	185
7.13	Cross-Correlations from T-Array Data	194
II.1	Linear Transformation Matrices of Mapping Equations for the Bispectrum	250



## NOTATIONS

### Symbols, Subscripts, and Abbreviations

$B_x(\omega_1, \omega_2)$	Bispectrum — double Fourier transform of $Q_x(\tau_1, \tau_2)$
$C_x(n)$	Complex Fourier coefficient for $x'$ at frequency $n$
$c_p$	Specific heat at constant pressure
$Co_x(n)$	Banded cospectrum estimate at frequency $n$ for $x'$ measured at two locations
$Co_{xy}(n)$	Banded cospectrum estimate at frequency $n$ for $x'$ and $y'$
$Coh_{xy}(n)$	Banded coherency spectrum estimate at frequency $n$ for $x'$ and $y'$
$E[x]$	Expectation of $x$
$F_m$	Upper frequency limit of single argument bispectral function
$F(z/L)$	Universal function of $z/L$
$f$	Nondimensional frequency, $nz/\bar{U}$
$f_x$	Nondimensional frequency exhibiting peak value of the spectrum $nS_x(n)$
$g$	Mean gravitational acceleration at the earth's surface
$H$	Heat flux (energy per unit area per unit time)
$Hz$	Hertz (cycles per second)
$h_n$	Effective cutoff frequency used in tanh filter
$k$	Von Karman's constant, empirically evaluated from 0.35 to 0.40
$K_h$	Coefficient of eddy diffusivity for heat
$K_m$	Coefficient of eddy diffusivity for momentum
$K_x$	Universal constant in numerator of empirical formulae for the spectral quantity, $nS_x(n)$
$L$	Anemometer distance constant (in Section III only)

# Contrails

L	The Monin-Obukov characteristic length
$L_o$	Length constant in exponential correlation function for turbulence in one spatial dimension
$M_{xy}$	Magnitude correlation of $x'$ , $y'$
m	Meters
mps	Meters per second
n	Frequency (cycles per unit time)
$n_c$	Highest frequency for which coherency is $e^{-1}$ or greater for a given data sample
$n_o$	Lowest frequency at which Taylor's hypothesis holds for a given data sample
$n_{1/2}$	Frequency above which anemometer response is less than 71%
p	Atmospheric pressure
$Q_x(\tau_1, \tau_2)$	Third-order covariance function for $x'$ with two time lags
$Qu_x(n)$	Banded quadrature spectrum estimate at frequency n for $x'$ measured at two locations
$Qu_{xy}(n)$	Banded quadrature spectrum estimate at frequency n for $x'$ and $y'$
$R_x(\tau)$	Autocorrelation function of $x'$ at time lag $\tau$
$\tilde{R}_x(\tau)$	Autocovariance function of $x'$ at time lag $\tau$
$R_{xy}(\tau)$	Cross-correlation function for $x'$ and $y'$ at time lag $\tau$
$\tilde{R}_{xy}(\tau)$	Cross-covariance function for $x'$ and $y'$ at time lag $\tau$
$R_x(\xi)$	Pseudo-spatial autocorrelation of $x'$ at space lag $\xi$
$\tilde{R}_x(\xi)$	Pseudo-spatial autocovariance of $x'$ at space lag $\xi$
$R_{xy}(\xi)$	Pseudo-spatial correlation of $x'$ and $y'$ , computed by time averaging field data for $x'$ and $y'$ from two sensors separated by distance $\xi$

# Contrails

$\tilde{R}_{yx}(\xi)$	Pseudo-spatial covariance of $x'$ and $y'$ , computed by time averaging field data for $x'$ and $y'$ from two sensors separated by distance $\xi$
$R_{xy}(\tau, \xi)$	Pseudo-spatial correlation of $x'$ and $y'$ with arguments for time lag and space lag
$\tilde{R}_{xy}(\tau, \xi)$	Pseudo-spatial covariance of $x'$ and $y'$ with arguments for time lag and space lag
$S_x(n)$	Banded power spectral estimate or empirical formula of power spectral estimate for $x'$ at frequency $n$ , $\approx S^*(n) + S^*(-n)$
$S_x^*(n)$	True power spectrum of $x'$ at frequency $n$
$t$	Time
$T$	Time span of data sample under consideration
$T_o$	Time constant in exponential correlation function for time series
$U, V, W$	Three dimensional velocity components with $U$ in direction of mean wind
$U_a, V_a$	Horizontal velocity components in an arbitrary frame of reference
$u', v', w'$	Three dimension wind components with means removed and with $u'$ in direction of mean wind
$u'_a, v'_a$	Horizontal velocity wind components in an arbitrary frame of reference, with means removed
$u^*$	Friction velocity, equal to the square root of $\tau_o/\rho$
$X_x(\xi)$	Spatial autocovariance of $x'$ at space lag $\xi$
$X_{xy}(\xi)$	Spatial covariance of $x'$ and $y'$ at space lag $\xi$
$x, y, z$	Right-handed coordinate system with $x$ in direction of mean wind
$x_a, y_a, z$	Right-handed coordinate system with $x'_a$ in an arbitrary horizontal direction
$x, y$	Generalized variables in this index

# Contrails

$x'$	Fluctuations in $x$
$\bar{x}$	Time average of $x$
$x_i$	First order tensor notation for $x'$
$x_{ij}$	Second-order tensor notation for $x'$
$x'_A$	$x'$ measured at location A
$x'_\alpha x'_\alpha$	Second-order tensor notation for $x'$ without summation
$x'_S$	$(x')_A + (x')_B$
$x'_d$	$(x')_A - (x')_B$
$z_c$	Any height in the constant flux layer
$z_o$	Length characterizing surface roughness
$\beta$	Anemometer phase lag
$\beta_x(n_1)$	$\int_{-\infty}^{\infty} B_x(n_1, n_2) dn_2$
$\tilde{\beta}_x(n_1)$	$\int_0^{\infty} B_x(n_1, n_2) dn_2$
$\tilde{\tilde{\beta}}_x(n_1)$	$\int_{n_1}^{\infty} B_x(n_1, n_2) dn_2$
$\Delta t$	Discrete sampling micro-time interval
$\theta$	Potential temperature
$\theta$	Absolute temperature
$\theta'$	Temperature fluctuation
$\kappa$	Wave number (radians per unit length), $2\pi/\lambda$
$\lambda$	Wave length

# Contrails

$\nu$	Kinematic viscosity
$\xi_1, \xi_2, \xi_3$	Space lags in three orthogonal directions
$\rho$	Density
$\sigma_x^2$	Variance of $x'$
$\tau$	Time lag in covariance function or correlation function
$\tau_m$	Time lag of maximum cross correlation between two stochastic variables
$\tau_o$	Surface stress
$T$	Anemometer time constant
$\phi(n)$	$\phi_{xy}(n)$ with subscripts suppressed
$\phi_o$	Theoretical value of phase spectrum for that frequency at which coherency falls below $e^{-1}$ for parallel wind components measured from separate towers
$\phi_e(z/L)$	Nondimensional dissipation
$\phi_m(z/L)$	Nondimensional mechanical turbulence energy or nondimensional shear
$\phi_{xy}(n)$	Banded phase spectrum estimate at frequency $n$ for $x'$ and $y'$ (Subscripts may be dropped when meaning is clear.)
$\omega$	Angular frequency (radians per unit time)

## SECTION I

### INTRODUCTION

Turbulence encountered during take-off and landing can at times present serious hazards to aircraft and, in particular, to V/STOL aircraft. The temporal aspects of turbulence near the ground have been studied and modeling of its structure has been given some attention. However, aircraft experience a field of turbulence both temporally and spatially, and little is known about the spatial aspects of turbulence. Consequently, the Take-Off and Landing Critical Atmospheric Turbulence Project (TOLCAT) was initiated to develop experimentally the necessary knowledge of turbulence in the boundary layer, its dependence on height, terrain features and meteorological variables, and to determine the interrelationship between temporal and spatial characteristics. To accomplish these ends, it was recognized that investigations of turbulence from multiple towers, undertaken for the Air Force by Battelle, Pacific Northwest Laboratories, should place emphasis on several objectives. These are:

- to evaluate and select supports and mountings to assure adequate turbulence measurements;
- to establish and optimize field data recording and logging capabilities;
- to establish and optimize data handling procedures, including digitizing, editing, and instrument corrections;
- to develop analysis programs for describing characteristics of turbulence structure pertinent to aircraft design and operation;
- to collect data for demonstrating and testing the measurement system and analysis techniques; and
- to determine meteorological aspects from the data analysis concerning the validity of Taylor's hypothesis and the definition of



# Contrails

spatial turbulence scales existing at various levels, alongwind and crosswind, such that the minimum number of measurement points and their optimum spacing can be determined for further experiments.

The initial TOLCAT experimental measurement system investigation was conducted during 1968 and 1969. Results of that investigation are presented in Technical Report AFFDL-TR-70-117 entitled, "Take-Off and Landing Critical Atmospheric Turbulence (TOLCAT) Experimental Investigation" (hereafter this report will be referred to as the TOLCAT Interim Report (Reference 1.1)). This investigation accomplished some of the above objectives, including an initial evaluation of instruments and their operation in a widely dispersed measurement system, and the final selection of instruments to be used for continued testing and identification of useful modifications to those instruments. Initial selections of supports and mountings were made and these were evaluated both from an operational standpoint and in relation to effects on the data collected. Necessary improvements on instrument mounting equipment were identified to overcome vibrations, tower influences, and sensor leveling and orientation difficulties. An analog field recording system was also established for accepting up to 26 signals from turbulence sensors. A medium range, multiple-purpose computer, SEL 840A, was utilized for data processing tasks, which transferred the data from the field analog tapes to computer compatible digital tapes, accomplishing the necessary editing and instrument corrections. Both hardware and software improvements were identified for future investigations. Analysis programs were also written for the UNIVAC 1108 to perform fast Fourier transform spectral and cross-spectral calculations, correlation function calculations, and probability distribution determinations. Finally, seven field experiments were conducted to be used in evaluating the measurement system and the techniques of data reduction and analysis.

To complete the overall TOLCAT objectives, a second experimental investigation was conducted and is the subject of this report. The first experimental investigation results are only briefly reviewed and related to objectives



# Contrails

and results of this second experimental phase of the TOLCAT project. For details of the first experimental phase, reference is made to the Interim Report. The second experimental phase of TOLCAT, then, undertook to modify and test the turbulence sensors and select the final instrument configuration to be used in the future experiments and to expand the field tape recording ability with digital recording. Furthermore, the transfer of field data to computer compatible digital tape was to be made more versatile by broadening the digitizing rate capability, by improving data editing, and by providing for the TOLCAT data handling hardware and software on the SEL 840A to accommodate field digital tapes as well as analog tapes. Analysis programs were also to be refined, allowing more efficient joint analyses of various wind component signals by adapting UNIVAC 1108 drum storage for the data, to provide detrending options, and to establish bispectral calculation capabilities for better evaluation of intermittent and nonsymmetric aspects of turbulence. Considerable emphasis for this second experimental phase of TOLCAT was directed toward measurement of turbulence data suitable for meteorological analyses and conclusions. These, in turn, would be used to optimize the measurement array configurations, i.e., to minimize the number of sensors and determine the best separations at various heights on towers for continued experimental investigation of TOLCAT.

## SECTION II

### THEORY

The physical phenomenon under investigation in the TOLCAT studies is the atmospheric turbulence in the lowest few hundred feet immediately above the ground. This phenomenon may properly be called boundary layer turbulence, which for purpose of study, is considered to be homogeneous in any horizontal direction and of changing statistical properties in the vertical.

By definition all turbulent motion is stochastic, three-dimensional, rotational, and dissipative. In the atmospheric boundary layer, turbulence is the end result of two very different physical situations that deform flow that would otherwise be uniform over the length scales that characterize turbulent flow.

The first of these is inherent in all boundary layer flow. In such flow the fluid is required to obey the no-slip boundary condition at the surface and to follow a free-stream velocity at some height above the surface. Thus the boundary layer can be envisioned as a region of competing forces that are inertial on one side and viscous on the other side. The fundamental physical equilibrium in boundary layer flow must be found between inertial and viscous forces. (Large scale generative forces are included as inertial forces.) In laminar flow the molecular viscous force is sufficient to offset the inertial forces. But when the molecular viscous force is small compared to the inertial force (as is the case in the atmosphere), the fluid becomes hydrodynamically unstable. The viscous side of the struggle acquires an enormous ally called turbulence that deforms the original flow into a continuum of eddy sizes, the largest of which are related to the height of the boundary layer and the smallest of which are the length scale where the molecular viscosity can act as the final sink — the eddy size with a Reynolds number of unity.

# Contrails

This type of turbulence is commonly called mechanical turbulence and is thus distinguished from convective turbulence, which will be described in the next paragraph. But before leaving the subject of mechanical turbulence, it must be born in mind that in the atmospheric boundary layer, the essential shearing pattern that develops — composed of a primary shear,  $d\bar{U}/dz$ , and shears of other orders associated with the turbulence — is influenced by the character of roughness elements at the surface.

The second cause of deformation of the atmospheric boundary layer flow is departure of the temperature lapse rate in the vertical from the adiabatic. When the rate of temperature decrease with height is greater than the adiabatic, upward turbulence motion is correlated with importation of lesser density, and further upward motion is thus encouraged. Likewise downwind turbulence motions import higher density and further downward motion is thus encouraged. This condition is commonly referred to as instability, or the unstable case. When instability is slight, the turbulence regime is referred to as forced convection, and in modeling studies this type of turbulence is treated as a modification of mechanical turbulence. When the instability is greater, the regime is referred to as free convection and must be modeled by different characteristic parameters than those used for modeling mechanical turbulence and/or forced convection (Reference 2.1). This type of turbulence is most likely to contain marked intermittent features such as plumes, dust devils, and other thermal effects at greater heights leading to the formation of deep convective clouds.

When the vertical temperature gradient is less than the adiabatic (or when the temperature increases with height), the vertical motions of turbulence are discouraged. This condition is commonly referred to as the stable case. Although it is generally expected that turbulence will be inhibited in stable air, this is not always the case. Stable stratification can be shown (Reference 2.2) to be a physical mechanism for generating turbulence as well as for inhibiting it.

To summarize, it may be said that any given sample of turbulence can be made up in varying proportions of two very different physical phenomena which interact with each other to a limited extent in ways not yet fully understood. One is called mechanical turbulence and at the present state-of-the-art is the most clearly understood. The other, convective turbulence, includes stable stratification, forced convection, and free convection. In the lowest few hundred feet these types may be simultaneously present in different layers, each in its own way modifying or supplanting the mechanical turbulence. This is the combination at which unified and comprehensive explanation, description, and modeling must ultimately be aimed.

## BASIC MATHEMATICAL DESCRIPTION OF TURBULENCE

Boundary layer turbulence is customarily described in a right-handed Cartesian coordinate system (x, y, z) with the x-axis oriented in the direction of the mean wind (assumed horizontal) and the z-axis oriented vertically. The total wind components along the x, y, and z axis are called U, V, and W, respectively. The turbulence components, u', v', and w' are fluctuations about a mean defined with reference to a time scale, T, that is long compared to the time scale of the fluctuations. The wind fluctuation, u', is related to U by the equation

$$U(t) = \bar{U} + u'(t) \quad (2.1)$$

where  $\bar{U}$  is the mean value of the wind in the x direction, and is given over time, T, by

$$\bar{U} = \frac{1}{T} \int_0^T U(t) dt \quad (2.2)$$

Because of the orientation of the axes, the mean values of V and W are zero, therefore

$$V(t) = v'(t) \quad (2.3)$$

$$W(t) = w'(t) \quad (2.4)$$

Since these variables are stochastic, the more sophisticated turbulence descriptors are all probabilistic in nature. Moments, spectral decomposition of these moments, correlation functions (mutual Fourier transforms with the spectra) and probability distributions are defined and computed from  $u'$ ,  $w'$ , and  $w'$ , both individually and jointly.

Definitions of the above turbulence descriptors are given below in mathematical tensor notation. The arguments of the functions below are in time and frequency as is appropriate for time series analysis. The expectation operator,  $E$ , is considered equivalent to time averaging. All the functions below may also be defined with arguments in space, or with arguments of both space and time. For all these definitions,  $i = 1, 2, 3$ ;  $j = 1, 2, 3$ , applies.

Second order moments

$$\overline{u_i u_j} = E[u_i u_j] \quad (2.5)$$

Covariance tensor

$$\tilde{R}_{ij}(\tau) = E[u_i(t) u_j(t+\tau)] \quad (2.6)$$

Spectral tensor

$$S_{ij}^*(n) = \int_{-\infty}^{\infty} \tilde{R}_{ij}(\tau) e^{-i2\pi n\tau} d\tau \quad (2.7)$$

Spectral tensor as computed

# Contrails

$$\hat{S}_{ij}(n) = \frac{1}{T} \overline{C_i(n)} C_j(n) \quad (2.8)$$

where

$$C_i(n) = \int_{-\infty}^{\infty} u_i(t) e^{-i2\pi nt} dt \quad (2.9)$$

and the bar, in Equation 2.8, denotes the complex conjugate.

The moments are related to the computed spectra by

$$u_i u_j = \int_{-\infty}^{\infty} S^*_{ij}(n) dn \quad (2.10)$$

Excellent systematic expositions of these descriptors can be found in References 2.3 and 2.4.

Orienting the coordinate system with the mean wind is not always desirable. An aircraft in turbulent flow has its own right-handed coordinate system with the x-axis along the fuselage; therefore, it is necessary to define turbulence components also in this frame of reference and to analyze them with the above descriptors. The notation ( $x_a$ ,  $y_a$ , and  $z$ ) will be used for this arbitrary direction of the coordinate system relative to the field of turbulence. The lack of a subscript for  $z$  indicates that horizontal orientation of the fuselage is assumed. In the arbitrary frame of reference the total wind components will be called  $U_a$ ,  $V_a$ , and  $W$ ; the average values,  $\bar{U}_a$ ,  $\bar{V}_a$ , and  $\bar{W}$ ; and the turbulence components  $u'_a$ ,  $v'_a$ , and  $w'$ . Here, both  $\bar{U}_a$  and  $\bar{V}_a$  will have non-zero values.

Turbulence description with respect to the arbitrary frame of reference is a function of the azimuth angle between the fuselage orientation and the mean wind direction as seen by the aircraft.



## CHARACTERISTIC VELOCITIES AND LENGTHS

In order to model turbulence it is necessary to have measures of velocity and length that are uniquely characteristic of the physical process. Two velocities immediately suggest themselves — the average speed in the direction of the mean flow and some measure of the deviations from that mean. In the surface boundary layer  $\bar{U}$  and  $u^*$ , respectively, are usually considered to be these characteristic velocities. The latter quantity, friction velocity, is the square root of the stress exerted by the atmosphere on the surface. Mathematically it is the moment defined by Equation 2.5 when  $i = 1$  and  $j = 3$  and may be calculated from the correlation induced in the longitudinal and vertical components of the wind by the downward transfer of momentum producing the surface stress. The relation may be written

$$u^{*2} = \tau_0 / \rho = - \overline{u'w'}(z_c) \quad (2.11)$$

where  $z_c$  is any height in a layer across which  $\overline{u'w'}$  is expected to be constant, while  $\bar{U}(z)$  increases with height. Although this layer is usually considered as prevailing across the first few decades of meters above the surface, analysis of recent measurements suggest that profiles of both  $\overline{u'w'}$  and  $\bar{U}$  are influenced by convective activity and by the character of surface roughness elements.

In connection with the previous discussion of the balance between inertial and turbulence-viscous forces, it seems natural to consider  $\bar{U}(z)$  as representative of the inertial force and  $u^*$  as representative of the turbulence-viscous force. Since the ratio in the constant flux layer,  $\bar{U}(z)/u^*$ , is characteristically 10 or greater, the numerical inequality is apparently characteristic of equilibrium. Perhaps heuristic insight may be gained by noting that the inertial force acts theoretically in one direction only, whereas the turbulence-viscous force acts in all directions, thus compensating for its lower numerical value — lower by an order of magnitude or more. This is all very well for later convenience, as will be seen in the



# Contrails

discussion of Taylor's hypothesis. The primary condition for its validity is that  $\bar{U}(z)/u^*$  be large.

When the turbulence is convectively modified, there is a height range across which the turbulence exhibits a transition from being predominantly mechanical to predominantly convective. A length that is characteristic of this transition would be directly proportional to the intensity of the mechanical turbulence, and inversely proportional to the intensity of the convective activity. By assuming that the essential theoretical basis of boundary layer turbulence can be formulated from consideration of the surface stress,  $u^{*2}$ , the surface heat flux,  $H/\rho c_p$ , and the buoyancy parameter,  $g/\theta$ , and then by combining these parameters so as to obtain a parameter with the dimension of length, the Monin-Obukov  $L$  is derived.

This stability length is expressed as

$$L = \frac{-u^{*3}}{\frac{kg}{\theta} \frac{H}{\rho c_p}} \quad (2.12)$$

where  $k$  is Von Karman's constant.

Because of the sign of the heat flux, the  $L$  is positive for stable conditions and negative for unstable conditions.  $L$  is infinite for neutral conditions.

The characteristic length that is used to nondimensionalize actual turbulent eddy size dimensions in the boundary layer is the height,  $z$ , above the boundary. The nondimensional height  $z/L$  is considered proportional to the ratios of convective to mechanical production of the turbulence. Boundary layer turbulence is modeled as a function of this quantity.

## THE FUNDAMENTAL TOLCAT INVESTIGATION

Turbulence is a phenomenon of variation in both time and in three-dimensional space. However, the TOLCAT studies are primarily concerned with two types of time series as shown in Figure 2.1.

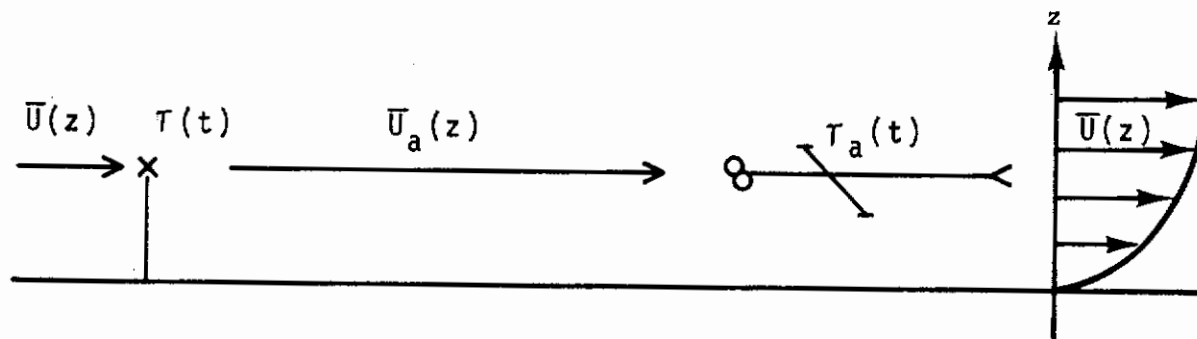


Figure 2.1 Turbulence as seen by an Anemometer and by an Aircraft

The first of these is the variation with time,  $u'$ ,  $v'$ , and  $w'$  encountered by a turbulence sensor exposed to the turbulence from a stationary mount. The turbulence,  $\tau(t)$ , is brought to the sensor by the mean wind speed,  $\bar{U}(z)$ . The second type of time series,  $\tau_a$  is that experienced by the moving aircraft. It is the same turbulence, brought to the aircraft by a mean wind speed,  $\bar{U}_a(z)$ , as seen by the aircraft, i.e., the magnitude of the vector difference between the mean wind velocity vector and the flight velocity vector of the aircraft. Both views of the turbulence are related to the three-dimensional spatial turbulence. The primary purpose of the TOLCAT work is to provide, through turbulence time series from a limited number of sensors on stationary mounts, a partial description of the spatial features of the turbulence (a complete description would require

# Contrails

an impossible number of sensors), such that turbulence characteristics experienced by an aircraft moving through the same fluid could be inferred.

The theory needed to relate the turbulence as seen from both the stationary and moving platforms to the spatial description of turbulence can be provided by first considering the special case of the turbulence along the direction of mean flow. Beginning with the equation of motion for incompressible flow of constant viscosity it may be written

$$\frac{\partial u_i}{\partial t} + \bar{U} \frac{\partial u_i}{\partial x_1} = - u_j \frac{\partial u_i}{\partial x_j} - \frac{1}{\rho} \frac{\partial p}{\partial x_i} + \nu \frac{\partial^2 u_i}{\partial x_k \partial x_k} + g \frac{\theta}{\theta} \delta_{i3} . \quad (2.13)$$

Usually for such flow the ratio  $\bar{U}^2/u'^2$  turns out to be quite large (100 or more), and under such conditions all the terms on the right of Equation 2.13 are small compared to those on the left (Reference 2.3). Under these conditions the following relation holds approximately to

$$\frac{\partial u_i}{\partial t} \approx - \bar{U} \frac{\partial u_i}{\partial x_1} \quad i = 1, 2, 3 \quad . \quad (2.14)$$

Equation 2.14 predicts that the turbulence variations in time at one point are the same as the one-dimensional variations of the turbulence components in the direction of the mean wind advected past the point.

Even though this concept of "frozen turbulence" cannot be exactly so, the approximation may be close enough that statistical analyses of the time series for each component  $u'$ ,  $v'$ , and  $w'$  will correspond to the statistical properties of the same components in space in the direction of the mean wind.

To be specific, if the process possesses second order stationarity, second order expectation tensors for the time series at a single point are defined

# Contrails

by Equation 2.6. If  $i = j$  this is an autocovariance function. Otherwise it is a cross-covariance function. Along the direction of the mean wind the spatial correlations may be defined in the same way, i.e.,

$$X_{ij}(\xi_1) = E[u_i(x_1) u_j(x_1 + \xi_1)] \quad . \quad (2.15)$$

Assuming that the following relation also holds

$$(\bar{U}/u^*)^2 \gg 1 \quad , \quad (2.16)$$

the concept proposed by Equation 2.14 can now be generalized to assume

$$\tilde{R}_{ij}(\tau) \approx X_{ij}(\xi) \quad \text{when } \xi = \bar{U}\tau \quad . \quad (2.17)$$

This is commonly known as Taylor's hypothesis.

Considering now the turbulence encountered by the aircraft, the first observation to be made is that both the stationary sensor and the aircraft are moving points relative to the fluid. Also, initially considering the case where the following inequalities hold:

$$(\bar{U}_a/u^*)^2 > (\bar{U}/u^*)^2 \gg 1 \quad . \quad (2.18)$$

By the same method of hypothesis, Taylor's reasoning may be extended to apply to a point (the aircraft) moving in the direction of the mean wind, and the following may be written:

$$\left( \frac{\partial u_i}{\partial t} \right)_a \approx - \bar{U}_a \frac{\partial u_i}{\partial x_1} \quad (2.19)$$

and

$$\tilde{R}_{ij}(\tau_a) \approx X_{ij}(\xi) \quad \text{when } \xi = \tau_a \bar{U}_a \quad . \quad (2.20)$$

For the conditions of the first inequality in Equation 2.18, the approximations in Equations 2.19 and 2.20 should be better than the corresponding approximations for the stationary point equations. Finally, then, one would expect that the following approximation, suggested by Equations 2.17 and 2.20, holds:

$$\tilde{R}_{ij}(\tau_a) = R_{ij}(\tau) \quad \text{when } \bar{U}\tau = \bar{U}_a \tau_a \quad . \quad (2.21)$$

The hypothesis now indicates that the covariance tensor applying to the turbulence at the stationary point is essentially the same function as the covariance tensor applying to the turbulence for the moving point but on a different time scale. If this is so, the spectral transforms of these two covariance tensors are the same spectral function on different frequency scales, shifted by the ratio of the aircraft speed to the wind speed. The model thus described involves certain very restrictive assumptions about the flight of the aircraft. They are:

1. The flight of the aircraft is in a single horizontal direction such that the mean wind velocity vector seen by the aircraft is head-on.
2. The aircraft may be considered as a point mass moving at a height at which the time series characteristics of the turbulence is known.
3. The turbulence is horizontally homogeneous over the flight path.

For shear flow, such as prevails in the surface boundary layer, Lin (Reference 2.5) concluded that Taylor's hypothesis holds only for those waves with wave number above a certain lower limit. He expressed this limitation by writing that Taylor's hypothesis should hold for all wave numbers,  $\kappa$ , such that

# Contrails

$$\kappa \bar{U} \gg \partial \bar{U} / \partial z \quad . \quad (2.22)$$

The wave number  $\kappa$  is related to the wave length  $\gamma$  by  $\kappa \gamma = 2\pi$ .

For all  $\kappa$  for which Equation 2.22 holds, Taylor's hypothesis relates the wave number and the frequency,  $n$ , at which the wave causes variation at a stationary sensor by

$$\kappa \bar{U} = 2\pi n \quad . \quad (2.23)$$

Substituting Equation 2.23 into 2.22, the condition for Taylor's hypothesis to hold, which becomes a companion condition to Equation 2.16, may be written

$$\frac{2\pi n}{\partial \bar{U} / \partial z} \gg 1 \quad . \quad (2.24)$$

Equation 2.24 predicts no upper limit for the frequency range over which Taylor's hypothesis applies. In subsequent turbulence investigations the assumption of no effective upper limit frequency has been an indispensable feature of the spectral modeling that has become accepted from single point time series data; see for example Reference 2.6. These models indicate that for the frequencies of the inertial subrange, the power spectrum is proportional to the minus 5/3 power of the frequency,  $n$ . Kolmogoroff's similarity theory establishes the essential physical relationship using wave number,  $\kappa$ , rather than frequency. Therefore spectral modeling as a function of  $\kappa$  is more primary than spectral modeling as a function of  $n/\bar{U}$ , the latter being justified only if Taylor's hypothesis is assumed to hold throughout the frequency range under investigation.

However, since spectral plots exhibit the same behavior for  $n$  at high frequencies as is expected for  $\kappa$ , namely the minus 5/3 slope, and especially since spectra from different tests show consistent agreement



in the high frequency ranges, Taylor's hypothesis may be assumed to hold for the higher frequencies subject to investigation, at least for a certain eddy translation speed which may or may not be equal to the mean wind speed.

Therefore two evaluations of Taylor's hypothesis must be made that cannot be made from the correlation function alone -- the lower frequency limit at which Taylor's hypothesis applies and the relationship of the eddy translation speed to the mean wind speed.

A convenient tool for both investigations is the phase spectrum between parallel components measured at two locations in the alongwind direction. If a cross-spectral analysis is made between one of the three turbulence components as measured at two locations separated by a distance,  $\xi$ , Taylor's hypothesis predicts that the phase spectrum in radians for a given frequency,  $n$ , will be

$$\phi(n) = \frac{2\pi n \xi}{U} \quad (2.25)$$

This relation may be derived from the definition of the phase spectrum and the assumption of Taylor's hypothesis as shown in Appendix I.

When phase spectra from field data are plotted in graphs of  $\phi(n)$  versus  $n$ , the range over which they follow the equation can be determined. Also, whether or not a different eddy translation speed would better model the data is readily apparent from any consistent displacement of the data from the curve given by Equation 2.25.

To summarize, for the special case of the spatial turbulence characteristics along the direction of mean flow, verification will first be sought that temporal and one-dimensional spatial turbulence are related to a good approximation in the manner expected from Equation 2.17. (Initial investigations have been only for the autocovariance components of the tensor.)



If this approximation holds the relation involving turbulence as seen by the aircraft expressed in Equations 2.20 and 2.21 may also be assumed valid, by extending Taylor's method of hypothesis to apply to a moving point. Finally, by using Equation 2.25 a lower limit will be established for the frequencies over which Taylor's hypothesis applies and for the frequency range over which spectra measured at stationary points can appropriately be shifted by the ratio of aircraft speed to wind speed to provide a portion of the spectra encountered by the aircraft.

Consider now removing some of the restrictions of the foregoing discussion. First, consider that the first inequality in Equation 2.18 no longer holds. If Equation 2.19 is thought of as a filtered version of the equation of motion applying to an aircraft flying at an airspeed greater than the mean wind,  $\bar{U}$ , there is interest in considering a very different filtered version applying to the aircraft hovering at airspeed zero, or at ground speed,  $\bar{U}$ . The equation applying here is the following modified form of Equation 2.13,

$$\left(\frac{\partial u_i}{\partial t}\right)_a = -u_j \frac{\partial u_i}{\partial x_j} - \frac{1}{\rho} \frac{\partial p}{\partial x_i} - v \frac{\partial^2 u_i}{\partial x_k \partial x_k} + g \frac{\theta}{\theta} \delta_{i3} \quad (2.26)$$

In contrast to Equation 2.19, which shows the turbulence as seen by the aircraft to be linearly related to the variation of the turbulence in the longitudinal direction, Equation 2.26 shows the turbulence as seen by the aircraft to be related to the spatial turbulence in a nonlinear manner. The two filters show the same spatial turbulence energy in different frequency distributions.

If an aircraft can be imagined to fly first at airspeed zero and then gradually to attain a considerable airspeed, the turbulence as seen by the aircraft would be first of the type represented by Equation 2.26. This would gradually fade out and be replaced by turbulence of the type represented by Equation 2.19. In other words the turbulence as seen by the aircraft in this flight pattern is seen through one filter that is being

"turned off" while another filter is being "turned on."

An aircraft moving through space in the direction and at the speed of the mean wind would experience a turbulence time series having the following correlation function for, say, the longitudinal wind component

$$\tilde{R}(\tau) = E[u'_x(t) u'_{x+\xi}(t+\xi/\bar{U})] \quad . \quad (2.27)$$

For a given separation,  $\xi$ , the aircraft would sample over several points in space as it moved, to form the expectation indicated. Moving at the mean wind speed, however, would result in a relatively small volume of air, also moving with the mean wind speed, being continuously encountered by the aircraft.

The same expression as Equation 2.27 describes the correlation function determined for measurements taken from a line of fixed towers at the height of the aircraft oriented along the mean wind. In this case,  $x$  and  $x + \xi$  are the fixed locations of two towers, and the expectation is a time average. Also, expectations formed from these data result from sampling a quite different volume of air. Here, the air moves continuously by the sensor and includes only a small portion, that volume from which the aircraft samples.

Thus because turbulence is highly intermittent, the correlation function experienced by a single aircraft may differ significantly from that determined from the series of towers. However, the tower results should be representative of what would be experienced, on the average, by a number of aircraft, moving at the mean wind speed. Theoretically the ergodic assumption to the effect that for a stationary homogeneous process all types of averaging are equivalent is involved.

The desired correlation function along the flight path may be obtained on the space-time correlation diagram of Figure 2.2 by drawing a line  $\xi = U_a \tau_a$

across the isopleths of correlation and projecting this line on the  $\tau$ -axis (Reference 2.7). Also, the power spectrum along the flight path can be obtained as the Fourier transform of the correlation function.

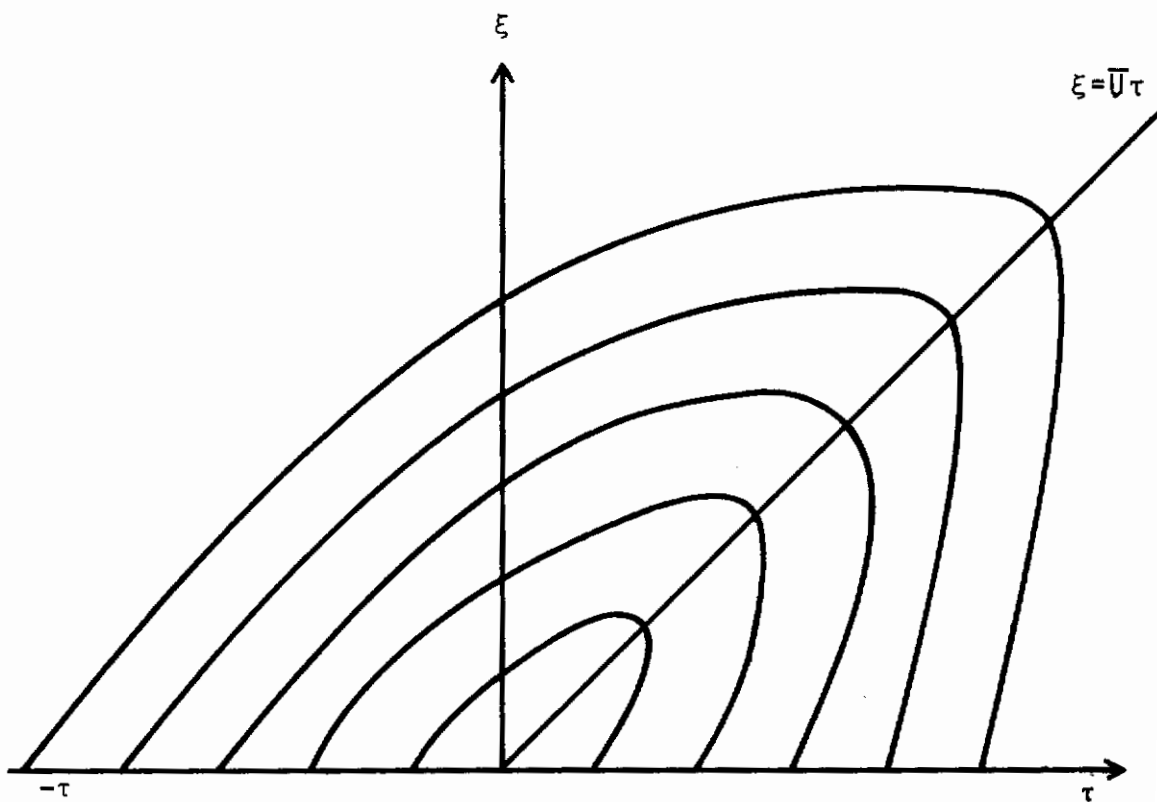


Figure 2.2 Isopleths of  $R(\tau, \xi)$

## THE MINIMUM AND MAXIMUM TURBULENCE SCALES TO WHICH AIRCRAFT RESPOND

It has been suggested by Skelton (Reference 2.7), that minimum turbulence wave length to which an aircraft responds depends on the dimensions of the aircraft. In Skelton's analysis the wing-chord is selected for the critical dimensions, which is given as 2 meters. There is no speed dependency. On the other hand, the maximum wave length to which an aircraft responds depends on the airspeed of the aircraft at the moment, rather than its dimensions. The maximum wave length corresponds to a frequency of 0.1 Hz aboard the aircraft. This criterion is obviously to some extent a function of pilot control.

Therefore, an aircraft traveling through the atmosphere responds to turbulence as a variable band-pass filter, both the largest wave length and the width of the band being dependent on the airspeed. For V/STOL aircraft with a take-off and landing speed of, say, 20 mps, the response is to about two frequency decades. For more conventional aircraft with take-off and landing speeds up to 60 or 70 mps, the response is to about 2-1/4 decades. Because the filter is not ideal, there must be some response in the latter case to 3 decades.

## THIRD MOMENT ANALYSIS

When aircraft fly near a solid boundary the effect of sudden vertical gusts on the aircraft may be quite different for downward gusts than for upward gusts. Since even moment analysis of the vertical component has no parameters that distinguish upward from downward characteristics, it is recommended that the final method of analyzing atmospheric turbulence in relation to aeronautical responses include the option to analyze the odd moments. The third moment is the simplest and most easily interpreted.

A third-order autocovariance function, with 2 time lags, may be defined for the vertical component by

$$Q_w(\tau_1, \tau_2) = \overline{w(t) w(t+\tau_1) w(t+\tau_2)} \quad . \quad (2.28)$$

This function may be Fourier transformed into a bispectrum according to

$$B_w(\omega_1, \omega_2) = \iint_{-\infty}^{\infty} e^{-i(\omega_1 \tau_1 + \omega_2 \tau_2)} Q_w(\tau_1, \tau_2) d\tau_1 d\tau_2 \quad . \quad (2.29)$$

A discussion of the physical characteristics shown by these functions is given in Appendix II along with a practical method for computing the bispectrum without going through the third-order covariance function.

## SECTION III

### SENSOR DESCRIPTION AND EVALUATION

Four different types of wind sensors, or anemometers, were considered for the measurement system. They are, from left to right in Figure 3.1, the VectorVane, Wind Component Meter, Gill three propeller anemometer, and the sonic anemometer. Short descriptions of each of these sensors and their performance characteristics are given in this section.

The final system is a combination of two of these instruments: the fast response sonic anemometer provides high frequency information corresponding to the small spatial detail which to some extent parameterizes the meteorological conditions, and the slower response Gill anemometer is the major component of widely separated spatial arrays intended to measure the large scale structure of the turbulence. In order to properly determine the limits within which each of these two anemometers faithfully records the actual wind, sensors were set up adjacent to each other in configurations intended to assure that they were sampling winds which were close to being identical. The detailed conclusions drawn from evaluation and comparison of the actual wind records and statistical summaries of these records are included with the instrument descriptions below.

#### WIND COMPONENT METER

The WCM, a turbulence sensor which has been utilized at Hanford for a number of years, is a heated thermocouple wire anemometer which senses the three components of the wind within a small volume of air, a cube about 2 cm on a side. The instrument produces continuous signals related to the three spherical components of the wind. A V-shaped heated platinum wire in the horizontal plane provides an error signal to a servo motor which drives a sensor head to null the signal, orienting the head continuously into the instantaneous wind. A potentiometer connected to the motor shaft provides



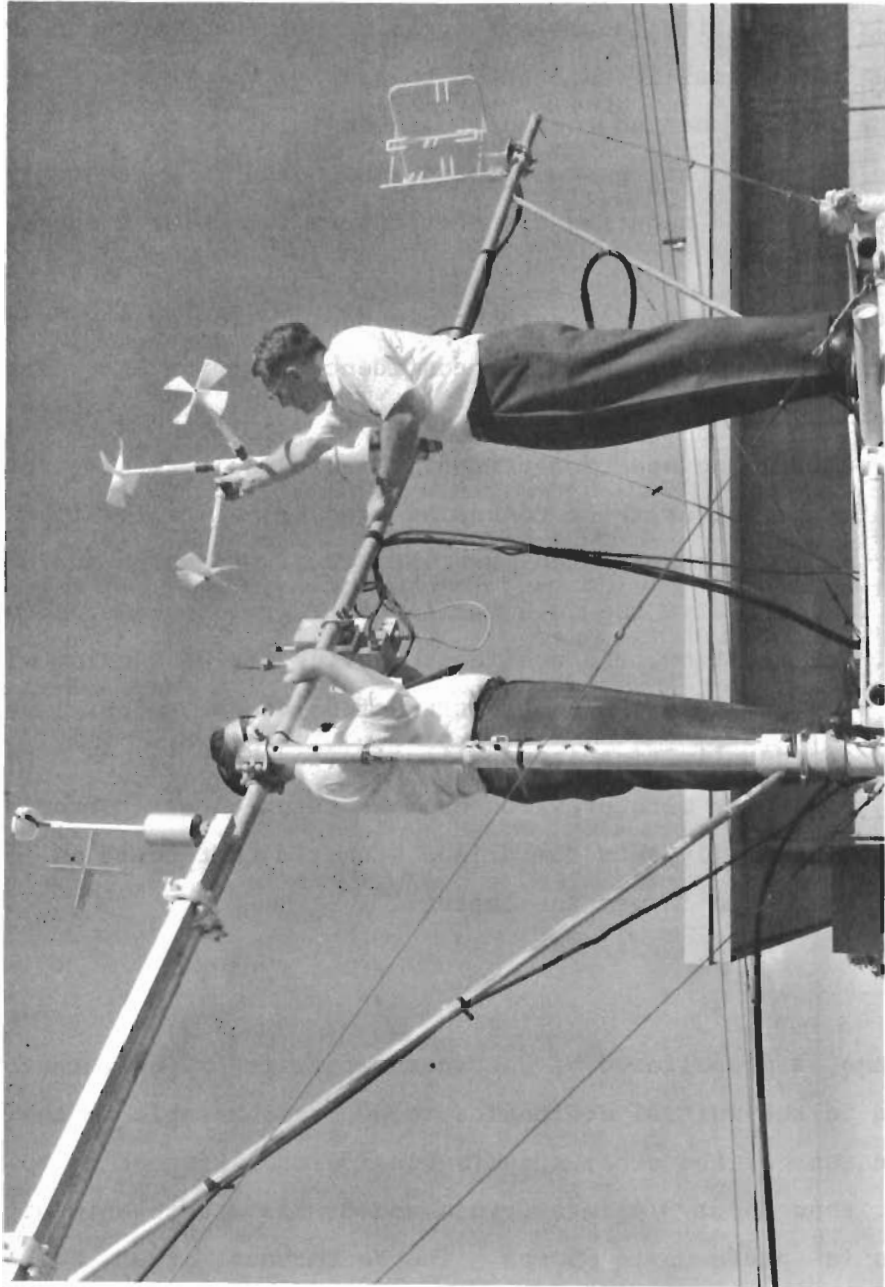


Figure 3.1 Sensors used in TOLCAT Measurement System

# Contrails

a voltage proportional to the varying horizontal angle. A second V-arrangement constructed of heated chromel-alumel thermocouple wires is oriented in the vertical plane. The thermocouples suspended in the center of each leg of the "V" produce opposing voltages as each is cooled by the wind, such that a resultant positive (negative) signal is produced by a downward (upward) gust. This signal is calibrated to provide the vertical angle of the wind. Another set of heated thermocouples, maintained normal to the instantaneous wind by the rotating sensor head, is cooled to a greater or lesser extent by positive and negative fluctuations in the total wind speed.

This instrument has a reasonably fast response, following 4-Hz wind fluctuations. Considerable experience and confidence in turbulence measurement have been gained through its past use at Hanford (Reference 3.1). However, its fragile nature, the need for periodic heating adjustments, and the requirement for occasional time consuming wind tunnel calibration demonstrated that it would require too much individual attention and would be impractical for extensive use in a multi-sensor, remote tower-mounted application. In addition, the nonlinear cooling of the sensing wires as a function of wind speed causes the instrument to become rather insensitive at high wind speeds, limiting its application to about 15 mps. Consequently, to maintain continuity with previous Hanford turbulence measurements, the WCM has served primarily as a comparison standard that could be located in close proximity to the larger anemometers.

## VECTORVANE

The VectorVane, a propellered bivane anemometer, is an instrument which was demonstrated in the initial evaluation to be less suitable in the present context than some of the other sensors considered. Responding to eddy sizes larger than about 3/4 meter, this sensor has a threshold of 1/4 mps and operates in speeds up to 55 mps. The VectorVane, like other bivanes, measures fluctuations in the azimuth and elevation angles of the wind by means of vane-driven potentiometers. In addition, it measures the total wind speed with a nose-mounted propeller whose axis is always maintained

parallel to the instantaneous wind vector. This presents a clear advantage for the total wind speed determination since calibration of the propeller for nonparallel flow need not be considered. However, the behavior of the vane presents some serious difficulties for the experimental methods utilized in TOLCAT.

To prevent a false rotation of the coordinate system, it was necessary to periodically balance the sensing head of the VectorVane, thus assuring proper sensor orientation. In addition, while the potentiometer output for each of the two direction measurements provides a continuously noise-free trace on strip chart recordings, frequent maintenance and cleaning of the potentiometers are required when recording on magnetic tape to avoid high frequency noise spikes detected by the tape recorder. The inaccessible tower mounting of the turbulence sensors and the considerable care that must be taken in leveling and balancing them thus made the VectorVane impractical for this application. Though the VectorVane was not used extensively for data collection, it was found very useful with strip chart recording for monitoring and making qualitative assessments during and following the conduction of experiments.

## SONIC ANEMOMETER

The sonic anemometer is an absolute instrument in that its calibration is completely determinable from the simple physical principles upon which its operation is based, known physical constants and a few easily measured parameters of the instrument, rather than being derived from comparison with an independent measurement of the wind speed. Three of these instruments were obtained for the system. The absolute character of its calibration, comparison experiments with the WCM and intercomparison between sonics have proved it to be the most accurate and responsive sensor and established it as the reference anemometer.

The sonic anemometer measures three components of the wind, the W component in the vertical direction and two others, called the A and B components

# Contrails

at  $120^\circ$  to each other in the horizontal plane. The wind components are determined by transmission of ultrasonic pulses along each of the three component-paths, the differences in transit time in opposite directions along a given path providing a measure of the magnitude of that wind component. The resolution of the sensor is 2 cm/sec, determined by the signal-to-noise ratio of the received ultrasonic pulse. Since the instrument depends in no way on inertial properties, the threshold is limited only by the sensitivity and is also 2 cm/sec. The full scale range of the  $\pm 1$  volt analog output is selectable at  $\pm 3$  mps,  $\pm 10$  mps and  $\pm 30$  mps for each of the horizontal components and  $\pm 1$  mps,  $\pm 3$  mps and  $\pm 10$  mps for the vertical. The maximum values are limited only arbitrarily by reasonable choice to avoid losing resolution in recording values within the range.

The atmospheric temperature can also be measured with the sonic anemometer, using the average of the transmission times for opposing pulses along the vertical path to measure variation of the speed of sound produced by the changing virtual temperature of the air. A temperature range of  $\pm 10^\circ\text{C}$  and a resolution of  $\pm 0.1^\circ\text{C}$  are provided by the analog output.

The averaging of the smaller eddies over the 20 cm path length separating the transmitting and receiving transducers is the primary limitation on the frequency response of the sonic, but only for eddy sizes smaller than 1 meter are the amplitudes attenuated by more than 5 percent. Eddies smaller than 1 meter are presently thought to have little relevance to the TOLCAT study, but should they be of interest, corrections can be made to the spectral estimates from theoretical response functions (Reference 3.2). A problem of overshoot or attenuated response at some frequency would be seen as an anomalous peak or valley at that frequency in the measured power spectrum. The flat frequency response of the sonic down to a wave length of 1 meter has been demonstrated by spectral estimates from a comparison experiment in which the WCM was placed within 20 cm of the measurement volume of a sonic anemometer (see TOLCAT Interim Report) and by comparisons with theoretical models of the power spectra.



# Contrails

Additional evidence for the reliability of the sonic anemometer is presented in the TOLCAT Interim Report. The individual probability distributions of the measurements of various gust magnitudes by the WCM and the sonic anemometer provide, as does the Fourier analysis, a measure of agreement on the average between the two sensors. Inspection of the actual time histories of the wind as recorded by the two anemometers demonstrated that even the high frequency characteristics, up to several Hz, were reproduced indentially by the two anemometers.

The errors associated with linearizing the theoretical equation describing the operation of the sonic anemometer and with the dependence of the calibration on temperature and humidity (caused by the dependence of the speed of sound on these meteorological variables) are discussed in the TOLCAT Interim Report as well as Reference 3.3. These errors are of the order of 3 percent or less and are easily corrected in the data analysis. There is, in addition, an inherent uncertainty of 1 - 2 percent in the digital-to-analog conversion circuit and a need for conscientious performance of the zero-wind-speed adjustment to avoid an erroneous bias on the signal. This latter operation is performed with the sensing head in an enclosure isolated from air movement and adjusts electronically for differences in the travel distance for pulses transmitted in opposite directions along a given path.

Operation of the sonic anemometer and data analysis pointed to a number of procedures and modifications which were needed for reliable, noise-free operation. These are detailed below.

Noise spikes generated by the original sensor receiver heads were caused by stresses which developed between the receiver crystal and its protective rubber covering when the ambient temperature dropped below about 10°C. This problem was temporarily alleviated by wrapping the heads with heating cables to maintain them at an acceptable temperature. Heads with modified protective coverings have since been obtained from the manufacturer and these have eliminated the problem.

Noise spikes can also be produced when a large shift in the wind changes the proper amplification level for the received ultrasonic pulses. Careful adjustments must be made operationally within the signal conditioning electronics to eliminate this source of noise.

Elimination of the above mentioned noise sources led to the diagnosis of a third source of noise in the sensor probe. Frayed insulation caused by wire routing past sharp edges within the probe and inadequate insulation in the transmitter head assembly produced intermittent grounding of the 5000 volt pulses. The probes are currently being rebuilt to correct this problem. Rebuilding of the probes has also been necessary to properly align the component paths relative to each other to avoid cross-contamination between the horizontal and vertical wind components.

#### GILL UVW ANEMOMETER

The Gill UVW three-propeller anemometer, has consistently demonstrated dependable, trouble-free operation. Though the effective frequency range of this sensor is limited at high frequencies, the initial instrument evaluation demonstrated it to be the most promising low-cost sensor for use in slow rate sampling of larger eddies. The Gill anemometer utilizes propellers, the shafts of which are parallel to each of the three orthogonal coordinate axes. The arms to which the propellers are attached extend 40 cm along each of the axes. The polystyrene propellers have four blades and are constructed to turn one revolution for each 31.7 cm of air passing the propeller. Calibration of the system is performed by driving the sensor at a known rpm with a synchronous motor calibrating unit. Each arm contains a miniature tachometer generator, turned by the propeller, which produces the wind component signal. A variety of propellers are available; the propellers utilized in TOLCAT have a threshold of 20 cm/sec and operate to a maximum head-on-wind of 35 mps. The distant constant is about 1 meter.



Cosine Response

The Gill propeller was designed to follow a cosine response, sensing only the component of the wind parallel to the propeller shaft. However, the manufacturer's calibration shows a deviation from the cosine curve which becomes larger as the angle between the wind and the propeller axis increases (Horizontal Axis, Table 3.1). Since it can be shown from this table that the percent error in the horizontal wind vector will be minimized when the wind is blowing at an angle of 45° to both the U and V arms, this orientation relative to the mean wind has been utilized for most TOLCAT data collection. The cosine response is the worst for the W arm, the wind fluctuating about an angle of 90°, and hence the calibration of this arm is increased by 25 percent to bring the response closer to the cosine law within the expected input range of 60° to 120° (Vertical Axis, Table 3.1).

TABLE 3.1

FRACTION OF COSINE RESPONSE FOR GILL ANEMOMETER

<u>HORIZONTAL AXIS</u>				<u>VERTICAL AXIS</u>	
<u>Angle</u> (deg)	<u>Fraction</u>	<u>Angle</u> (deg)	<u>Fraction</u>	<u>Angle</u> (deg)	<u>Fraction</u>
5	1.00	175	.99	60	1.00
10	.99	170	.99	65	.97
15	.99	165	.99	70	.93
20	.98	160	.98	75	.89
25	.97	155	.97	80	.86
30	.95	150	.96	85	.75
35	.93	145	.94	90	---
40	.90	140	.92	95	.75
45	.87	135	.88	100	.92
50	.84	130	.84	105	.96
55	.81	125	.82	110	.96
60	.78	120	.81	115	.97
65	.76	115	.82	120	.96
70	.70	110	.85		
75	.69	105	.86		
80	.66	100	.86		
85	.57	95	.75		

Power spectra are shown in Figures 3.2 - 3.4 from a comparison experiment in which a Gill anemometer was placed between two sonic anemometers separated by 3 meters along a line approximately normal to the mean wind. Figure 3.2 shows the alongwind and vertical component power spectra of the two sonics. Since differences between these two spectra can be attributed mainly to differences in the winds being sampled, this figure gives a measure of the agreement to be expected between the sonic and Gill anemometers when corrections are made for all errors in the Gill anemometer. The difference in the vertical spectra at  $1.5 - 5 \times 10^{-3}$  Hz might be due to interference between the instruments, but probably reflects actual inhomogeneity in the wind field. Figures 3.3 and 3.4 compare the Gill spectra (dotted lines) to the sonic spectra (solid lines) for both the alongwind and vertical wind components. Below 0.3 Hz the differences are principally due to the noncosine response. A computer subroutine, described in Section VI, has been written to correct each wind data sample for this error. The spectra of the corrected data, plotted as dashed lines in Figures 3.3 and 3.4, agree well with the statistics measured by the sonic anemometer.

As the distance separating two anemometers is reduced, the cospectrum between like components of the wind measured by each anemometer should approach the power spectrum of that wind component as measured by either instrument. The cospectra have been calculated between the sonic and Gill anemometers (see TOLCAT Interim Report) and they agree with the power spectra throughout the frequency range where the power spectra compare favorably with each other. This demonstrates the extent to which these dissimilar instruments can be validly used to measure the correlation between winds at different locations.

### Frequency Response

The dynamic response of a propeller to a change in the wind, neglecting bearing friction, is described by a first order differential equation

$$T \frac{dU}{dt} = g(t) - U \quad , \quad (3.1)$$

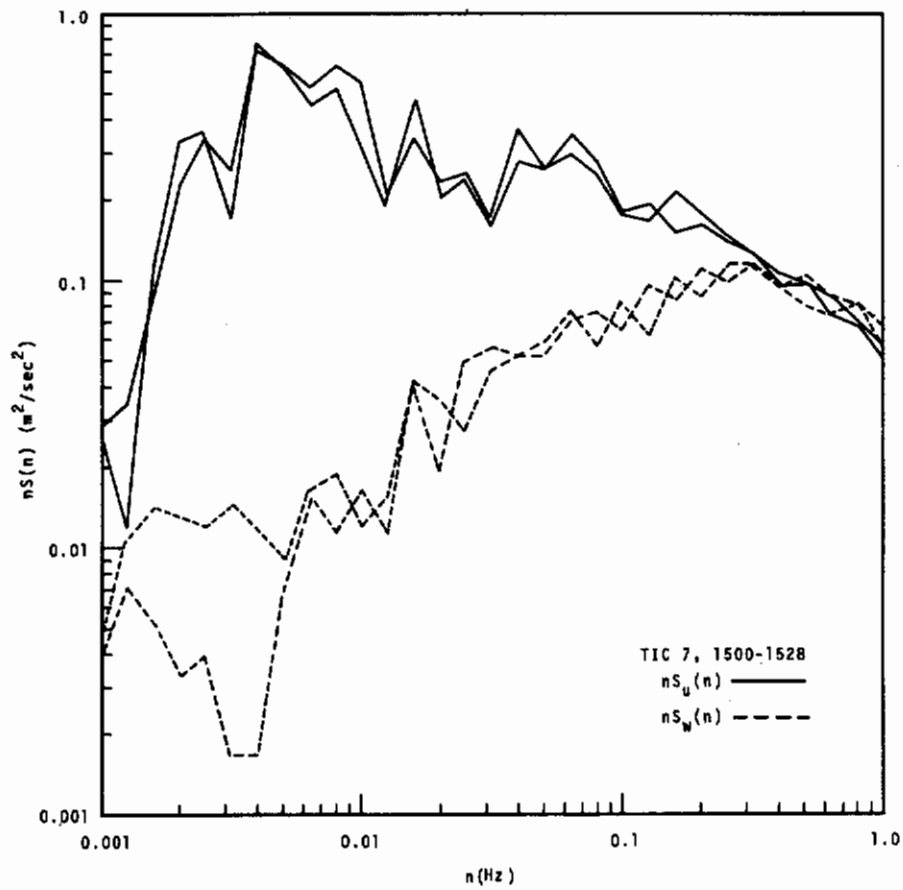


Figure 3.2 Power Spectra Measured by Adjacent Sonic Anemometers

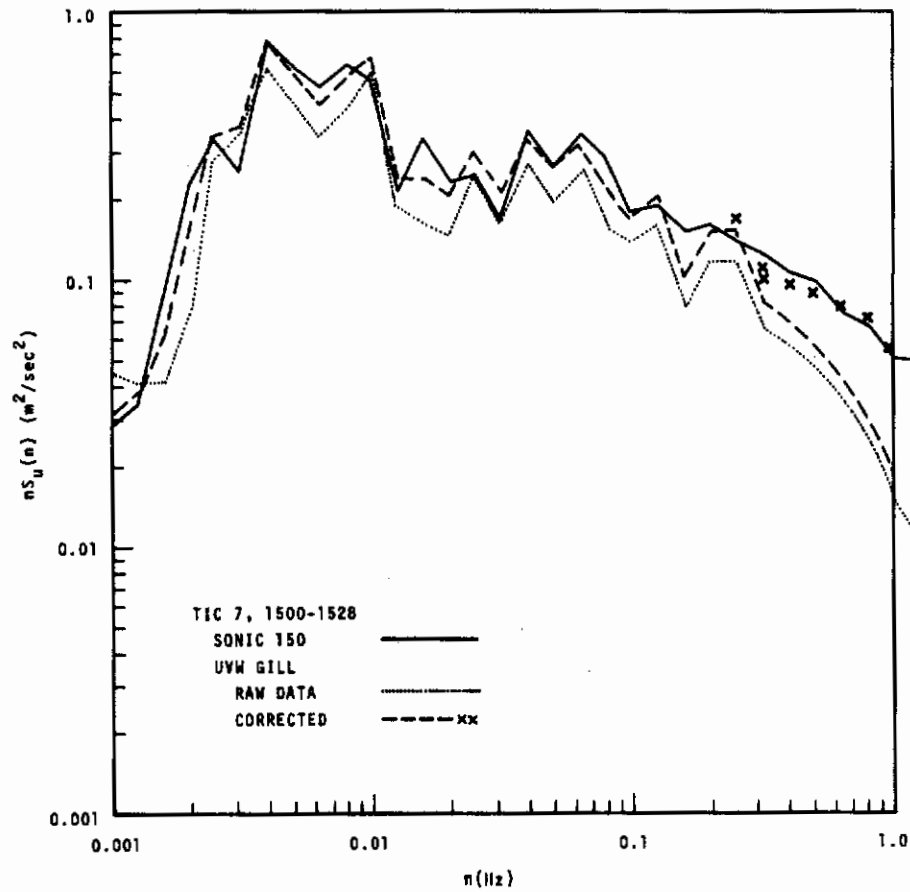


Figure 3.3 Alongwind Power Spectra Measured by Adjacent Gill UVW and Sonic Anemometers

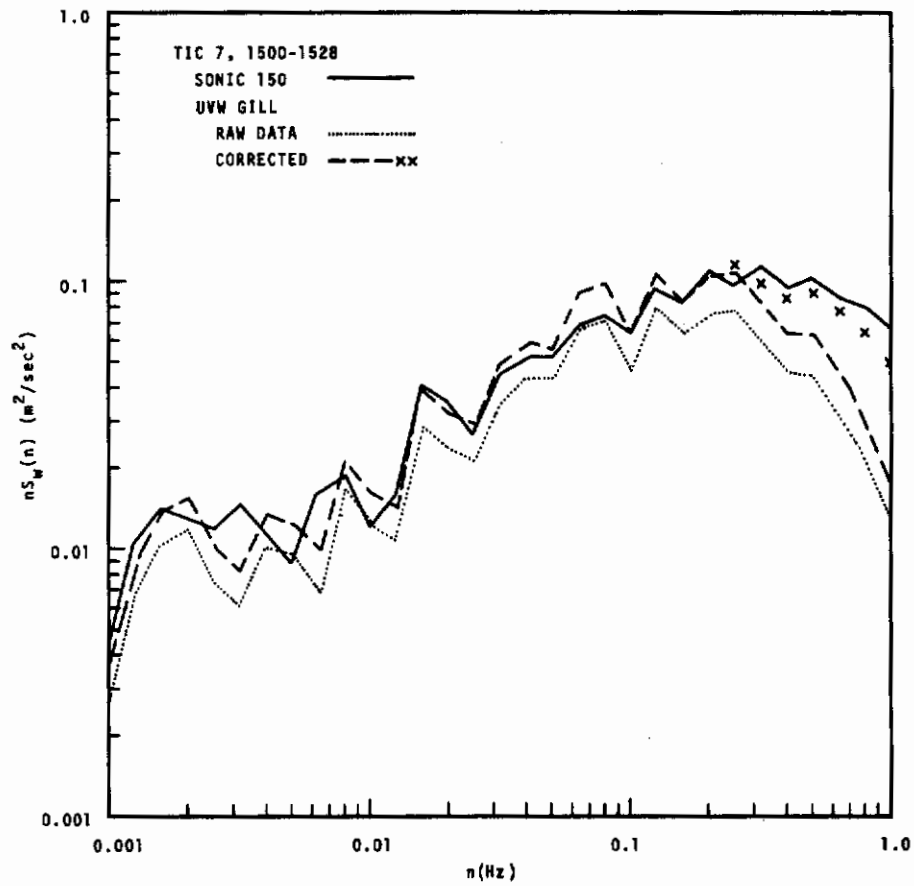


Figure 3.4 Vertical Power Spectra Measured by Adjacent Gill UVW and Sonic Anemometers

# Contrails

where  $U$  is the indicated wind speed,  $g(t)$  is the real wind, and  $T$  is a time constant characteristic of the system. It can be shown (Reference 3.4) that for a propeller with its axis parallel to the wind,

$$T = \frac{L}{\bar{U}} \quad , \quad (3.2)$$

where  $\bar{U}$  is the mean wind and  $L$  is a distance constant independent of the mean wind. The response of the propeller anemometer to a sinusoidal input,

$$g(t) = A \sin \omega t \quad , \quad (3.3)$$

is

$$U = A(1 + \omega^2 T^2)^{-1/2} \sin (\omega t - \beta) \quad , \quad (3.4)$$

where  $\beta$  is a phase lag,

$$\beta = \tan^{-1} \omega T \quad . \quad (3.5)$$

Thus the power spectra for the Gill anemometer will be attenuated by a frequency dependent factor,

$$(1 + 4\pi^2 n^2 L^2 / \bar{U}^2)^{-1} \quad . \quad (3.6)$$

This will give a half-power point, corresponding to a reduction in the signal of 29 percent, at

$$n_{1/2} = \frac{\bar{U}}{2\pi L} \quad . \quad (3.7)$$

$L$  is listed by the manufacturer to be 0.95 meter, giving a time constant of 0.19 second and a half-power point of 0.85 Hz for a mean wind of 5 mps.



Actually the Gill anemometer also incorporates an RC low-pass filter, the effect of which is described by an equation identical to 3.1. The combined effect of the propeller response and the RC filter is multiplicative in the amplitude attenuation and additive in the phase angle (Equation 3.4). The spectra which have been corrected for noncosine response are seen to rapidly drop below that of the sonic anemometer above about 0.25 Hz. These spectra have been corrected for the 0.215-second time constant of the RC filter and are plotted as crosses in Figures 3.3 and 3.4. However, using any reasonable value for the mean wind in Expression 3.6 to additionally account for the propeller response would obviously over-correct the spectra. This points to the fact that the form which Equation 3.2 takes as the wind shifts to one side of the propeller axis is still a matter in need of resolution (Reference 3.5).

## Threshold Response

As seen in Table 3.1, the noncosine response problem of the Gill becomes most acute as the angle between the propeller axis and the wind approaches 90°. As the component of the wind available to rotate the propeller (i.e., that parallel to the propeller axis) becomes smaller, the torque on the propeller eventually becomes less than the amount necessary to overcome the internal friction of the rotating parts. Increasing slippage occurs below a wind speed of 1 mps until, at the threshold level of 20 cm/sec, the wind is unable to turn the propeller.

Since the mean wind is at an angle of 90° to the W arm of the Gill anemometer, the threshold response problem is most evident in this component. The vertical axis propeller must frequently pass through the threshold "dead" region as the vertical component of the wind approaches zero or changes sign. Figure 3.5 is a plot of the cumulative probability distribution of the vertical wind component as measured by the sonic and Gill anemometers. A large number of vertical gusts sensed by the sonic anemometer have, to some degree, not been recorded properly by the propeller and

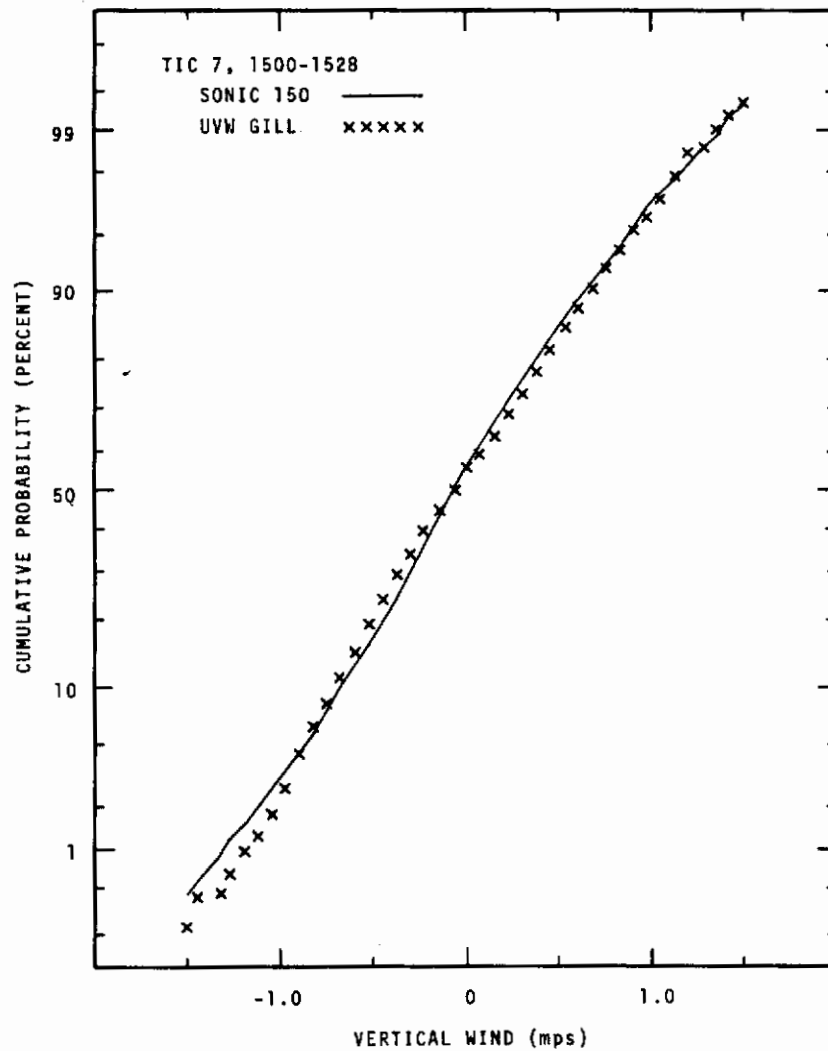


Figure 3.5 Probability Distributions of the Vertical Wind Measured by Adjacent UVW Gill and Sonic Anemometers

this, combined with the cosine response correction, leads to the probability distribution shown. (The cosine response error alone would simply have led to a line of greater slope.)

To the degree that the U arm of the anemometer is directed into the wind, this threshold response problem is also serious for the V arm. When both the lateral and longitudinal components of the turbulence are of interest, as in the present study, the anemometer must be oriented so that the mean wind is between the U and V propeller axes. A similar method can be used to avoid the threshold problem for the W arm by tilting it  $45^\circ$  into the wind. This can be accomplished either by rotating the entire UVW anemometer or by replacing the W arm with a nonorthogonal arm in the vertical plane. The three propellers of the resulting configuration are all facing into the mean wind and will always rotate in the same direction.

Such a nonorthogonal (UVR) array was constructed and tested in the comparison experiment mentioned above. Figure 3.6 shows the cumulative probability distributions of the vertical wind as measured by the UVR anemometer and the same sonic anemometer used in Figure 3.5. The improvement is quite obvious, the most noticeable remaining differences occurring for the stronger vertical gusts (which would be close to normal to the tilted R propeller axis). However, the power spectra from these three sensors, plotted in Figure 3.7, show that the improvement (and hence the problem) is apparently limited to the higher frequencies. Since there already are uncertainties with this portion of the spectrum, the improvement afforded by a tilted "W" axis may be of value for the measurement of only a limited number of statistics.

A number of other modifications, detailed below, have been made to the Gill anemometer to adapt it to the needs of the TOLCAT program and to improve its accuracy or reliability. Extended field use and discussions with the manufacturer have established the need for stronger bonding of the two parts which make up an individual four-blade propeller. In addition,

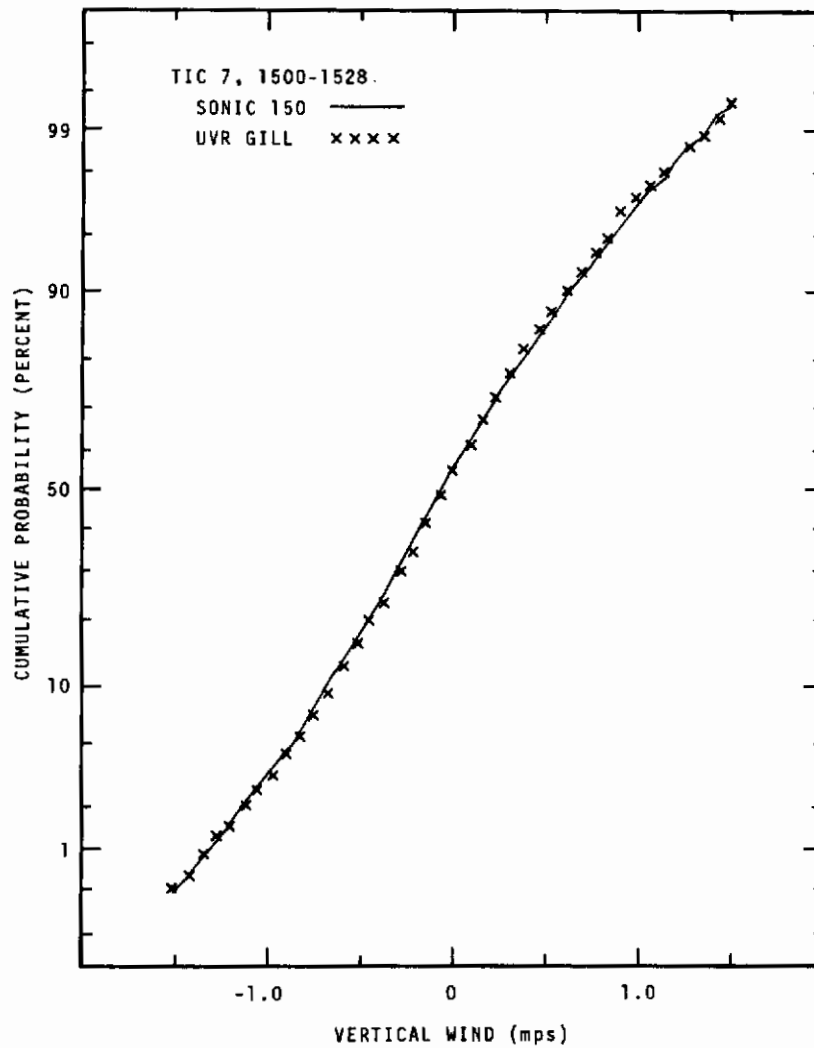


Figure 3.6 Probability Distributions of the Vertical Wind Measured by Adjacent UVR Gill and Sonic Anemometers

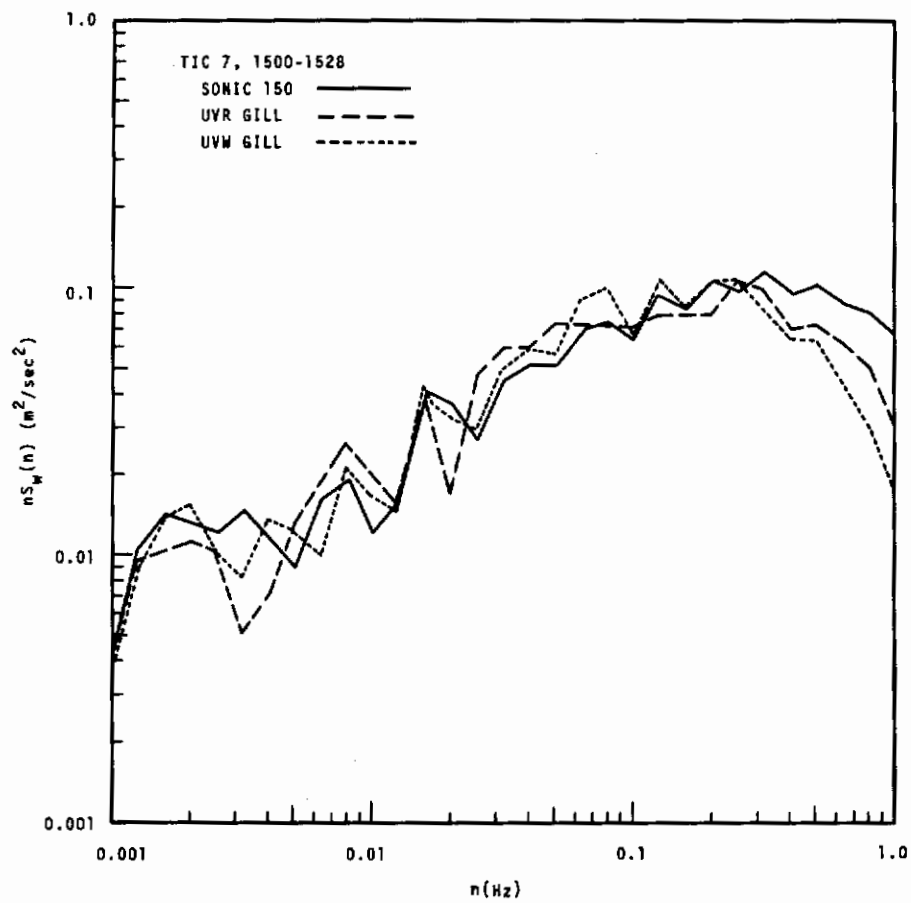


Figure 3.7 Vertical Power Spectra Measured by Adjacent Sonic, UVR Gill and UVW Gill Anemometers

modifications have been made to the orthogonal mast on which the three propeller arms are mounted and to the individual mounting fittings in order to improve their structural integrity and alignment reliability.

Extension of the signal cables to lengths of up to 2000 feet caused a significant mutual contamination of the signals due to the common reference wire used by all three components. Spare leads in the cable were utilized as independent references and a variable resistance was wired in series with each signal lead in order to permit adjustment to a uniform effective line resistance regardless of varying cable lengths.

Finally, finer resolution potentiometers have been used for the voltage divider within the readout unit to allow improved adjustment during calibration.

## CONCLUSIONS

The two instruments utilized in the final system are the Gill UVW and sonic anemometers. A typical TOLCAT system is composed of a spatial array of Gill anemometers to measure the large eddy structure of the wind field, supplemented by a small number of sonic anemometers to obtain high frequency turbulence information and parameterize the meteorological situation. It has been demonstrated that valid cross-correlations can be obtained by combining the data from an array of these dissimilar instruments.

When corrected during data reduction for its noncosine response and when proper consideration is taken of its frequency response, the Gill anemometer can be readily applied in multiple point arrays to give the bulk of the data needed for the TOLCAT study, its chief virtues being relatively trouble-free operation and low cost. Due to the threshold problem and the questionable frequency response of a vertically oriented propeller, certain statistics might best be obtained with a tilted "W" propeller. The sonic anemometer, although presently requiring skilled attention to assure best



# *Contrails*

performance, is a very responsive and accurate sensor. The absolute nature of its calibration has established it as the standard, or reference anemometer.

## SECTION IV

### MEASUREMENT SYSTEMS AND FIELD ARRAYS

The TOLCAT system was developed, deployed, and utilized in conjunction with the existing meteorological facilities at the Hanford site. Available towers, instrumentation supports, and available general purpose analog tape recording equipment were utilized along with a variety of "off the shelf" turbulence instruments. This allowed the instruments to be evaluated and also revealed the problems to be overcome in deploying and operating equipment over an extensive area in the field. In addition, data were provided for establishing and evaluating techniques used in digitizing, reduction and analysis, and for delineating spatial scales of turbulence to be encountered at various heights in the atmospheric layer of interest.

Initial field arrays, measurement systems, test series, data reduction techniques and analyses are presented in detail in the Interim Report, May 1971. The equipment and arrays utilized initially are also summarized here to provide continuity in describing problems overcome, and improvements made in equipment and procedures when the final TOLCAT system was placed in operation.

The TOLCAT system was placed in the field, utilizing fixed and portable towers which were arranged in a variety of configurations to measure spatial characteristics of turbulence and determine optimum arrays for future experiments. Remotely monitored leveling sensors for instruments and remotely operated devices for reorienting and indicating the direction heading of sensors were adapted to each of the field turbulence instruments. Direct digital data acquisition recording techniques were tested for the future optimized data acquisition system.

Data acquisition and storage methods developed in the laboratory through multiple playback of analog field recorded data into the computer controlled

digitizing system provided the basis for projection towards the field located optimized data system. This optimized system is described in detail in Section VIII.

Existing facilities and equipment utilized in the TOLCAT turbulence study included the 125-meter Hanford meteorology tower and measuring system (Figure 4.1), and the four 62-meter towers (Figure 4.2) on the 1600-meter arc on the Hanford diffusion grid. The 125-meter meteorology tower is equipped to measure the mean atmospheric variables, and acts as the central point of the Hanford grid of concentric air sampling arcs. Atmospheric variables measured at 15-meter intervals are temperature, wind speed, and wind direction. Each of these variables are recorded continuously on strip chart recorders, either as single point or multiple point printout (Figure 4.3). One of the 62-meter towers utilized for TOLCAT, Tower 106, is instrumented with micrometeorological equipment for measuring temperature, wind direction, and wind speed at 2, 4, 8, 16, 32, and 46-meter heights. These atmospheric variables are sampled at 5-second intervals and digitally recorded on both printed and punched tape.

Each of the individual TOLCAT tests was coordinated with the continuously collected weather station information to maintain an overall environmental assessment during each test.

## SENSORS

Atmospheric turbulence measurements require sensors capable of measuring the three components of the wind. Four sensors were initially evaluated and operated in parallel to identify the most desirable combination. A detailed sensor description and review of sensor comparison and evaluation are presented in Section III.

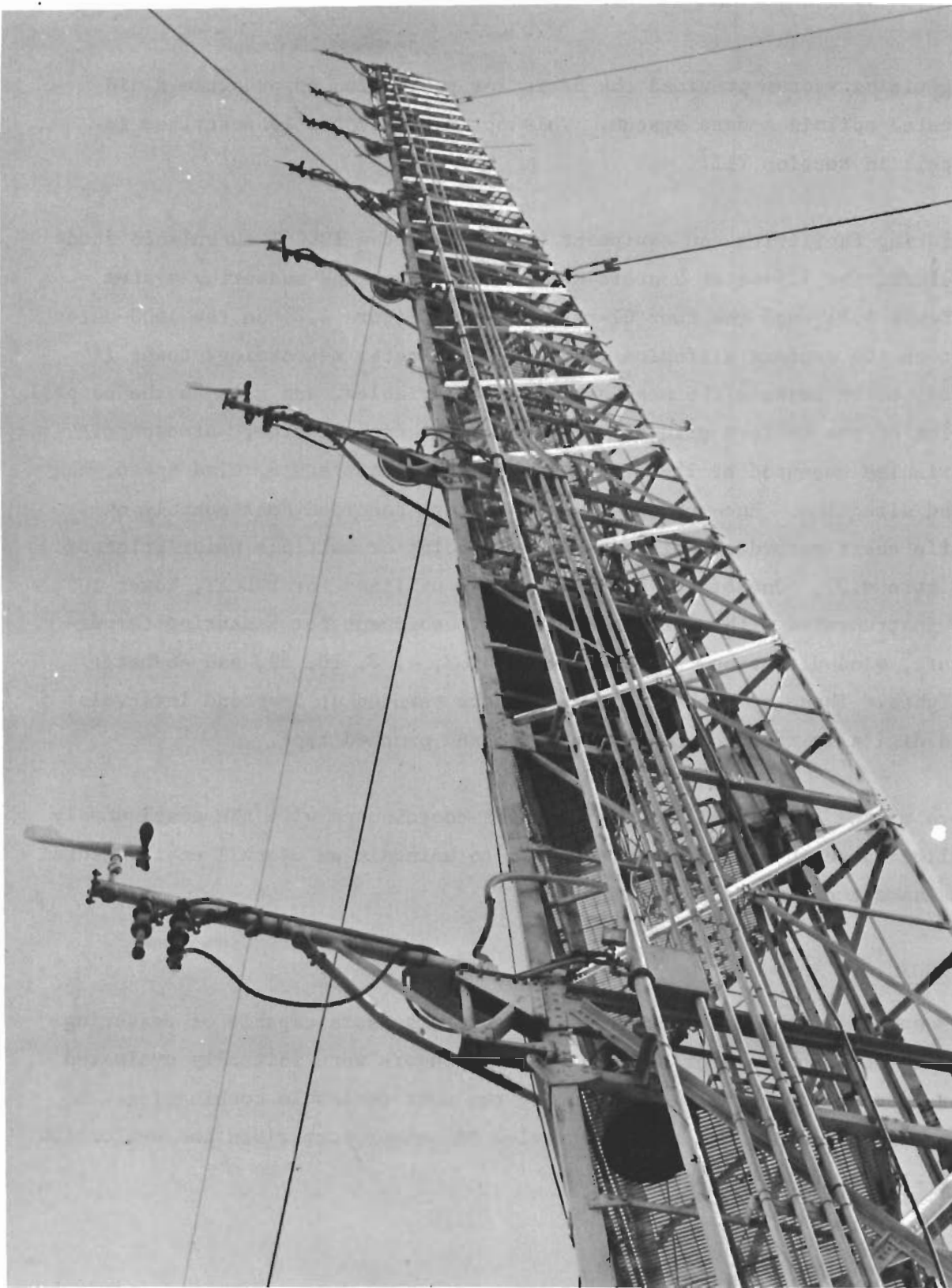


Figure 4.1 The 125-meter Hanford Meteorology Tower



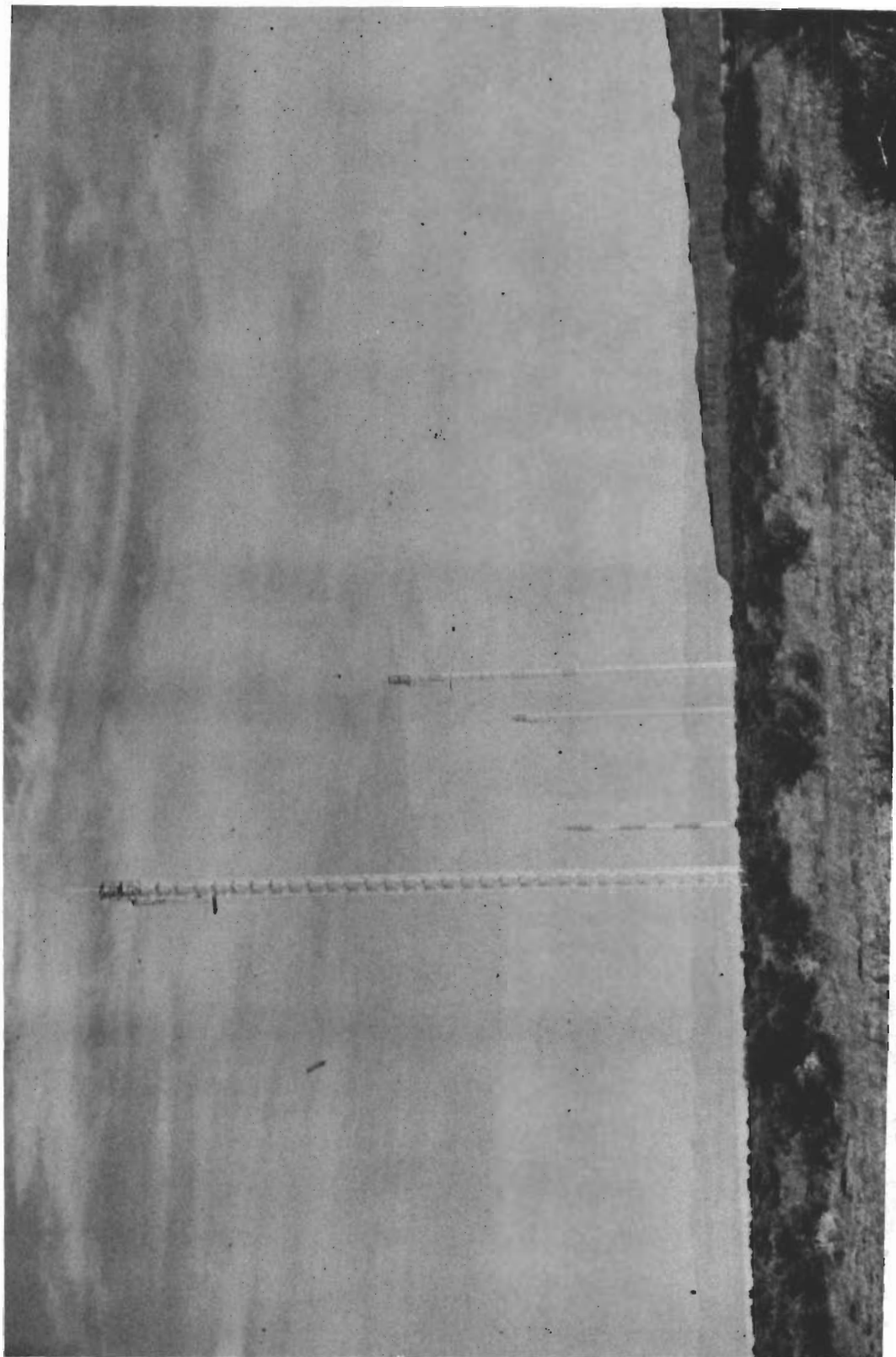


Figure 4.2 Four 62-meter Towers on the 1600-meter Arc

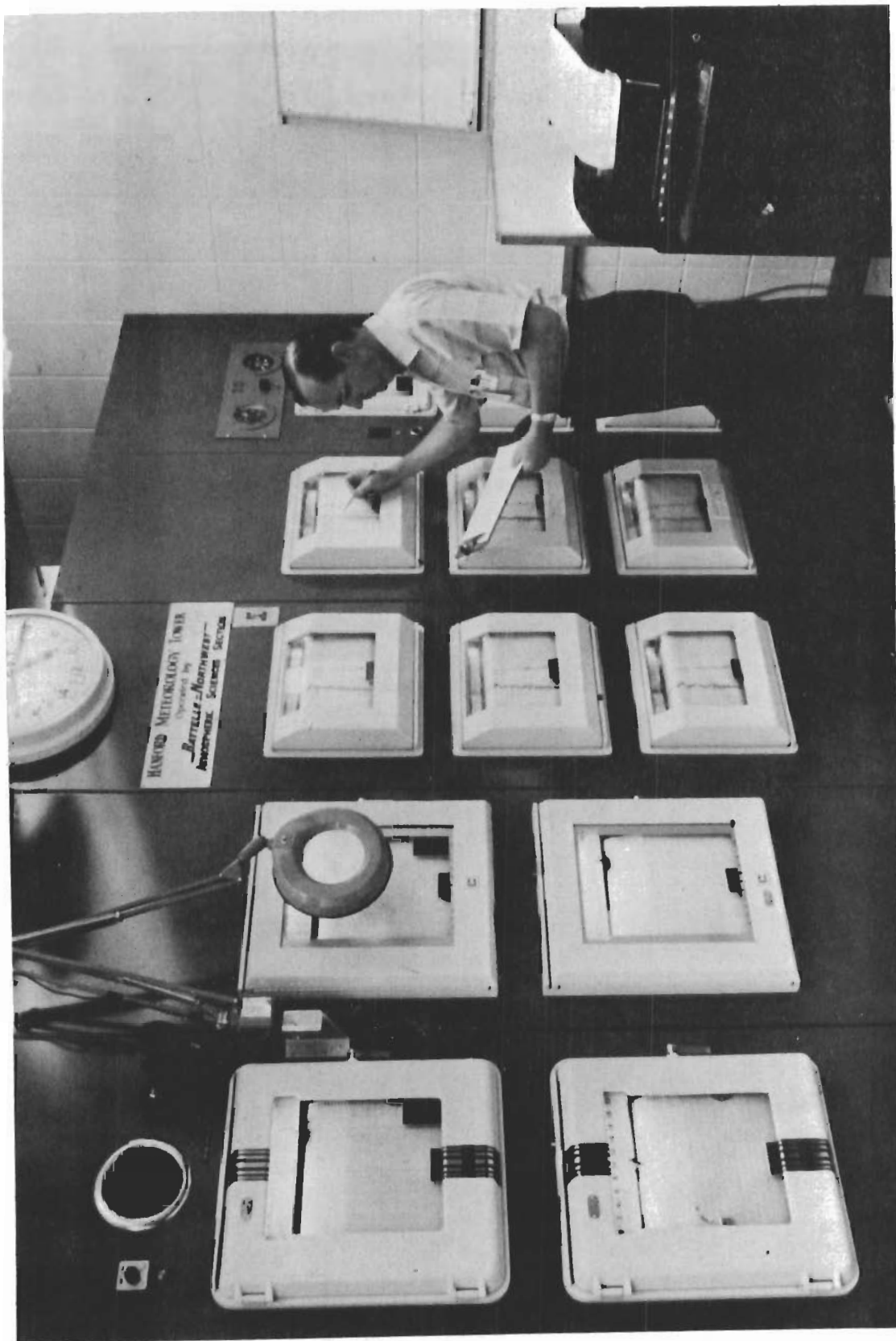


Figure 4.3 125-meter Meteorology Tower Data Recording Center



## INSTRUMENT LEVEL DETECTORS

Instrument level error was determined to be very critical during the first TOLCAT experiments. A  $1^\circ$  out-of-level contributed recognized errors in the u, v, and w wind vector components, their covariances, and their spectral and cross-spectral distributions. Proper alignment of sensor components in the u-v, u-w, v-w planes was also determined to be very important.

Instrument leveling in remote locations such as on booms and tops of towers was difficult and not accurate enough with conventional methods utilizing transits. Electrolytic levelers, recommended by the Air Force Cambridge Research Laboratory, Boundary Layer Branch, which utilized a bubble level similar to a conventional carpenter's level, were adapted to the sonic anemometer (Figure 4.4) and to the Gill anemometer (Figure 4.5). One of the two levelers was aligned with the reference axis, bisecting the A and B components on the sonic and bisecting the u and v components on the Gill (as shown in Figure 4.6). The remaining bubble was established at  $90^\circ$  to the reference axis on each instrument.

Each of the sonic and Gill anemometers was set up on a surface plate to check and adjust alignment and install levelers. Figure 4.7 shows a working surface plate with a level in the horizontal plane traceable to the National Bureau of Standards. With the A and B components of the sonics and the u and v components of the Gills established in the horizontal plane, along with the true vertical direction determined for the w components for each anemometer, the electrolytic bubbles were mounted on the sensor frames. The leveler bubbles were balanced to zero relative to the reference surface plate.

Electrolytic levelers and the level monitor readout (Figure 4.8) were calibrated using the standard laboratory surface plate and a sine plate for angular deviations from the horizontal. The detailed calibration data appear in Figures III.2 and III.3 of Appendix III. The electrolytic level sensor is a double resistance element which forms the top half of a

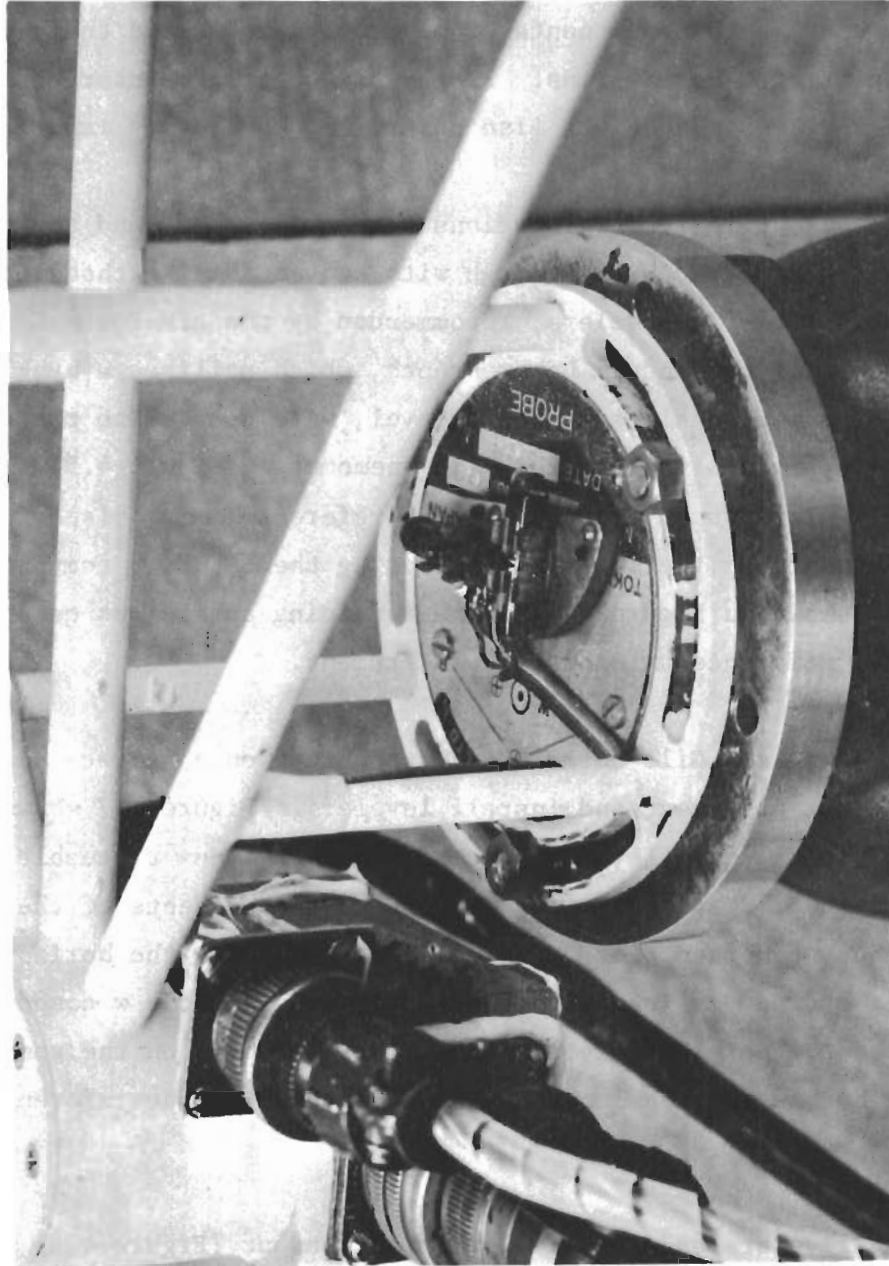


Figure 4.4 Sonic Anemometer with Electrolytic Levelers

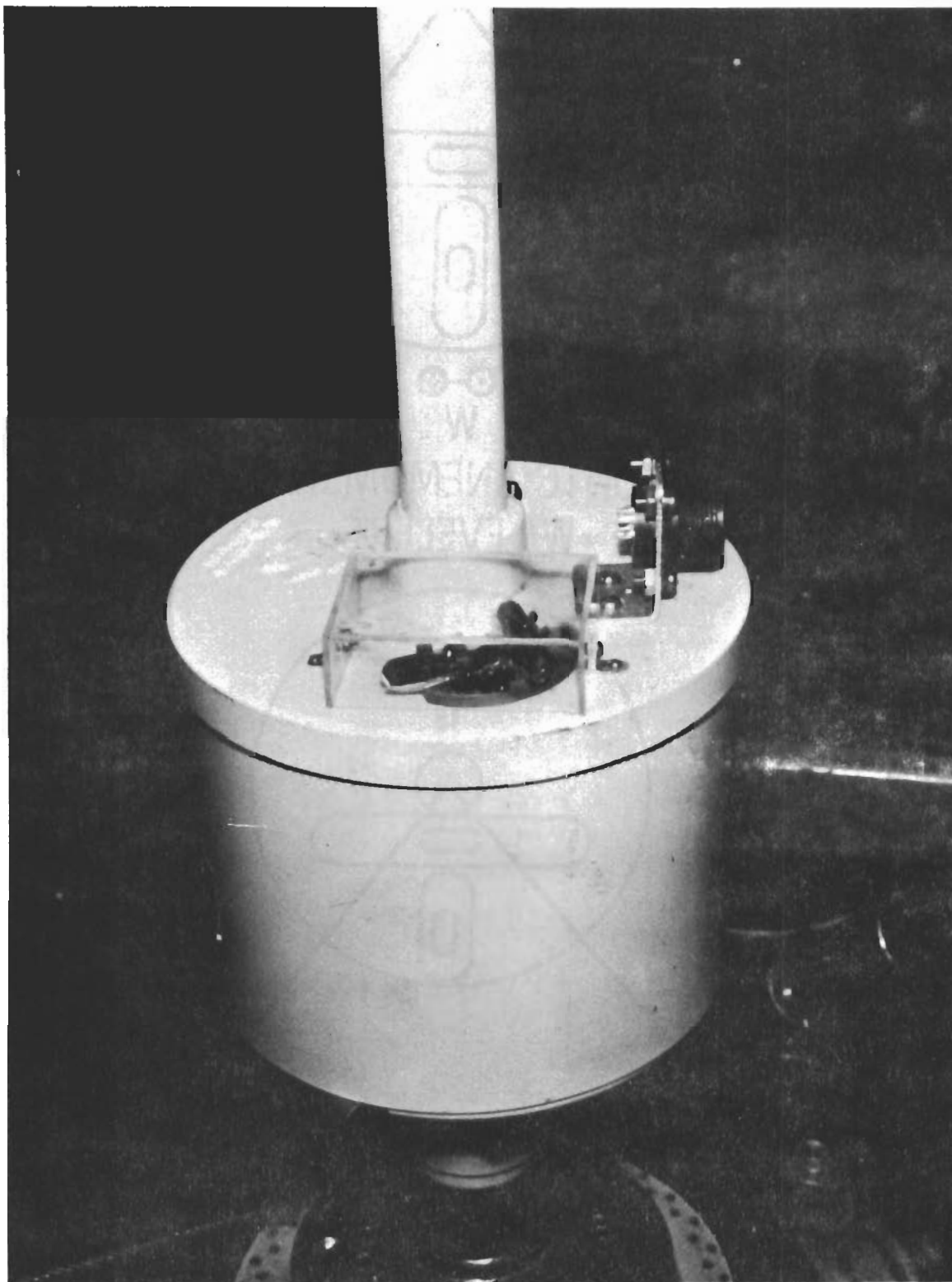
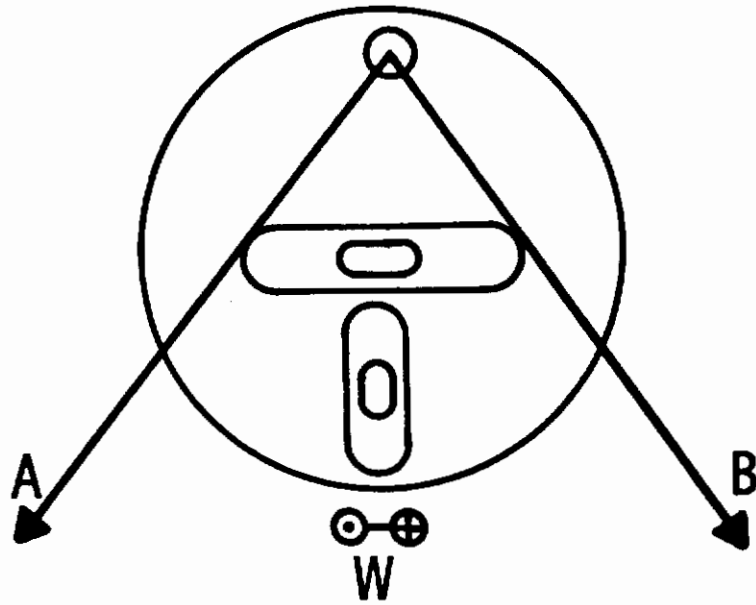
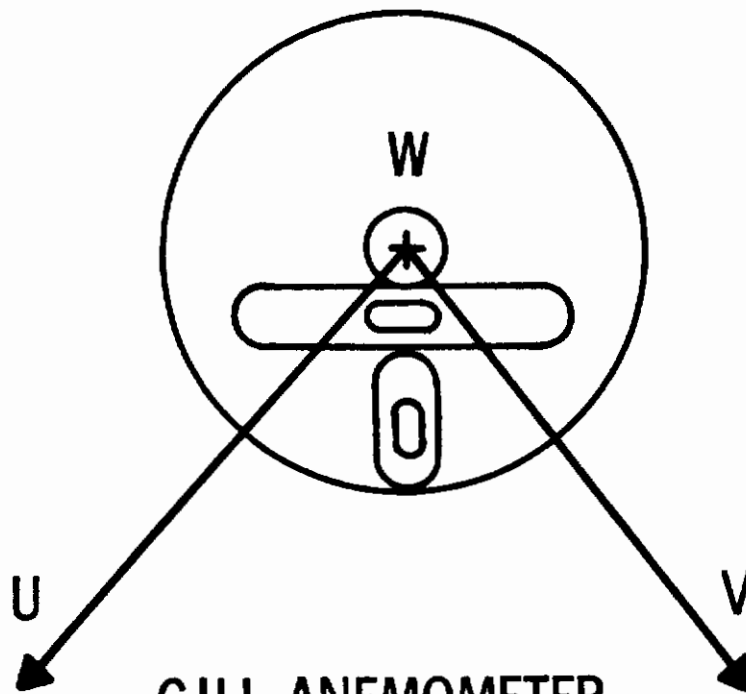


Figure 4.5 Gill Anemometer with Electrolytic Levelers



**SONIC ANEMOMETER  
W/LEVELERS**



**GILL ANEMOMETER  
W/LEVELERS**

**Figure 4.6** Electrolytic Leveler Location Relative to Sensor Axes

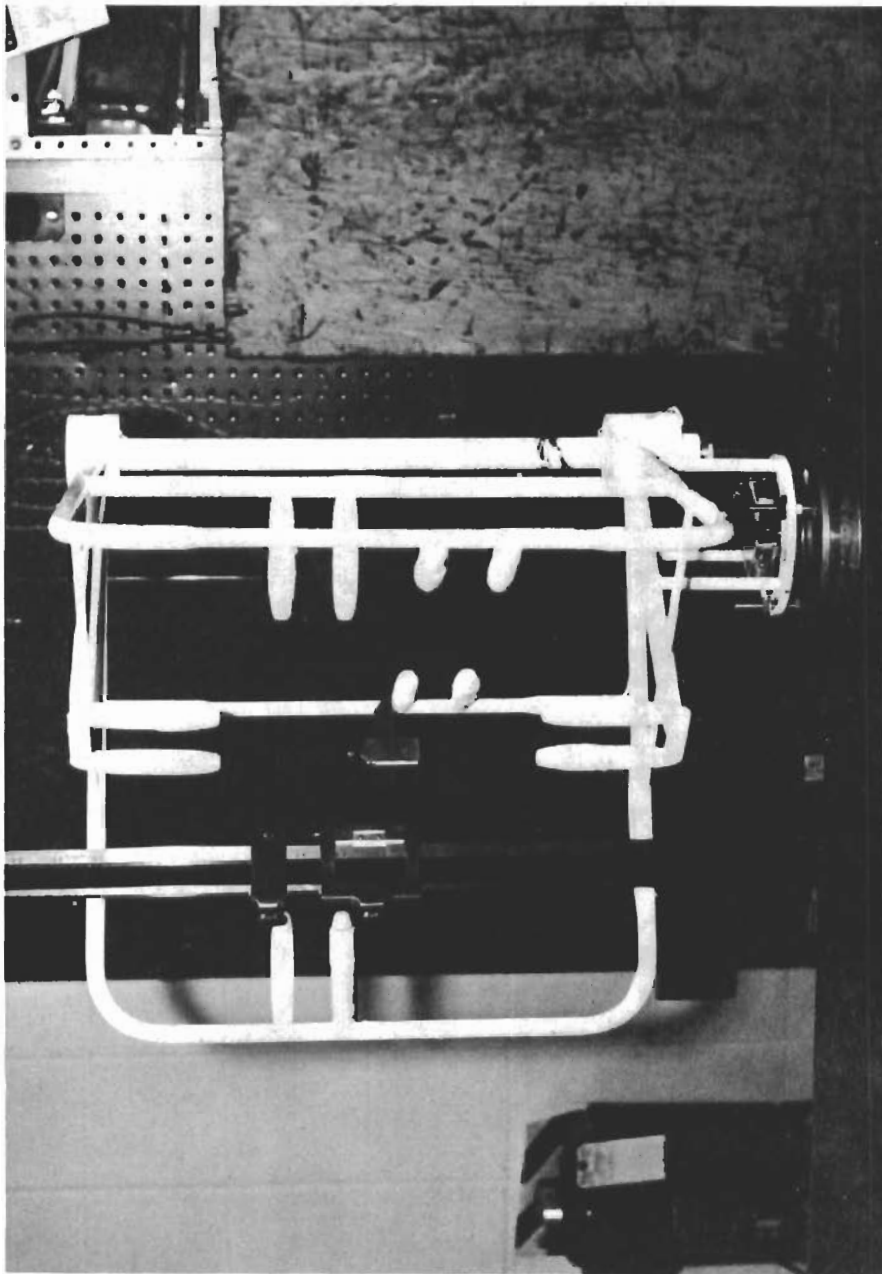


**Figure 4.7** Sensor Alignment Check and Calibration Relative to Standard Level Surface Plates



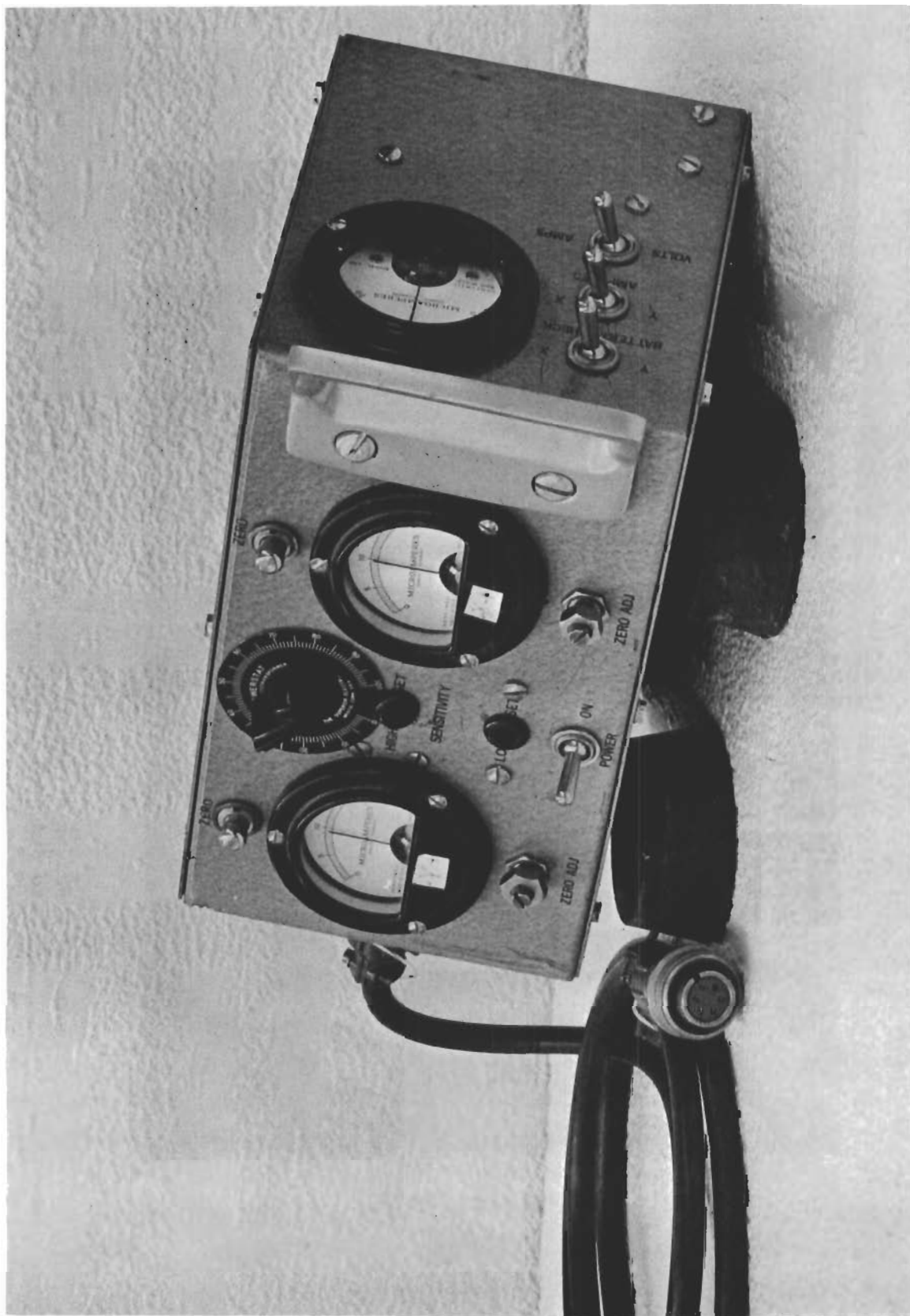


Figure 4.8 Electrolytic Leveler Monitor and Readout



resistance bridge. As the bubble moves from center to the right or left, the resistance from one side of the bubble level increases and the other side decreases. When a static level is reached the resistance bridge measures and monitors the electrolytic level status (see Figure III.1 in Appendix III). Two identical bridge circuits were adapted into a readout monitor (Figure 4.9). Sensitivity control was developed to permit coarse leveling and ultimately very precise leveling. The ultimate usable precise leveling sensitivity was 10 to 15 seconds per division. A nominal remote level acceptance was  $\pm 2$  to  $\pm 5$  divisions, or  $\pm 20$  to  $\pm 75$  seconds off of true level. These data are recorded during turbulence measurement periods and utilized by a computer program if needed to correct the data. By adding an amplifier to each of the null meter output terminals, and adjusting the proper amplifier gain (approximately  $\times 100$  to  $\times 500$ ), the off level deviation may be recorded. During all TOLCAT second-phase test series, the deviation was checked before, during, and after each test and was recorded for future correction if needed.

By utilizing the bridge null balance concept, the leadwire length and resistance changes are compensated. Thus, lead lengths of 500, 1000, 2000, and 5000 feet are acceptable with the null bridge level detector system.

## INSTRUMENT REORIENTING EQUIPMENT

Rotation of the sensors was required prior to each TOLCAT test. The objective was to orient the sensors so that the average wind vector was bisecting the A and B component arms of the sonics and the u and v component arms of the Gill anemometers. During the first experimental phase test series (discussed in the Interim Report), the rotation was accomplished by hand and the resultant direction heading read from an indexed wheel. This procedure was not only time consuming but subject to human error, especially after climbing one or more 62-meter towers to make the realignment. During the latter TOLCAT test series, antenna rotors were adapted to tower and boom mountings for sensor rotation. Figure 4.10 illustrates the tower installation for rotor control of sonic anemometers. Figure 4.11 illustrates

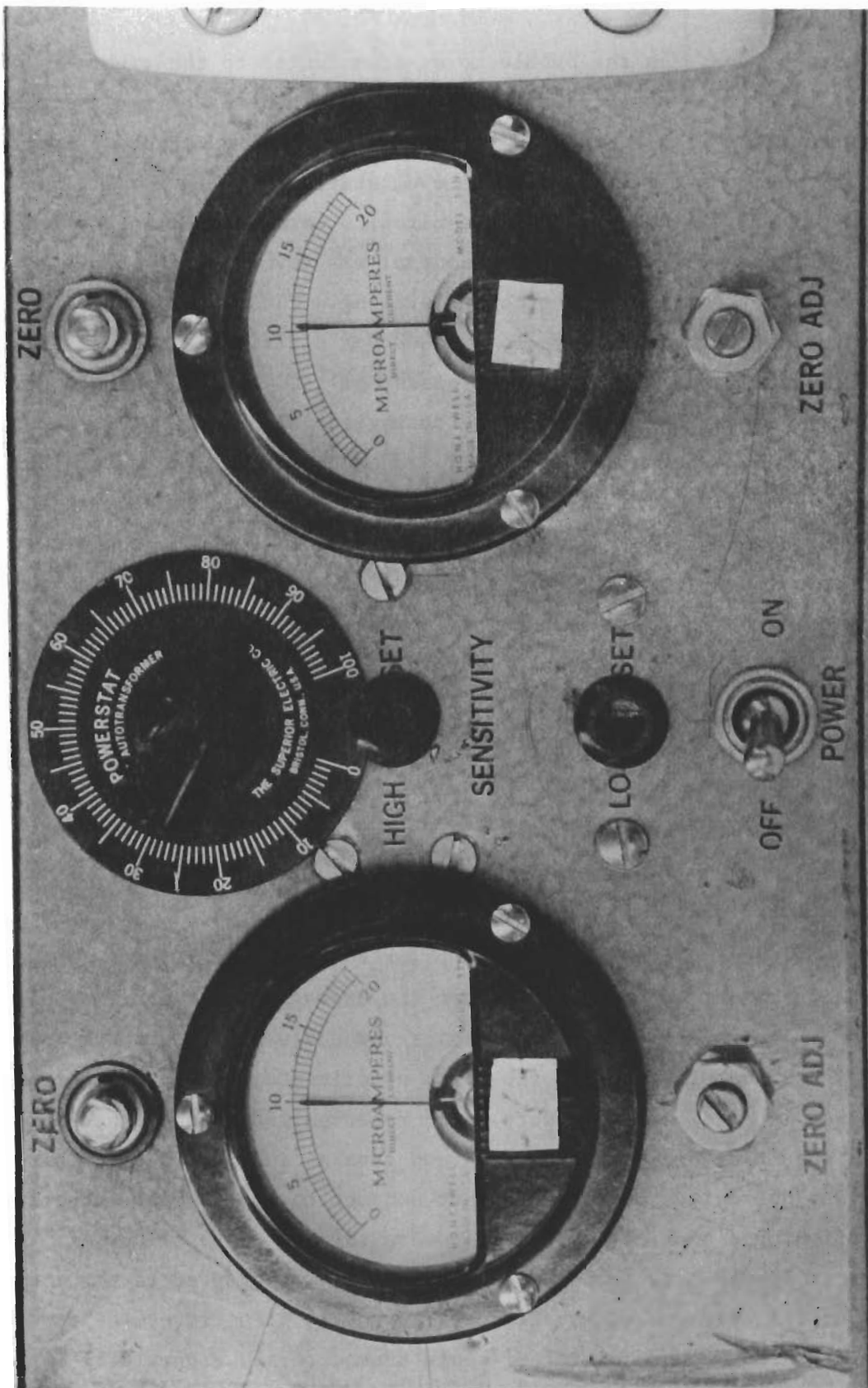


Figure 4.9 Two-Axis Level Deviation Monitor

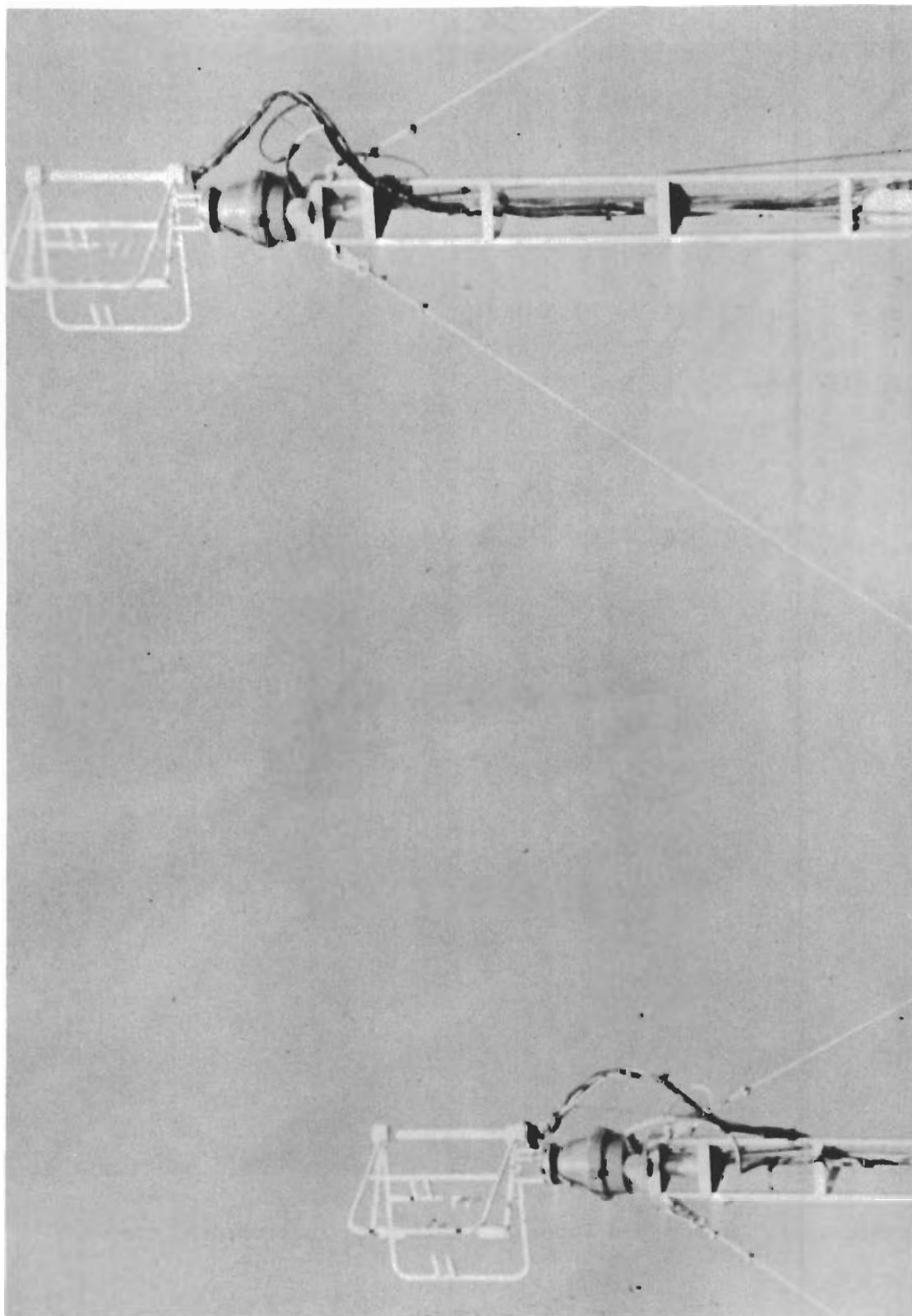


Figure 4.10 Sensor and Rotor Adaptation to Tower Top Mounting



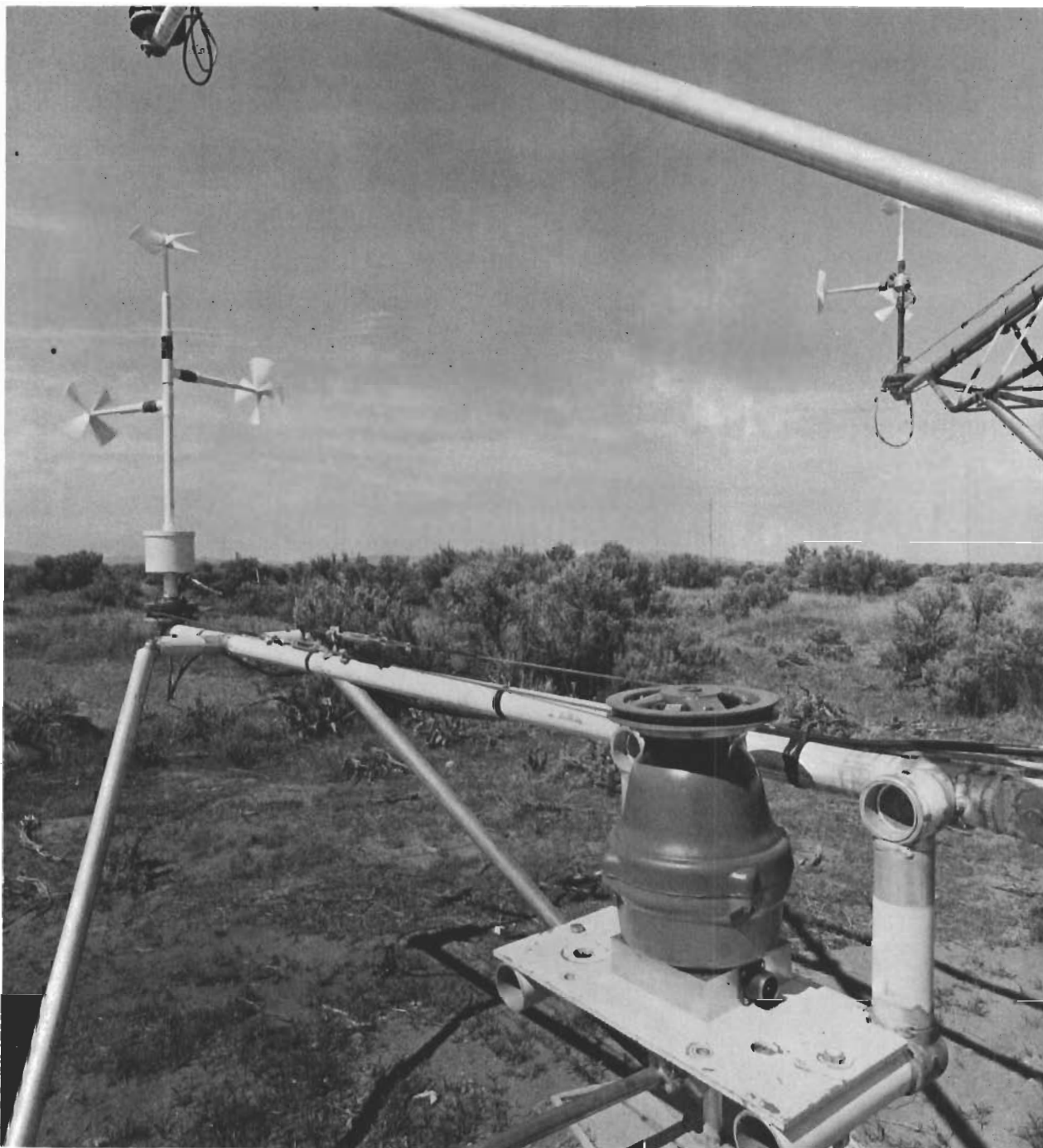


Figure 4.11 Sensor and Rotor Adaptation to Instrument Booms

# Contrails

the instrument boom-mounted rotor control for a Gill anemometer.

Antenna rotors with an associated controller and direction heading indicator were modified for the TOLCAT tower system. Mechanical modifications were necessary to provide a flat mounting surface for adapting the instrument sensors to their respective mounting plates. The normal antenna pipe clamping yoke was cut off and a flat 4-inch by 4-inch aluminum plate was welded to the rotor cap. A nominal 0.010 inch was machined off the mating surface of the upper rotor cap to improve the bearing race spacing, i.e., to tighten the bearing clearance.

Control and direction signal cable run lengths of 500, 1000, 2000, and 5000 feet were required to provide central control and direction indication for the instrument rotor (Figure 4.12). Modifications and circuit redesign were provided to permit the long run rotor control and accurate direction indication. Detailed drawings are provided in Appendix III, Figures III.4 and III.5. Normal antenna rotor operation, as provided by the manufacturer, was limited to a maximum of 150 to 200 feet, without special concern for cable size (wire gauge greater than #16 AWG) and errors of direction heading. Relocation of the rotor motor direction control capacitor from the control-indicator box to the antenna rotor housing reduced the number of load current carrying leads to the rotor. The motor power transformer was removed from the control box and relocated in a junction box 25 feet from the antenna rotor (Figure 4.13). A multiple voltage step-up transformer was located in the junction box with the normal power transformer to permit selective power voltage boosts of 6, 12, 24, or 48 volts as required for various cable run lengths of 500, 1000, 2000, or 5000 feet. With these changes, the multiple conductor cables between the rotor controller, rotor junction box, and to the antenna rotor are all #16 AWG wire gauge.

The direction heading sensing circuitry provided with the antenna rotor was redesigned to operate as a three-wire resistance bridge. The redesign

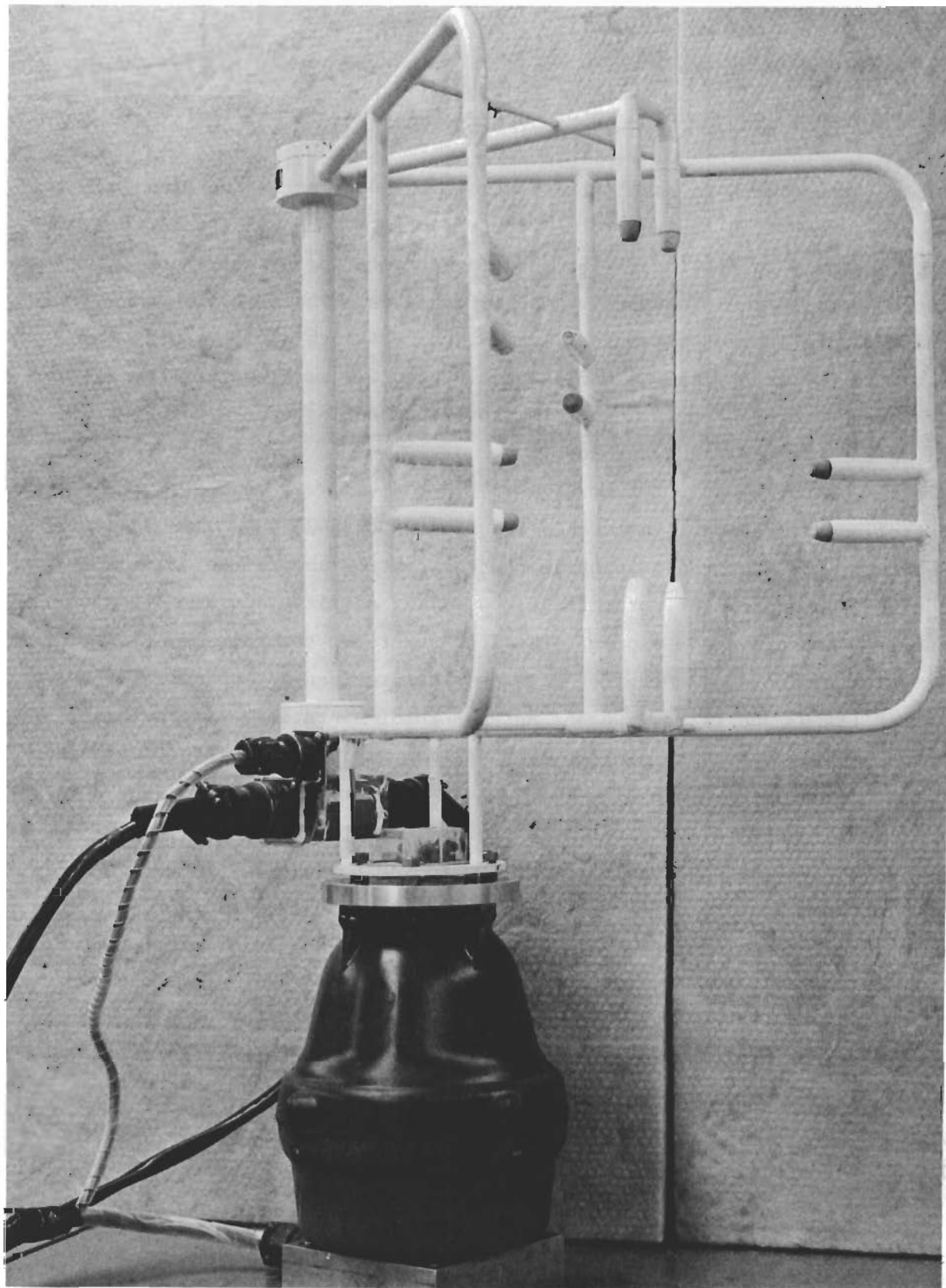


Figure 4.12 Sensor and Rotor with Direction Sensing and Control Cables



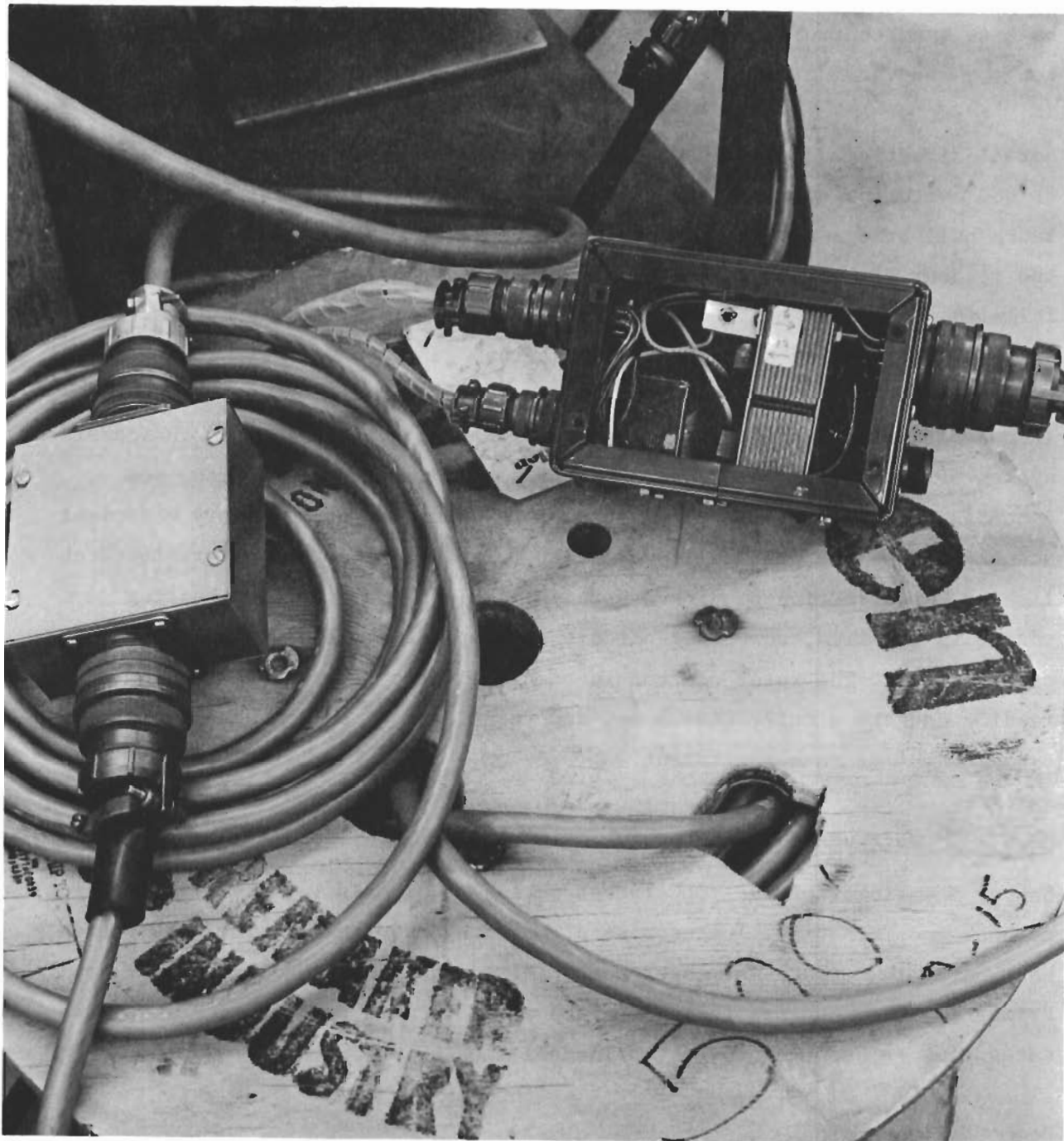


Figure 4.13 Rotor Power Junction Box

(Appendix III, Figure III.6) increased the accuracy, permitting a null balance type control and eliminated errors contributed by the long cable lengths and varying lead resistance.

Normal direction heading readout, as provided by the manufacturer, was  $0^{\circ}$  to  $360^{\circ}$  with incremental readout of  $15^{\circ}$  segments. By utilizing the resistance null bridge system, the readout capability was increased to permit the readout of  $1.875^{\circ}$  increments. A heading change of the rotor always falls in  $3.75^{\circ}$  increments due to the rotor gear-tooth locking system, which sustains the heading selected. The internal gear has 96 teeth for a  $360^{\circ}$  rotation. A single antenna rotor controller and heading indicator system (Figure 4.14) and a multiple channel (10-channel) controller and indicator system (Figure 4.15) were developed and placed in service. (Also, see Appendix III, Figure III.7.) The multiple channel system is very efficient and eliminates the possibility of interpretation and set-up errors in establishing the direction heading desired. Also, when a direction heading change is required, an offset circuit sets up the new heading on the indicator system. The rotor control is then activated to bring the indicator reading back to a null, thus a new and identified direction heading is established for each instrument.

## MOUNTING CONFIGURATIONS

Sensor mountings for the TOLCAT test series required a variety of supporting methods and mechanics. Categories of mounting requirements included stands, horizontal pipe mountings, tower booms (fixed and traveling), and tower tops. Primarily, the mounting techniques and adaptors were unified to satisfy two categories — boom and tower top installation.

### Boom Configurations

All boom configurations provide a 2-1/4-inch pipe segment for sensor mounting. Sonic or Gill anemometers are mounted on a rotatable surface plate which is strapped to the 2-1/4-inch horizontal pipe. The rotatable surface plate



Figure 4.14 Single Rotor Control and Direction Heading Controller



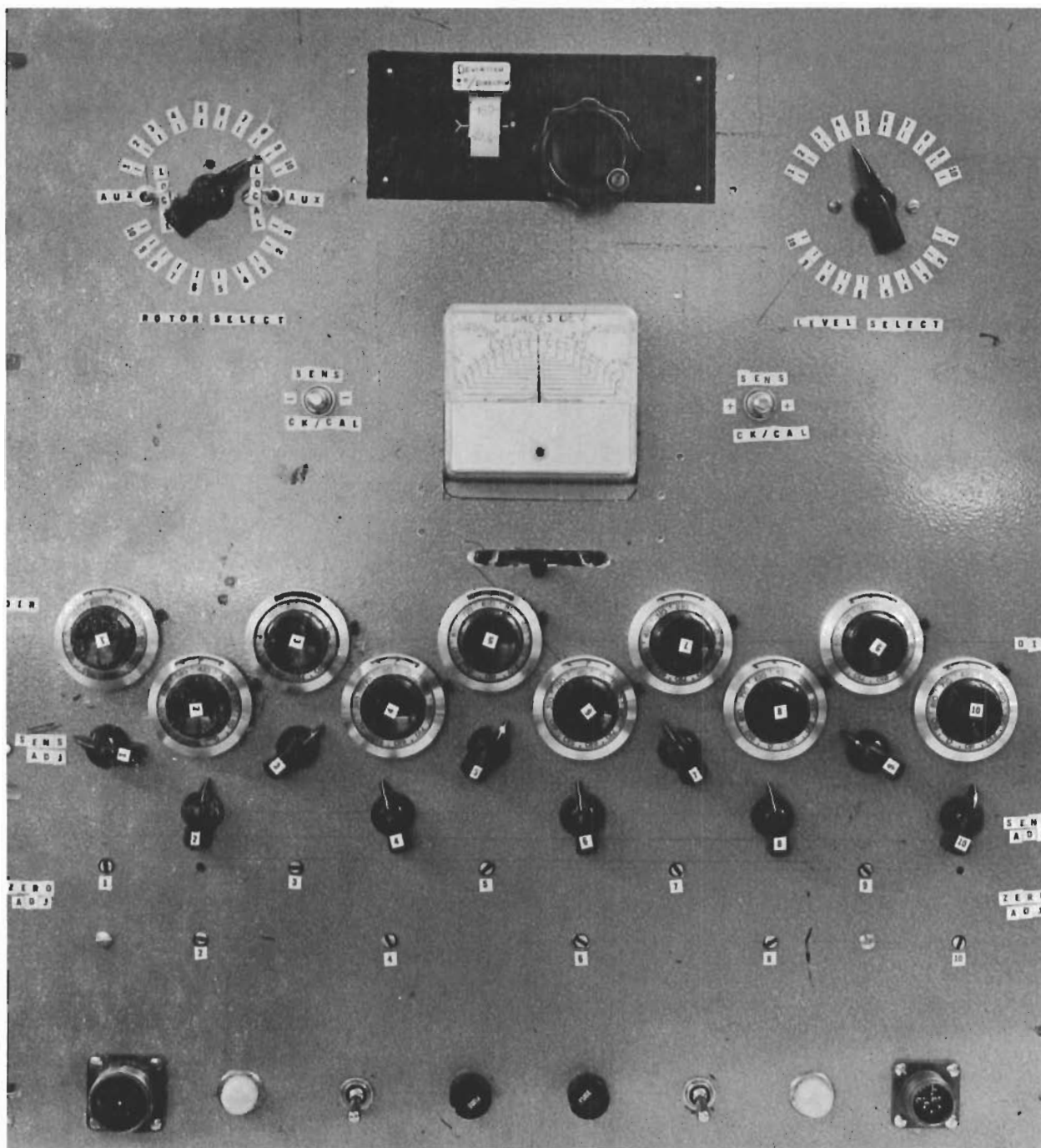


Figure 4.15 Multiple Channel (10) Rotor Control and Direction Heading Controller

# Contrails

is supported on three ball bearing races for freedom of rolling motion and to establish a rotating level plane. Rotation may be accomplished by hand if the sensor and surface plate are readily accessible. When the sensor and surface plate are inaccessible, an aircraft cable interconnects the sensor rotatable surface plate with a duplicate surface plate and rotator wheel at the accessible end of the boom. In each case, the duplicate rotator wheel was punched on  $3^\circ$  centers to provide discrete, known direction headings and also has a locking device to inhibit motion. This manual rotator has been replaced in the final boom configuration with the electrical-mechanical rotator, described previously, which is remotely controlled and monitored for direction heading (Figure 4.11).

Leveling and vibration control were two of the prime boom design requirements. Leveling was initially established by a ground set-up of theodolites and transits. Errors of greater than  $1/2^\circ$  to  $1-1/2^\circ$  were identified by data analysis and ultimately by comparison with the new electrolytic levelers, which reduced the errors to less than 1 minute when booms were properly adjusted. Rigid booms of triangular cross-sections 6.1 meters in length (3 tower diameters) were supported by adjustable support arms. These support arms provided two-axis leveling capability as well as vibration control. Boom vibration was measured with accelerometers and established to be of a high frequency, beyond the range of analytical interest (100 to 600 Hz), and of a very small magnitude (tenths of an inch). Single pipe booms were found to be less desirable for turbulence measurements since vibrations were found at the high end of the frequency range of interest. Boom manipulating davits provided easy handling, raising, and lowering of the booms for installation, calibration, maintenance, and leveling. The 6.1 meter booms were utilized with the rectangular towers (4 x 6 foot in cross-section), but are adaptable to other towers (including rectangular) having an open-faced width of at least  $1/3$  meter.

## Tower Top Mountings

Adaptation of the sensor rotors to the tops of towers utilized a mating plate, universally mountable on all towers. For the experiments of primary analysis interest in this report, direct mounting of turbulence sensors on 30 meter collapsible triangular towers was utilized. These towers are 15 cm on a side at the top, assuring minimal influence of the tower on the measurements. The manner in which the sensor base plate was mated to the top plate of the rotor assembly and the rotator assembly and universal mating plate to the tower is shown in Figure 4.16.

Leveling and vibration control on the towers was accomplished by adjusting the upper three guy wires holding the upper tower section, sensor, and rotor assembly. Towers were initially set up using a transit, with final sensor leveling accomplished using the electrolytic levelers and level monitor.

Utilization of the "Guy As You Erect" (GAYE) kit and system on the collapsible towers eliminated the need for the extra anti-tower rotation guying normally required. The GAYE kit and system, besides being the only realistic safe way to erect the towers, also locks each tower section as it is guyed. The locking of the tower sections, primarily the upper section, to the next supporting section, stabilizes the tower and sensor against vibration and rotation.

## DATA ACQUISITION SYSTEM

Signal cables along with control and monitor cables connect the tower mounted sensors to the data acquisition system. Stable, reliable power is provided to operate both the sensors and the data acquisition system. The data acquisition system generally used throughout the TOLCAT experimentation is illustrated in Figure 4.17. This system includes the sensor inputs from the Gill anemometers (G) and sonic anemometers (S), the required signal conditioning in the case of the Gill anemometers, and their related amplifiers, followed by the data reference module providing reference voltages



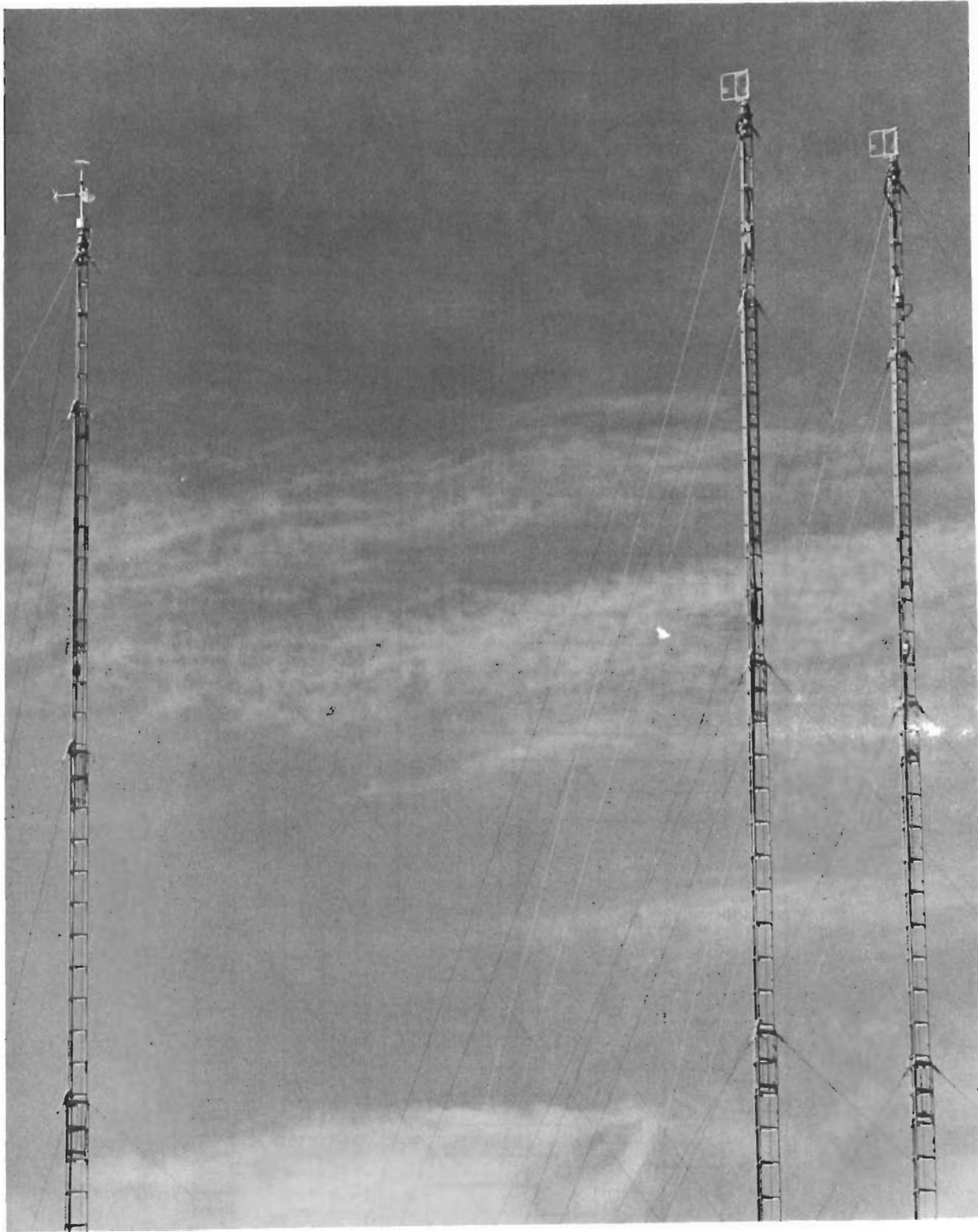


Figure 4.16 Sonic and Gill Anemometers with Rotor Adaptation to Tower Top Mountings

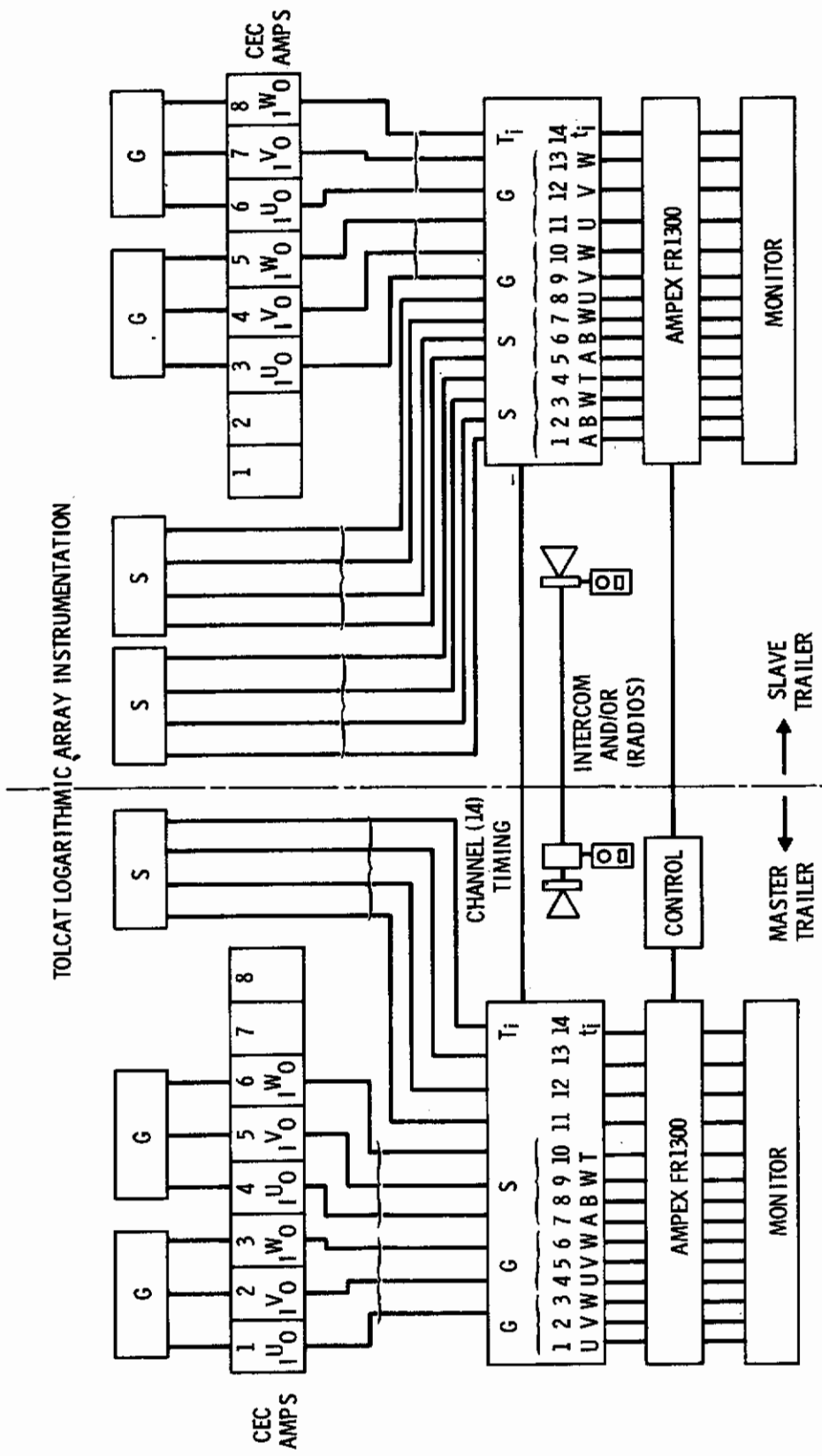


Figure 4.17 Typical Instrumentation System for TOLCAT Experiments

of + 1 volt, - 1 volt, 0 volt, and the related timing time pulse. The data are all input into two 14-channel analog FR-1300 Ampex tape recorders. The recorded analog data are monitored milliseconds later by the readout tape recorder heads and visually observed by the test data monitor panel. Control of the recorders and reference signals is accomplished from the so-called Master Trailer. This system is typical of all the TOLCAT tests and test data accumulation.

A parallel recording scheme was utilized in the final test series. A digital data recorder, the Metrodata DL-620A, was jointly operated with the FR-1300 to demonstrate an optimized field recording digital data acquisition system. This optimized data acquisition system is discussed in Section VIII.

## FIELD ARRAYS

The sensors, sensor mounting equipment, towers, and data recording equipment just described were used together in a variety of configurations. Two basic arrangements of equipment were established in the field for supporting the variety of measurements planned. The first arrangement was used in the first experimental phase and utilized the four 62-meter towers, seven 4-meter stands, two recording trailers, and a power generator (shown in Figure 4.18). The various sensors required for different experiments were repositioned within this basic field arrangement of support equipment.

The second basic arrangement utilized eight collapsible towers, one 62-meter tower, the two recording trailers, and the power generator (Figure 4.19). The sensors were moved within this arrangement to the various heights and locations as necessary for most of the experiments in the second experimental phase. Two exceptions were the 12-meter instrument evaluation test setup which utilized a separate pipe-stand arrangement and the final test at 131 meters atop the Hanford Meteorology Tower.

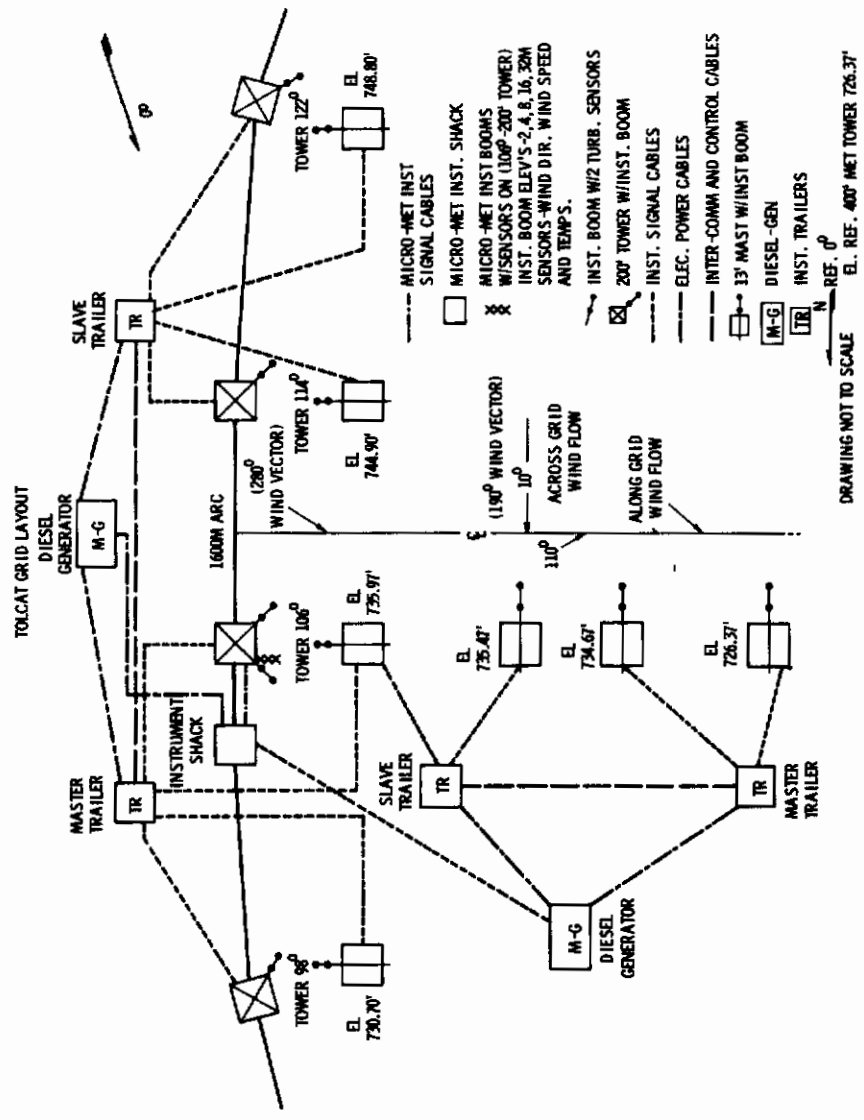


Figure 4.18 TOLCAT Grid Tower and Equipment Layout for First Phase Experiments

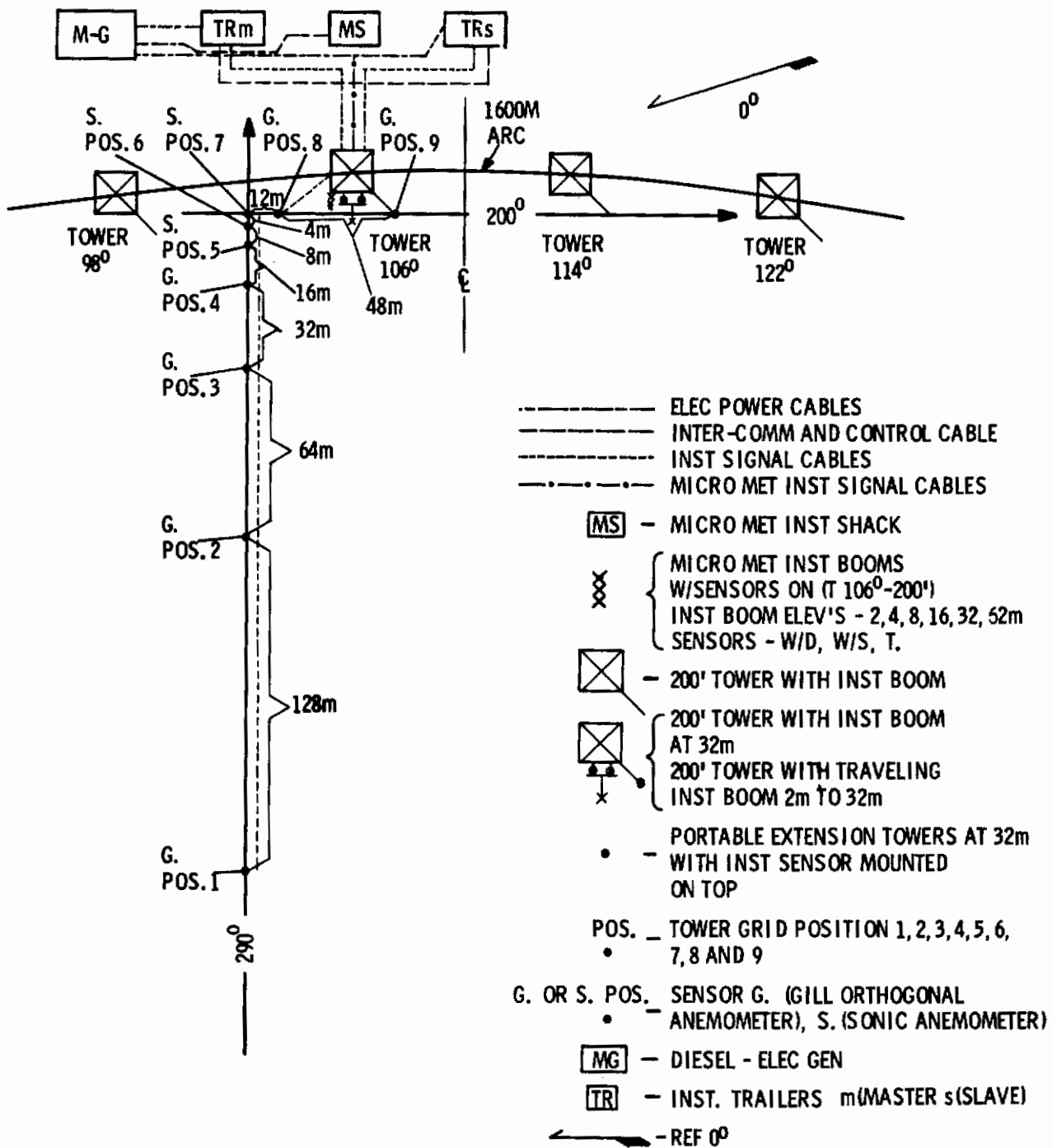


Figure 4.19 TOLCAT Grid Tower and Equipment Layout for Second Phase Experiments



# Contrails

There were eight individual experimental arrays used during the period March 1968 to June 1971, each for separate scientific objectives. The individual arrays are listed below.

1. 58-meter height, 223-meter spacing between each of 4 towers
2. 58-meter height, T-shaped array on a single tower
3. 4-meter height, log spacing of stands over a total of 1023 meters
4. 12-meter height, 1.5-meter spacing on a single stand
5. 1.88-meter to 60-meter height, vertical log spacing on a single tower.
6. 15-meter height, L-array, log spacing over a total of 256 meters
7. 30-meter height, L-array, log spacing over a total of 256 meters
8. 131-meter height, single sensor

The initial tower array consisted of four 62-meter towers spaced 223 meters apart on the 1600-meter arc. Instrument supporting booms 6.1 meters long were installed with sensors at the 58-meter height on each tower. A sonic anemometer was installed on each of the four booms and one of the following anemometers was installed for comparison on each boom: Wind component Meter on Tower 098 (towers are designated in Figure 4.18), VectorVane on Tower 114, and Gill anemometer on Tower 122. (A hot-film anemometer which did not become available in time for this comparison was intended for the fourth tower, Tower 106.)

The second test series array was a T configuration at the 58-meter level of Tower 106 (Figure 4.20). The instrument configuration T formation was made up of three sonic anemometers and one Gill anemometer. Sonic anemometers were at the extremities of the T, with the Gill anemometer at the midpoint of the T-leg. The arrangement of sensors was variable from a small array to a large array.

The third array utilized the eight stands 4 meters in height, which were spaced logarithmically over a total distance of 1023 meters with instruments

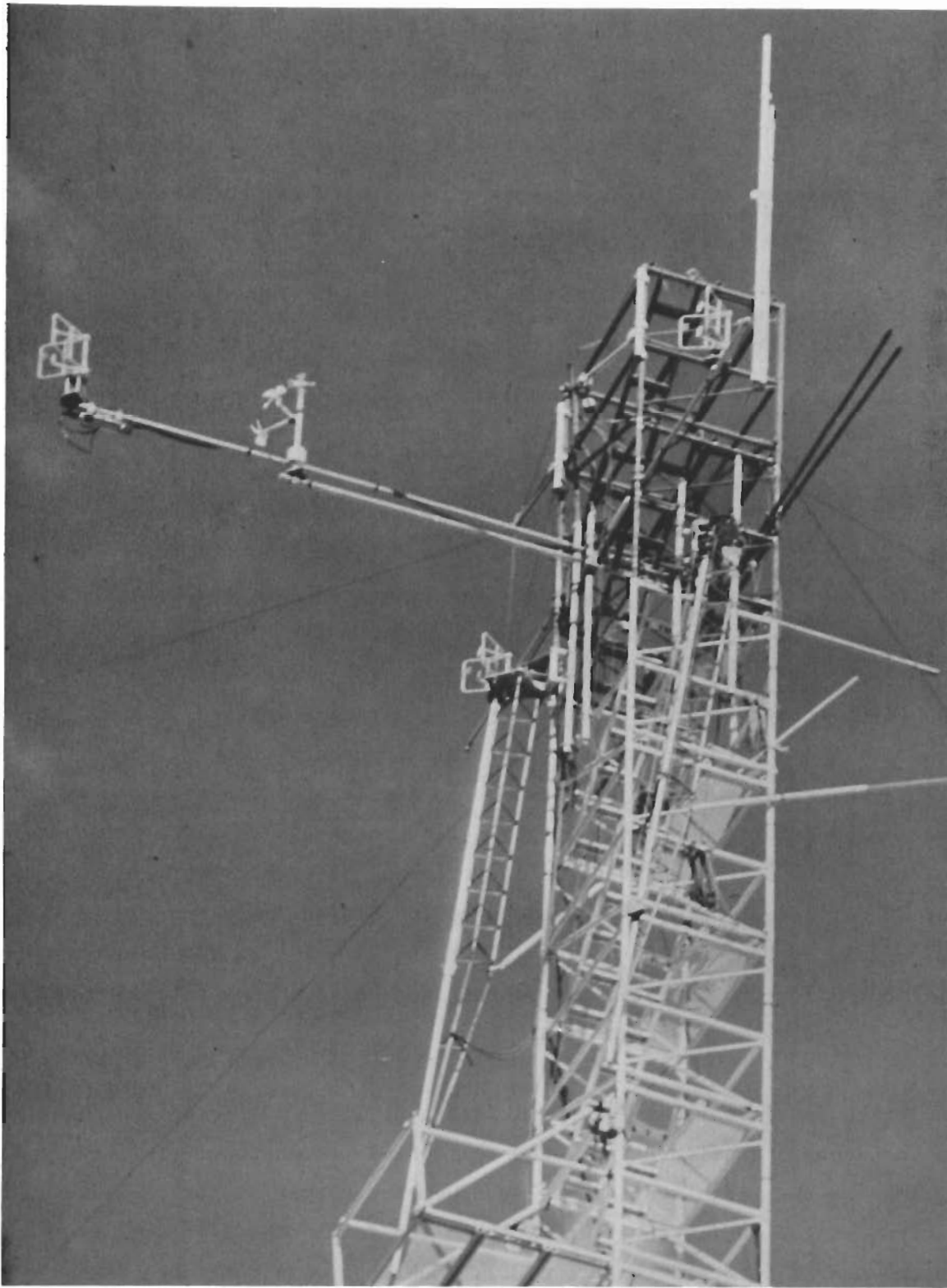


Figure 4.20 TOLCAT Tower "T" Configuration at the 58-meter Level

at 31, 32, 64, 128, 256, and 512 meter separations. The 4-meter stands and the horizontal pipe supports for sensors were instrumented with three sonic anemometers and four Gill anemometers.

The fourth array was a single 12-meter stand with six turbulence sensors spaced 1.5 meters apart. These sensors were aligned, laboratory calibrated, and checked out for field comparison tests. The sensors were located on the evaluation stand as shown in Figure 4.21: on the right, a conventional three-component Gill anemometer, followed by a sonic anemometer, an experimental four-component Gill anemometer, a sonic anemometer, a bivane anemometer, and a VectorVane anemometer. The various anemometers were inter-compared with the sonic anemometer. The sonic anemometers were compared against themselves for statistical comparison and characteristics. The results of these evaluations were discussed in Section III. The sonic anemometer was and still is considered the reference standard for all measurements.

The fifth array utilized Tower 106 and developed a vertical logarithmic sensor alignment to acquire vertical turbulence distribution data. The array was established and utilized for a series of experiments conducted and analyzed for the AEC (References 4.1 through 4.3). These results were related to TOLCAT objectives and the original data were further analyzed for TOLCAT needs. Sensors were located in a logarithmic profile at 1.88, 3.75, 7.5, 15, 30, and 60 meters (Figure 4.22). The Gill anemometers were at 1.88, 3.75, and 30 meter elevations, and sonic anemometers were at the 7.5, 15, and 60 meter elevations.

The sixth and seventh experimental arrays utilized mobile collapsible towers in an L-shaped configuration. The collapsible towers were at 15-meter elevation for the sixth test series and 30-meter elevation for the seventh test series. Eight mobile towers plus Tower 106 formed the L-logarithmic-array spaced over 256 meters (Figure 4.23). Mobile towers 1 through 7 were spaced 4, 8, 16, 32, 64, and 128 meters apart on the long leg of the L-array.

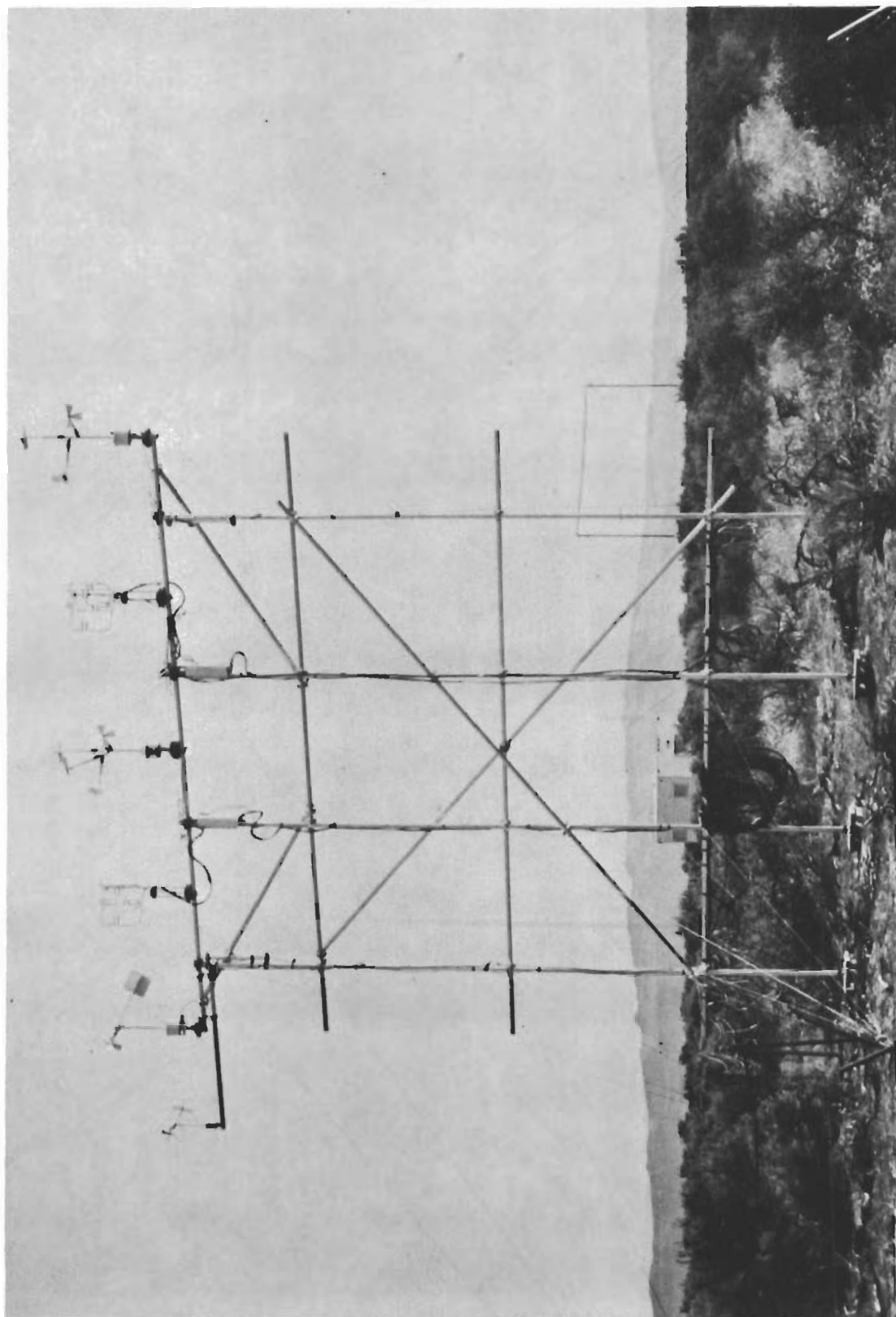


Figure 4.21 Sensor Array for Comparison Tests



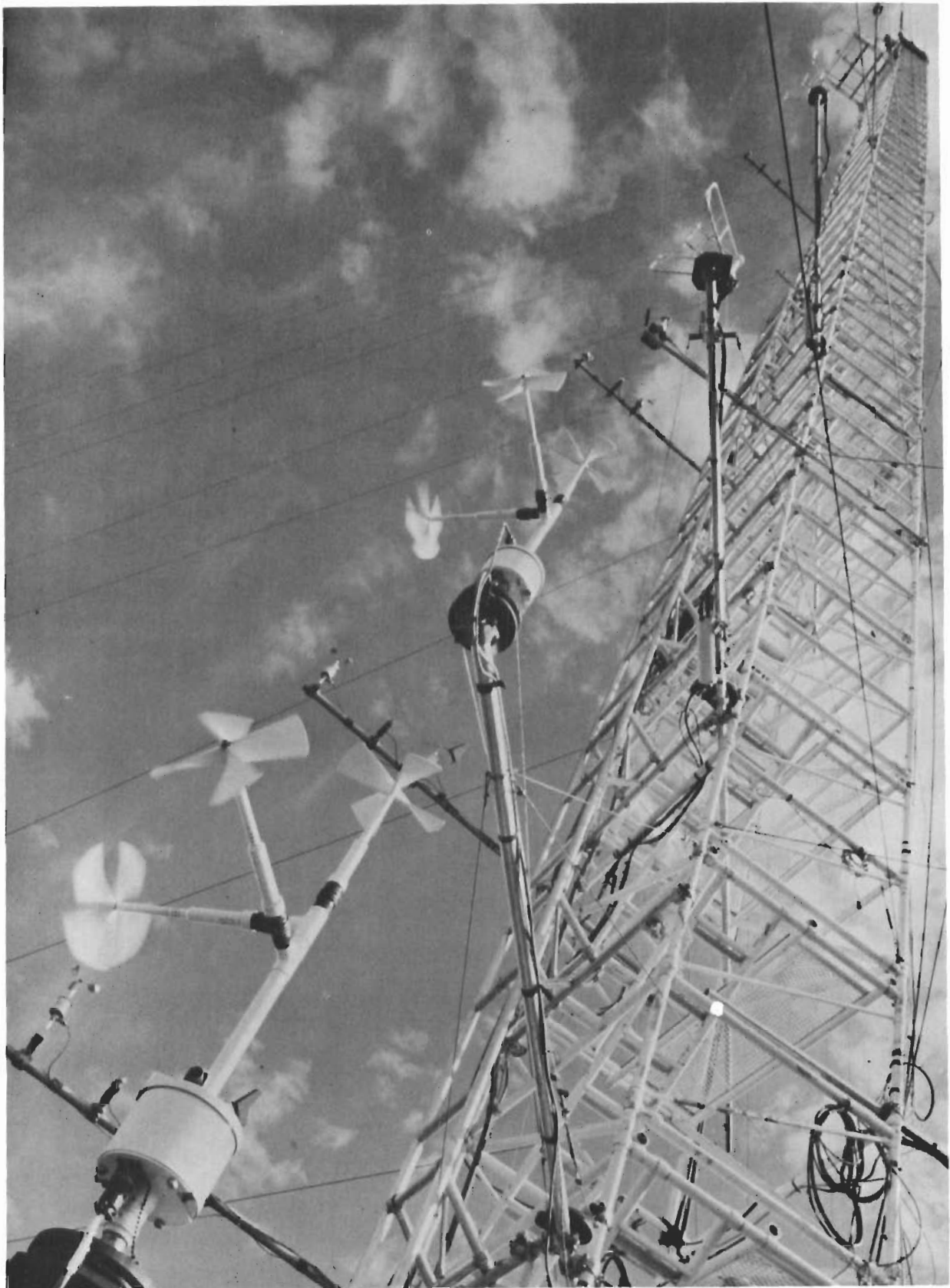


Figure 4.22 Vertical Logarithmic Sensor Spacing for Single Tower Array



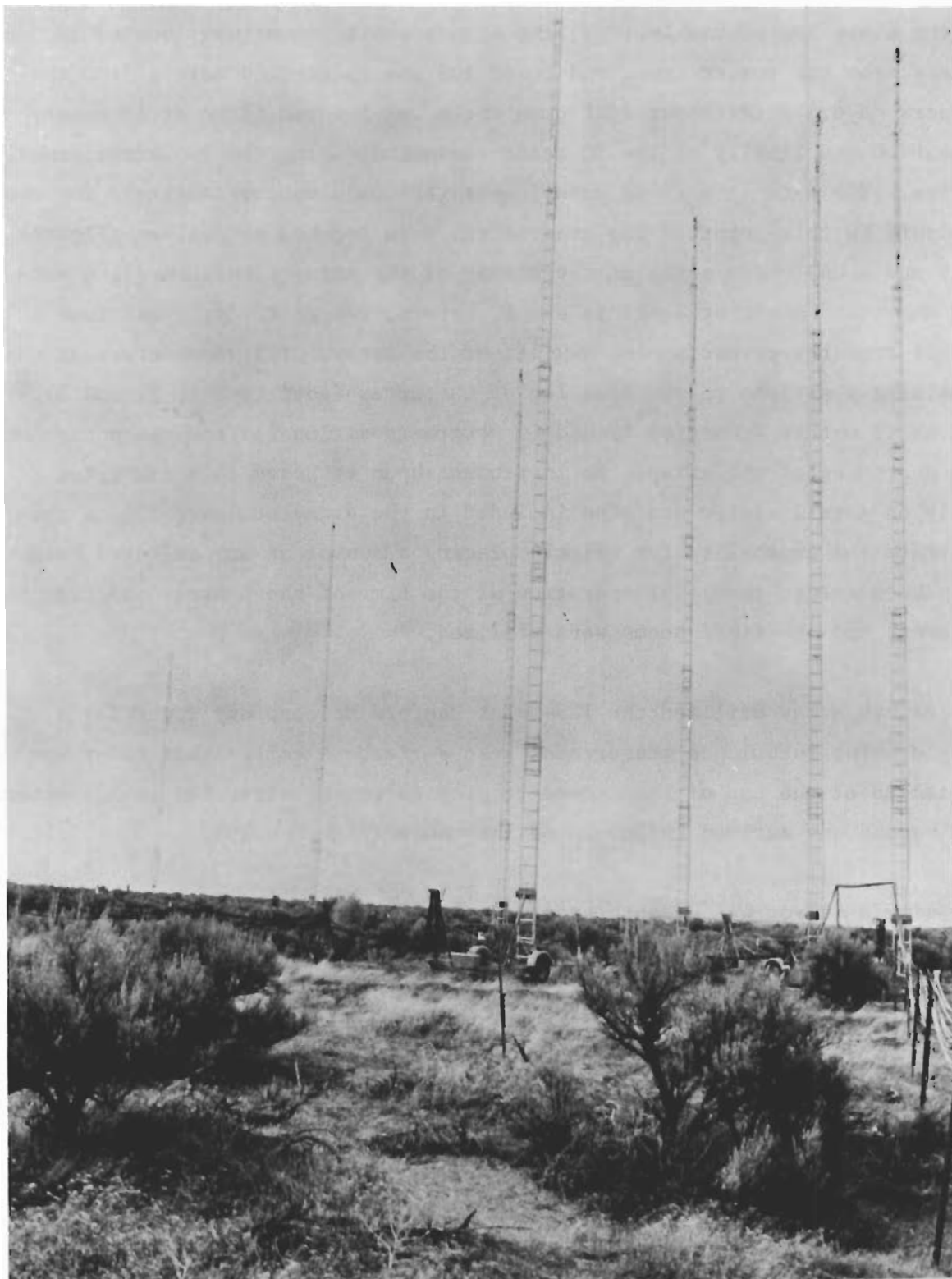


Figure 4.23 Logarithmically-Spaced "L" Configuration of Portable Collapsible Towers at 32-meter Height

# Contrails

On the short leg of the L-array, the eighth mobile tower was located 12 meters from the corner tower and Tower 106 was located 60 meters from the corner. A 6.1 meter tower instrument boom was located first at 15 meter elevation and finally at the 30 meter elevation during the two experimental series. The data from these experiments were used most extensively for the analysis in this report. The anemometers were located as follows (Figures 4.19 and 4.24): one sonic at the corner of the array (position 7), a second and third sonic at 4 meters and 12 meters, respectively, (positions 6 and 5) from the corner on the long leg of the array; Gill anemometers at the remaining positions on the long leg of the array (positions 1, 2, and 3), and at 12 meters (position 8) and 60 meters (position 9) from the corner on the short leg of the array. An instrument boom attached to a traveling dolly on a rail system was also included in the array at Tower 106 to demonstrate the capability for quickly placing a sensor at any selected height. This boom was not ready for operation at the time of the L-array experiments, however, and the fixed booms were utilized.

The eighth array utilized the 125-meter Hanford Meteorology Tower for a single point turbulence measurement test series. A collapsible tower was installed at the top of this tower to provide sensor elevation to 131 meters and beyond any serious influence of the tower (Figure 4.25).

The single sensor was a sonic anemometer used to measure the higher elevation turbulence. This test configuration was also utilized as an evaluation test for data accumulation in direct digital form.

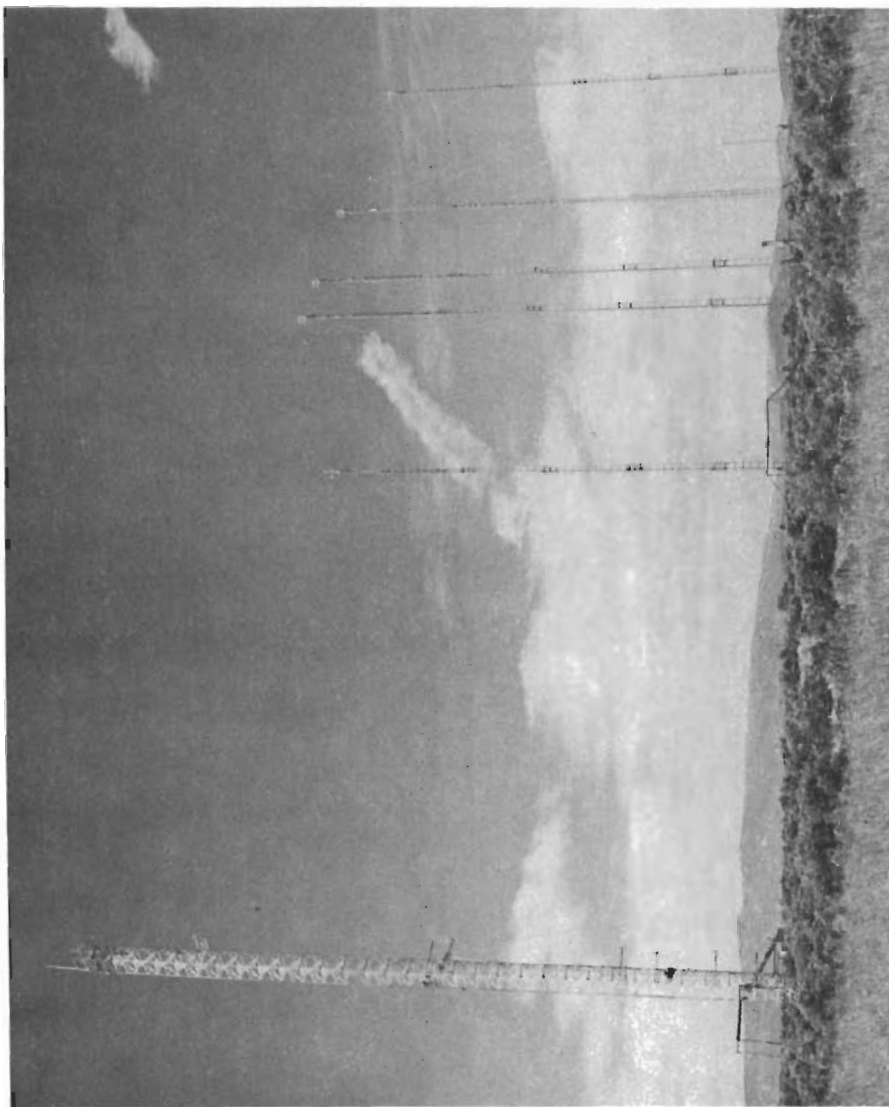


Figure 4.24 Logarithmically-Spaced "L" Array Including Tower 106 with Instrument Boom and Collapsible Towers at 32-Meter Height



Figure 4.25 Single Sensor - Sonic Anemometer - On Top of a Collapsible Tower Utilizing the 125-meter Meteorology Tower



## SECTION V

### DATA CONVERSION SYSTEM

Data measured at the field site locations, as described earlier, were recorded in analog form on 14-channel magnetic tape or digital form on 4-track cassette tape. The data analysis and reporting were performed on a large batch processing computer (UNIVAC 1108) remote from the field site. Since most large computers will not accept field data in these formats as input, the data had to be converted to an input compatible form before processing. Suitable input methods included digital magnetic tape, punched paper tape, punched cards, or direct lines to the computer. The major problem was to provide an economic means of data conversion without compromising the technical requirements of the task. The system developed to perform the sensor data conversion utilized a medium-sized data acquisition computer which has the ability to read analog or cassette tapes and to write IBM compatible digital magnetic tapes. The use of this system permitted not only data format conversion, but also added the capability for data verification and preliminary data transformation. In effect, this system simulates the use of a medium-sized computer programmed for data acquisition at the field site location. This simulation permits an extrapolation of the technical requirements for future field located systems.

#### HARDWARE

The overall data processing system configuration is shown in block diagram in Figure 5.1. The central processor, a Systems Engineering Laboratory SEL 840A, is a single address, fixed-word length (24 bits) parallel arithmetic computer. The cycle time of the 16,384 word memory is 1.75 microseconds. The following peripheral devices are connected to the system:



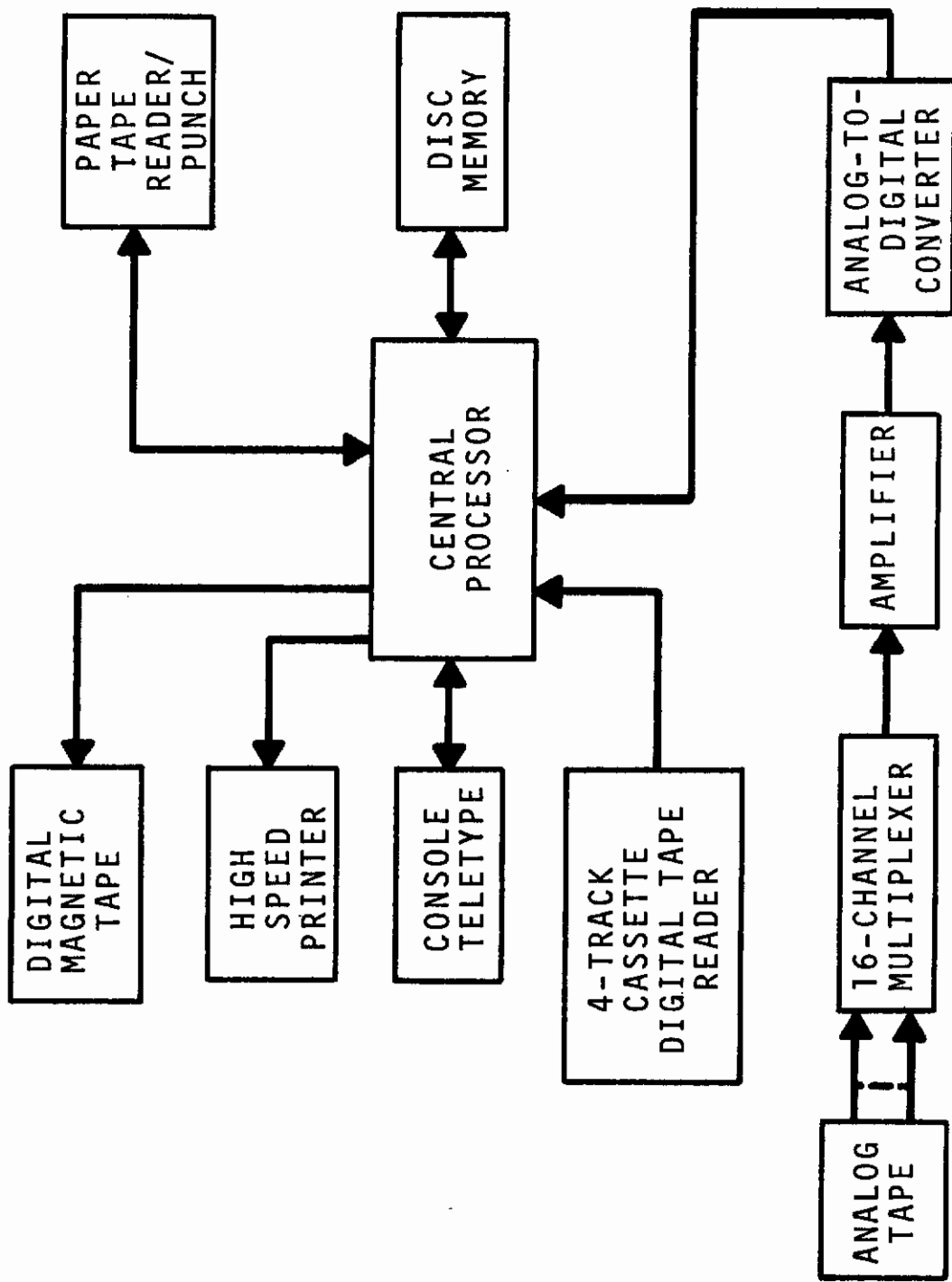


Figure 5.1 Diagram of the Data Conversion and Processing System

# Contrails

1. A KSR-35 teletype used as the principal operator communication device. System operation is controlled from the teletype and it is used for hard copy printed output.
2. A 1-million word disc memory used for storing the operating system and user programs.
3. A high speed paper tape reader/punch used for input/output of paper tape data and programs.
4. A high speed electrostatic printer (1,700 lines/minute) with alphanumeric listing capability and graphics output capability.
5. An analog-to-digital conversion system which includes a 16-channel multiplexer, a fixed gain amplifier, and a 12-bit analog-to-digital converter.
6. A 4-track magnetic tape cassette digital tape reader.
7. An IBM-compatible, 7-track magnetic tape unit.

Fourteen channels of information are provided from the analog recorder as input to the system. The data structure is 13 channels for analog data and utilizes one recorder channel for timing marks to insure the maintenance of timing integrity of the two concurrent tapes throughout the conversion run. The 13 analog data channels are sampled sequentially by the multiplexer and the data are converted to digital form and stored in the computer. Alternately, data recorded in digital form on 4-track cassette magnetic tape are input to the data conversion system on the cassette reader.

After the data verification, scaling and coordinate transformations are made, the data are output to the digital magnetic tape. The technical specifications of the input and output systems are as follows:

# Contrails

## 1. Multiplexer

Number of channels: 16  
Maximum Input Voltage:  $\pm 5$  volt  
Switching Time: 1 microsecond  
Accuracy:  $\pm 0.1\%$

## 2. Amplifier

Gain: 7.07  
Frequency Response: D.C. to 1 MHz  
Gain Accuracy:  $\pm 0.1\%$

## 3. Analog-to-Digital Converter

Number of Bits: 12 (11 data + sign)  
Accuracy: 0.1%  
Conversion Time: 8 microseconds

## 4. Magnetic Tape Cassette Reader

Packing Density: 20 data channels per record  
Format: 4-bit binary-coded decimal  
Reel Characteristics: Cartridge containing endless loop  
1/4 inch tape  
Tape Speed: 2.4 records per second

## 5. Digital Magnetic Tape Unit

Packing Density: 556 characters per inch  
Format: IBM compatible NRZ1  
Reel Characteristics: Standard 1-1/2 inch reels using  
1/2 inch x 2400 foot tape  
Tape Speed: 45 inches per second

The resultant digital data tapes are compatible with industry standard computers and are ready for immediate input to the UNIVAC 1108. The data are then available for the multiple analysis programs.

## SOFTWARE

Most of the calculations involved in scaling and converting the field data to scientific units were done with FORTRAN-IV coded routines to permit easy program modifications as experimental objectives and plans varied. Input and output operations, however, were coded in SEL 840A assembly-language, due to the real-time requirements of the overall system.

The software was structured in a modular fashion according to function, so that any programmed function could be modified without the necessity of reassembling the entire software system. Each of these modules is described below.

### The Main Program

Operation of the software system is initiated by the operator, who activates the TOLCAT main program by typing a directive to the SEL 840A operating system. The TOLCAT program then queries the operator for information about the data to be processed.

The first item input by the operator indicates whether the data are to be read from analog tape or from the digital magnetic tape cassette reader. The computer then requests information concerning the type of data recorded on each analog or digital tape channel. As each data input channel is identified by the operator, the computer requests type-in of necessary scale factors for conversion of that particular data type to scientific units.

After the input data have been described to the computer, and if the input medium is analog tape, the computer requests type-in of the desired sampling rate. This value is used in determining how often the analog tape will be read by the computer via the analog-to-digital converter and also the number of readings that are to be averaged to obtain one smoothed sample of input data. In the case of digital cassette tape input this operation

is not performed, as the sampling rate is fixed at the time of recording.

When the operator/computer conversation is complete, the program waits for the operator to start the input device and then proceeds to transfer control to a series of subroutines which read the data, perform the necessary calculations, and write the output tape.

## The Subroutines

The subroutines called by the main program can be divided into three classifications: (1) Input of raw field data to the computer's memory, (2) conversion of these data from voltages to scientific units, i.e., degrees centigrade and centimeters per second, and (3) output of the converted values to magnetic tape.

## Input Routines

Two input routines exist in the TOLCAT software system; one for each type of input unit used. Subroutine MET is called by the main program when the magnetic tape cassette reader is used to supply input data. This routine responds to a hardware interrupt from the tape reader which occurs whenever a character is available for input. MET assembles these characters into binary numbers corresponding to recorded voltages on the cassette tape and stores these numbers in the system's input buffer in core memory.

When analog tape is used as the input medium, the other input subroutine, TIM, is called. TIM is entered in response to a hardware interrupt generated by a hardware sampling clock in the SEL 840A system. Each time this clock interrupts (usually every 0.01 second) TIM reads the appropriate channels on the analog tape recorder via the multiplexed analog-to-digital converter and saves these values in a temporary buffer. As soon as each channel of input data has been sampled the required number of times, TIM averages the values so obtained and stores the averaged values for each channel in the system's input buffer in core memory.



# Contrails

Both TIM and MET perform a reasonableness check on the incoming data to insure that the readings are within prescribed limits. If a reading from a particular data channel is found to be unreasonable, that value is discarded and the previous value for that channel is substituted for it. In this way large noise spikes are eliminated from the data record.

## Conversion Routines

When the main TOLCAT program detects that raw data have been placed in the system's input buffer by subroutine TIM or MET, it picks up the current value of input data for each channel and transfers it to a specialized calculation routine. One conversion routine for each different type of input data (i.e., each type of anemometer) is included in the system. Currently, the routines are as follows:

- SONIC1: Three-component sonic anemometer
- SONIC2: Four-component (3 wind components plus temperature) sonic
- GILL: Three-component Gill anemometer
- WCM: Wind Component Meter

Each data item is passed to the appropriate conversion routine, where the following operations are performed as required:

- Orthogonalization of the wind components
- Correction for instrument orientation
- Conversion to centimeters per second or degrees centigrade

## Output Routines

Since neither the cassette tape reader nor the analog tape unit can be stopped in the middle of a run to allow calculations and output of converted

data to be performed, a special output routine, MTD, was developed to allow magnetic tape output to occur concurrently with data input and conversion. MTD is called by the conversion routines each time a final value is ready for output. MTD accepts these values and places them in an output buffer in core memory. When enough values are obtained to produce one physical record on the output tape, MTD initiates a magnetic tape write operation using the SEL 840A's block transfer data channel. It then proceeds to route incoming values to a second buffer so that incoming data can be processed while outgoing data is being written. Thus, a continuous flow of data from the input unit to the output tape is maintained. MTD also checks for magnetic tape parity errors and will rewrite a record in the event that one was written improperly.

When the operator terminates the run, the main program transfers control to a routine called CAT3 which types out a summary of the run, including the number of errors detected in the input data by subroutines TIM or MET and the number of tape errors encountered by subroutine MTD.

### Program Verification and Equipment Testing

Several utility programs have been developed for the purpose of checking the integrity of the TOLCAT system. A test program is available for the analog-to-digital conversion equipment which accepts known analog voltage inputs and prints out interpreted results; a second test program lists the contents of a cassette tape on the printer; and a third routine verifies and prints the contents of the output tape prior to processing on the UNIVAC 1108.

## SECTION VI

### COMPUTER PROGRAMMING FOR ANALYSIS

The three computer programs developed for execution on the UNIVAC 1108 computer, used for TOLCAT analysis, have the following functions.

1. An initial tape is made for each segment of a field experiment to be analyzed. These segments are usually 1 to 1-1/2 hours in length. The data for this tape are taken from the SEL 840A generated digital tape and contain all the variables measured in the field.
2. A permanent storage, or master tape, is made from the initial UNIVAC 1108 tape. All data are edited, and all Gill data are corrected for noncosine response. The horizontal wind data are rotated so that the component designated as  $U_a$  is in the direction simulated by the array as head-on.
3. Selected segments of data from one or two master tapes (each log array experiment required two tapes to record the data) are subjected to spectral analysis, probability analysis, or bispectral analysis.

#### INITIAL UNIVAC 1108 TAPE Program

This program is the same as the first program described in detail in the Interim Report. Its workings will only be summarized here. The program first writes a header, or leader, record on the initial UNIVAC 1108 tape, containing pertinent specifics about the test, such as time, date, instrumentation, meteorological stability, dimensions of the data record, etc. The remainder of the operation consists of reading the data from the SEL-generated tape, scaling velocities to centimeters per second, scaling temperatures to  $0.01^\circ$  Centigrade and packing the scaled data on the initial UNIVAC 1108 tape. The data are written in separate records, each of which

is one minute long. If the data came from, say three anemometers, one of which recorded temperature,  $\theta$ , in addition to the three-wind components,  $U_a$ ,  $V_a$ , and  $W$ , the tape would contain three sets of  $U_a$ ,  $V_a$ , and  $W$  and one set of  $U_a$ ,  $V_a$ ,  $W$ , and  $\theta$  making 13 channels in all. The first 13 data numbers would be the second values of the 13 parameters occurring  $\Delta t$  seconds after the initial values, etc. The interval,  $\Delta t$ , between consecutive samples was usually either 0.05 or 0.2 seconds as determined from the selected digitizing rate on the SEL 840A. If  $M$  data channels were incorporated into the tape, the total number of data in a one-minute record would be  $60M/\Delta t$ .

## FINAL MASTER TAPE PROGRAM

This program was created during the second phase of the TOLCAT studies. It has three principals function:

1. Editing,
2. Correction of data for noncosine response, and
3. Reorienting the horizontal wind data in any arbitrary direction.

### Editing

The editing subroutine checks each set of successive data points in each channel with respect to an arbitrary tolerance,  $T_e$ . If two successive data points differ by more than  $T_e$ , i.e., if

$$|V(t) - V(t-\Delta t)| > T_e \quad , \quad (6.1)$$

one of three types of editing is employed:

Type A.  $V(t)$  is set equal to  $V(t-\Delta t)$  unless one of the two conditions listed below are found to apply.

Type B.  $V(t-2\Delta t)$  is also checked. If

$$|V(t) - V(t-2\Delta t)| \leq 0.5 T_e \quad , \quad (6.2)$$

$V(t)$  is left unchanged and  $V(t-\Delta t)$  is set equal to the arithmetic mean of  $V(t)$  and  $V(t-2\Delta t)$ .

Type C. If Type B editing is not performed, the programs also check  $V(t+\Delta t)$  and  $V(t+2\Delta t)$ . If

$$|V(t) - V(t+\Delta t)| + |V(t+\Delta t) - V(t+2\Delta t)| \leq 0.5 T_e, \quad (6.3)$$

no values are changed, but a notation describing the data discontinuity is printed out.

As stated above, if neither Type B nor Type C editing is performed, Type A editing is performed to all  $V(t)$  where tolerance is exceeded. The usual  $T_e$  employed was 3 mps. Each time any type of editing is employed, a notation is printed out, and a score is kept for the following:

1. The total editing on each channel per minute.
2. The sum of the previous over all channels.
3. The cumulative editing on each channel.
4. The sums of the cumulative editing over all channels.

Maximum tolerances for the accumulations under 2 and 4 are specified. When these are exceeded, the program terminates. If examination of the editing record printed out reveals that all the channels with the exception of a certain few were relatively clean, the program can be run again on the same data, leaving those channels unedited. In this way, the good data channels from the experiment can be preserved, although existing alongside other data unfit for use.

### Correction of Gill Data for Noncosine Response

The program has three Gill correction subroutines. The first, and the only one used on data analyzed in the analysis section (Section VII), is for the



# Contrails

upright 3-component Gill. The other Gill correction subroutines are for an upright 4-component Gill and a tipped 3-component Gill, respectively. The last of these is for a Gill tipped forward  $45^\circ$  in the plane bisecting the U and V axes.

The noncosine response correction is effected by an iterative scheme. Because the correction needed depends on the direction cosines that the instantaneous wind vector makes with the orientation of the three propellers, and because the apparent direction cosines change when this correction is made, iteration must be carried out until the results converge. The correction subroutines are written so that iteration takes place until either all three direction cosines change by less than  $2^\circ$  by further iteration or until 6 iterations have been performed. If the latter occurs first, the last set of direction cosines is used, and notation printed out to indicate lack of convergence. On records of 1200 data points per channel, this number is seldom more than 5 per Gill and is therefore not of concern.

The first two subroutines are equipped to handle data from Gills oriented either with the U arm facing the direction defined as the X-axis for sonic data or with the X-axis of the sonic data bisecting the angle between the U and V arms of the Gill. The latter is the usual method of installation in the field. After the noncosine response corrections to these data are made, the horizontal data are rotated  $45^\circ$  to make them compatible with sonic data.

The program also has the capability of averaging the Gill data together, N data points at a time, before noncosine correction. If the loss of detail can be tolerated, the reduction of the UNIVAC 1108 operating time recommends this procedure.

## Reorientation of all Data with Respect to an Arbitrary X-Axis

The initial data handling involves recognition of two sets of X-axes. The first orientation is chosen in the field just before the recording begins

# Contrails

in the apparent direction of the mean wind. The sonic anemometers are orientated so that the first X-axis bisects the angle between the A and B arms, and the Gills are oriented so that the same axis bisects the angles between the U and V arms. The other X-axis is the simulated fuselage direction of the aircraft. In the case of the logarithmic array, this is simply the upwind direction of the tower line. After editing and Gill corrections are applied, the data must be reoriented in the direction of the second X-axis unless by chance the instrument orientation was along-tower-line. After this rotation is performed, the data are in their final form.

## ANALYSIS PROGRAM

For those experiments in which all the data are recorded on one or two AMPEX recorders and for which as many final master digital tapes are made this program can input all data channels recorded during the experiment on one or two UNIVAC 1108 Drum Files and proceed to analyze and cross-analyze as many combinations of two or three channels at a time as are desired over any selected combination of segments in time. However, because such a one-shot operation can be expensive, and because something unexpected could go wrong, the work is usually broken down into three or more submissions, each result being scrutinized for credibility before the next submission.

The total array of subroutines of this program requires a core allocation that far exceeds the available core of the UNIVAC 1108. Therefore, several sets of subroutines are called into core successively by a main program that keeps the drum files intact while the analysis subroutine sets succeed each other in using the same core allocation.

There are five subroutine sets that may succeed each other.

1. The first set does all the data handling involving drum files. The one or two master tapes are read onto two drum files that

# Contrails

are called the Master Drum Files. Then, two or three data channels are selected for analysis, and the appropriate segments are unpacked and incorporated onto what is called the Principal Drum Files. (The Principal Drum Files correspond to the special tapes mentioned in the Interim Report.) After all desired analyses have been performed by other subroutine sets on these files, the data handling set can be called again to select another set of two or three channels from the Master Drum Files for incorporation onto the Principal Drum Files, which in turn may be analyzed.

This set also has an optional subroutine that creates differenced data as needed to simulate wing shears. It reads from the Master Drum file U, V, and W as recorded at two locations, A and B, and forms the strings:

$$U_d(t) = U_A(t) - U_B(t), \text{ etc.} \quad (6.4)$$

2. The second set is used instead of the first set when data are to be read in from special tapes, each tape containing time series data from one variable. The data from each special tape are read directly onto the Principal Drum Files prior to analysis. Because special tapes have not been made since the capability of analyzing directly from master tapes was made available, this option is seldom used.
3. The third set corresponds to the probability program described in the Interim Report. The probability set begins operations by reading the data into core from the Principal Drum Files. There are several options that may be exercised before analysis begins. They are:
  - a) Block averaging of successive data points,  $n$  at a time, for each variable.
  - b) Rotation of the horizontal components so as to align the U

component with the mean horizontal wind direction.

- c) Substituting for two original series,  $U_1(t)$  and  $U_2(t)$

$$U_s(t) = U_1(t) + U_2(t)$$

$$U_d(t) = U_1(t) - U_2(t) \quad .$$

- d) Differencing the data, substituting  $U(t)$ ,  $U(t+\Delta t) - U(t)$ .  
e) Editing -- not used when data have been edited by the program that creates the final master tapes.  
f) Plotting the data.

After as many of these handling options as desired have been exercised, the data in its current form are stored on three more drum files, which are called the Secondary Drum Files, that are read by the set of subroutines that performs spectral calculations. These new files are created before the probability analysis begins because a further option for high-pass filtering the data, which shortens the series, may be exercised.

After the final version of the data has been established in core, the mean value of each component is subtracted out. Next the second and third order moments,  $\overline{u_i u_j}$  and  $\overline{u_i u_j u_k}$ ,  $i, j, k = 1, 2, 3$  are computed along with the skewness and kurtosis for each individual series. The computation of the joint moments is optional.

Another option provides for computation of magnitude correlations which may be described as follows. For two series of turbulence data,  $u'(t)$  and  $v'(t)$ , each with zero mean and with variances  $\sigma_u^2$  and  $\sigma_v^2$ , respectively, let

$$x(t) = u'^2(t) - \sigma_u^2 \quad (6.5)$$

and

$$y(t) = v'^2(t) = -\sigma_v^2 \quad . \quad (6.6)$$

Then

$$M_{uv} = \frac{\overline{x(t) y(t)}}{[\overline{x^2(t)} \overline{y^2(t)}]^{1/2}} \quad (6.7)$$

is the desired magnitude correlation.

The next option provides for individual histograms, pdf's, over a previously designated range distributed among a previously designated number of segments. Usually the range is 10 mps and the segment length is 0.25 mps, making 41 segments with center values, -5.0, -4.75, . . . , 0.00, 0.25, . . . , 4.75, 5.00. Values that fall outside the range are printed out individually along with their ordinal number in the series. A count is maintained of the outside values. If these are too numerous, the analysis may be repeated via another submission using a larger range and a correspondingly larger individual segment length. The pdf's are given in three columns for each variable. The first column is the raw count, the second column is the fraction in each segment, and the third column is the integral of the second column, necessarily running from zero to unity.

The next option computes joint probability distributions, jpdf's, for each set of two series in core. If there are three series in core, three jpdf's are available. The linear dimension of the boxes is twice that used for the pdf's, making an array of 21 x 21 boxes. Two versions of the jpdf's are given. The first is raw count, while in the second the count is normalized for a box with dimensions of 1 (mps)<sup>2</sup>.



# Contrails

The final option provides for high-pass filtering of the series. This is done by subtracting a running mean of a specified length from the original series. After this is done all the moment and probability analyses specified by the options are repeated for the filtered data. The filtered series are necessarily shorter than the original series. After the filtered data have been analyzed the filtering may be repeated a second and third time, each time with a shorter running mean. When the original series is 8192 points, the number of points in each successively applied running mean is usually 1501, 301, and 61. This makes possible the computation of pdf's and jpdf's based on variation over shorter and shorter periods of time.

4. After all moment and probability analyses have been completed, the set of subroutines that performs the power spectral and cross-spectral analysis is called into core. The data are read in from the Secondary Drum Files, and are detrended and tapered before analysis.

The analysis corresponds to that performed by the fast Fourier program described in the Interim Report, while including several new options.

- a) The first option is merely procedural. The spectral program described in the Interim Report did not analyze, U, V, and W with one submission because it read into core only two series at a time — then proceeded to analyze by treating one series as the real part and the other series as the imaginary part of a complex number. With the drum capability added, U, V, and W are available from the drums simultaneously, and may be read in successively — U and V, then U and W, then V and W — to secure all cross analyses.

# Contrails

- b) The second option computes the best fitting first or second order polynomial for each series and subtracts this out. The coefficients for each polynomial are also given. This is the only detrending used on the data. After detrending the sine-squared bell taper is applied, as described in the Interim Report. Usually the best second order polynomial was subtracted out and the taper applied to the 5 percent at each end of the detrended data.
- c) Another option permits computing of the covariances from spectra from which the low frequency content has been removed. At first this was done by zeroing out the estimates for an arbitrary number of harmonics before the covariances were computed from the spectra. In its present state the program replaces the sharp cutoff with a gradual cutoff involving the hyperbolic tangent function. If the option is asked to remove the spectral energy below the  $n$ th harmonic, the  $\tanh$  routine is applied so that the energy in the  $n$ th harmonic is halved, the energy in the harmonics below  $n$  are reduced by lesser amounts. If  $S_m$  is the spectral estimate for the  $m$ th harmonic, the reduction steps in the program are:

$$A = 1/2(m-n)$$

$$B = 1/2[1 + \tanh (A)]$$

$$S_{m,r} = B S_m$$

where  $S_{m,r}$  is the reduced spectral estimate to be used for covariance computation. The coefficient,  $1/2$ , in the first step is adjustable and determines the sharpness of the cutoff. After the data preparation is completed, the power spectral and cross-spectral analyses are performed, yielding 10 banded estimates per decade, as stated in the Interim Report. Also, autocorrelations and cross-correlations may be computed by processing the spectra through the fast Fourier subroutine.

5. Another set of subroutines is available for performing bispectral analysis, see Equations 2.28 and 2.29. Although the initial bispectral computations have not been comprehensive enough to offer representative results, the intent, the theory, and the application of fast Fourier techniques are described in Appendix II. The crux of the whole computation problem is to get the bispectrum from the complex Fourier coefficient already in core, according to the relation

$$B_i(\omega_1, \omega_2) = C_i(\omega_1) C_i(\omega_2) C_i^*(\omega_1 + \omega_2) \quad (6.8)$$

where

$$C_i(\omega) = \int_{-\infty}^{\infty} u_i(t) e^{-i\omega t} dt \quad (6.9)$$

and  $C_i^*(\omega)$  is the complex conjugate.

The Fourier coefficients,  $C(\omega)$ , are available by fast Fourier analysis. Since they are estimates for truncated data, the final quantity  $C^*(\omega_1 + \omega_2)C(\omega_1)C(\omega_2)$  is also an estimate. In actual computation this function is computed for only one octant of the  $(\omega_1, \omega_2)$  plane since this one octant can be shown to map into the other seven octants. The estimates were banded together into rectangular logarithmically spaced bands, each dimension containing ten bands per decade. This gives 100 banded estimates per square decade in the  $(\omega_1, \omega_2)$  plane. The final estimates for each rectangle were multiplied by central values of  $\omega_1$  and  $\omega_2$  to make the bispectral dimensions those of velocity cubed which may be compared to the velocity squared dimensions of the frequency multiplied ordinary spectra.

SECTION VII

EXPERIMENTS AND ANALYSIS

THE EXPERIMENTS

The data analyzed in this section were taken from six of the eight sensor arrays discussed in Section IV. These arrays, numbered as in Section IV, are given in Table 7.1

TABLE 7.1

EXPERIMENTAL ARRAYS FOR METEOROLOGICAL ANALYSIS

<u>Number</u>	<u>Array</u>	<u>Dates of Operation</u>
1	Initial 58-meter	November, December, 1968
2	58-meter T-shaped	September 1969
5	Energy-budget array (AEC)	July 1970
6	15-meter L-shaped	December 1970, January 1971
7	30-meter L-shaped	March 1971
8	131-meter single position	June 1971

The first array consisted of four positions at a height of 48 meters on separate towers 223 meters apart (Figure 4.18). In addition to collecting data for evaluating instruments, field operating procedures, and data processing procedures (discussed in previous sections), the meteorological purposes for this array were

- to secure data for single point analysis, and
- to compare time correlations with space correlations at large lags.

The second series of experiments was conducted from a T-shaped array consisting of four sensors mounted on one tower (Figure 4.20). The purpose

of this array was to simulate wing positions A and B (9 meters apart), fuselage position, and tail position C (6 meters from wings) on an aircraft and thereby compute correlations for various gust and shear combinations that the aircraft responds to.

The vertical line array was installed for purposes of AEC turbulence research. Six sensor positions were logarithmically spaced on one tower with sonic anemometers installed at 60, 15, and 7.5 meters, and Gill anemometers installed at 30, 3.75, and 1.88 meters above the ground. Since TOLCAT arrays were aimed at describing turbulence characteristics in a horizontal plane at a given level, it was useful to summarize the AEC results as they apply to TOLCAT interests in turbulence relationships in the vertical and to further analyze those data for other TOLCAT needs.

The L-shaped arrays included nine sensors horizontally dispersed as shown in Figure 4.19. The principal leg of the L consisted of seven logarithmically spaced positions with separation distances between consecutive sensors varying from 4 to 128 meters. The purpose of this line of sensors was to make possible the comparison of time and space analyses when the wind blew from various azimuth angles to the principal line. The short leg of the L had two positions, 12 and 60 meters from the origin (corresponding to the distances of position 5 and 3 from the origin on the principal line). The purpose of the short line of sensors was to make possible comparison of correlations in two directions at 12 and 60 meters.

The design of the array also allowed the use of positions 5, 7, and 8 for a T-shaped array when the wind blew from a  $245^\circ$  angle. However, one of the sonics became inoperative at the beginning of the testing period and a Gill anemometer was placed at position 8. No improvement over previous T-array analysis was expected with this mixed sensor array. Thus, further T-array analysis was not undertaken and the analysis of data from the L-arrays was limited to that from the principal line of sensors.



# Contrails

The same tower locations were used for both the 15-meter and the 30-meter L-array. The only difference was the height at which the instruments were mounted. The purpose was again to obtain spatial correlations and cross spectra to compare with time series analyses.

In the final TOLCAT experiment, a single sensor was mounted atop the Hanford 125-meter tower in order to obtain samples of data at elevations above the surface layer, where the existing turbulence is related less to the local wind shear and more to convection and vertical transport of turbulence from below.

Several tests were conducted with the sensors in each of the arrays described above. The list of the 12 data segments of highest quality chosen for analysis is given in Table 7.2. In the numbering shown in the first column, the first digit gives the array number, and the remaining digits give a serial number identifying the particular test within the series.

Tests T105 and T202 were the fifth and ninth tests conducted during the first phase of the TOLCAT work at 58-meter height. They were called Experiment 5, Series 1, and Experiment 2, Series 2, respectively, in the Interim Report where they were analyzed in considerable detail.

The analysis topics to be discussed in this section are:

- Spectral gap analysis
- Taylor's hypothesis verification - limits of coherency
- Gust moments
- Spectral form
- Correlation in time and space
- Shear moments
- Bispectra
- Probability distributions

TABLE 7.2

TESTS ANALYZED FOR TOLCAT

<u>Number</u>	<u>Date</u>	<u>Segment Time</u>	<u>Stability</u>	<u>Mean Wind</u>		<u>Height (m)</u>
				<u>Direction (deg)</u>	<u>Speed (mps)</u>	
T105	02 Dec 68	1345-1426	Slightly Stable	212	8	58
T202	25 Sep 69	1552-1647	Slightly Stable	296	9	58
T603	19 Jan 71	1323-1351	Slightly Stable	300	6	15
T701	03 Mar 71	1316-1344	Unstable	243	14	30
T703	24 Mar 71	0945-1013	Unstable	303	7	30
T704	26 Mar 71	1031-1059	Unstable	200	13	30
T803	07 Jun 71	1143-1224	Unstable	297	5	131
T805	21 Jun 71	1059-1154	Unstable	50	3.6	131
E501a	20 Jul 70	1537-1605	Unstable	320	9	60*
E501b	20 Jul 70	1619-1647	Unstable	304	10	60*
E506	23 Jul 70	2143-2238	Stable	301	12	60*
E508	28 Jul 70	1910-2005	Neutral	303	9	60*

\*Turbulence measurements were taken at lower heights also.

This order of presentation accommodates the following plan. First, the validity of the traditional descriptors of turbulence is examined with respect to the atmospheric boundary layer. Second, the justification of implying spatial description of turbulence from time series analysis is examined. Detailed statistical analysis begins with the moments since they are the most gross descriptors. Subsequent analysis concerns the spectra, which are decompositions of moments and correlations, and are Fourier transforms of the spectra. The shear analysis and bispectral analyses, being more unusual, are reserved until after analysis with conventional descriptors. Probability analyses (individual and joint histograms) are

reserved for the end of the section due to the greater distinction between this type of analysis and the other types.

The discussion can only illustrate the results obtained thus far and suggest the type of array and measurements needed to model boundary layer turbulence.

## SPECTRAL GAP ANALYSIS

In the Interim Report it was indicated, on the basis of analysis of data from the Hanford 125-meter tower and the micrometeorological mast installation, that the existence or location of a spectral gap was not easily recognized during conditions other than unstable. Since then, further analysis has been made of TOLCAT data to study the spectral gap hypothesis. Final results show agreement with Van der Hoven's original statement (Reference 7.1) of the existence of the spectral gap. However, it is recognized that the spectral depression within the gap is not great enough to prevent the concept from being misinterpreted or misapplied.

The problem is complex, depending as much on the viewpoint of the observer as on the physics of atmospheric motion in the boundary layer. A good way to launch into the problem is to look at it heuristically first, and then to examine the data which form the basis for the final arguments.

## Heuristic Arguments

Roth (Reference 7.2) has stated, effectively, that a source of turbulence energy may be active at a frequency that would otherwise be in the inertial subrange of some lower-frequency source of energy. Such a spectrum would appear as shown in Figure 7.1.

If Van der Hoven's spectrum is plotted as  $S(n)$  on a log-log plot instead of  $nS(n)$  on a semi-log plot (Figure 7.2) it resembles the spectra that Roth discussed, having two frequency ranges of  $-5/3$  slope separated by a slight

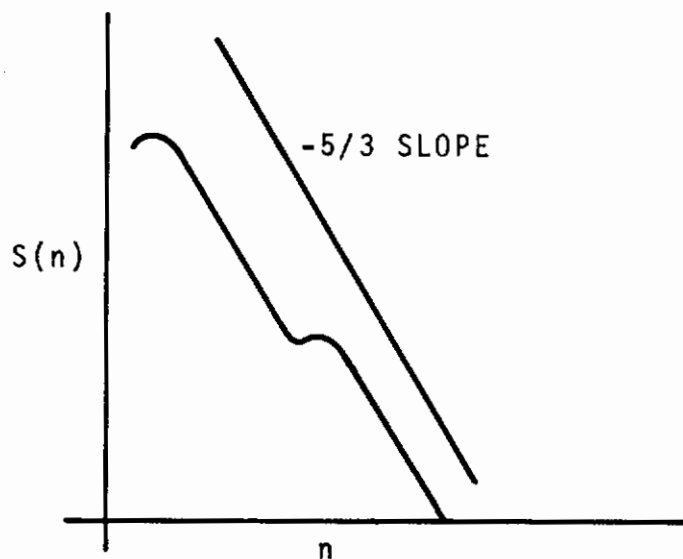


Figure 7.1 Hypothetical Spectrum,  $S(n)$ , with Two Energy Sources  
(After Roth, Reference 7.2)

hump. Since Van der Hoven's peaks are at frequencies separated by orders of magnitude, there must be separate sources of physical energy operating at frequencies thus separated. Since all variation in the horizontal wind is caused by inhomogeneities of mean energy on some scale, it is interesting to speculate that the low frequency peak may be due to mean horizontal inhomogeneities which exist in scales all the way up to hemispheric dimensions of  $10^4$  kilometers from equator to pole while the turbulence peak is associated more with mean vertical inhomogeneities in the planetary boundary layer (the variation of  $\bar{U}$  with height) which has a thickness on the order of 1 kilometer. In other words, the frequency ratios between the two peaks in Van der Hoven's spectrum is roughly the same as the ratio of the length scales of vertical and horizontal inhomogeneity in the planetary boundary layer. Hence these could be the sources

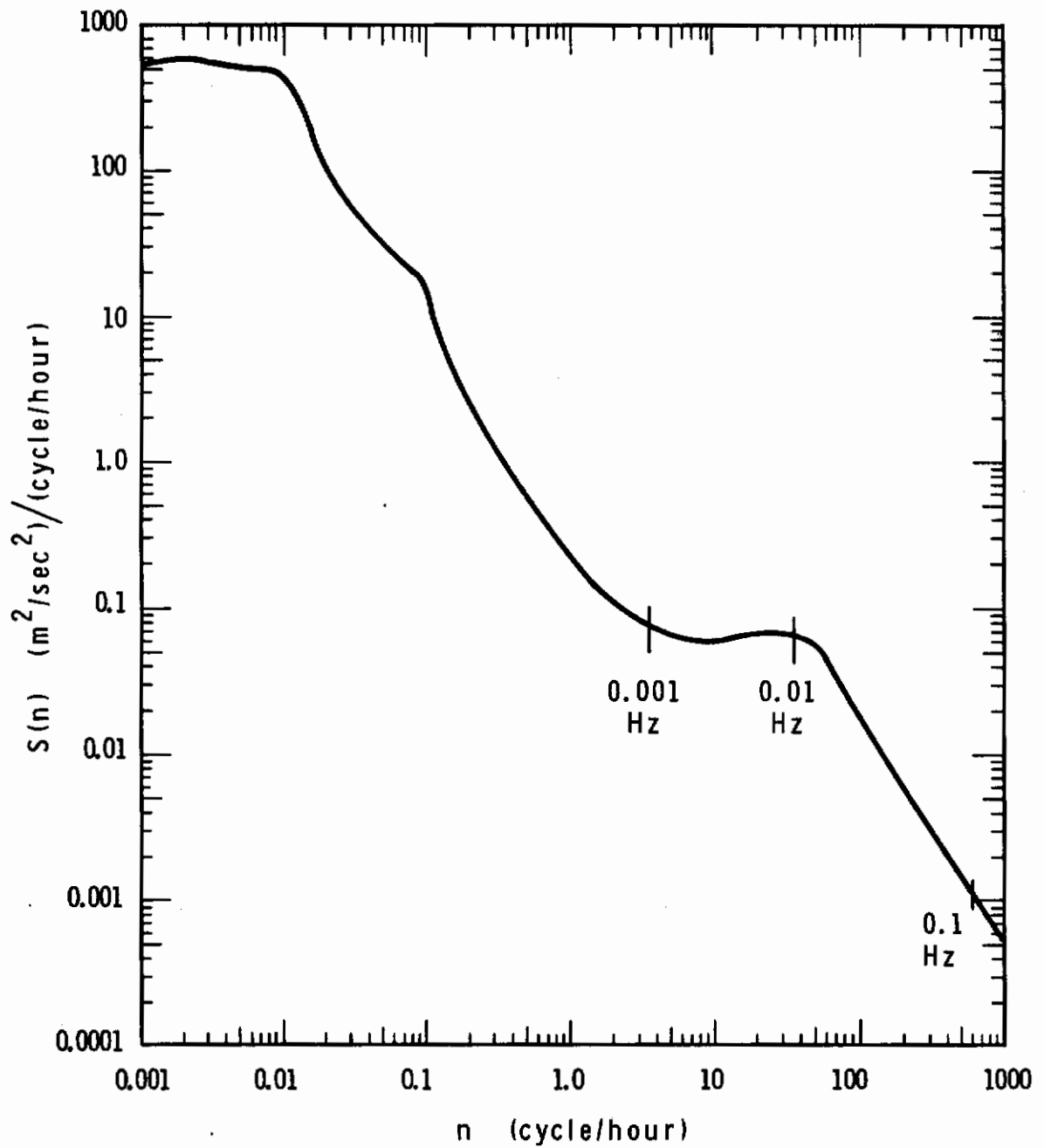


Figure 7.2 Van der Hoven's Spectrum of Horizontal Wind Speed,  $S(n)$



of energy for the two peaks in Van der Hoven's spectrum.

## Analytical Results

The initial spectral gap study, reported in the Interim Report, showed a low frequency hump similar to Van der Hoven's, except that the peak energy in the spectrum from the TOLCAT analysis of Hanford data was at a higher frequency. Van der Hoven's low-frequency hump peaks at one cycle per four days, suggesting changes due to the passage of major storm systems, whereas the peak energy in the Hanford low-frequency hump was at one cycle per 18 hours, which is closer to a diurnal frequency.

Having established that the low-frequency peak exists, and using Roth's reasoning, it appears that some sort of spectral gap can be inferred using micrometeorological data alone if sufficient departure (flattening) from the  $-5/3$  slope can be shown in the low-frequency portion of the spectrum followed by a genuine  $-5/3$  slope through the higher frequencies.

The longest analysis period commonly used in the Hanford analysis has been 55 minutes, and the lowest frequency at which spectral analysis has been attempted for these runs is 0.001 Hz. If the two lowest frequency decades in Van der Hoven's spectrum (Figure 7.2) following 0.001 Hz are examined, the spectrum is seen to be essentially flat from 0.001 Hz to 0.01 Hz, and essentially follows the  $-5/3$  slope from 0.01 Hz to 0.1 Hz. Several spectra have been computed from the TOLCAT 55-minute data segments, without using the detrending, so that results may be compared.

There are two good reasons for not anticipating strikingly similar results. In the first place the Hanford spectra are for the  $u'$ ,  $v'$ , and  $w'$  while Van der Hoven's spectrum is for horizontal wind speed. The second reason is that Van der Hoven's micrometeorological hump is from hurricane data. The maximum reading for  $nS(n)$  in his original spectrum was  $3.0 \text{ m}^2/\text{sec}^2$ , which is twice as great as any peaks characteristic of the Hanford tests analyzed to date.

# Contrails

All the Hanford spectra showed a flattening departure from the  $-5/3$  slope in the low-frequency portions. But the spectra for the horizontal component showed less departure than Van der Hoven's spectrum, while the vertical component spectra showed more departure. The spectra from the two tests showing the strongest departure are shown in Figures 7.3 and 7.4.

The heights from which the two sets of data were taken were 60 meters for Test E508 and 15 meters for Test T603. None of the horizontal components exhibit a flat slope across the entire first decade, but one of the  $u'$  components shows a flat slope for about 60 percent of a decade. Both  $w'$  component spectra show departure slopes for about two decades.

Generally, this verification is considered weaker than Van der Hoven's because none of the horizontal spectra show genuine humps (unless the rise is at lower frequencies than those included in the analysis and therefore, lower than the frequencies at which the rise in Van der Hoven's  $S(n)$  spectrum occurs) and because the verification shown by these spectra is better than average for the TOLCAT data.

The spectra shown in the LO-LOCAT reports and the HICAT reports are power spectral density,  $S$ , with a spatial argument. It is worthwhile to note that some of the spectra from these reports illustrate the features under discussion, i.e., have two parallel  $-5/3$  slopes separated by a hump (Figure 7.1). Attention is called in particular to Figures 137E and 137F from Appendix VII from the Project HICAT Report AFDL-TR-67-123, Volume II (Reference 7.3). These are reproduced as Figures 7.5 and 7.6 of the present report. The dashed extension of the lower frequency slope in each case was added by the present authors. It is seen that the extension of the lower frequency slope is displaced more than an order of magnitude below the measured spectral densities in the higher frequency range and somewhat less than an order of magnitude for the longitudinal component.

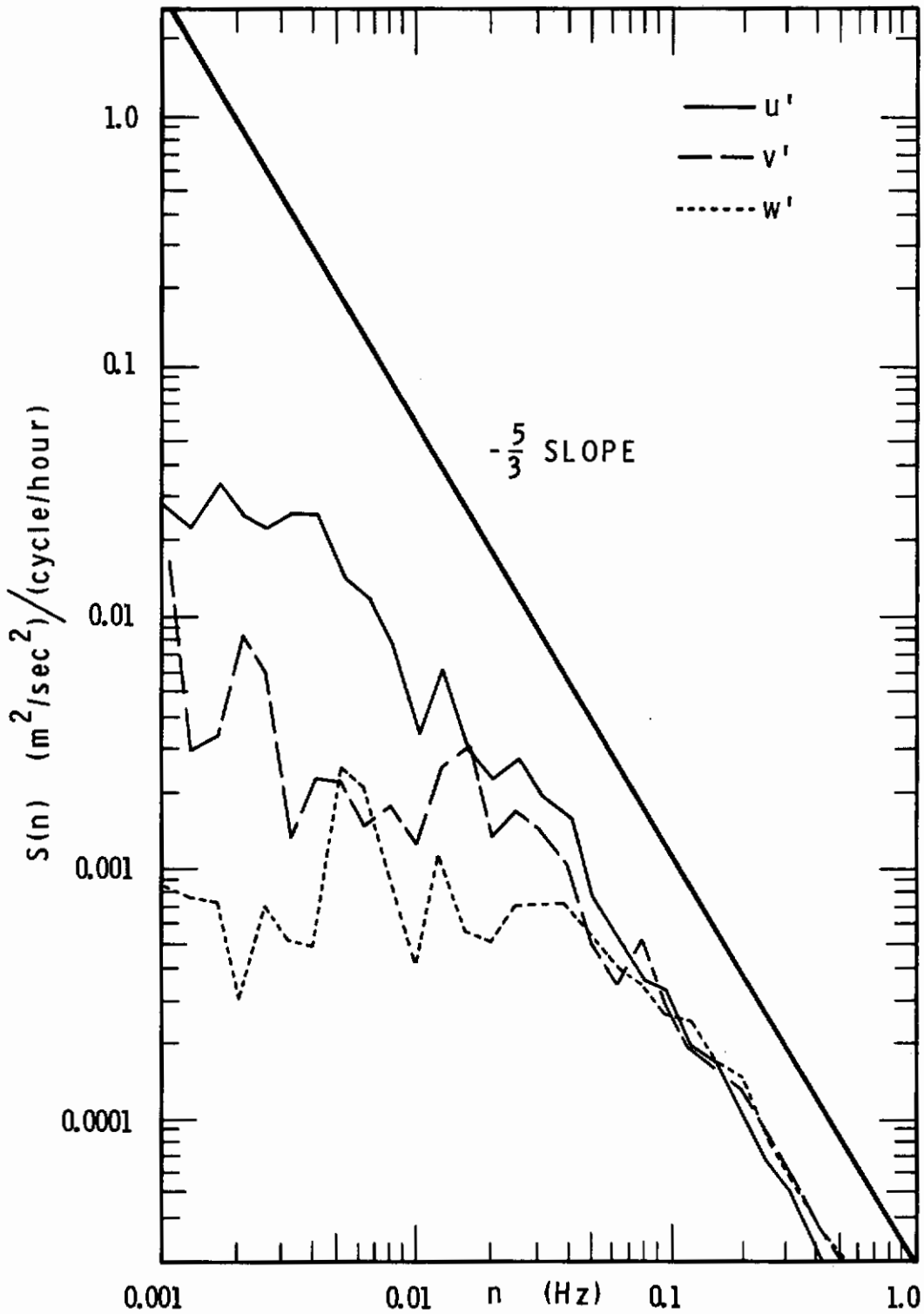


Figure 7.3 Power Spectral Density,  $S(n)$ , at 60 Meters, Test E508

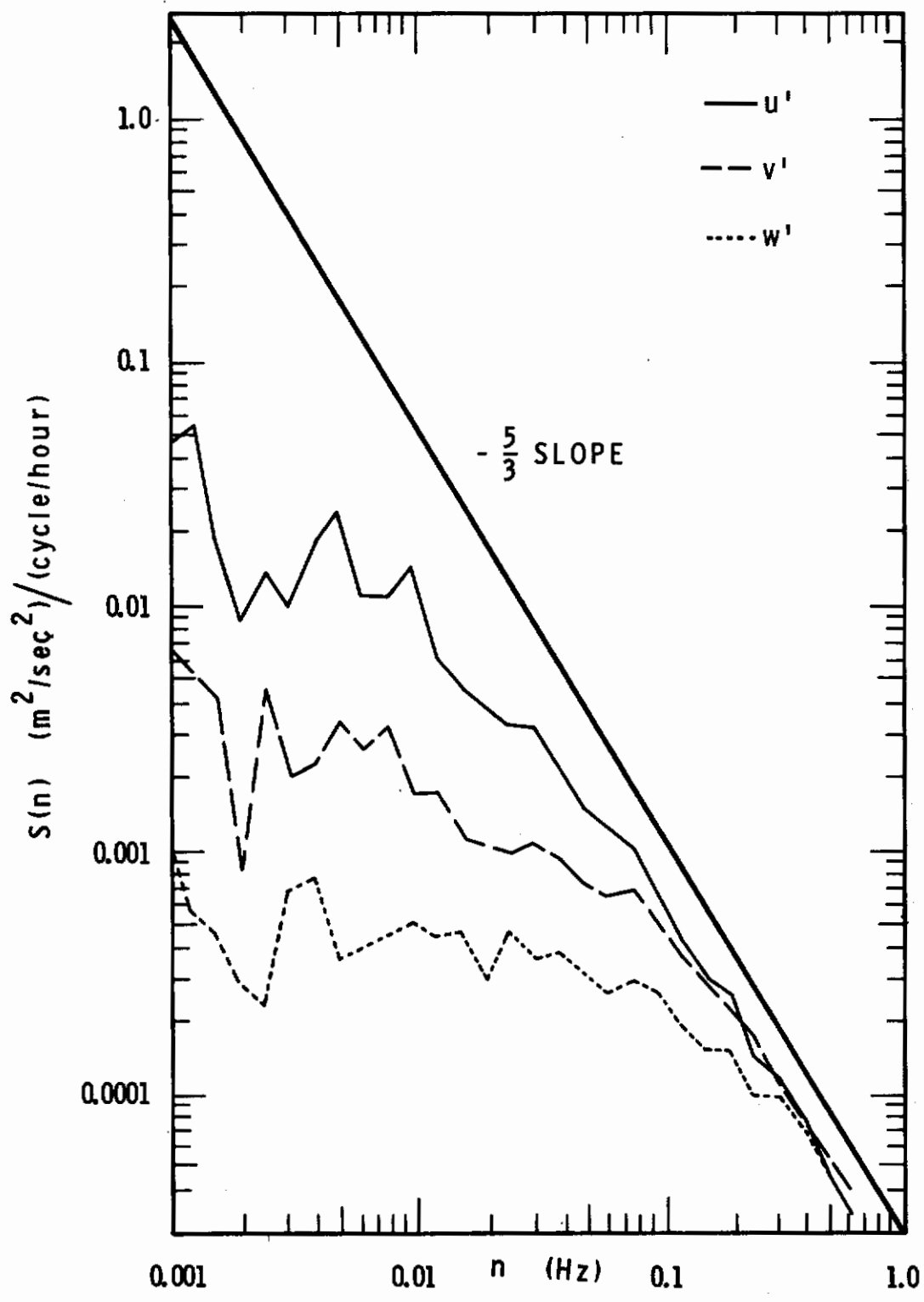


Figure 7.4 Power Spectral Density,  $S(n)$ , at 15 Meters, Test T603

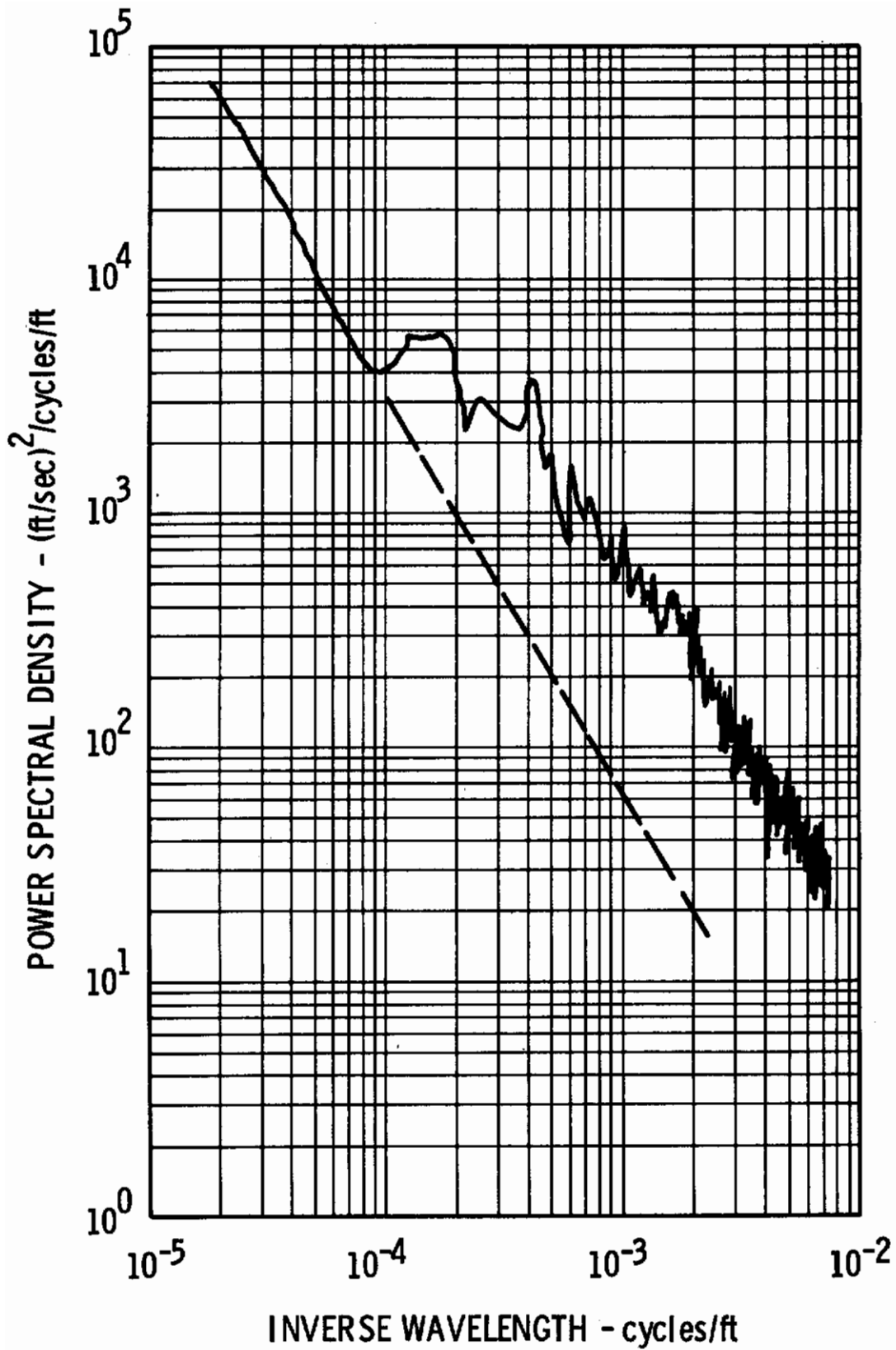


Figure 7.5 HICAT Power Spectrum of Lateral Gust Velocity, Test T107, Run 18, 500 Lags



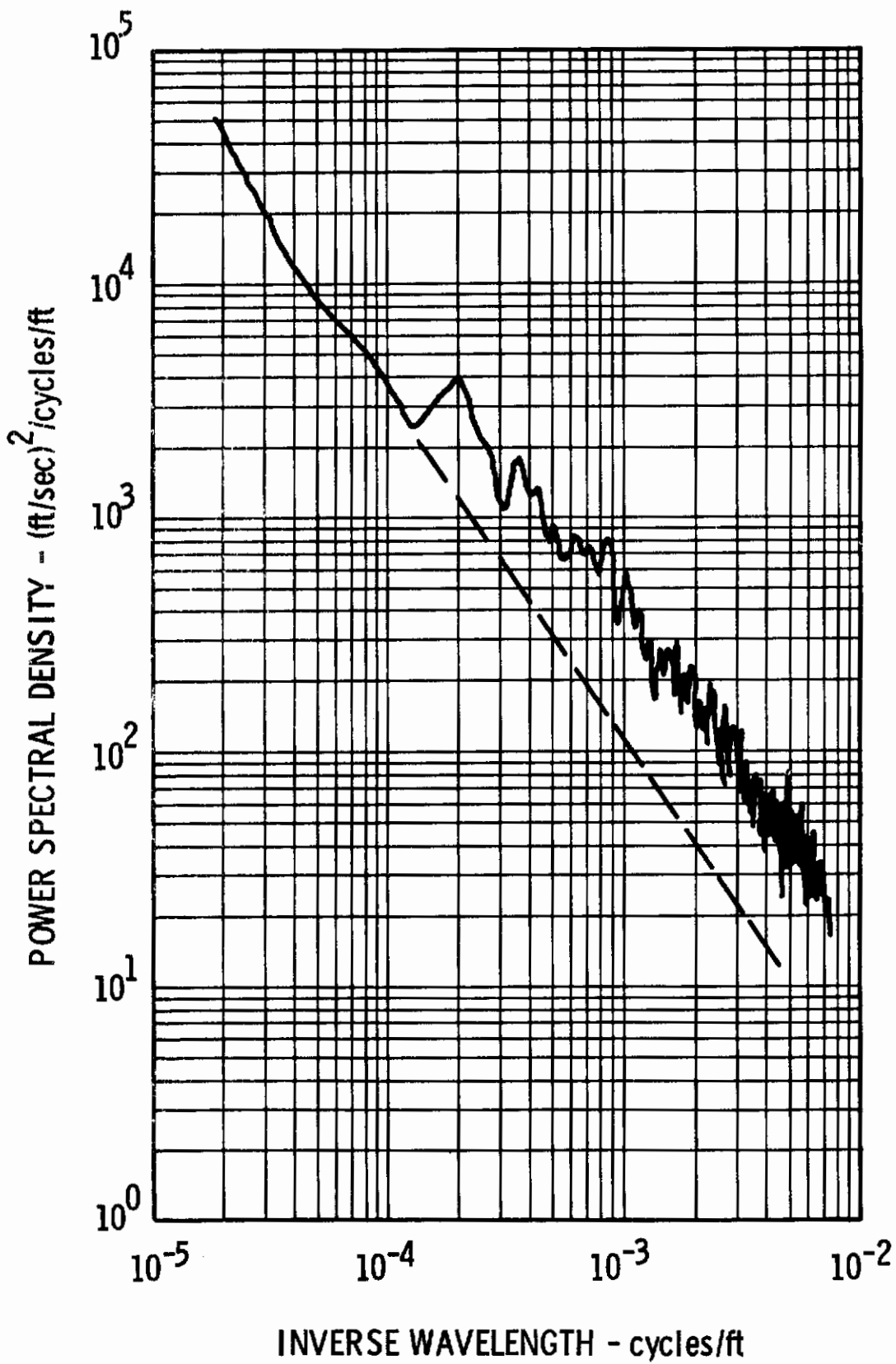


Figure 7.6 HICAT Power Spectrum of Longitudinal Gust Velocity, Test T107, Run 18, 500 Lags

The spectral gap shown in these two figures is at about 3000 meters. A corresponding figure for TOLCAT data may be found by dividing the prevailing mean wind speed by frequencies where flattening occurs, yielding lengths on the order of 1500 meters. Although the discussion of Taylor's hypothesis, found later in this section, does not indicate that this procedure is strictly valid for the length obtained, since it is considerably greater than 10 times the height of measurement, it is interesting to note that the two lengths, 1500 and 3000 meters are not too far apart; considering the fact that the HICAT flights were made at heights exceeding 15,000 meters.

When spectra are plotted in this manner there is often a temptation to smooth over features, such as these humps, that appear to be irregularities deviating about some average condition that may be represented by a faired curve. However, in this case an important physical feature, the spectral gap, would be eliminated by such smoothing.

### Aspects of Weak Spectral Gap Verification

It is very easy and tempting to read more into the spectral gap hypothesis than is actually there. For example, by inspection of Van der Hoven's spectrum in its original form (Figure 7.7), the variance contributed by the frequencies between 0.5 and 10 cycles per hour is insignificant compared to the variance in the micrometeorological hump between 20 and 200 cycles per hour. Therefore, the computed variances of turbulence should be quasi-independent of the total measuring time if that time is the reciprocal of some frequency in the spectral gap. Such a measuring time could be one hour.

However, if the micrometeorological hump in Figure 7.7 is redrawn to represent typical atmospheric conditions, with turbulence energy not exceeding  $1 \text{ (mps)}^2$ , then the variance contributed by the frequencies in the spectral gap appear quite significant, and a low frequency,  $N$ , such that the computed variance

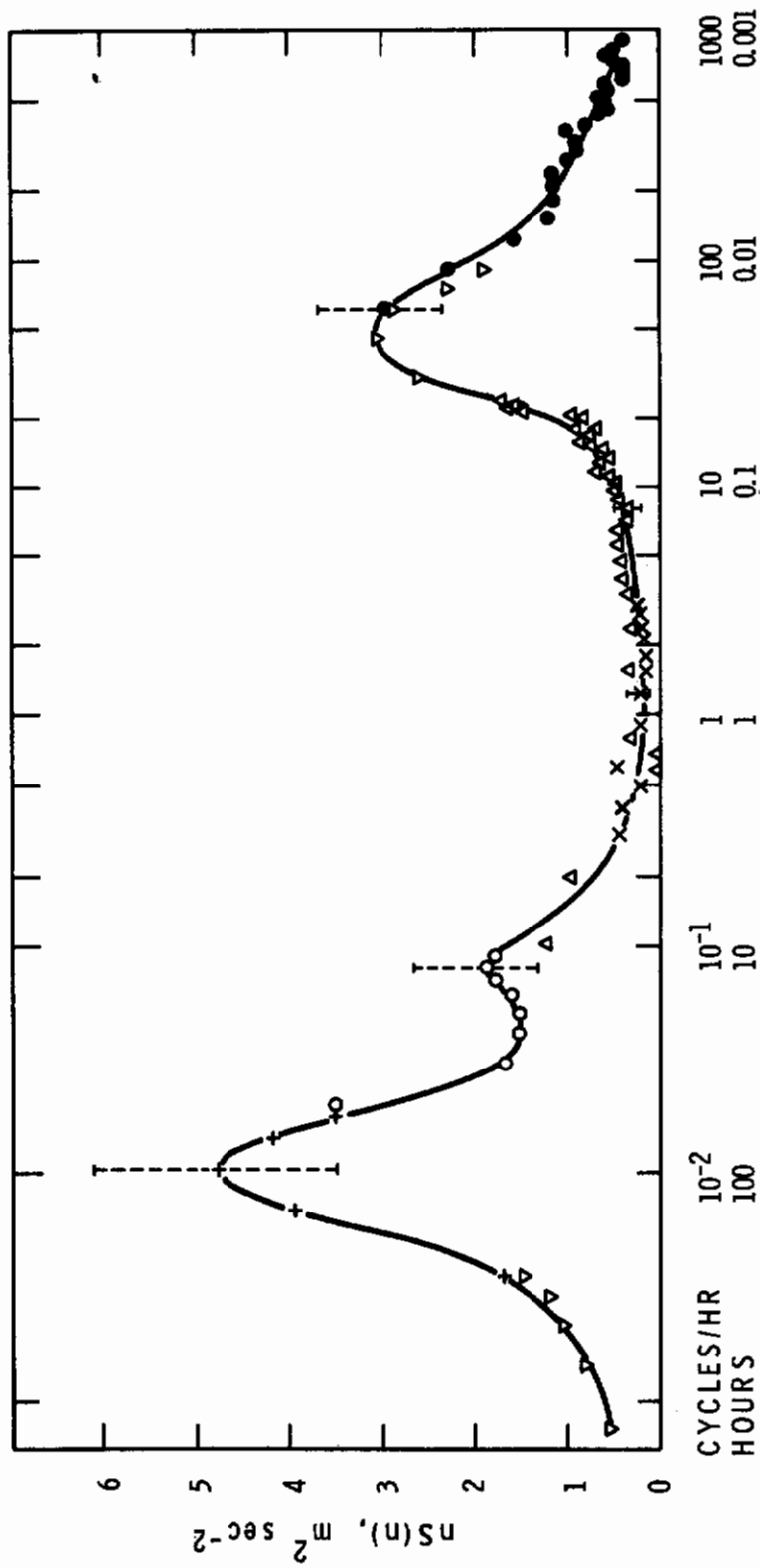


Figure 7.7 Van der Hoven's Spectrum,  $nS(n)$

# Contrails

$$u_{\alpha} u_{\alpha} = \frac{1}{T} \sum_N^M S_{\alpha}(n) \quad (7.1)$$

is quasi-independent of  $N$ , cannot be found ( $M$  is an upper cutoff frequency in the inertial subrange). This point is not obvious to scientists and engineers who may utilize Van der Hoven's final result without being aware of the circumstances under which the data were taken.

In the part of this section on moment analysis, the change of variance computations with change of the lower frequency limit is shown to be considerable, at least for  $u'$  and  $v'$ , although for  $w'$ , variance computations appear to be quasi-independent of the lower limit for some tests, when the upper cutoff frequency is 1.0 to 2.5 Hz.

The existence of a spectral gap is interpreted to show that the total atmospheric motion may divide into a rapidly varying portion superimposed over a slowly varying portion such that the rapid variation is statistically independent of the slow variation and such that the statistics of the slow variation may be used as predictors of the statistics of the rapid variations.

This statement forms the very basis of turbulence study from both a theoretical and a practical point of view. Its applicability to wind tunnel turbulence may be assumed without question, and in general, the same reasoning has been carried over into the study of atmospheric turbulence. This idea still looks reasonable. If in Figure 7.2 the  $-5/3$  slope of the low-frequency energy is extended down into the high-frequency range, it intersects energy levels about two orders of magnitude lower than those of the high-frequency curve. However, for typical conditions half an order of magnitude of the difference would be lost. Therefore, the separation of scales does not appear to be complete enough to be taken for granted when experimental and theoretical results do not agree. For

example, the lack of separation is a possible explanation for different values of Von Karman's constant calculated using atmospheric data versus wind tunnel data (Reference 7.4). From the points just discussed, it is easy to see that different investigators could disagree on the "existence" of a spectral gap just because they use different criteria to test it. This may account for the controversy surrounding the subject today. The whole point of the above discussion is that the usefulness of the spectral gap hypothesis depends entirely on what part of the spectrum an investigator must deal with and what the particular application is.

With respect to TOLCAT analysis the spectral gap phenomenon in the atmospheric boundary layer will be assumed strong enough to provide a separation of scales sufficient that turbulence statistics can, in principal at least, be predicted from knowledge of prevailing mean value statistics such as wind shear, temperature lapse rate and local and upwind roughness. At the same time the spectral gap phenomenon will not be strong enough to justify the assumption that turbulence statistics may be measured and calculated quasi-independently of the total record length analyzed.

## TAYLOR'S HYPOTHESIS VERIFICATION

In Section II of this report it was shown that turbulence spectral statistics from tower based data cannot be confidently related to turbulence encountered by aircraft unless it can first be shown that the covariance functions in space and in time are related according to (Equation 2.17)

$$\tilde{R}_{ij}(\tau) = X_{ij}(\xi), \quad \tau = \xi/\bar{U} \quad .$$

Also, the work of Lin (Reference 2.5) regarding application of Taylor's hypothesis in shear flow must be considered. Lin gave a first approximation for a lower limit of the wave number range over which Taylor's hypothesis applies. Translating the wave number into frequency by using Taylor's hypothesis (which is certainly allowable over that wave number



range to which Taylor's hypothesis applies), Lin's lower limit expression may be written (Equation 2.24)

$$\frac{2\pi n}{d\bar{U}/dz} \gg 1 .$$

It is desirable to replace this equation by one expressing a more exact relation employing the symbol  $\geq$  with respect to some experimentally determined constant rather than  $\gg 1$ .

### Analysis of Space and Time Correlations

This subsection will demonstrate qualified empirical verification for Equation 2.6 for autocovariances, i.e., for  $i = j$  in the tensor notation. Because genuine spatial covariances (taking averages over space) are not practical to measure, the right side of Equation 2.17 will be replaced by the pseudo-spatial covariance function

$$\tilde{R}_{\alpha\alpha}(\xi) = \frac{1}{T} \int_0^T u_{\alpha}(x_0, t) u_{\alpha}(x_0 + \xi, t) dt$$

$\alpha = 1, 2, 3 \quad , \quad (7.2)$

where  $u_{\alpha}$  is measured at those two points separated by distance,  $\xi$ . The pseudo-spatial covariance will hereafter be referred to as the spatial covariance, for simplicity.

The most applicable set of data for this purpose, with the wind direction essentially along the sampling line, comes from Test T603 during which good data were collected at a height of 15 meters from seven logarithmically spaced sensors (Section IV). More limited information is available from Tests T703, T105, and T202. Pertinent information regarding these tests are given in Table 7.3.

TABLE 7.3

PARAMETERS FOR TOLCAT TESTS

<u>Test Number</u>	<u>T603</u>	<u>T703</u>	<u>T105</u>	<u>T202</u>
Height (m)	15	30	58	58
Stability	Stable	Unstable	Stable	Unstable
$\bar{U}$ (mps)	6.4	7.0	8.3	8.8
$u^* = \sqrt{-\overline{u'w'}} (mps)$	0.47	0.40	0.41	0.51
$(u^*/\bar{U})^2$	0.0054	0.0033	0.0024	0.0038
$d\bar{U}/dz (sec^{-1})$	0.057	0.020	0.022	0.015
$u^*/kz (sec^{-1})$	0.078	0.033	0.018	0.022

Before time and space correlations can be compared from an array using sonic and Gill anemometers jointly, some reconciliation must be made for the difference in high frequency responsiveness between the two instruments. Each Gill anemometer was equipped with a 500 microfarad capacitor to eliminate noise from the data. The spectra for the Gill data show a slope steeper than the slope found in the spectra for the sonic data for frequencies as low as 0.4 Hz (Section III). Rather than filter out the energy for almost an entire frequency decade from both records to make them comparable, another less drastic method of reconciliation was adopted.

Each space lag that is available in the logarithmic array is available from a unique combination of two sensors. The spatial correlations are necessarily computed by cross-correlating data from either two sonic anemometers or two Gill anemometers, or from one sonic and one Gill anemometer. The space lags for which correlations are computed from each anemometer combination are:

- Sonic to sonic:                   4, 8, 12 meters
- Gill to sonic:                    16, 24, 48, 252 meters
- Gill to Gill:                     32, 64, 96, 128, 192, 224 meters

# Contrails

Therefore, when time and space correlation functions are compared, space correlations for 4, 8, or 12 meters should be compared to sonic time correlations; space correlations for 32, 64, 96, 128, 192, or 224 meters should be compared to Gill time correlations; and space correlations for 16, 24, 48, or 252 meters should be compared to an intermediate value between the two time correlations.

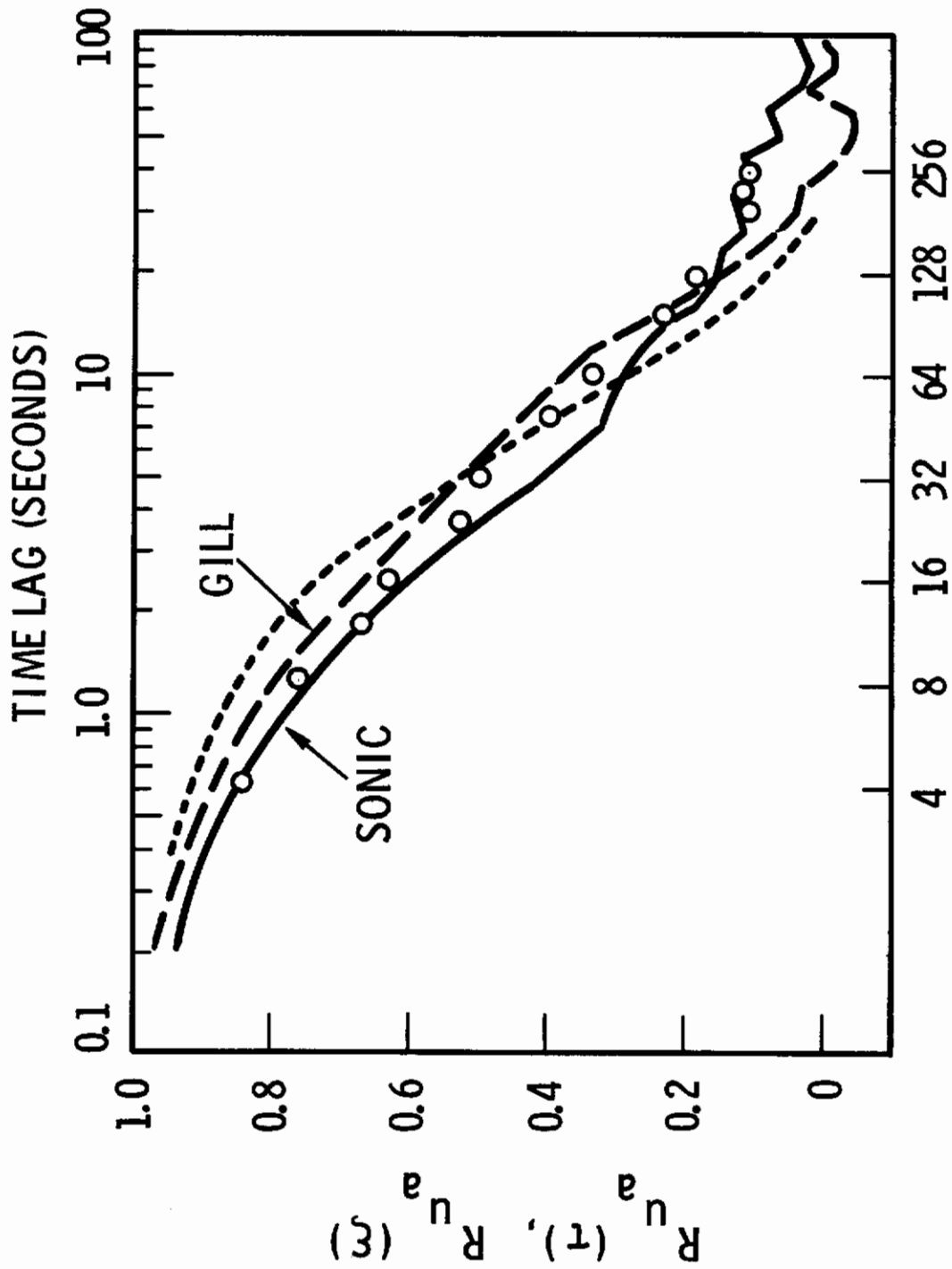
Since the  $9^\circ$  azimuth angle of Test T603 was the smallest azimuth angle recorded during any test using the logarithmic array, these data have been analyzed and the results presented here as representative of the along-wind case. Comparisons of the time and space correlations for the three components are shown in Figures 7.8, 7.9, and 7.10.

Each of these graphs exhibits four correlation functions, two scales for abscissa and one scale for the ordinate. The four correlation functions are:

1. Solid line - representative time autocorrelation from sonic data.
2. Dashed line - representative time autocorrelation from Gill data.
3. Large dots - spatial correlation.
4. Dotted line - exponential function  $R(\xi) = \exp(-\xi/L_0)$ , with  $L_0$  so determined that the exponential function matches the spatial autocorrelation where it becomes  $e^{-1}$ .

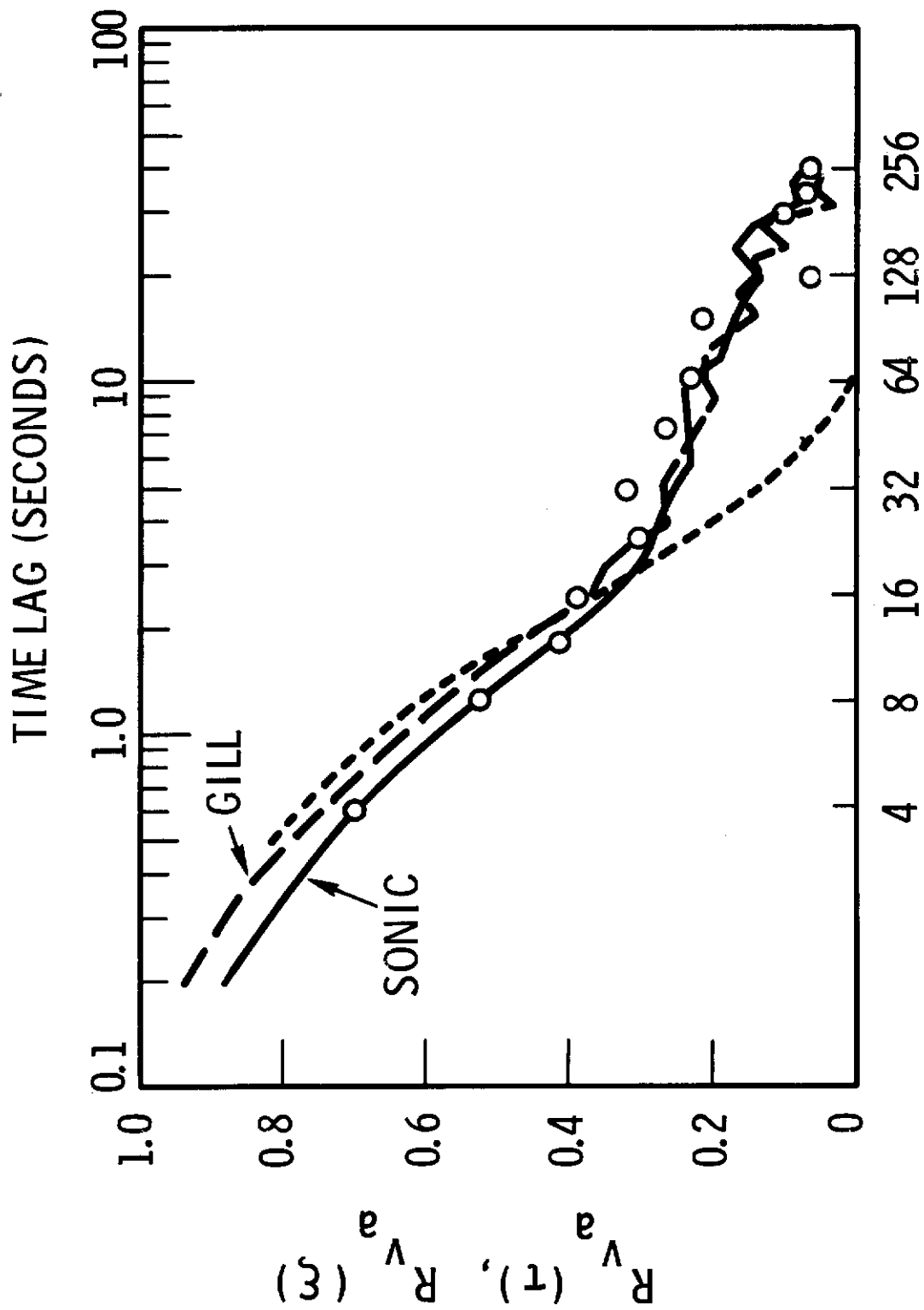
The scale for the abscissa along the top of the figure is for time lag. The scale for the abscissa along the bottom of the figure is for the space lag, which is scaled to match the time lag according to Equation 2.17. The scale along the ordinate is for the correlation values.

Figure 7.8 shows the model holding for  $u'_a$  quite well to separation distances as great as 128 meters. The spatial correlation for 4, 8, and 12 meters are on or very near the time correlation line for the sonic data as expected. The spatial correlations for 16 and 24 meters are intermediate



ALONG WIND SEPARATION DISTANCE,  $\xi$  (METERS)

Figure 7.8 Time and Space Correlations for  $u'_a$ , Test T603



ALONG WIND SEPARATION DISTANCE,  $\xi$  (METERS)

Figure 7.9 Time and Space Correlations for  $v'_a$ , Test T603



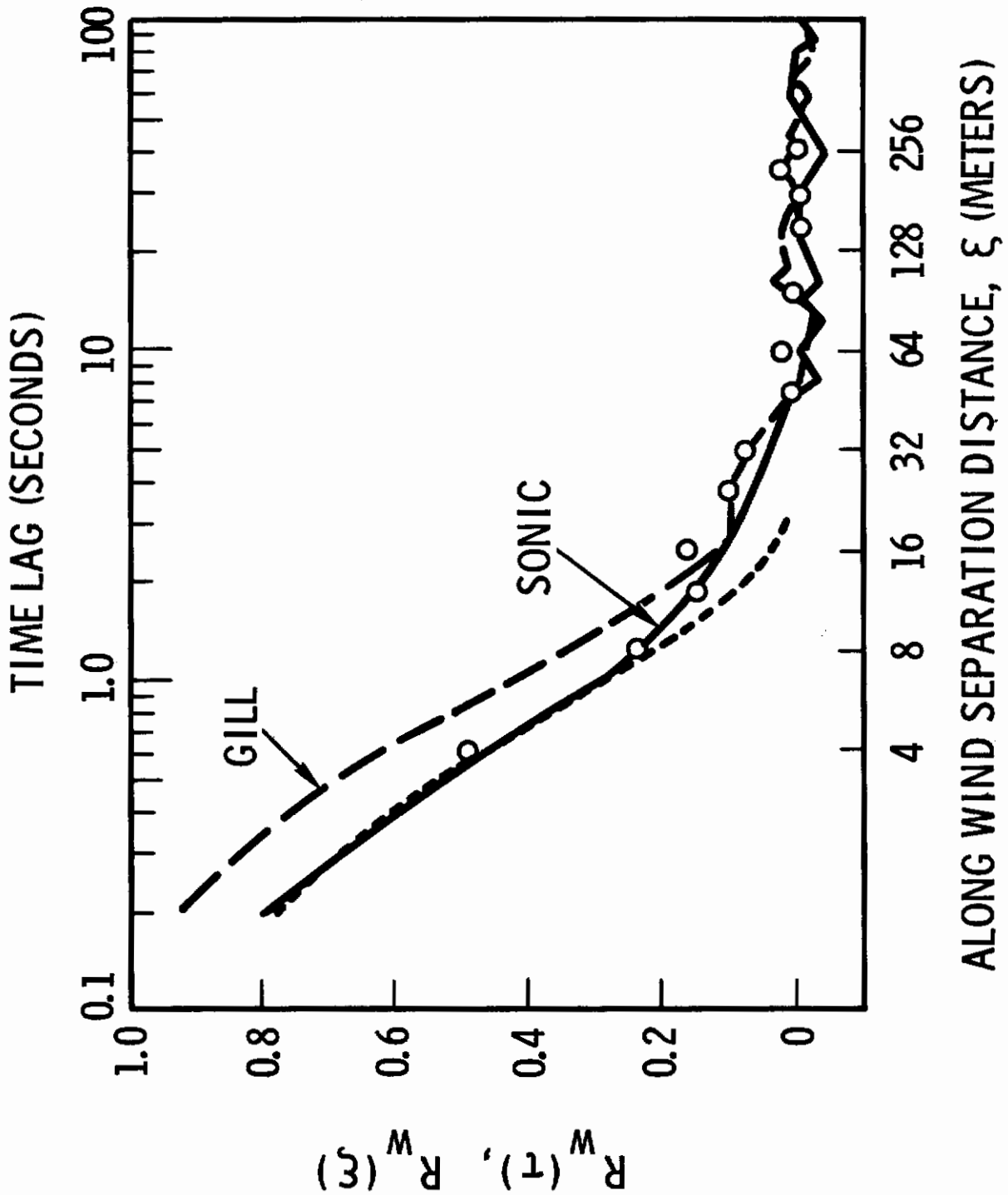


Figure 7.10 Time and Space Correlations for  $w'$ , Test T603

# Contrails

between the sonic and Gill correlation curves although close to the sonic curve. The spatial correlation for 32-meter separation is very close to the Gill curve, and the spatial correlation at 48 meters is between the two lines as would be expected. The spatial correlation for 64 meters is slightly low, that for 96 meters coincides with the Gill autocorrelation curve as expected, and that for 128 meters is slightly high. The last three spatial values follow the sonic rather than the Gill autocorrelation curve and are conspicuously high. Similar evaluations can be made for the correlation functions for  $v'_a$  and  $w'$ . The weakest verification is for  $v'_a$  although a smoothed curve through the spatial correlations compares reasonably well with the temporal autocorrelation functions for both  $v'_a$  and  $w'$ . Exponential form is followed best by the experimental curve for the vertical component.

The space lag for which the spatial correlation value for a particular test is  $e^{-1}$  may be defined as a characteristic length for that test, in the direction of the space lag. Correlation lengths of 51, 16, and 5 meters for  $u'_a$ ,  $v'_a$ , and  $w'$  are indicated for this particular data sample. The lengths are functions of  $T$  and  $\Delta t$ , which are 28 minutes and 0.2 seconds, respectively.

The period of the longest wave to which the aircraft responds is well below 28 minutes, but is variable, being a function of the design of the plane and of the speed of flight at the moment. The data may therefore be subjected to further analysis, in which the spectra to be Fourier transformed into correlation functions is truncated at various lower limits corresponding to different upper wave length limits of aircraft sensitivity. Also, characteristic lengths could be given as functions of the original spectra and the truncated spectra.

To summarize, it is pointed out that for two of the three components, Taylor's hypothesis holds out to 128 meters, and that for the third component,  $v'_a$  the verification is weaker but not entirely lacking.

# Contrails

Further testing of Taylor's hypothesis is available from other experiments at other azimuth angles. For Tests T703 and T202 the azimuth angle is larger, which means that more of the cross-wind dimension of the eddies is involved. Therefore, before looking at these results it is instructive to attempt a similar comparison for a test during which the wind was blowing at an azimuth of approximately  $90^\circ$ . In this case, the autocorrelation function can be considered to represent the along-wind space-correlation function which can now be compared in shape and scale with the directly measured cross-wind correlation function. Such a comparison can be made for Test T704. Conditions were unstable,  $u^*$  was 0.80 mps,  $\bar{U}$  was 13.5 mps,  $(u^*/\bar{U})^2$  was 0.0035, and the azimuth angle was  $87^\circ$ .

Figures 7.11, 7.12, and 7.13 show the correlations for  $u'_a$ ,  $v'_a$ , and  $w'$ , respectively, for the cross-wind case. The numerical space scale in meters along the abscissa is 13.5 times the numerical time scale in seconds along the same axis because the mean wind speed was 13.5 mps. In general, the space correlations are lower than the corresponding time correlations. Considering Taylor's hypothesis holds for the along-wind case, the time correlation substituted for the spatial correlation in the along-wind direction shows that the cross-wind dimensions of the eddies are less than the along-wind dimensions. There are other striking differences between the comparisons for Tests T704 and T603. The relation of the sonic anemometer time correlation function to the spatial correlation for the first three space lags is different for each of the three components. Only in the case of  $u'_a$  (along the tower line and, in this case, lateral to the mean wind direction) do the two functions have approximately the same slope. The figures also show that the ratio of the turbulence scales for the along-wind dimension to the cross-wind dimension is different for each of the different wind components. It is notably greater than unity for  $v'_a$  (in the direction of mean wind). Therefore, when data from tests involving larger azimuth angles than the  $9^\circ$  observed for Test T603 are analyzed for Taylor's hypothesis verification, there should be some contamination by results of the kind just described. An unanswered question is how large does the azimuth angle have to be before this becomes noticeable.

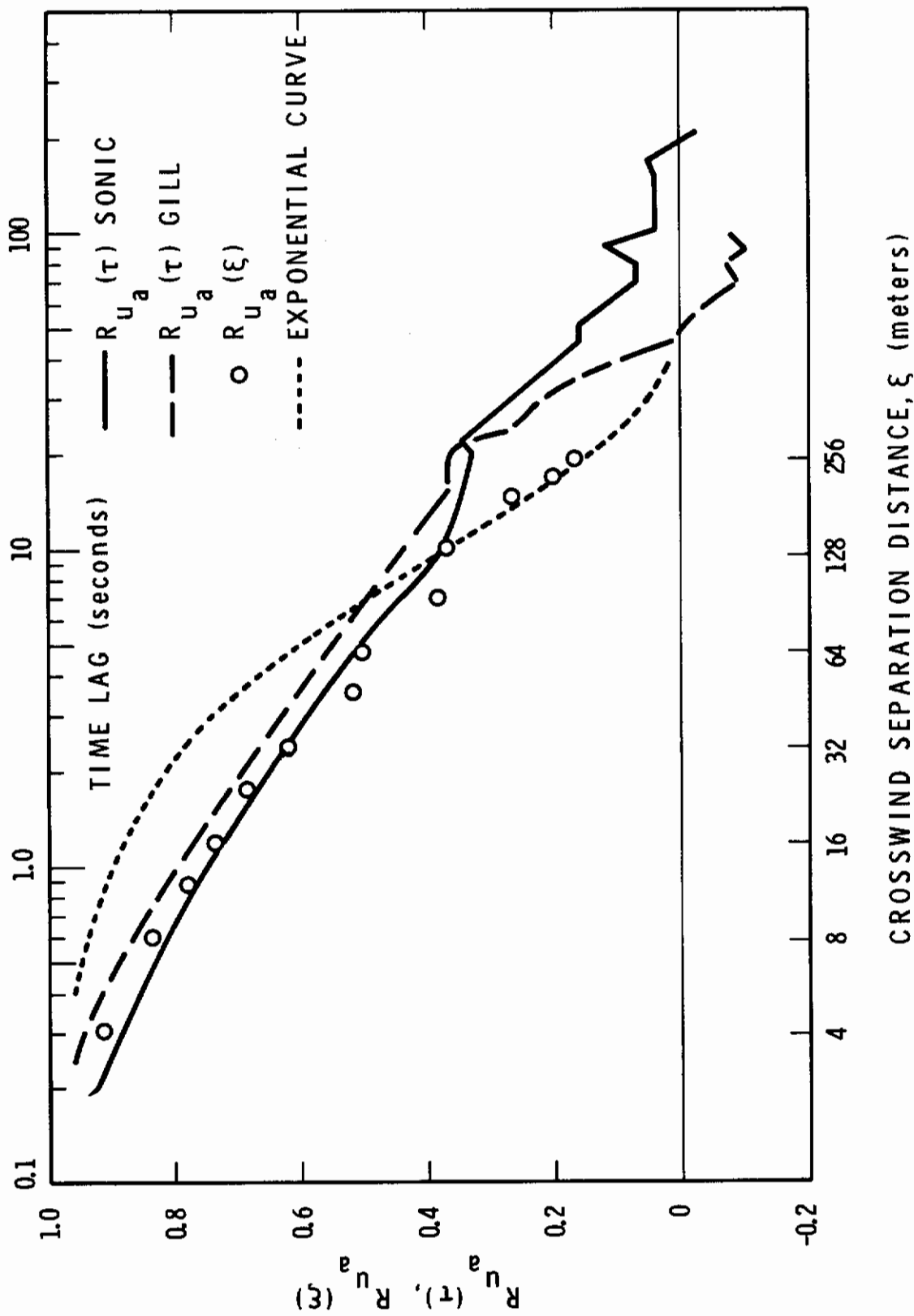


Figure 7.11 Time and Space Correlations for  $u'_a$ , Test T704

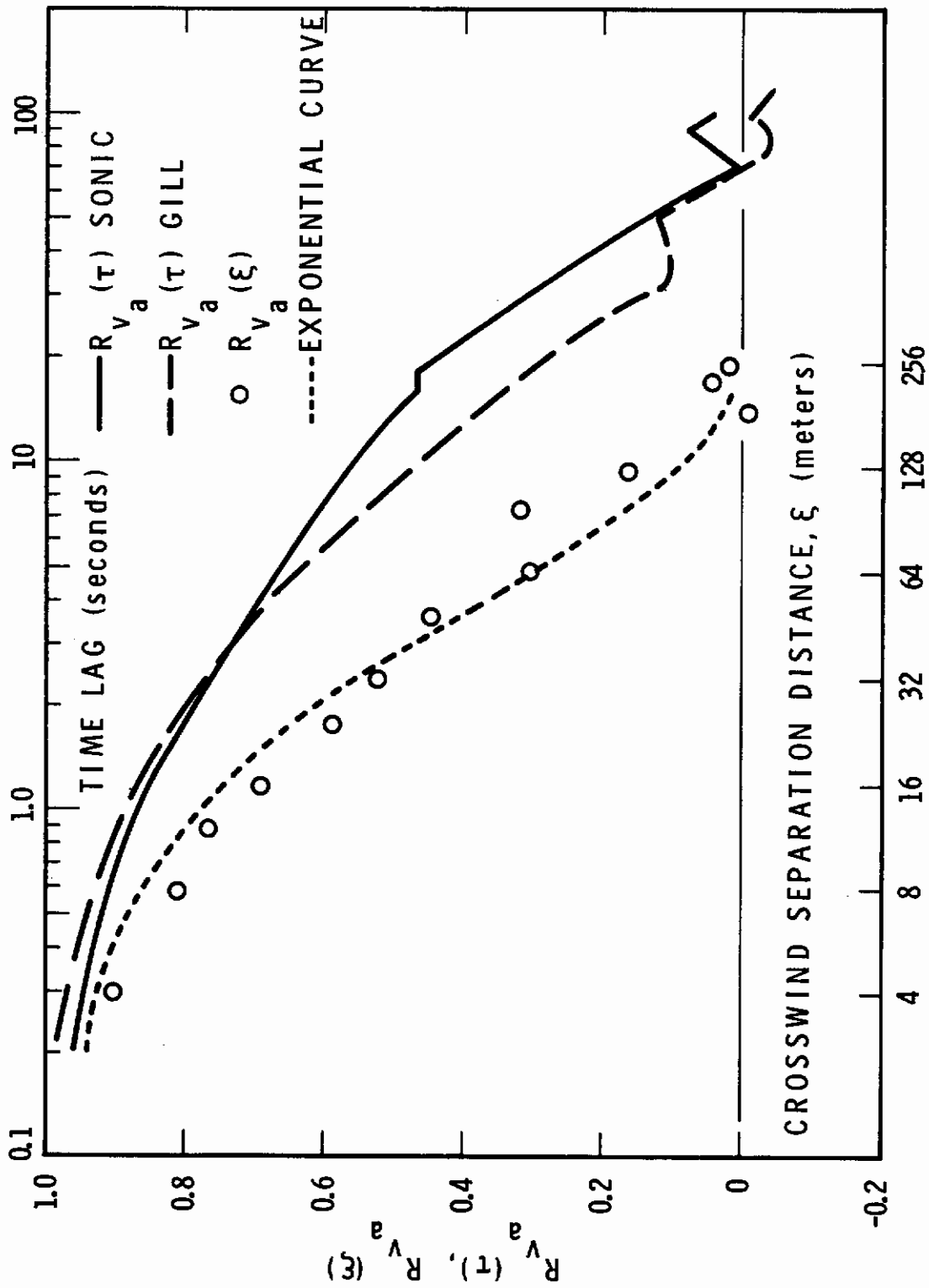


Figure 7.12 Time and Space Correlations for  $v'_a$ , Test T704



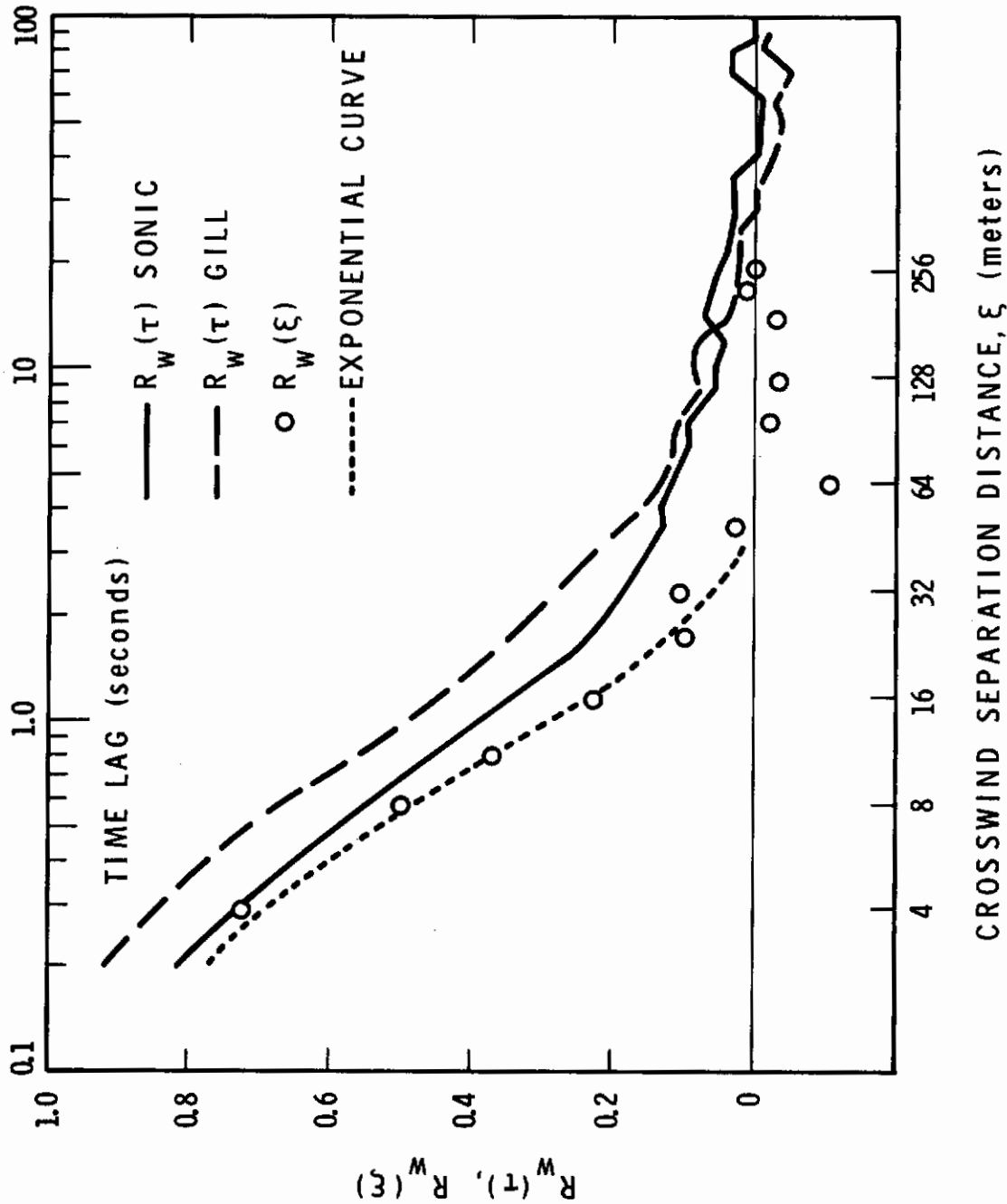


Figure 7.13 Time and Space Correlations for  $w'$ , Test T704

# Contrails

Although the present log of data available for analysis is not sufficient to provide the basis for a reliable answer, some interesting results are available. During the unstable Test T703, the average azimuth angle prevailing during the 28-minute segment analyzed was  $11^\circ$ . Although this is hardly more than  $9^\circ$ , the Taylor's hypothesis verification is considerably weaker, especially for the  $u'_a$  component. Because of the difference in stability, the difference cannot be assumed to be a function of azimuth angle alone. In fact the instability may be the primary reason for the difference. Because of noise in the sonic data from this test, only the Gill data has been analyzed for this report. Therefore the shortest spatial lag for which analysis was made was 32 meters.

Time and space autocorrelation functions  $u'_a$ ,  $v'_a$ , and  $w'$  are shown in Figures 7.14, 7.15, and 7.16, respectively. The behavior differs from one component to another —  $v'_a$  being the only one appearing to verify Taylor's hypothesis. The spatial correlation function for  $u'_a$  deviates from the time correlation function more rapidly than expected, all the points on the spatial curve being below the corresponding points on the time autocorrelation. Of the six points on the  $w'$  spatial correlation curve, four are on the line of the time correlation curve and two are well above the line.

The peculiar feature about the  $w'$  spatial correlation is the higher value at 64 meters than at 32 meters. The signs of maximum cross-correlation between  $w'$  at consecutive positions and the sign of the odd part of the cross-correlation for  $w'$  were checked to make sure that the four  $w'$  channels had not somehow gotten mixed up in the analysis. The check indicated that each  $w'$  series was from the correct location. The reason for the higher correlation at 64 meters must be that a characteristic length of the convective turbulence approximating 64 meters prevailed during this experiment.

The Monin-Obukov  $L$  characteristic length was computed using gradient values.

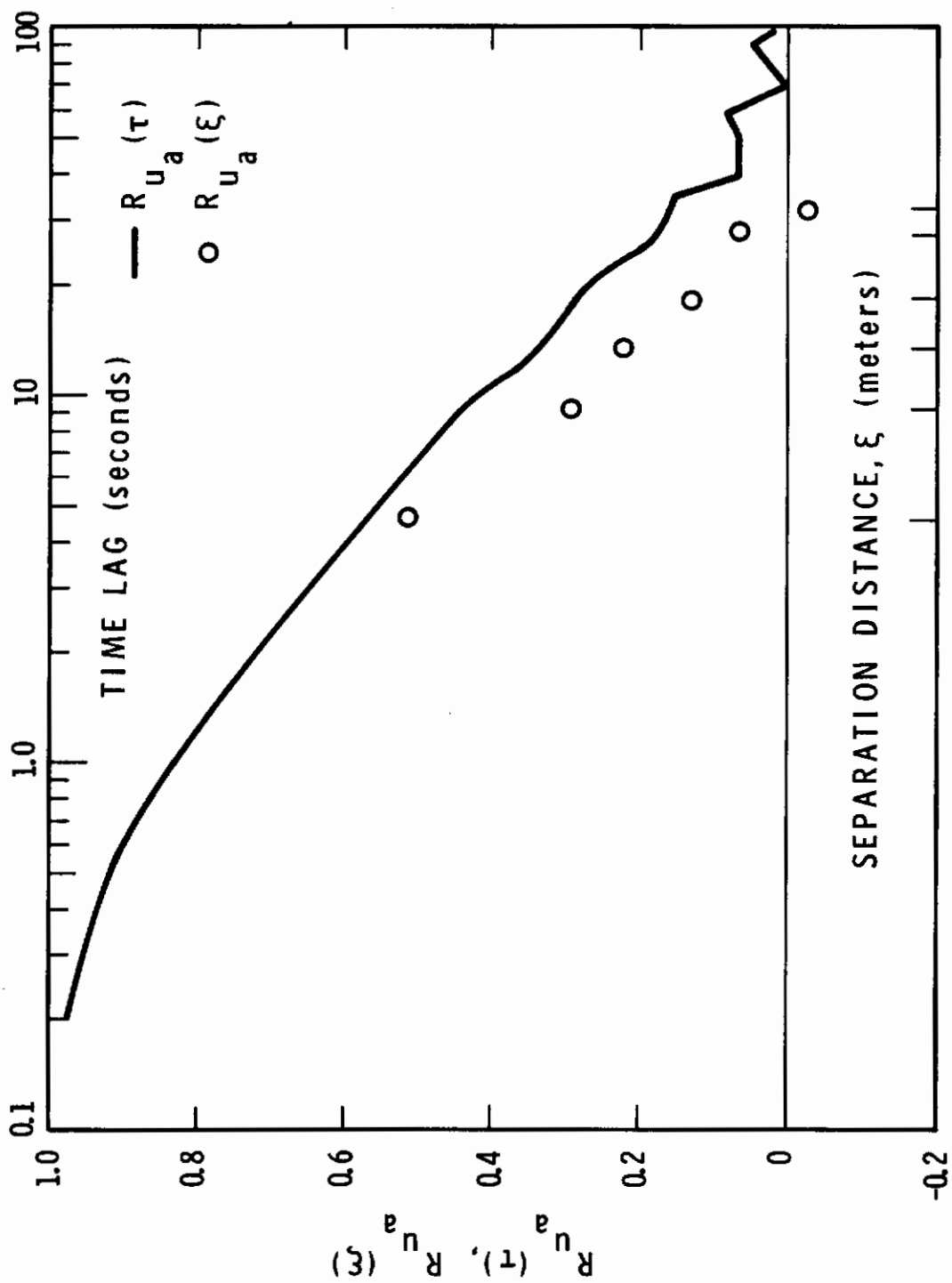


Figure 7.14 Time and Space Correlations for  $u'_a$ , Test T703

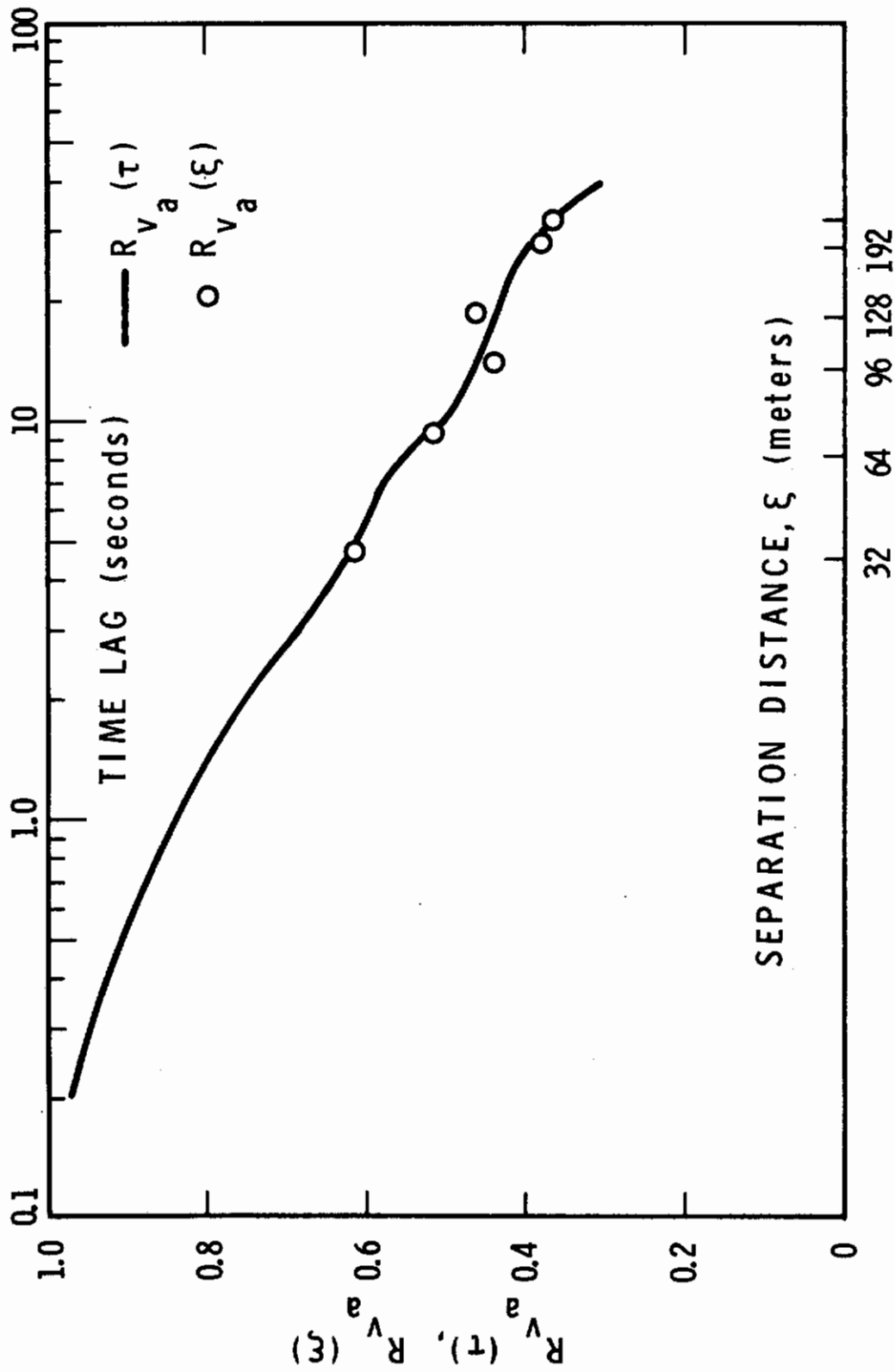


Figure 7.15 Time and Space Correlations for  $v'_a$ , Test T703

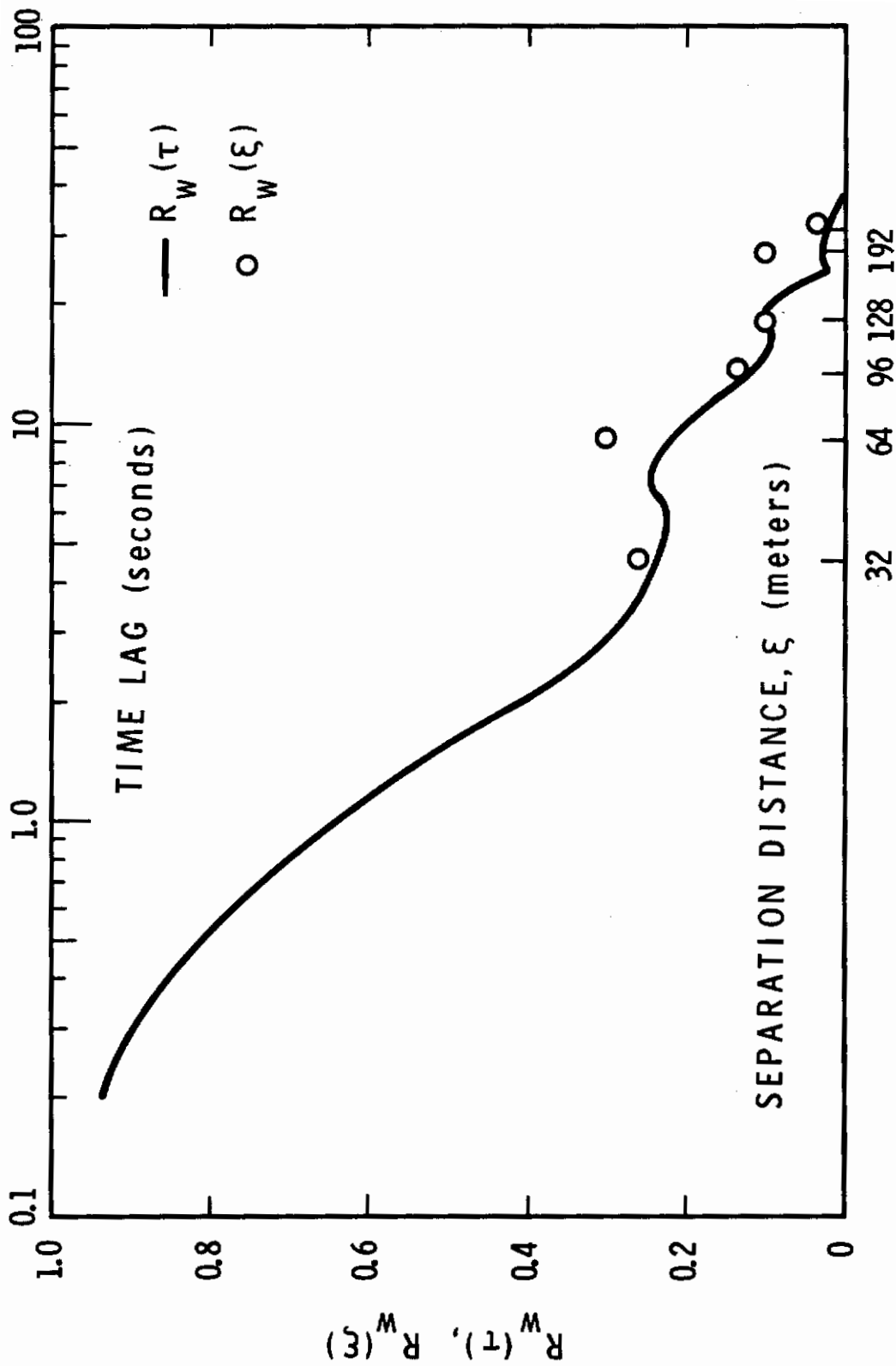


Figure 7.16 Time and Space Correlations for  $w'$ , Test T703



# Contrails

Using 0.4 for Von Karman's constant the value obtained for L was about -180 meters. (The minus sign is a convention applying to all Monin-Obukov L during unstable conditions.) The formula for L given from gradients is

$$L = \frac{K_m}{K_h} \frac{u^* (dV/dz) T}{kg \, d\theta/dz}$$

For reasons developed in Reference 4.1, Von Karman's constant, k, was considered to be intrinsically associated with mechanical turbulence and it was speculated that a length physically more characteristic of convective turbulence may possibly be found by deleting the k from the L computation. When this quantity,  $L^* = kL$  is computed using T703 data, a length of 72 meters is obtained, which compares rather closely with the 64-meter distance at which a peak in the spatial correlation function was found. The method of computing the L involved gradients because turbulence data for direct calculation of L were not available at lower elevations in the constant flux layer. This, therefore, resulted in a more gross estimate than desired. Nevertheless, finding physically characteristic lengths for convective turbulence is a necessary step for describing convection turbulence in the boundary layer. This description must be available before any general description of atmospheric boundary layer turbulence may be given that would be useful in predicting responses. Thus, the tentative result must be checked by future research.

A set of similar graphs was drawn for the correlations from Test T701, during which the mean azimuth angle was  $43^\circ$ . The correspondence between time and space correlations for these data was little better than for the  $90^\circ$  azimuth case represented by Test T704.

From Test T105, spatial correlations are available for a separation distance of 223 meters. Although the azimuth angle for this test was given as  $12^\circ$  in the Interim Report, the true azimuth angle with respect to the two towers from which data have been analyzed for this report was  $4^\circ$ . (The  $12^\circ$

applied to the second and third towers, and was the mean azimuth angle for the four-tower system.)

For this test the mean horizontal wind speed was 8.3 mps, making the 223 meters correspond to a transport time of 27 seconds according to Taylor's hypothesis. The spatial correlations at zero time lag and the time correlations at 27 seconds were 0.342 and 0.333 for  $u'_a$  and 0.444 and 0.447 for  $v'_a$ . Because the spatial correlation for  $w'$  was 0.007 and because the time correlation for  $w'$  became negative at 9 seconds, no comparison is made here. The comparisons made are obviously very strong.

Test T202, using the T-shaped configuration, should have yielded verification information because the direction of the mean horizontal wind was intermediate between the sampling line simulating the fuselage and the line between the tail and the right-wing position, at which a sensor was located. Defining the azimuth angle for this application as the angle between the mean wind direction and the line between the tail and right wing anemometers, the figure given for the 55 minute period is  $21^\circ$  at the tail and is  $6^\circ$  at the right wing. For the first 14-minute period of the 55 minutes, the corresponding azimuth angles are  $24^\circ$  and  $9^\circ$ . The mean wind speed was considered to be 8.6 mps for the 55-minute period and 8.8 mps for the 14-minute period. Because the tail and right-wing sensors were separated by 7.5 meters, Taylor's hypothesis predicts that the zero time lag spatial correlations will correspond to time correlations for 0.87 second for the 55-minute period and for 0.85 second for the 14-minute period. The actual correlation figures are shown in Table 7.4.

This table shows successful verification for  $w'$  for both time periods and for  $v'_a$  for the 14-minute analysis. The lack of verification for  $u'_a$  must have resulted from tower effects (Reference 1.1). Parenthetically  $u'_a$  and  $v'_a$  are the head-on and lateral directions relative to the line from the tail to the wing center. Therefore, it seems best to remember the successful verification for the vertical and to consider the horizontal analysis inconclusive.

TABLE 7.4

CORRELATION FROM TEST T20255-Minute Analysis

	<u>Tail</u> R(0.87 sec)	<u>Right-Wing</u> R(0.87 sec)	<u>Tail to Right-Wing</u> R(7.5 m)
u' <sub>a</sub>	0.900	0.836	0.734
v' <sub>a</sub>	0.858	0.847	0.792
w'	0.705	0.708	0.720

14-Minute Analysis

	<u>Tail</u> R(0.85 sec)	<u>Right-Wing</u> R(0.85 sec)	<u>Tail to Right-Wing</u> R(7.5 m)
u' <sub>a</sub>	0.812	0.708	0.648
v' <sub>a</sub>	0.746	0.780	0.745
w'	0.624	0.631	0.634

Summarizing all correlation results quoted here, it appears that good verification of Taylor's hypothesis exists for mean wind speeds on the order of 6 mps and larger for azimuth angles up to 10° and for heights up to 60 meters provided that marked instability is not present. However, a much wider sample of data is needed to make the results really credible.

Because of the shear in the boundary layer, the verification cannot be expected to be complete, and according to Lin holds only for those wave numbers above a certain lower limit — or in better language, only for those wave lengths below a certain upper limit. This investigation will next be given in detail.

## Phase Spectral Analysis

The required data for this type of analysis may be obtained by recording from at least two sensors, one of which is placed downwind of the other. In Section II it was shown that if the  $U_1$  component of the wind is recorded in this way, Taylor's hypothesis predicts that the phase spectrum calculated by cross spectral-analyzing  $U_1$  from both sensors will be, as previously specified by (Equation 2.25)

$$\phi(n) = \frac{360n\xi}{\bar{U}},$$

in degrees.

For Test T603 data for  $u'_a$ ,  $v'_a$ , and  $w'$  are available from the entire logarithmic line of seven sensors. The phase spectral analysis to be presented draws chiefly on the results from this test. Investigation of height dependency is initiated by introducing results based on analysis of data from fewer sensors from Tests T703, T105, and T202.

The results from Test T603 can best be seen by examining the set of eight phase spectral plots as a group (Figures 7.17 through 7.24). There is one graph for each separation distance for which phase spectra showing any organization could be plotted. These distances were 4, 8, 12, 16, 24, 32, 48, and 64 meters. Items requiring explanation on the graphs are as follows.

1. The heavy diagonal line across each figure is the theoretical phase spectrum predicted by Taylor's hypothesis.
2. The equation of this line, Equation 2.25 is given elsewhere on the figure, first in general form and then in final calculated form, using  $\bar{U} = 6.4$  mps.
3. The dashed vertical line indicates the lower frequency limit at which the phase spectra for the three components appear organizable.

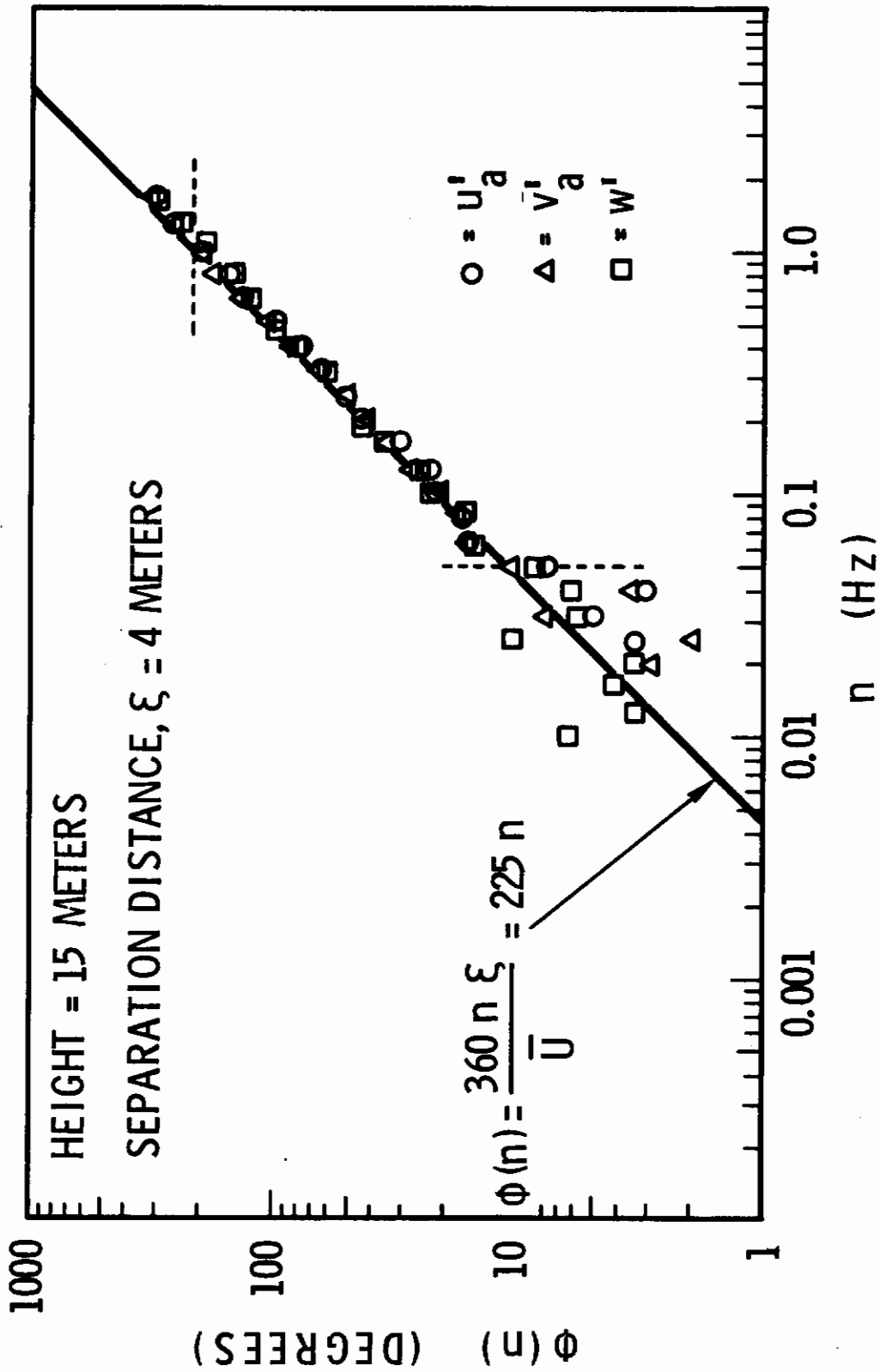


Figure 7.17 Phase Spectra - Separation Distance 4 Meters, Test T603

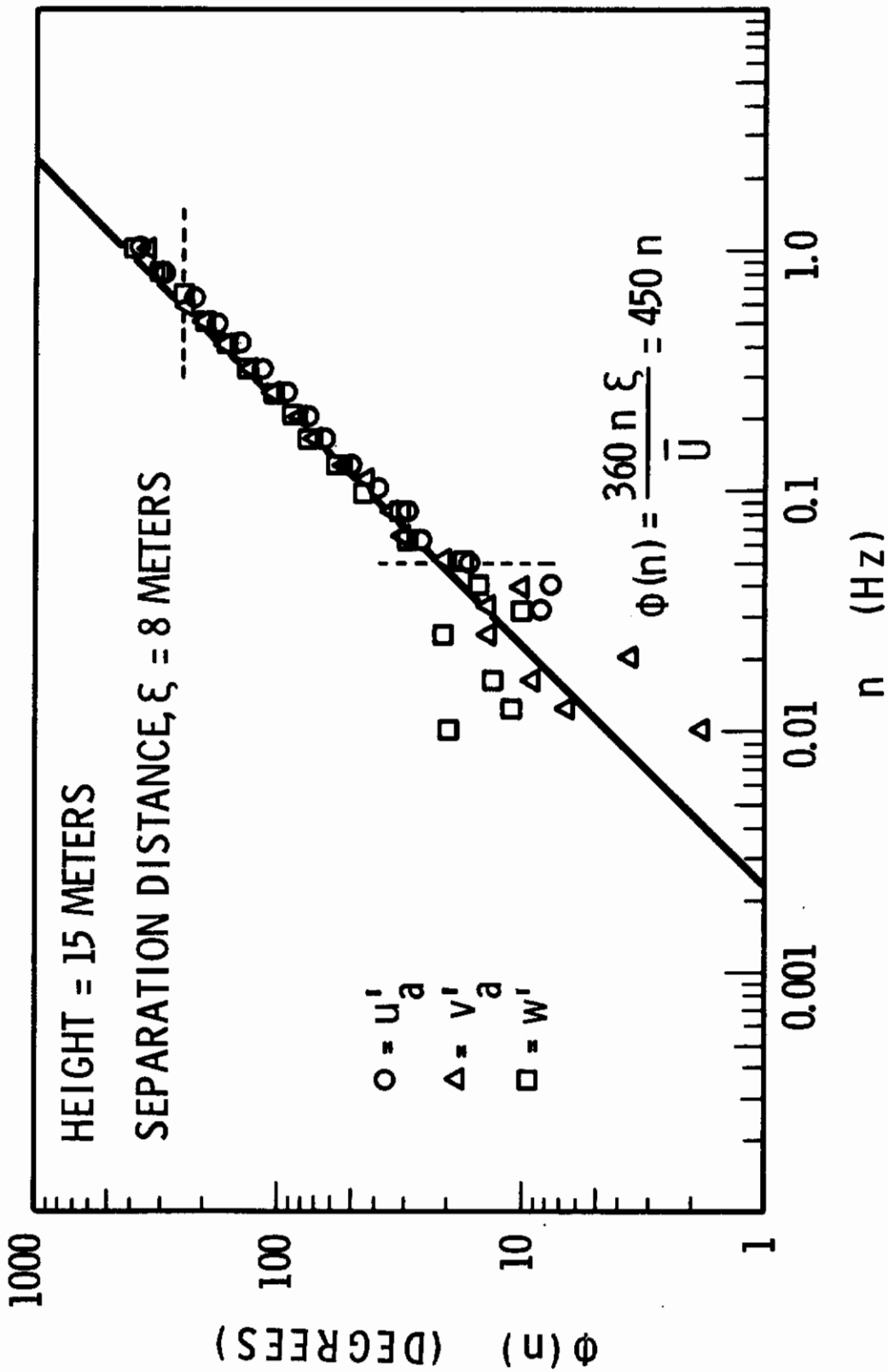


Figure 7.18 Phase Spectra - Separation Distance 8 Meters, Test T603



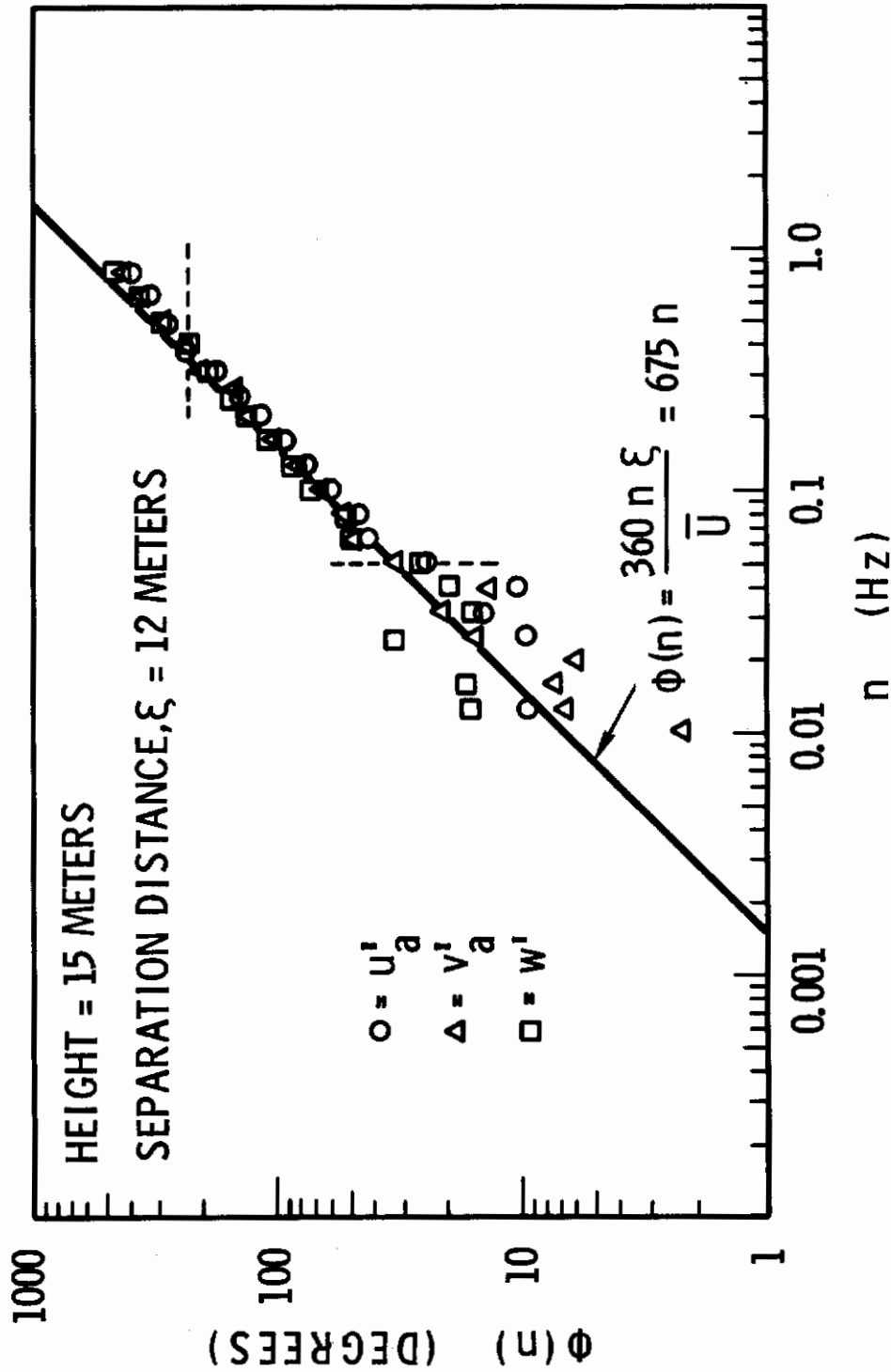


Figure 7.19 Phase Spectra - Separation Distance 12 Meters, Test T603

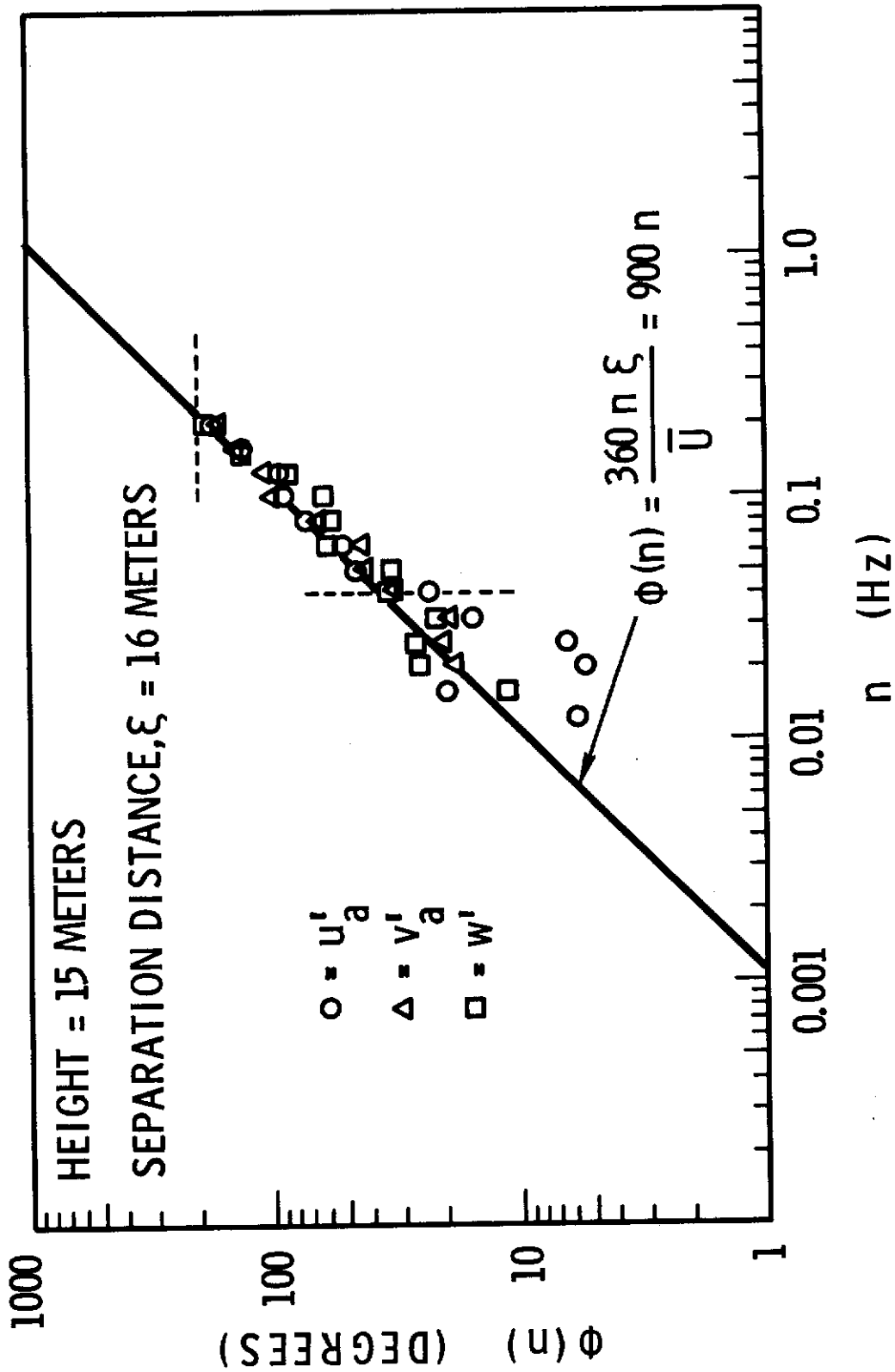


Figure 7.20 Phase Spectra - Separation Distance 16 Meters, Test T603

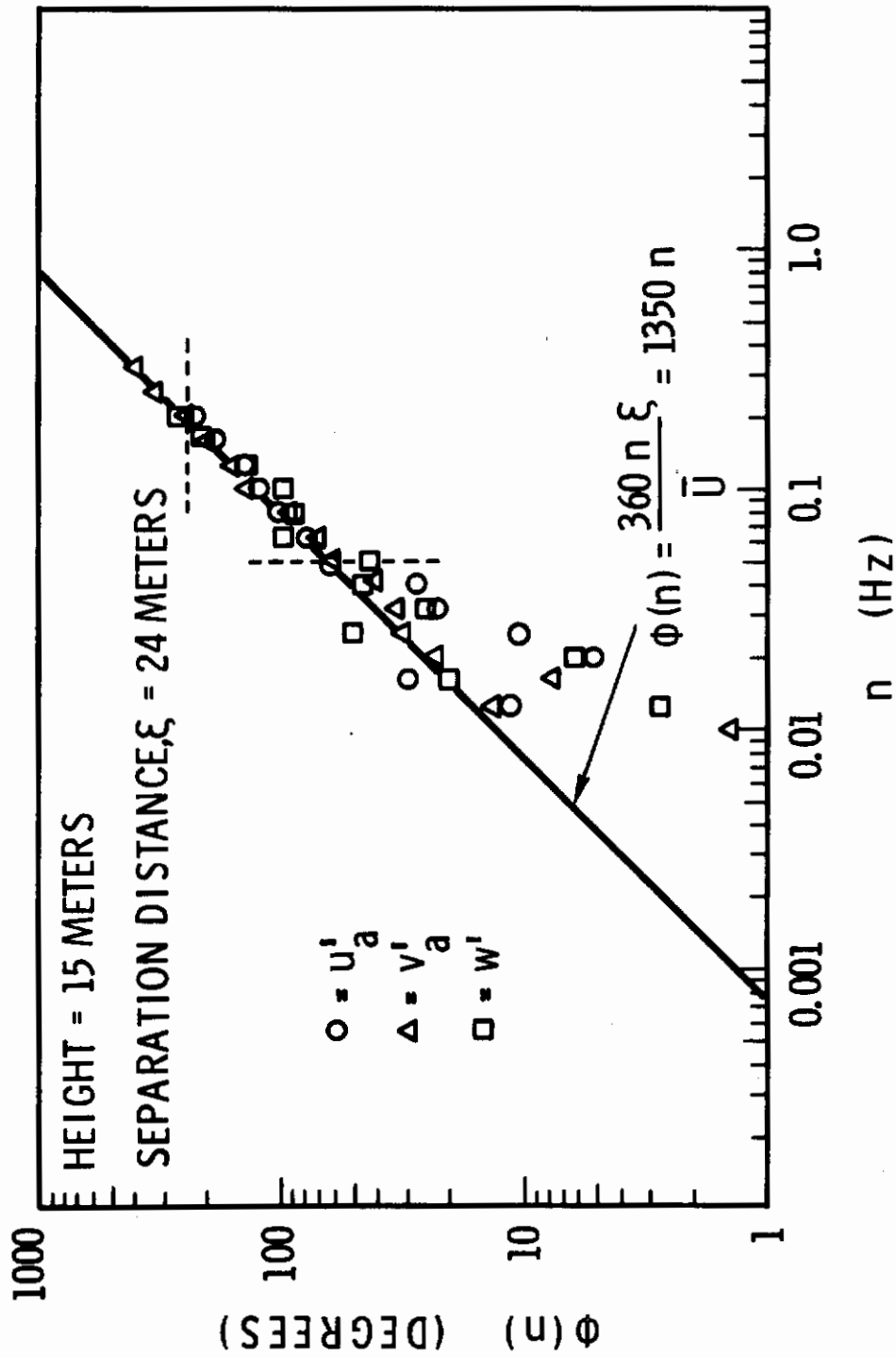


Figure 7.21 Phase Spectra - Separation Distance 24 Meters, Test T603

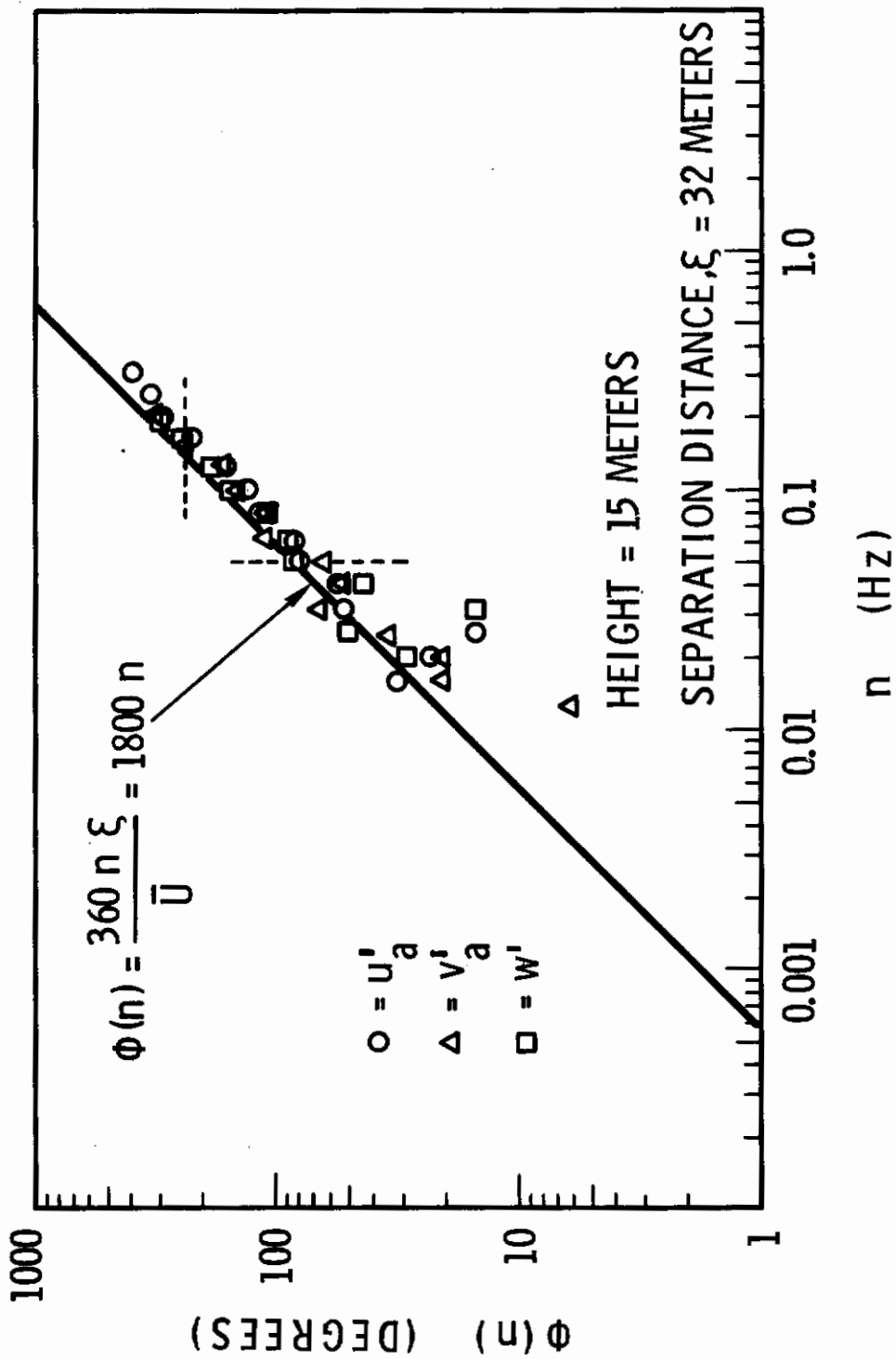


Figure 7.22 Phase Spectra - Separation Distance 32 Meters, Test T603

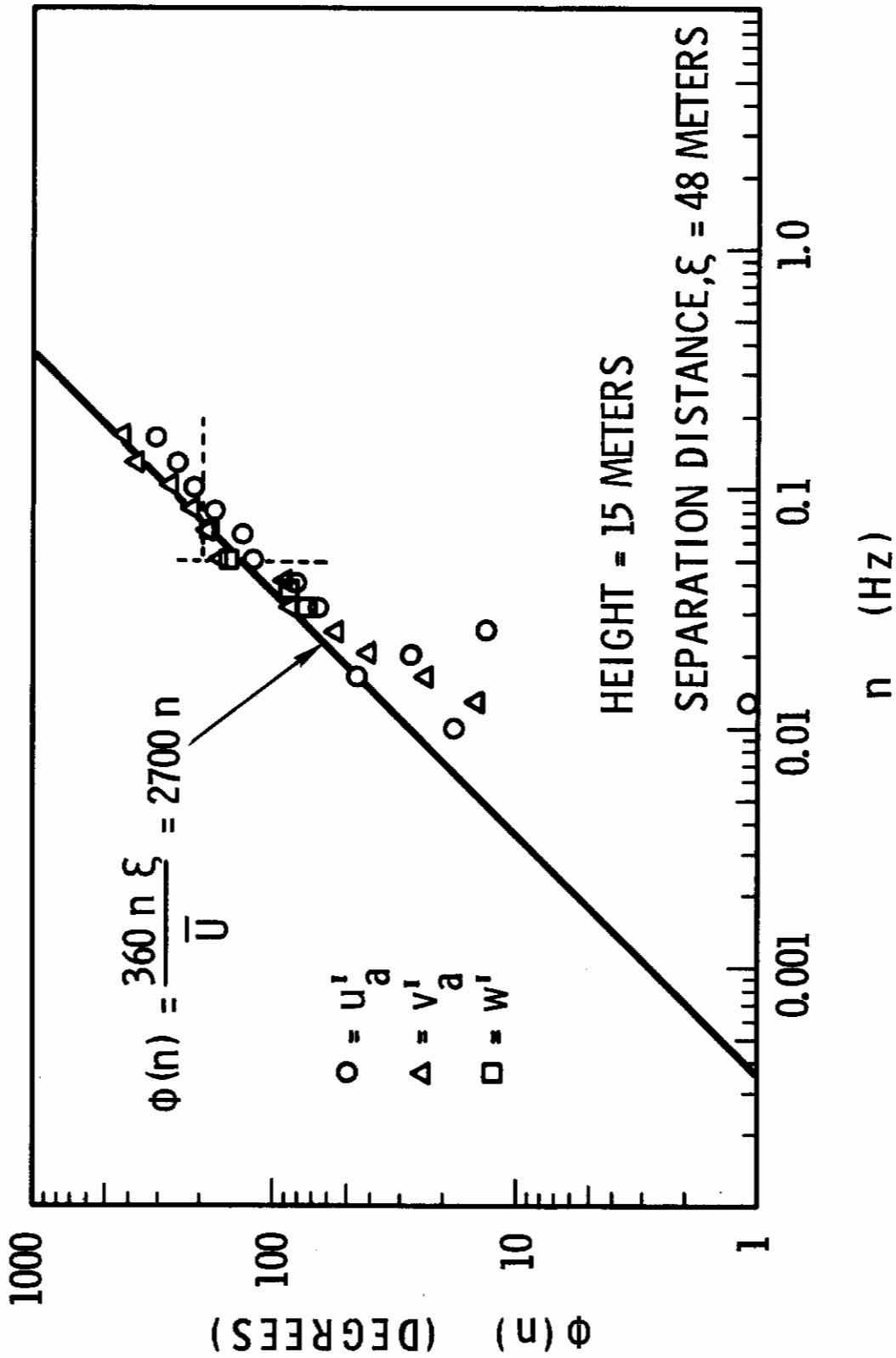


Figure 7.23 Phase Spectra - Separation Distance 48 Meters, Test T603

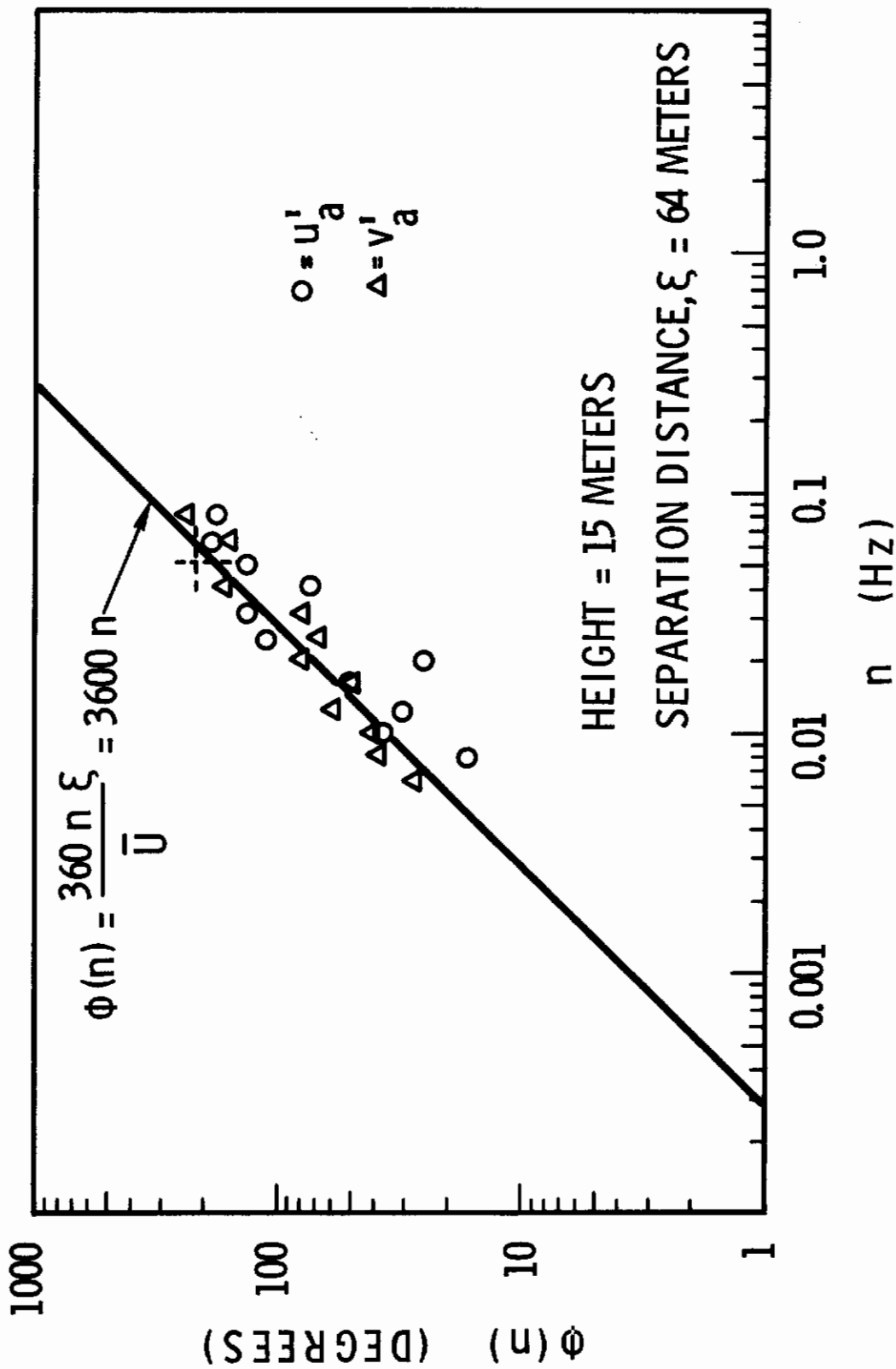


Figure 7.24 Phase Spectra - Separation Distance 64 Meters, Test T603



4. The horizontal dashed line is an upper limit of coherency, the significance of which is explained immediately below.

The upper limit of coherency involves ideas that could have been presented in Section II with the main body of the theory. Since these results are a by-product of the investigation, rather than intrinsic to establishing the principal ideas, discussion has been deferred to this part of the report.

Consider once more the passage of turbulence from the location of one sensor to that of another in the downwind direction. Assume that the sensors are close enough together so that the larger scale variations on the turbulence maintain their characteristics, or individuality, over the path of advection. This part of the turbulence is coherency advected from one location to the other. Intuitively there must be a lower limit to the size of the variations that can be coherently advected over the given path and hence an upper limit to the frequencies representing these variations in the time series. This is important in phase spectral analysis because the phase spectra might not be expected to show organization at frequencies above the upper limit of coherency.

Because the coherency function is continuous, some arbitrary cutoff value of coherency must necessarily be selected before an upper frequency limit can be defined. Although the maximum frequency of eddies considered to be coherently advected will depend on what cutoff value of coherency is arbitrarily chosen, much may be learned from an extended study in which one cutoff value is uniformly applied. The cutoff value adopted for these studies is  $e^{-1}$ , or about 0.37. The upper limit of coherency is defined as that frequency of the  $u'_a$  spectrum at which the coherency function is  $e^{-1}$ . This value was chosen because the slope of the coherency function is usually quite steep through this value.

The best way to learn from the phase spectral graphs (Figures 7.17 through 7.24) is to examine them sequentially in order of increasing separation

# Contrails

distance, observing certain changes. As the separation distance increases, the line function for the ideal phase spectrum moves to a higher phase location on each succeeding graph, associating a larger value of the phase spectrum with the same frequency. Theory predicts that the vertical line, indicating the lowest frequency at which the phase spectrum is organized, should be at the same frequency regardless of separation distance. This frequency,  $n_0$ , appears to be reasonably estimated at 0.05 Hz from the analysis. The horizontal line, indicating the upper limit of coherency, appears at approximately the same phase angle,  $\phi_0$ , on each diagram. The placement varies slightly, but not significantly, about  $240^\circ$ . Phase spectral data have been plotted above this value where organized results were found. Therefore, as the graphs are viewed in order of increasing separation distance, the diagonal line rises and its intersections with the fixed cutoff lines for  $n_0$  and  $\phi_0$  converge, thereby decreasing the portion of the diagonal line that is followed by organized phase spectral functions. The graphs show 64 meters as the separation distance for which the horizontal and vertical lines intersect the diagonal at almost the point of convergence of these intersections. For greater separation distances the phase spectrum shows little tendency to correlate with the diagonal. Also for the 64-meter separation distance, only the phase spectra of the two horizontal components were well enough organized to constitute functions of frequency. If any of these functions are drawn by connecting consecutive data points for each wind component with straight lines, the difference of behavior between the organized portion contained above  $n_0$  and below  $\phi_0$  in comparison to the unorganized portion below  $n_0$  is made even more apparent by the extremes of slope variation in the phase spectral function in the unorganized region of low frequency.

The summary results are:

1. The phase spectra are organized from a frequency of 0.05 Hz up to or beyond the frequency of the coherency limit. This implies that during this test Taylor's hypothesis was valid for all frequencies above the lower limit, notwithstanding the upper limit of coherency.

# Contrails

2. The frequency limit of coherency was approximately  $240^\circ$ . This means that during this test eddies were coherently advected over a maximum distance of about  $2/3$  of their own along-wind dimension.
3. Most of the experimental data points are slightly below the line of the ideal spectrum. This indicates that the eddies are traveling faster than the mean wind speed. The ratio of the eddy translation speed to the mean wind speed may be estimated by computing for each separation distance,  $\xi$ , the quantity  $\xi/\bar{U}\tau_m$  where  $\tau_m$  is the time lag of the maximum cross correlation between the parallel components separated by distance  $\xi$ . When this was done for all  $\xi$  from 4 to 32 meters, the average results for  $u'_a$ ,  $v'_a$ , and  $w'$  were 1.12, 1.11, and 1.16, respectively. Also, the phase spectral data fall slightly below the theoretical curve and are consistent with a translation speed about 12 percent higher than the mean wind speed.

It may be argued that the first two conclusions depend on the length of the sample used. For example, if 7 minutes of data are analyzed rather than 28, banded spectral estimates for a given frequency from the 7-minute analyses will be based on approximately one-fourth as many degrees of freedom as from the 28-minute analyses. Therefore, if 7-minute data had been analyzed, the lower limit frequency at which Taylor's hypothesis applies and the upper limit frequency of coherency would both be higher for these analyses.

To verify this, a 7-minute segment was analyzed for the 4, 8, and 12-meter separation distances. This was accomplished by omitting the averaging of the data together, four points at a time, as was done for the 28-minute analyses. The results are shown in Table 7.5.

Altogether the figures in the table cannot be interpreted to show any reliable tendency of the limit frequencies to shift upward for 7-minute analyses versus 28-minute analyses. In general the phase spectral functions for the 7-minute analyses follow the ideal phase spectrum with slightly

more deviation than do those for the 28-minute analyses.

TABLE 7.5

COMPARABLE PHASE SPECTRAL AND COHERENCY ANALYSES FOR SEVEN-MINUTE DATA

<u>Separation Distance</u> (m)	<u>Lower Limit or T.H</u> (Hz)	<u>Upper Limit of Coherency</u> (deg)
4	0.05	310
8	0.063	190
12	0.063	230

Other similar phase and coherency spectral information is available from tests at 30 and 58-meter elevation. The total information from four tests is summarized in Table 7.6. Additional phase and coherency spectral plots are shown in Appendix IV.

If less consideration is given to the analysis of the Test T202 data because of the rather large and somewhat uncertain azimuth angle and because of the tower influences detected in the spectra, the following conclusions, both tentative and plausible may be drawn from the other data.

1. The lower limit frequency for Taylor's hypothesis,  $n_o$ , appears to vary inversely with height up to 60 meters, if stability is maintained constant. The frequency is higher for unstable conditions.
2. The statistic obtained by dividing  $n_o$  by  $u^*/kz$  appears more stable than Lin's expression, using  $d\bar{u}/dz$  in the denominator. This is probably because there is more certainty in measuring  $u^*$  than there is in measuring  $d\bar{u}/dz$ .
3. Adopting  $n_o/(u^*/kz)$  for modeling because of its lesser variability, the lower limits for Taylor's hypothesis are:

$$\text{Stable case: } n_o/(u^*/kz) \geq 2/3$$

Unstable case:  $n_o / (u^*/kz) \geq 1$  .

The latter figure would no doubt be larger, if not meaningless, for great instability.

4. The length of the longest eddies advected according to Taylor's hypothesis is 8 times the measuring height or more. The figure is indicated to be greater for stable conditions than for unstable conditions.
5. Computations for all three heights consistently indicate an eddy translation speed slightly greater than the mean wind speed.
6. If a value of  $e^{-1}$  is accepted as a lower limit of coherency, eddies are coherently advected over paths not greater than their own along-wind dimension. Height and stability dependence are not yet clear.

TABLE 7.6

SUMMARY OF PHASE SPECTRAL AND COHERENCY ANALYSES

	Test Number			
	T603	T703	T105	T202
Height (m)	15	30	58	58
Stability	Stable	Unstable	Stable	Unstable
$n_o$ (Hz)	0.050	0.030	0.012	0.040
$n_o (d\bar{U}/dz)$ (cycles)	0.88	1.5	0.55	2.7
$n_o / (u^*/kz)$ (cycles)	0.64	1.0	0.67	1.8
$\lambda = \bar{U}/n_o$ (m/cycle)	128	233	692	220
$\lambda/z = (n_o z/\bar{U})^{-1}$ (m/cycle)	8.5	7.8	11.9	3.8
$\xi/\bar{U}\tau_m$ (average value)	1.13	1.07	1.09	---
$\phi_o$ (degree)	240	240	340	---

## VARIANCES AND COVARIANCES

In atmospheric boundary layer turbulence there are many variances and covariances that can be measured. It is important to realize that physically some of them are more significant than others. Two primary covariances are indigenous contributors to turbulence generation and are useful in modeling other covariances. The  $\overline{u'w'}$  covariance of mechanical turbulence is the primary result of turbulent response to the boundary layer mean wind shear. The  $\overline{w'\theta'}$  covariance is associated in a similar way with the lapse rate of the mean potential temperature. The effect of these latter convective fluctuations is either to modify the mechanical turbulence or to supplant it, depending on relative strength.

The primary covariances induce variances in the flow in all directions. The variances must be dependent on the primary covariances.

In addition to the physical dependencies, measured variances are also dependent on the wave number range of the turbulence that is incorporated into the time series measurements and retained in the filtered version of data that are analyzed. This is an important problem for TOLCAT modeling because only by coincidence would the wave number range analyzed correspond to the wave number range to which a given aircraft traveling at a given speed respond. Therefore, the discussion will emphasize the change of the variance and covariances with filtering.

Not all of the horizontal variance in the flow can be accounted for as physically derived from the primary covariances. No sharp scalewise separation has been found between turbulent fluctuations of the physical nature described above and mesoscale fluctuation of other origin.

### Problems in Modeling the Variances

Data recorded at Hanford prior to the TOLCAT experiments produced ratios of  $\sigma_u^2$ ,  $\sigma_v^2$ , and  $\sigma_w^2$  to  $\overline{u'w'}$  of 7.8/4.0/1.7/1.0, as summarized by Skelton



(Reference 2.7). This summary is based on data recorded at 3, 6, and 12 meters, while more recent data from Hanford were recorded at 15, 30, 60, and 131 meters. An array of variances is presented in Table 7.7 to demonstrate the complexity of designating these ratios.

Measurements of  $\overline{u'w'}$  and  $\overline{w'\theta'}$  from a standard height in the constant flux layer were not taken during the TOLCAT runs since it had not been anticipated that they would vary as significantly with height as they did. Consequently, the best parameter available for modeling is  $\bar{U}^2$  at a constant level, namely 15 meters. In Table 7.7, modeling by  $\bar{U}^2(15)$  is compared to modeling by  $-\overline{u'w'}(z)$ , where  $z$  is the height of measurement.

The variances from the unfiltered data and the 300 second filtered data are included for general information, while the variances from filters of 60 seconds and 12 seconds correspond more to the variances experienced by flying and hovering aircraft, respectively, during take-off and landing. Skelton's statement (Reference 2.7) that aircraft do not respond to frequencies (as seen by the aircraft) of less than 0.1 Hz probably rests on the assumption that either the natural motion of the craft filters these out or at worst the pilot can prevent the aircraft from responding critically to the lower frequencies. With this understanding, one can see that for hovering aircraft the low frequency end of the sensitivity band approximates the 12-second high pass filter for the tower data, while for conventional aircraft, the 60-second high pass filter for the tower data corresponds better to the low frequency end of the sensitivity band that applies to the aircraft forward motion. To assume that variances as seen through the 60-second filter corresponds to the experience of aircraft flying into the mean wind at four or five times the mean wind speed would be over-exact since Taylor's hypothesis was shown to apply only to the wave lengths on the order of eight times the height of flow or shorter. Therefore, the simulation of the experience of flying aircraft by the output from the 60-second filter applied to tower data is more indefinite than is simulation of the experience of hovering aircraft by the 12-second filter output.

TABLE 7.7

RATIOS OF VARIANCE ( $\sigma_u^2$ ,  $\sigma_v^2$ ,  $\sigma_w^2$ ) TO  $-\overline{u'w'}$  (z) AND TO  $\bar{U}^2(15)$

Running Mean Filter (sec)	Ratios to $-\overline{u'w'}$ (z)			Ratios to $\bar{U}^2(15)$		
	( $\sigma_u^2$ )	( $\sigma_v^2$ )	( $\sigma_w^2$ )	( $\sigma_u^2$ )	( $\sigma_v^2$ )	( $\sigma_w^2$ )
<b>Height - 15 m: 4 Tests*:</b> $-\overline{u'w'} = 0.34$ , $\bar{U}^2 = 58$						
No filter	6.6	3.1	1.6	.038	.018	.009
300	5.6	2.8	1.6	.032	.016	.009
60	4.1	2.5	1.5	.023	.014	.008
12	1.8	1.7	1.2	.010	.010	.007
<b>Height - 30 m: 5 Tests**:</b> $-\overline{u'w'} = 0.46$ , $\bar{U}^2 = 93$						
No filter	5.7	3.8	2.0	.028	.018	.010
300	4.8	3.0	1.9	.025	.015	.010
60	3.1	2.1	1.7	.016	.011	.009
12	1.2	1.2	1.3	.006	.006	.007
<b>Height - 60 m: 5 Tests***:</b> $-\overline{u'w'} = 0.24$ , $\bar{U}^2 = 58$						
No filter	6.0	4.2	1.7	.025	.017	.007
300	4.9	3.1	2.0	.020	.013	.008
60	2.9	2.5	1.8	.012	.010	.007
12	1.2	1.3	1.1	.005	.005	.005
<b>Height - 131 m: 2 Tests (unstable):</b> No definable $\overline{u'w'}$ , $\bar{U}^2 = 19.2$						
No filter				.143	.156	.092
500				.092	.080	.087
100				.033	.031	.042
20				.012	.013	.014
<b>Height - 15 m: Test E501a (unstable):</b> $-\overline{u'w'} = 0.38$ , $\bar{U}^2 = 59$						
No filter	7.0	9.9	1.8	.045	.063	.011
300	5.3	4.0	1.7	.034	.025	.011
60	3.6	2.6	1.7	.023	.016	.011
12	1.9	1.6	1.4	.012	.010	.009

- \* 1 unstable, 1 neutral, and 2 stable  
 \*\* 2 unstable, 1 neutral, and 2 stable  
 \*\*\* 2 unstable, 1 neutral, and 2 stable

Continued on page 150

TABLE 7.7 (CONTINUED)

Running Mean Filter (sec)	Ratios to $-\overline{u'w'}(z)$			Ratios to $\overline{U}^2(15)$		
	$(\sigma_u^2)$	$(\sigma_v^2)$	$(\sigma_w^2)$	$(\sigma_u^2)$	$(\sigma_v^2)$	$(\sigma_w^2)$
<u>Height - 30 m: Test E501a (unstable): <math>-\overline{u'w'} = 0.22, \overline{U}^2 = 59</math></u>						
No filter	10.5	17.2	3.7	.039	.064	.014
300	6.3	7.1	3.4	.024	.027	.013
60	3.5	3.5	3.0	.013	.013	.011
12	1.7	1.6	2.4	.007	.006	.009
<u>Height - 60 m: Test E501a (unstable): <math>-\overline{u'w'} = 0.07, \overline{U}^2 = 59</math></u>						
No filter	24.3	48.0	9.3	.029	.057	.011
300	14.1	18.6	8.6	.017	.022	.010
60	7.1	6.3	7.4	.008	.007	.009
12	3.3	3.6	4.7	.004	.004	.005

In Section II the two-sided nature of atmospheric boundary layer turbulence (mechanical and convective) was stressed, and Table 7.7 is organized to illustrate the difference. Initial analysis of the data revealed that all the measurements at 15 meters were of turbulence primarily mechanical in nature. However, at 30 meters and at 60 meters the averages of the variance ratios in Test E501a were conspicuously different from those of the other tests. The reason lies in the convective nature of the turbulence at these levels. Therefore, the E501a analysis is exhibited separately rather than averaged in with the other tests.

There are seven main points to be brought out regarding the table.

1. The mean wind speed at a single height and the  $\overline{u'w'}$  covariance at the height of turbulence measurement seem to model the mechanical turbulence about equally well. If the blocks of variance are compared by height, there is little in the way of observable trend in either column - certainly little that can be called a greater trend in one column than in the other.

# Contrails

2. Although the variance ratios to  $-\overline{u'w'}$  at 15 meters are similar for Test E501a and for the other tests, there is marked dissimilarity at 30 and 60 meters. This demonstrates that for Test E501a  $\overline{u'w'}(z)$  is not the characteristic velocity of the turbulence at 60 meters height.
3. The dissimilarity among the ratios of variances to  $\bar{U}^2(15)$  is much less than among ratios of variances to  $\overline{u'w'}(z)$ .
4. In all cases the dissimilarity in the ratios decreases with increased high pass filtering.
5. At 30 meters and 60 meters the variances from the 12-second filter are about equal for all three components.
6. The ratios of horizontal variances to  $-\overline{u'w'}$  used by Skelton, based on Hanford data taken at 3, 6, and 12 meters are higher than those obtained at 15, 30, and 60 meters, and in view of the variable filtering of the aircraft, are too specific.
7. The variance ratios to  $\bar{U}^2(15)$  for the 131-meter tests are much higher than any of the others, showing that the departure here from the mechanical model is more complete than the Test E501a data at 60 meters.

Further examination of the AEC data, which featured  $\overline{u'w'}$  at common levels for all tests, shows that modeling the variances by  $\overline{u'w'}(15)$  is more successful than by  $\bar{U}^2(15)$ . This is partly because increased stability decreases both  $-\overline{u'w'}$  and the variances without decreasing  $\bar{U}$ .

The AEC analysis (Reference 4.2) also indicated a true constant flux layer only for the neutral case. For both the unstable and stable cases,  $-\overline{u'w'}$  exhibited a pronounced decrease above 15 meters with a maximum value at either 7.5 or 15 meters. For the two unstable cases this was found to correlate with the Monin Obukov L. For Test E501a and E501b, L was found to be -98 and -225 meters, respectively, and a maximum value of  $-\overline{u'w'}$  was

measured at 7.5 and 15 meters, respectively. For Test E506, the stable test, the maximum  $-\overline{u'w'}$  was measured at 7.5 meters.

Because the maximum values of  $-\overline{u'w'}$  are unavoidable characteristic of the mechanical generation of the turbulence, the recommended array for future boundary layer turbulence measurements includes one sonic anemometer at a level where the maximum is likely to occur. Apparently, 10 meters would be an appropriate level for obtaining sonic data from which the primary covariances,  $\overline{u'w'}$  and  $\overline{w'\theta'}$  could be measured.

Because different aircraft filter out different portions of the high frequency turbulence, the effects in the turbulence of various values of sampling interval,  $\Delta t$ , over which the original data is averaged are shown in Table 7.8.

The table shows that doubling or halving  $\Delta t$ , about 0.4 second, changes the variance by about 3 percent for  $\sigma_u^2$ , 7 percent for  $\sigma_v^2$ , and 12 percent for  $\sigma_w^2$ . If the turbulence is isotropic in the wave length range of the wing-chord, the reduction of the two lateral variances should be 4/3 the reduction of the horizontal variance. Since this did not occur, the turbulence during this one stable case was not isotropic at 15 meters.

TABLE 7.8

EFFECTS ON HIGH FREQUENCY TRUNCATION ON VARIANCES AND  $\overline{u'w'}$

$\Delta$ (sec)	$\sigma_u^2$ (mps) <sup>2</sup>	$\sigma_v^2$ (mps) <sup>2</sup>	$\sigma_w^2$ (mps) <sup>2</sup>	$\overline{u'w'}$ (mps) <sup>2</sup>
0.2	1.32	0.71	0.337	-0.212
0.4	1.28	0.67	0.302	-0.208
0.8	1.24	0.61	0.257	-0.201
1.6	1.17	0.54	0.200	-0.182

## Magnitude Correlations

The fact that  $\overline{u'v'}$  and  $\overline{v'w'}$  are expected to be zero does not mean that the variables are physically independent. Because of the relations shown in the Navier-Stokes equations, the different components of the wind are not expected to be independent. Accordingly, magnitude correlations given by the following definition have been computed, and the results are summarized here.

Define

$$x_i(t) = u_i^2(t) - \sigma_{u_i}^2 \quad i = 1, 2, 3 \text{ (no summation)}$$

then the magnitude correlation is

$$M_{ij} = \frac{E[x_i(t) x_j(t)]}{\sqrt{E[x_i^2(t)] E[x_j^2(t)]}} \quad (7.4)$$

Test T202 was left out because of the tower effects noted in the analysis and the 131-meter data is exhibited separately.

Examination of the magnitude correlations as functions of height and of the various  $\overline{u_i u_j}$  showed a slight tendency of the values to increase with height, except for the 131-meter data, which analyzed so differently that the results are tabulated separately. Little dependency was shown of the magnitude correlations on  $\overline{u_i u_j}$ .

In Table 7.9 the magnitude correlations for all the data from 15, 30, and 60 meters are averaged together. For the unfiltered data, the averages are from 17 tests. In Table 7.10 the magnitude correlations from Tests T803 and T805, taken at 131 meters, are exhibited separately.



TABLE 7.9

MAGNITUDE CORRELATIONS FOR 15, 30, AND 60-METER DATA

High Pass Filter (sec)	$M_{uv}$	Number of Correlations		$M_{uw}$	Number of Correlations		$M_{vw}$	Correlations	
		Pos.	Neg.		Pos.	Neg.		Pos.	Neg.
None	0.012	11	6	0.060	16	1	0.040	14	3
300	0.023	11	6	0.092	17	0	0.054	14	3
60	0.072	14	3	0.137	17	0	0.085	17	0
12	0.124	8	0	0.151	8	0	0.139	8	0

TABLE 7.10

MAGNITUDE CORRELATIONS FOR 131-METER DATA

Test T803 (41 Min)				Test T805 (55 Min)			
Filter (sec)	$M_{uv}$	$M_{uw}$	$M_{vw}$	Filter (sec)	$M_{uv}$	$M_{uv}$	$M_{vw}$
None	0.157	0.135	0.143	None	-0.092	-0.086	0.051
450	0.330	0.272	0.209	600	0.054	-0.024	0.050
90	0.166	0.069	0.031	120	0.119	0.028	0.117
18	0.134	0.104	0.170	24	0.147	0.100	0.102

The table of averaged values (for 15, 30, and 60-meter data) shows the magnitude correlations to be all slightly positive. The correlation is stronger when one of the components is w'. Also, the correlations increase as the longer wave lengths are removed from the data. As expected, the correlation is strongest for u' and w'.

The analyses of the two tests at 131 meters differ widely from each other and from the analyses of the data from the lower levels. For Test T803, the

values do not increase with filtering, the largest values being with the first filtering. Also, these values are twice as large as any found in the analyses of the lower levels.

## POWER SPECTRAL ANALYSIS

### Vertical Component Models

All analytical forms proposed for modeling power spectra in the atmospheric boundary layer are empirical forms blending a mixture of state-of-the-art physical insight with necessary expediency. The forms to be discussed apply to the frequency-multiplied spectra,  $nS(n)$ . This quantity has the dimensions of velocity squared and is therefore properly normalized by the square of the characteristic velocity of the turbulence. The measurement used for the characteristic velocity squared is usually  $-\overline{u'w'}(z)$  at some low level at which the quantity is quasi-independent of  $z$ . Wherever this quantity is mentioned, it is usually designated  $u_*^2$ , the square of the friction velocity.

The frequency,  $n$ , is normalized by multiplying by the product of  $z/\bar{U}(z)$  and some function of stability. The whole normalizing multiplier may be called  $zF(z/L)/\bar{U}(z)$ , where  $F$  is a universal function of stability modifying the characteristic length. Normalizing the frequency with  $\bar{U}$  amounts to assuming Taylor's hypothesis. Using  $zF(z/L)$  amounts to stating that the length scale of turbulence is expected to vary with the height and stability. Instability increases the length scale applying at a given height, and stability decreases the length scale. Therefore,  $F(z/L)$  is greater than unity for unstable conditions and less than unity for stable conditions. By assuming that the nondimensional shear,  $\phi_m(z/L)$  is balanced in the turbulent energy budget by the nondimensional dissipation,  $\phi_e(z/L)$ , the normalization for stability can be expressed (Reference 4.2)

$$F(z/L) = \phi_m^{-1}(z/L) \quad . \quad (7.5)$$

This dependence is not universally agreed upon and further investigation of the assumption involved is warranted.

Empirical functions proposed by different investigators differ in the number of degrees of freedom used. One of the simplest of these may be written, say for the vertical component, as

$$\frac{nS_w(n)}{u_*^2} = \frac{K_w [fF(z/L)/f_w]}{1 + 1.5[fF(z/L)/f_w]^{5/3}}, \quad (7.6)$$

where  $f$  is the nondimensional frequency,  $nz/\bar{U}(z)$ , and  $f_w$  is the value of  $fF(z/L)$  for which  $nS_w(n)$  is the greatest.  $K_w$  is a universal constant. The nondimensional frequency of maximum energy,  $f_w$ , should also have a universal value, which is most easily assessed by analyzing data from a neutral test. The factor, 1.5, in the denominator is a necessary artifice to give the expression its maximum value when  $fF(z/L) = f_w$ .

Equation 7.6 can be correct only over that height range where the characteristic velocity of the turbulence is reasonably constant. Previous Hanford analysis (Reference 4.1) has shown that this is not true even as low as 30-meter height for the very unstable case. Other investigators have added additional degrees of freedom to Equation 7.6 to model the change of characteristic velocity with height and changes of the peakedness of the curve (Reference 7.5).

The use of an equation of the form of Equation 7.6 for the horizontal components requires different values for the constant in the numerator and for the frequency of maximum energy. The application is also less successful, especially for the lateral component.

## Universal Values Proposed for Spectral Forms

By examining data from several measuring sites, Busch and Panofsky (Reference 2.6) have proposed values of 1.075 for  $K_w$  and 0.32 for  $f_w$ . Using data from an experiment under neutral conditions at Hanford, with turbulence instrumentation at 60, 30, 15, 7.5, and 3.75 meters, Elderkin et al (Reference 4.3) have proposed values of 1.15 for  $K_w$  and 0.46 for  $f_w$ .

The difference in  $K_w$  is about 7 percent and could be the result of uncertainties in determining  $u_*^2$ . The Hanford value of  $f_w$  is more than 40 percent higher than the Busch-Panofsky figure. Part of the reason for the difference appears to be that Busch and Panofsky arrived at their figure by averaging together results from both neutral and unstable tests, which could give a value lower than that which is representative of the neutral case alone. Also, part of the difference may be due to the fact that the frequencies in the earlier data were normalized by using the mean horizontal wind speed rather than its component in the longitudinal direction. However, this difference is not expected to exceed 1 or 2 percent.

When spectral calculations from Equation 7.6 are compared with similar calculations using Kolmogoroff's law for the inertial subrange

$$\frac{nS_w(n)}{u_*^2} = \frac{4}{3} Ak^{-2/3} f^{-2/3}, \quad (7.7)$$

the results are about 15 percent greater than Equation 7.6 even when using the largest value proposed for A, 0.146, and the smallest value proposed for k, 0.35. The Hanford curve and the inertial subrange prediction are shown in Figure 7.25 along with the spectra from the neutral Test E508.

Spectra for  $w'$  from unstable conditions (Tests E501a and E501b) and for stable conditions (Test E506) were also compared to Equation 7.6 after computing a frequency translation based on the stability (Reference 4.3). The

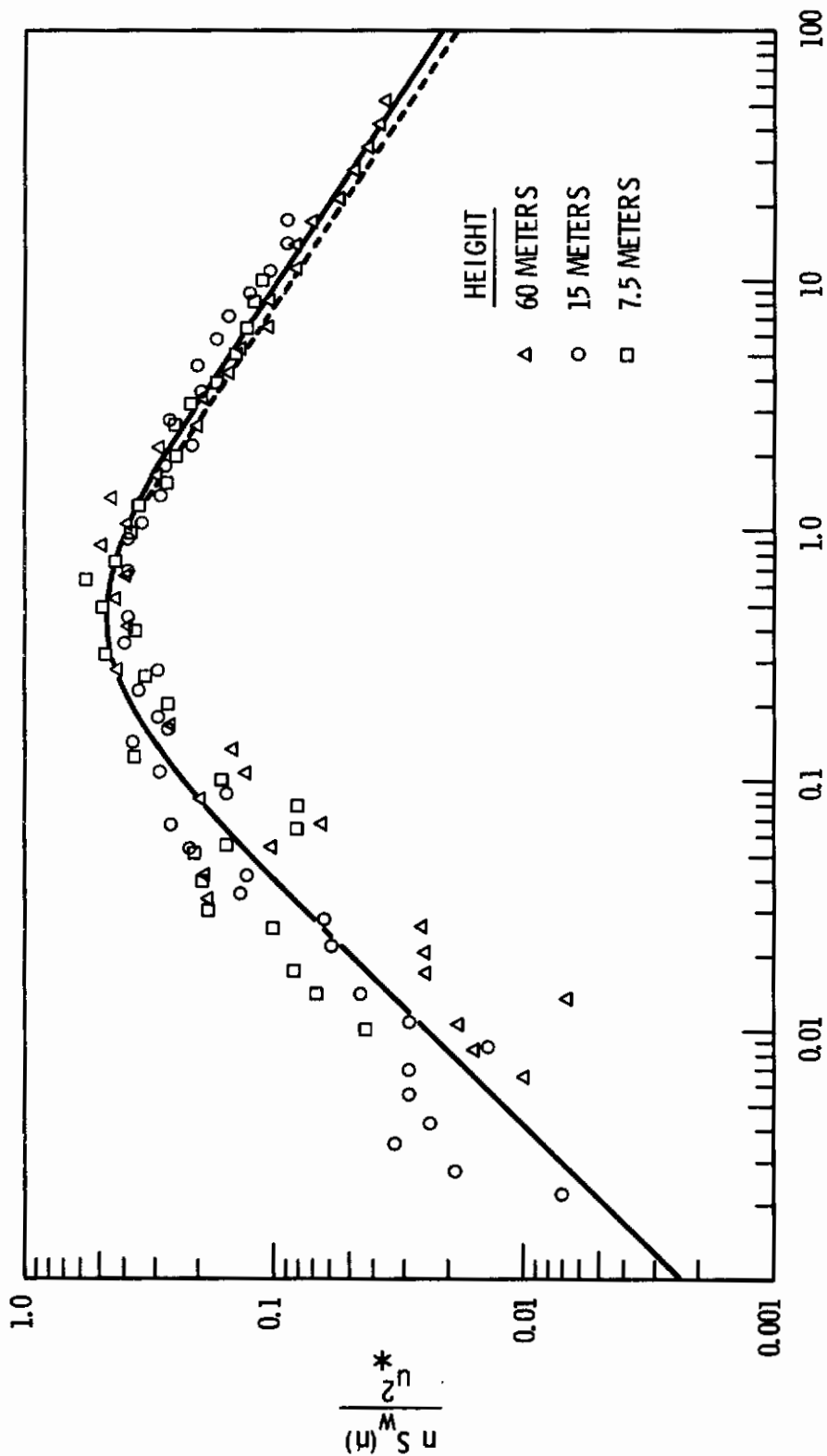


Figure 7.25 Nondimensional w' Spectra for 3 Heights - Neutral Case

stability factor defined in Equation 7.5 was used and  $\phi_m$  was calculated from  $z/L$  by using the curve given in Reference 2.6 relating these two quantities. These data also organize well using  $f_w = 0.46$ . However, at 60-meter height, the spectral peaks fell below the model for the unstable cases and the lowest frequency spectral estimates dropped off more rapidly for the 60-meter stable case than the model estimated. The agreement with Kolmogoroff's law was again quite good.

The character of the roughness elements at the Hanford site should also be mentioned. These roughness elements, scattered sagebrush plants and clumps of desert grasses, are of two orders of magnitude. These elements constitute the lower boundary condition of the flow field, and eddies will be generated at the surface with dimensions corresponding to the dimensions of the roughness elements. For the first few meters above the nominal 1-meter height of the sagebrush, the turbulence will be influenced by these elements. This complication is not part of spectral models conceived in harmony with the Monin-Obukhov similarity theory.

Similarly, when roughness elements in the vicinity of a site of concern include large terrain features or clusters of buildings, the modification of the lower boundary may be profound, and the deviation of the spectra from accepted models based on measurements taken elsewhere may be significant at flight levels. The need for more onsite measuring is clearly indicated for these cases.

### Horizontal Component Models

Corresponding constants can be determined for applying an equation of the form of Equation 7.6 to the longitudinal component; however, the reasoning applied in the Hanford analysis was different from that used by other investigators (Reference 4.3). The longitudinal component spectrum peak is usually considered to move to lower frequencies nonlinearly with height. In the Hanford spectra, however, two peaks were identified which were treated separately.



Figure 7.26 shows dimensional longitudinal spectra from Test E508 from four heights. The obvious features of the spectra include:

- A high frequency portion that requires organizing as a function of height. Note that the tops of the curves are further to the right for the lower heights.
- A low frequency portion that is approximately the same at all heights and requires no reorganizing.
- A narrow gap between the two regions at 0.01 Hz.

The gap at 0.01 Hz is not peculiar to Test E508. It can also be seen in the TOLCAT tests reported in the Interim Report; (see Figures 8.6 and 8.56 in that report).

The common peak in the low frequency portion of these spectra is regarded as derivative from variations in the horizontal wind that are approximately the same at all heights of measurement. These fluctuations may vary considerably from one test period to another, and cannot be modeled by the same physical reasoning that applies to the turbulence proper, seen in the high frequency peak. While this feature may be peculiar to Hanford, longitudinal spectra from other sites should be examined carefully to see if the double peaks are also present, but are being smoothed through in analysis and resulting in the nonlinear dependence on height for the single "smoothed" peak.

The modeling of the longitudinal component spectrum is therefore confined to the high frequency, height dependent peaks and the slopes to the right. Using these spectral regions, a value of 3.00 was determined for  $K_u$ , and 0.056 for  $f_u$ . When these values for  $K_u$  and  $f_u$  are inserted into Equation 7.6, the spectral values shown in the inertial subrange differ from calculations using Kolmogoroff's law (Equation 7.7 without the 4/3 factor, which does not apply to the longitudinal component) by less than 1 percent. The organization of the longitudinal spectra is shown in Figure 7.27.

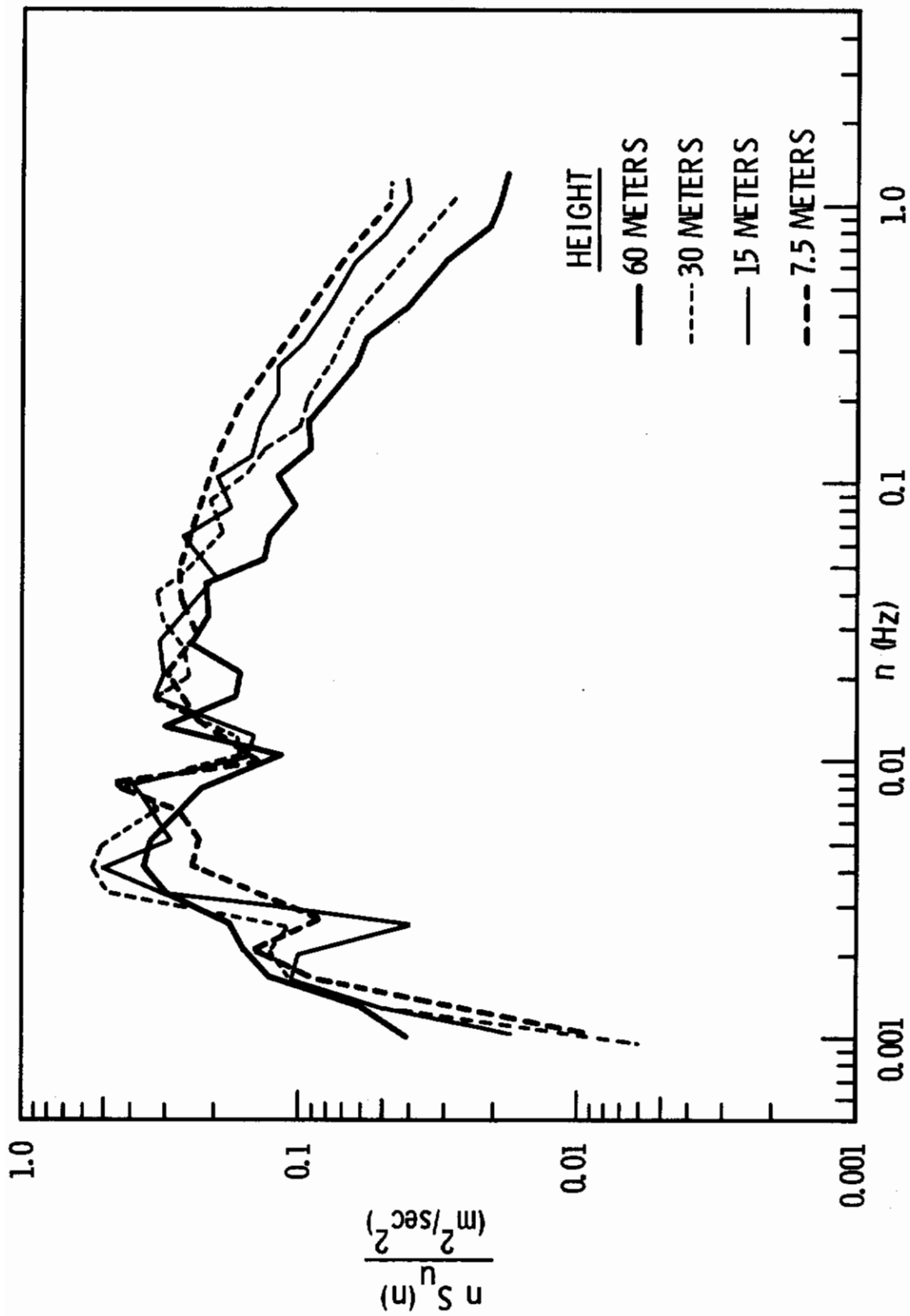


Figure 7.26 Dimensional u' Spectra for 4 Heights - Neutral Case

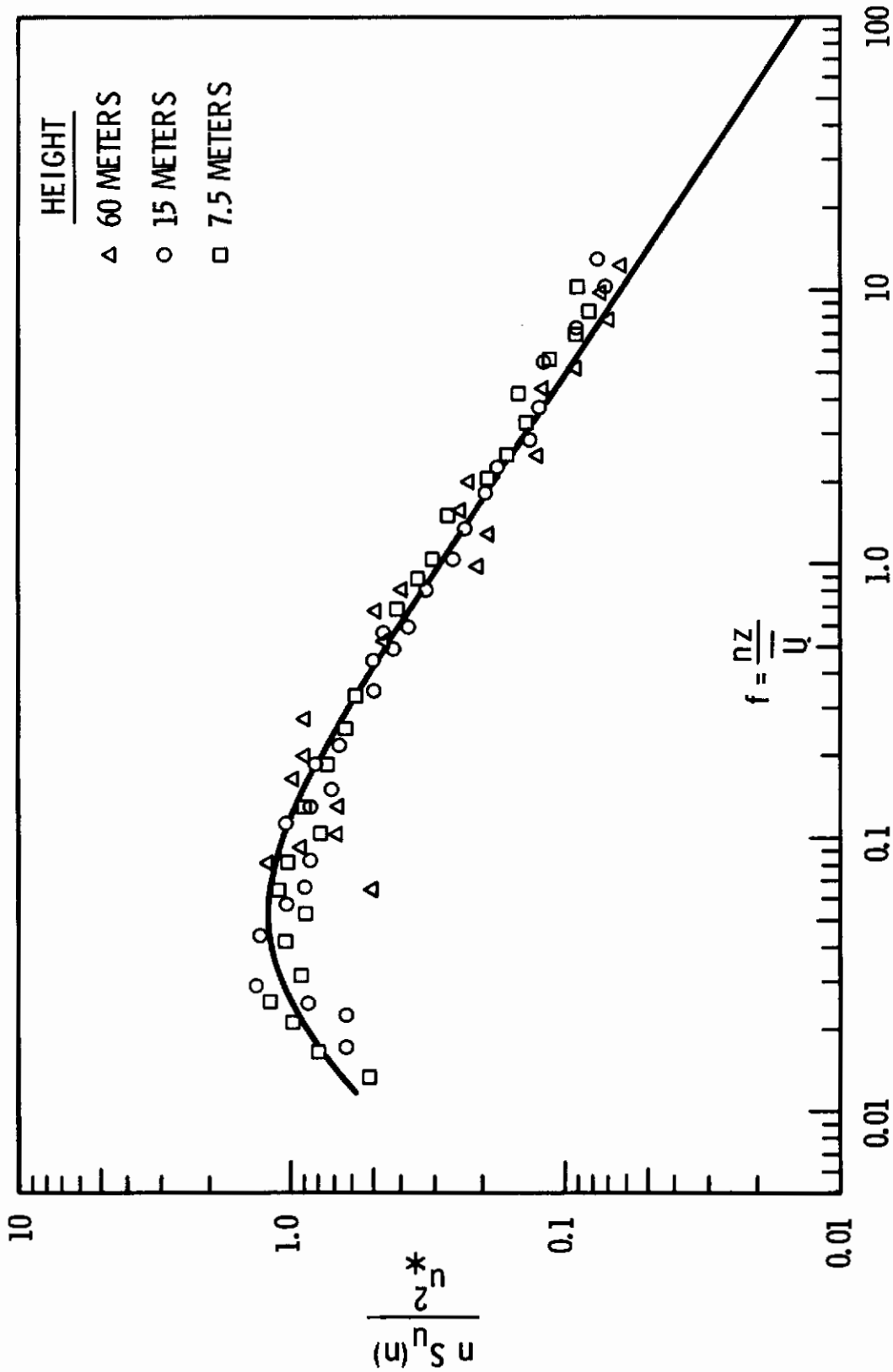


Figure 7.27 Nondimensional u' Spectra for 3 Heights - Neutral Case

Because horizontal deployment was maximized for the TOLCAT arrays, measurements of the fluxes of heat and momentum were not available from a fixed low level. Such measurements will be available from all future turbulence arrays, and are part of the recommended array for continuation of these studies.

However, a few general comments can be made. The vertical spectra from the 30-meter data were all notable in having large lower frequency projections above the model curve, when the right side of the curve is made to coincide with a probable extension of the Gill spectra into the inertial subrange.

Nondimensional power spectra,  $nS_1(n)$ , for the longitudinal and vertical components are shown in Figures 7.28 through 7.31, for the four tests, T603, T701, T703, and T704. The values of  $u^{*2}$  and  $\phi_m$  used for normalizing are given in Table 7.11.

TABLE 7.11

NORMALIZING PARAMETERS FOR FOUR TOLCAT TESTS

	T603	T701	T703	T704
$u^{*2}$ (m <sup>2</sup> sec <sup>-2</sup> )	0.22	0.67	0.18	0.81
$\bar{U}$ (m sec <sup>-1</sup> )	6.40	13.90	6.60	13.50
$\phi_m$	1.40	0.83	0.72	0.85

The computations of  $\phi_m$  were facilitated by calculating the Monin-Obukhov L using gradients according to Equation 7.3, using  $K_h/K_m$  as 1.3.

For Test T603, at 15 meters, the fit for  $u'$  is quite good, although the  $w'$  spectrum is well to the left of its model. In general, the three tests at 30 meters show better fits for  $u'$  than for  $w'$ , the latter spectrum always being slightly to the left of its model. This suggests the value of

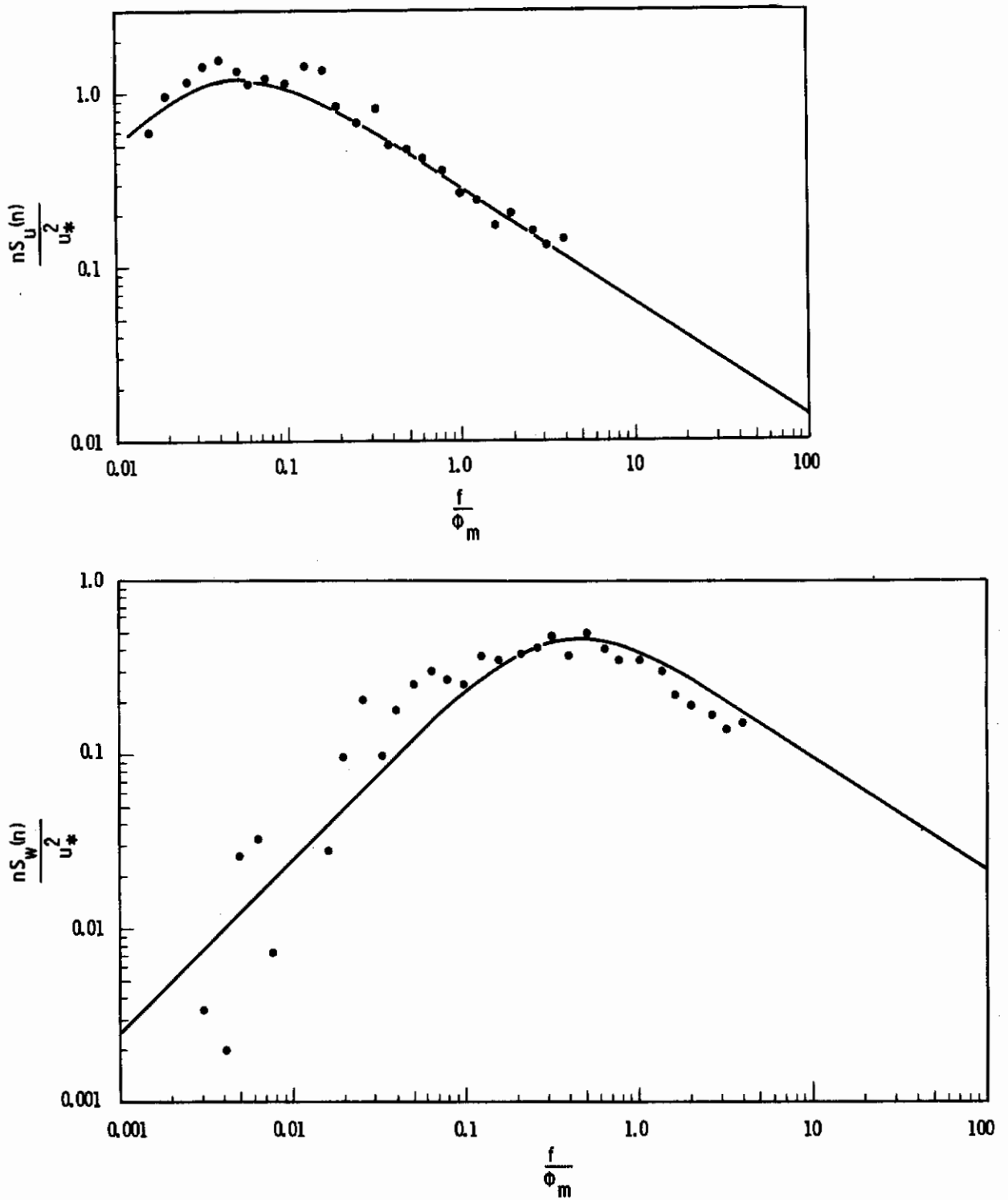


Figure 7.28 Nondimensional u' and w' Spectra, Test T603

# Contrails

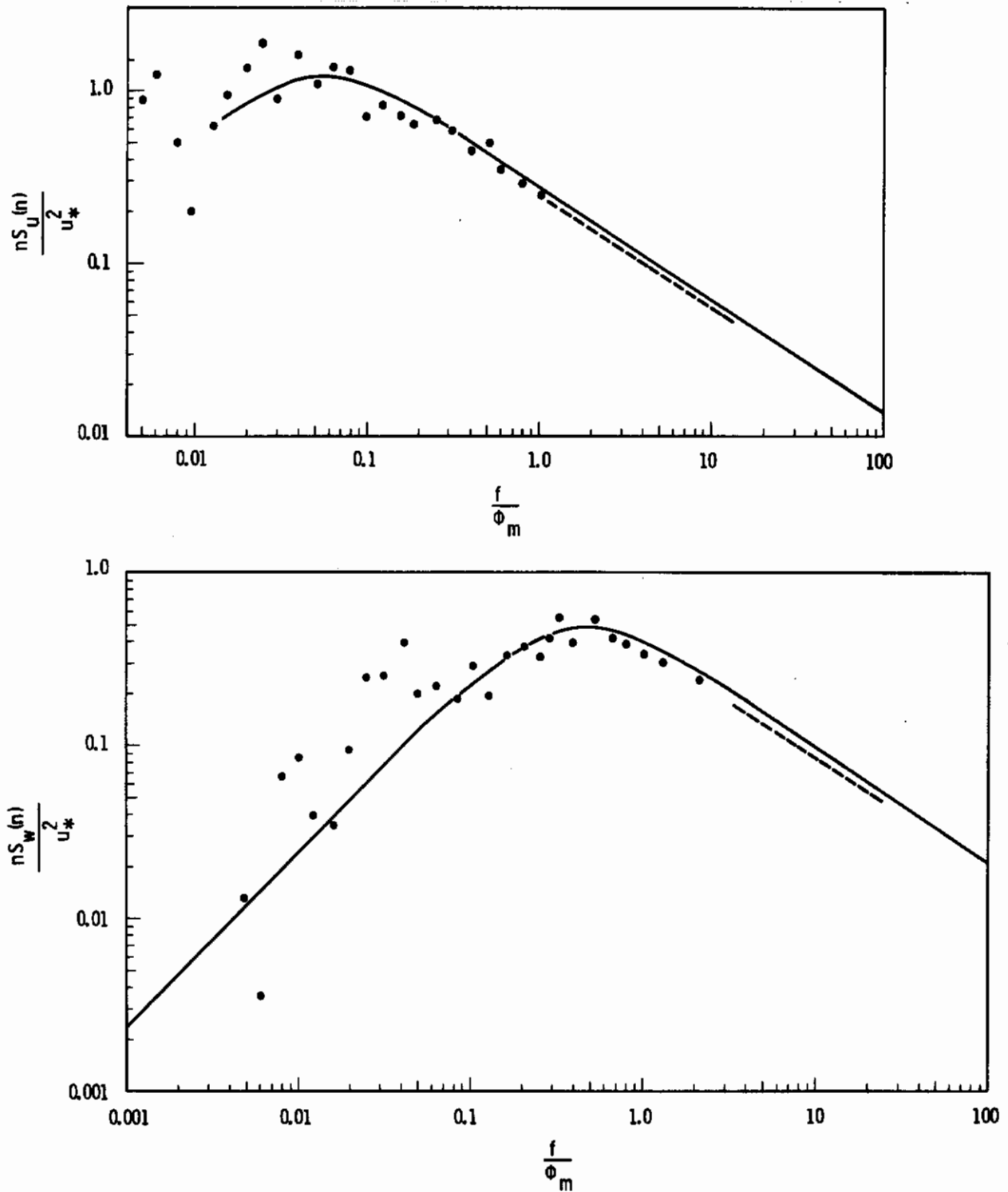


Figure 7.29 Nondimensional  $u'$  and  $w'$  Spectra, Test T701



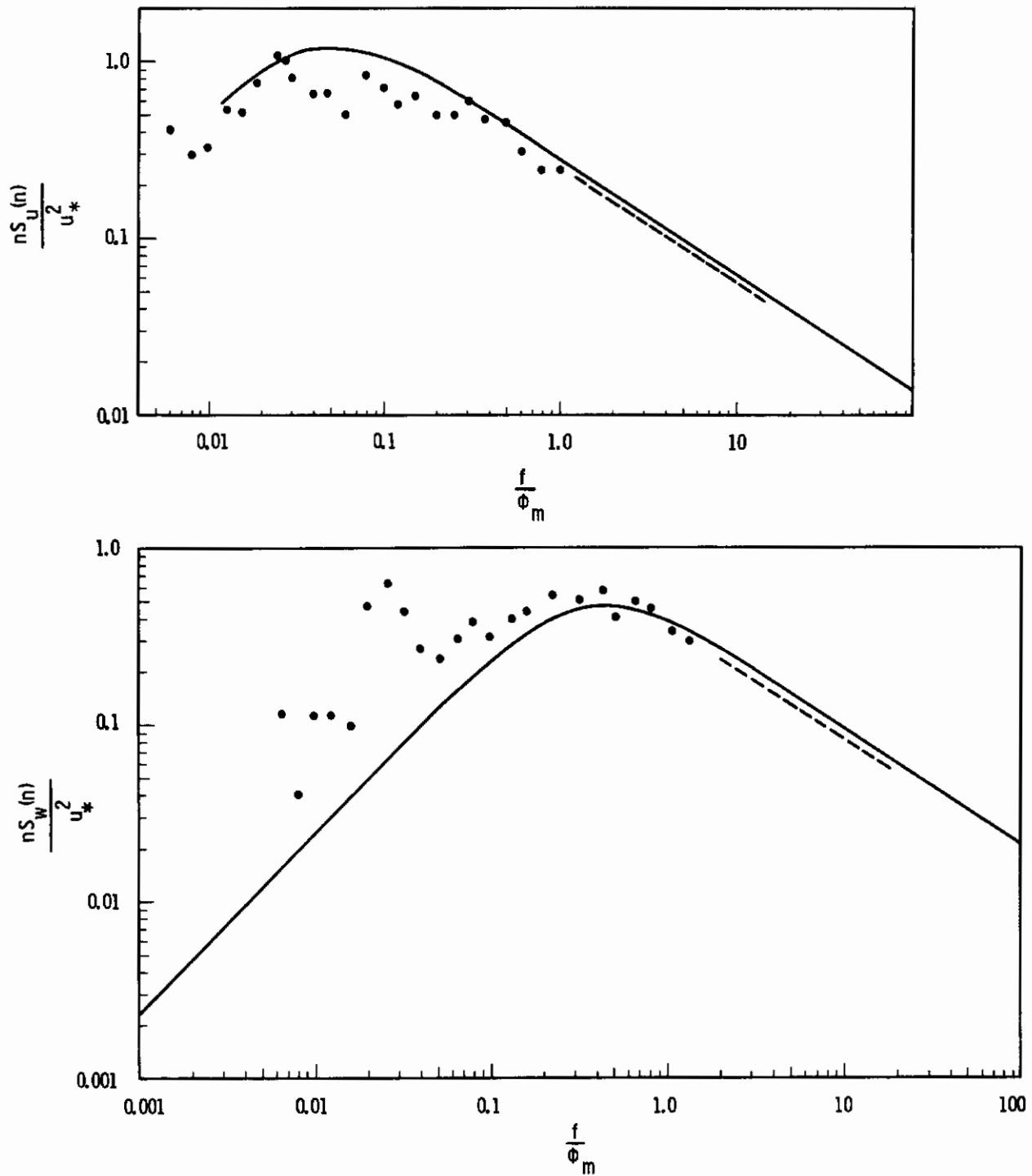


Figure 7.30 Nondimensional u' and w' Spectra, Test T703

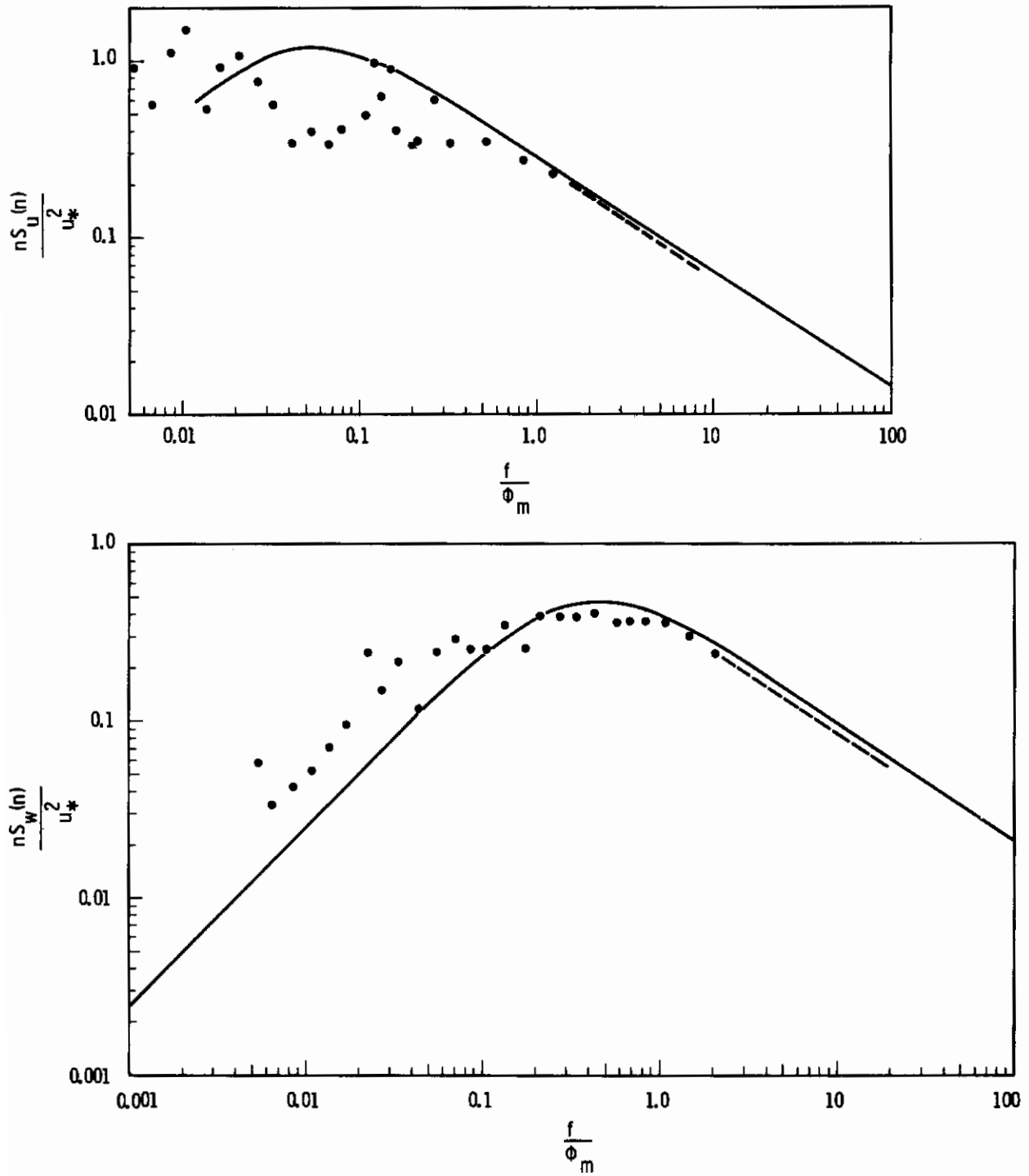


Figure 7.31 Nondimensional  $u'$  and  $w'$  Spectra, Test T704

0.46 for  $f_w$  calculated from summer data (AEC tests) may have been too high. A value of 0.35 for  $f_w$  would fit the TOLCAT data quite well. Another feature worthy of note is the extensive elevation of the low frequency part of the  $w'$  spectra above the model curve for the unstable tests. These peaks are at 0.02 Hz to 0.05 Hz, and probably represent convective activity beyond the scope of the model Equation 7.6.

The dashed lines on the right of the Gill data are extrapolations beyond the frequency region of accurate response of the Gill assuming the inertial subrange has been reached.

The spectra for the two TOLCAT tests at 131 meters that were analyzed are of special interest and are given in Figure 7.32. As expected at this elevation, the spectra show the greatest spectral energy at the lowest frequencies. In the inertial subrange, one test shows approximately the same energy for all components, while the other shows somewhat less energy for longitudinal components, as predicted by inertial subrange theory.

The lateral component spectra are the most difficult to model, chiefly because their flow frequency content varies more with the meander of the mean wind direction than does the longitudinal component. In the inertial subrange, the values of the lateral and vertical spectra should be  $4/3$  the values of the longitudinal spectrum. This feature has been observed, roughly, in 60 percent of the spectra examined.

In summary, it is emphasized that spectra from different sites having unusual surface features differ significantly. Onsite measurements are recommended for locations of concern for ascertaining spectral properties rather than depending on models of turbulence measured elsewhere. An example of such a site is in the vicinity of large buildings which could influence the statistical characteristics of the turbulence when the wind blows from the direction of the buildings toward the site of measurement.

# Contrails

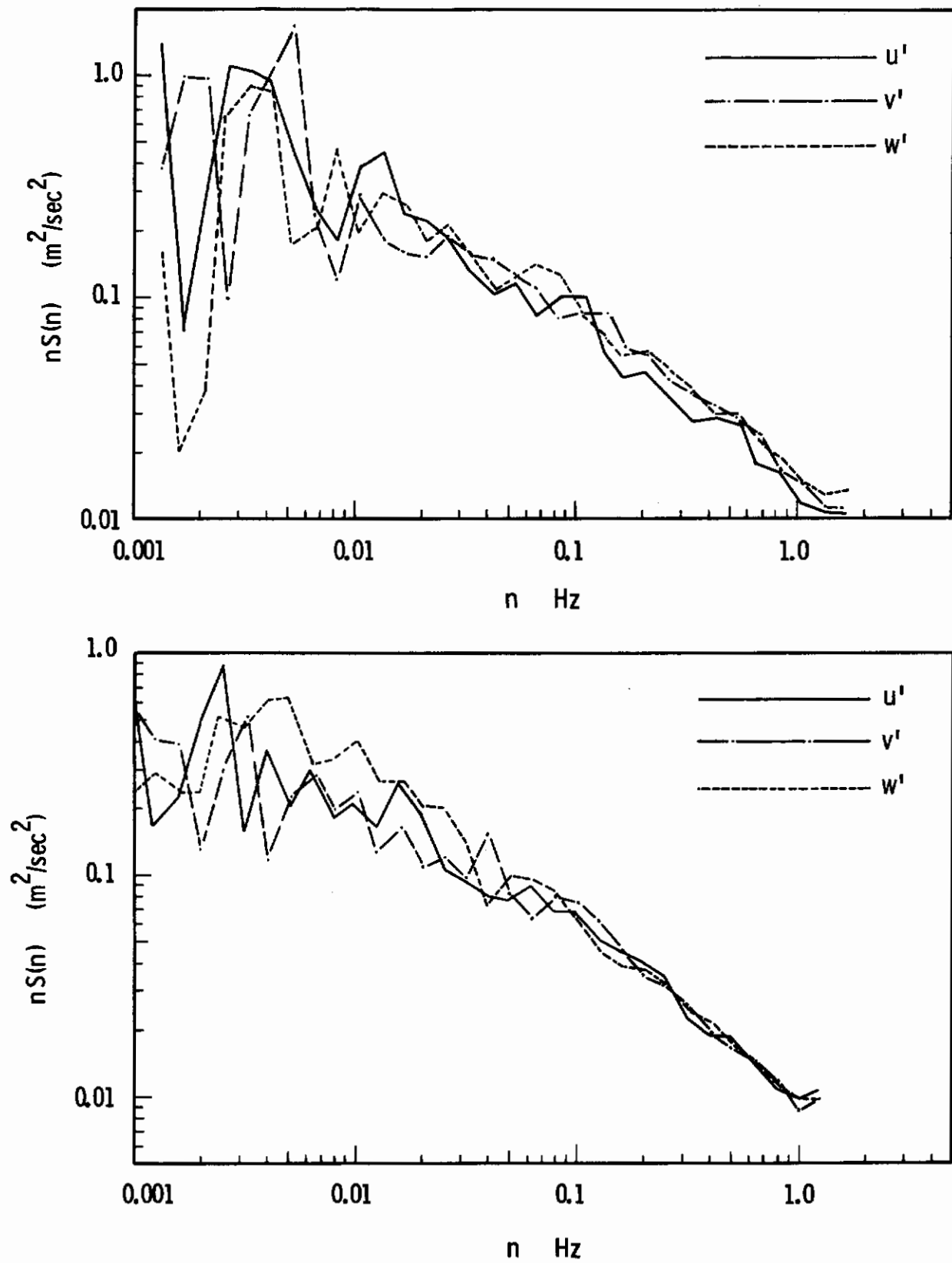


Figure 7.32 Power Spectra from Two Tests at 131 Meters

# Contrails

The cospectra and quadrature spectra corresponding to the phase spectra discussed in connection with Taylor's hypothesis are shown in Figures 7.33 through 7.38. Each of these spectra is for parallel components, i.e., for  $u'_a$  as measured at two locations or for  $v'_a$  or  $w'$  in the same manner. The data are for Test T603, for which the azimuth angle between the mean wind direction and the tower line direction was  $9^\circ$ , which is considered as essentially zero azimuth. The separation distance for which cross spectra were drawn on the graphs are 4, 8, 16, 32, and 64 meters.

These spectra are the Fourier transforms of the cross-correlation functions that were used to construct one of the space and time correlation graphs discussed later in this section.

Since it is known (Reference 7.6) that the covariance of cross spectral estimates about the "true cross spectrum" is a function of the power spectral content within both processes as well as the cross spectral content between the two processes, the values found in the first frequency decade of these spectra are of questionable statistical reliability. This is particularly true of the apparent quadrature spectral content for  $v'_a$  at frequencies in the lowest decade. Also, the cospectra showing close agreement for certain separation distances at low frequencies are of questionable meaning. For separation distances greater than 64 meters, both co- and quadrature spectra show a random large amplitude in the lowest frequency decade, putting these estimates still more in question.

As expected, the highest value for the cospectra are for the shortest separation distance. However, for the quadrature spectra, the highest values are for lags of 8 or 16 meters, if values within the lowest frequency decade are discounted. For separation distances greater than 16 meters both spectra drop off to lower values.

The maximum values for the quadrature spectra are expected to occur at frequencies inversely proportional to the separation distances. Although

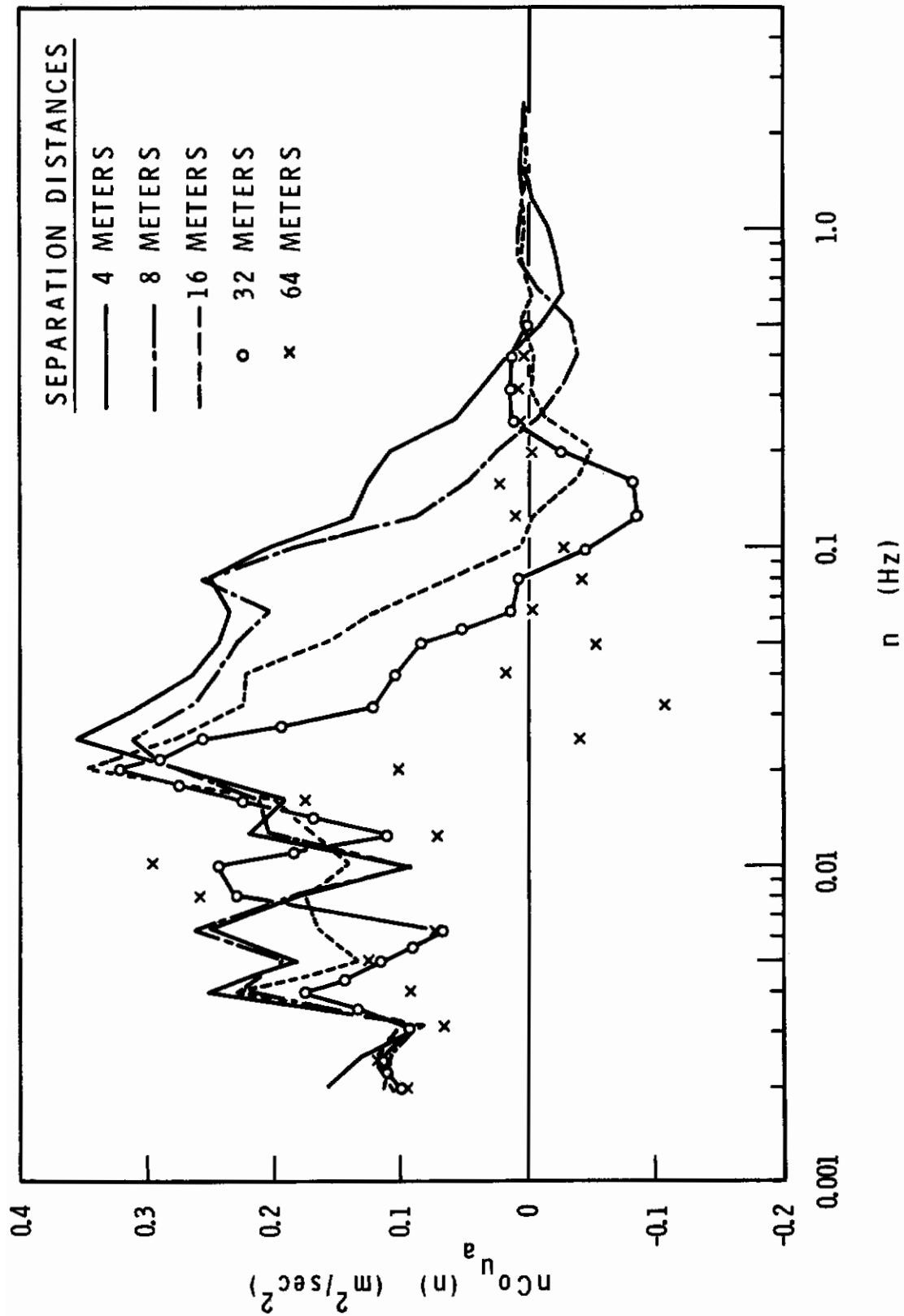


Figure 7.33 Cospectra for  $u'_a$ , Test T603



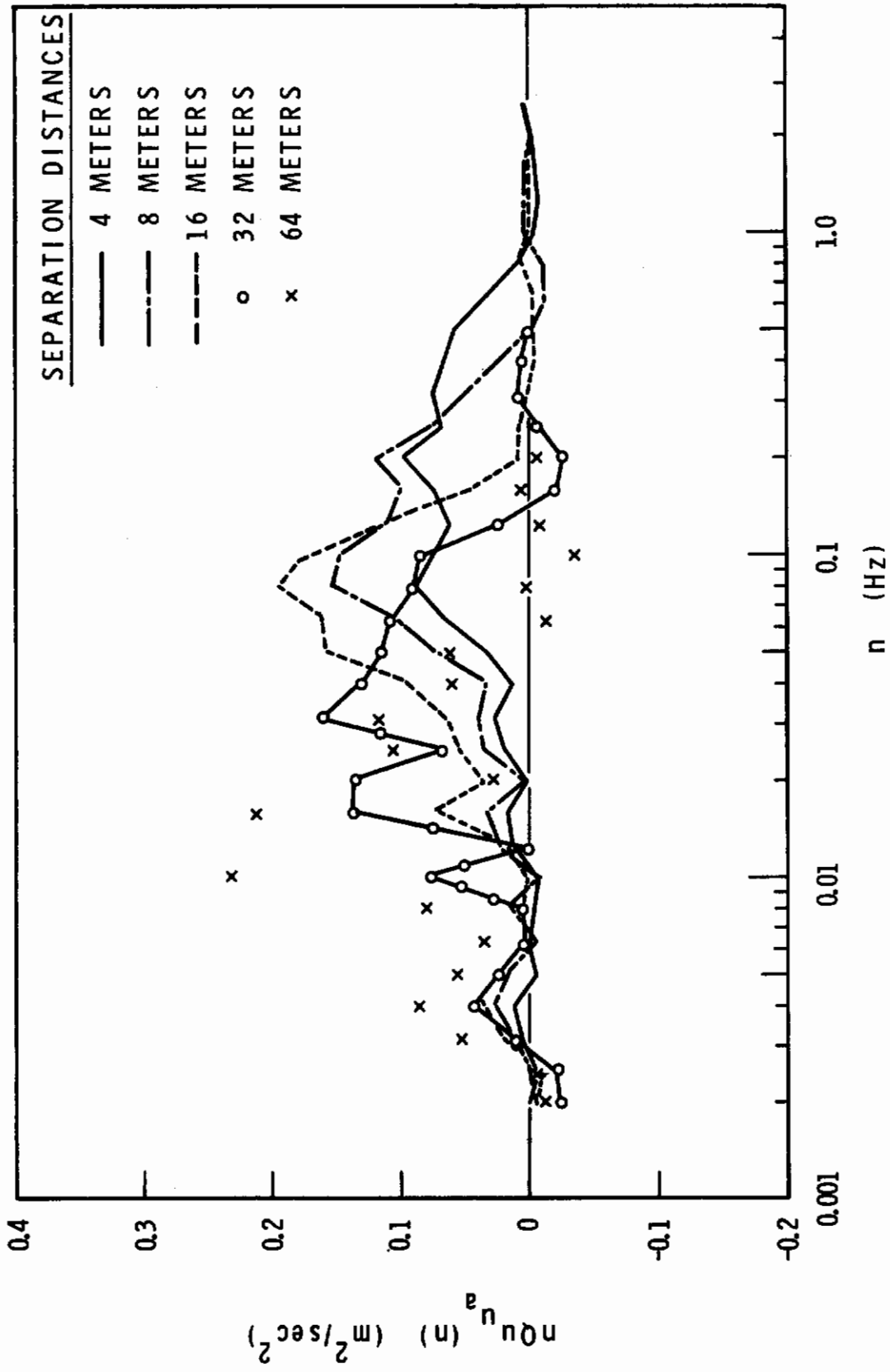


Figure 7.34 Quirature Spectra for  $u'_a$ , Test T603

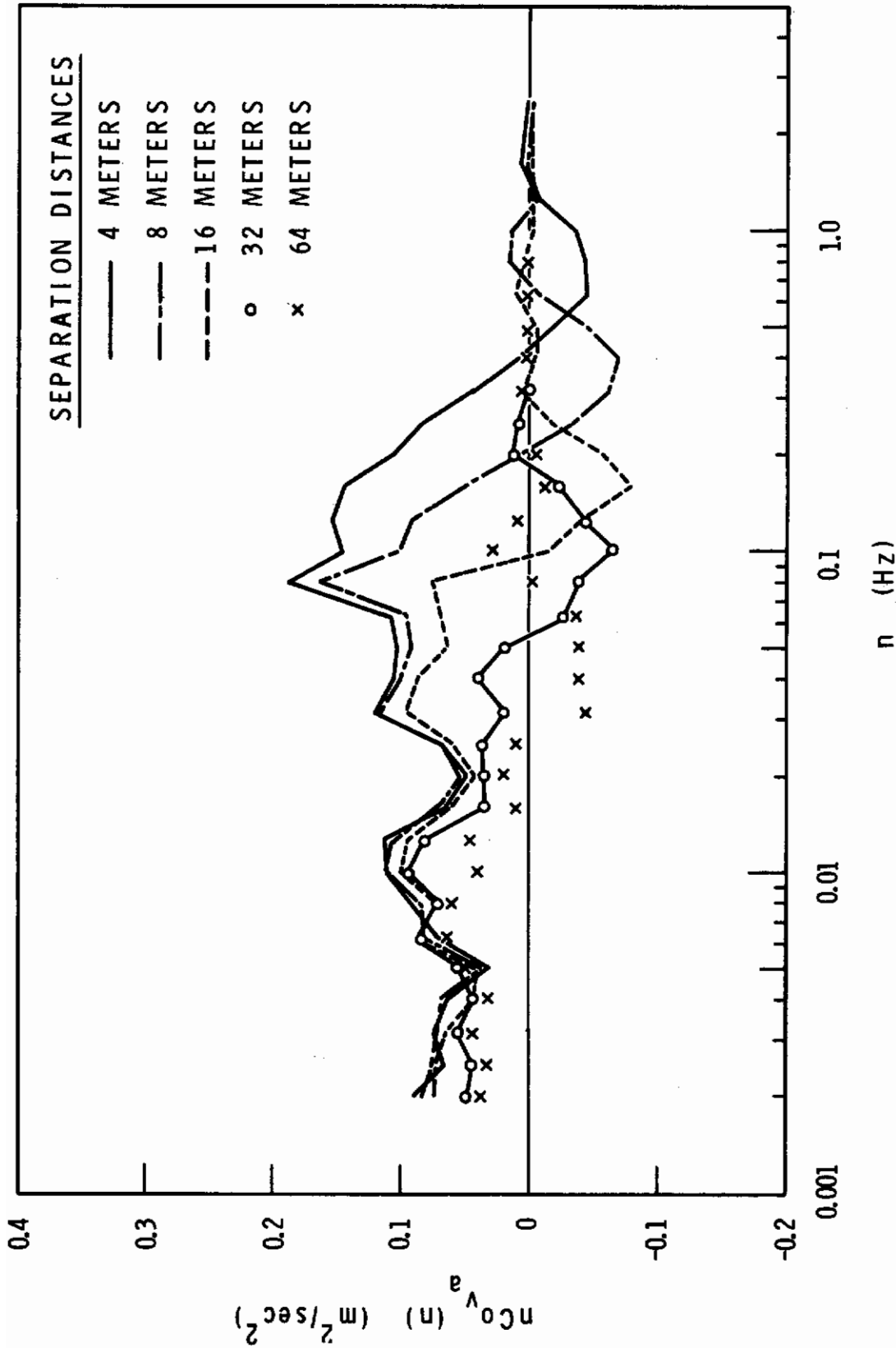


Figure 7.35 Cospectra for  $v'_a$ , Test T603

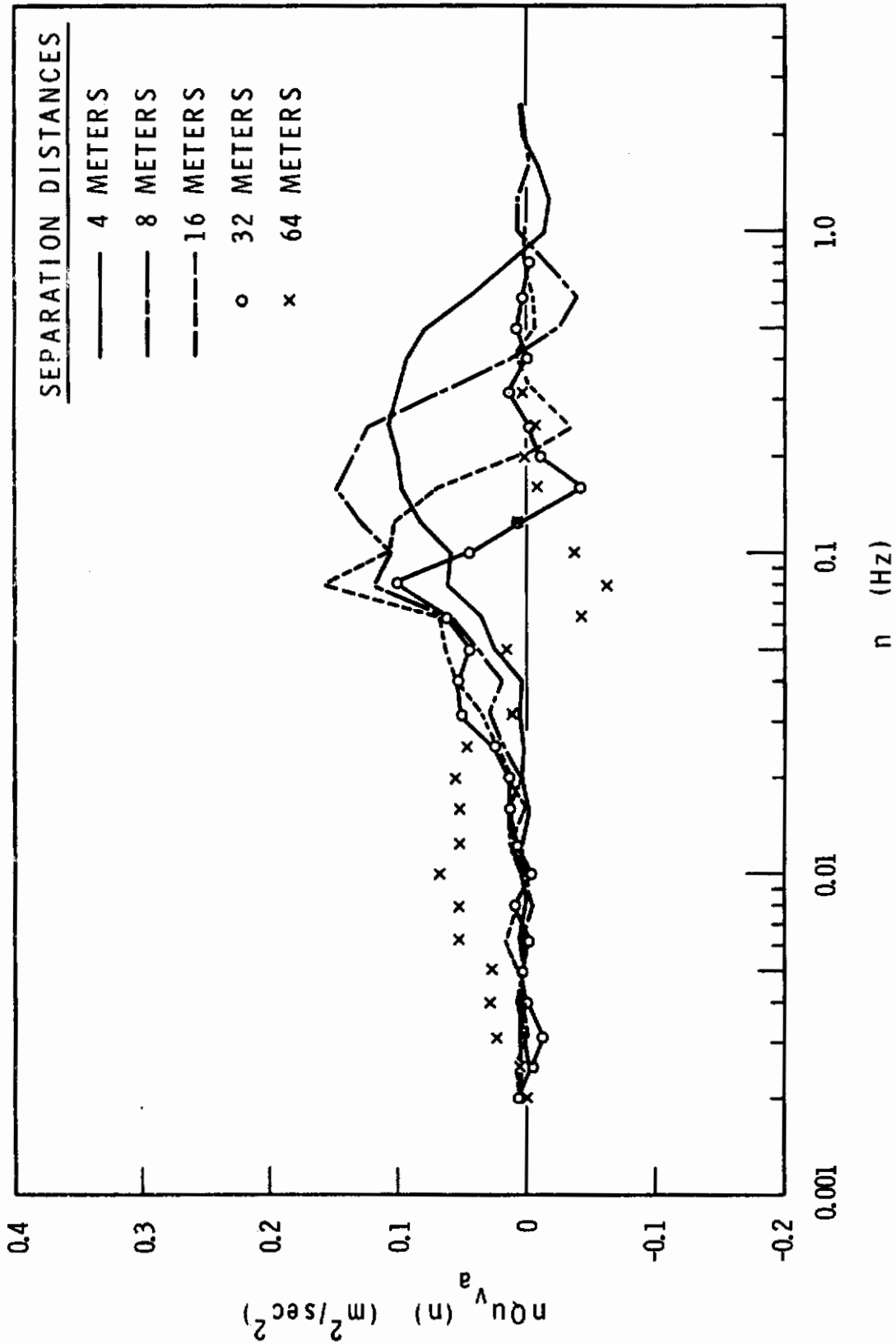


Figure 7.36 Quadrature Spectra for  $v'_a$ , Test T603

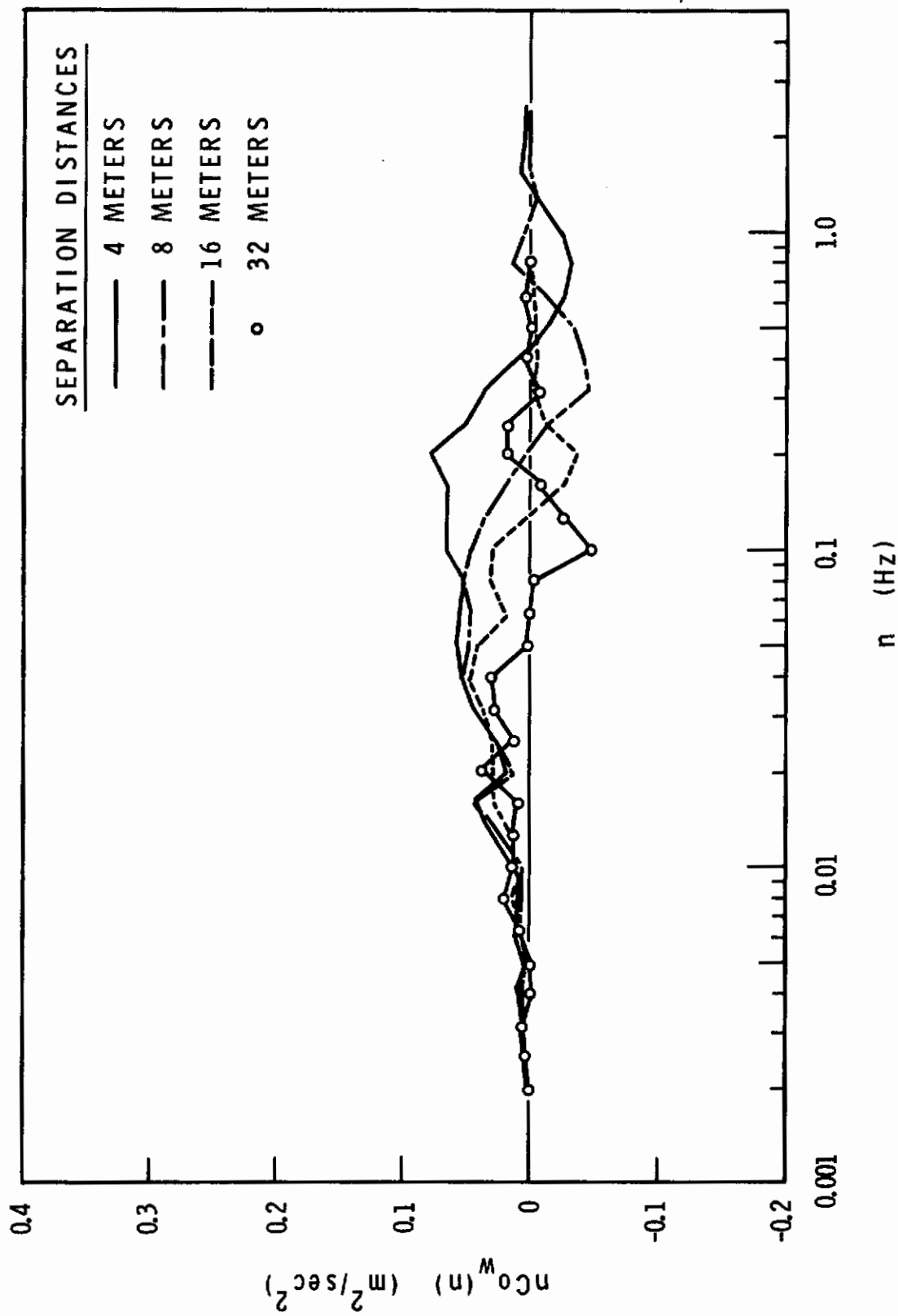


Figure 7.37 Cospectra for  $w'$ . Test T603

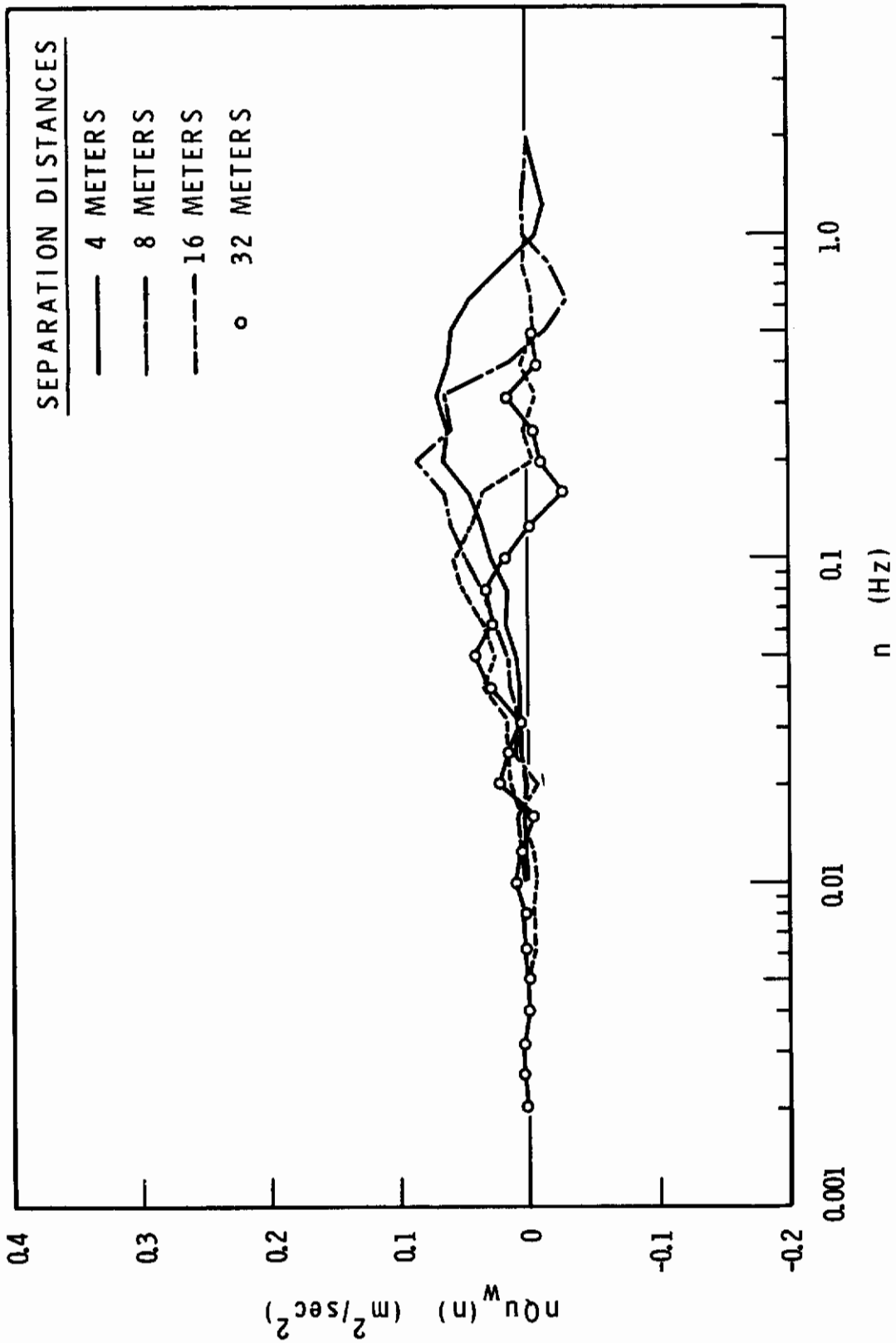


Figure 7.38 Quadrature Spectra for  $w'$ , Test T603

this tendency is observed, there are notable exceptions, namely, the occurrence of the maximum values in quadrature spectra for  $u'_a$  at 0.08 Hz for both 8 and 16-meter separation distances.

The graphs are presented to show that the analysis can be projected in this way. However, it was found that both phase and coherency spectral analyses and correlation functions in space in time were more revealing of atmospheric physics. Both of these analyses are discussed at some length within this section.

## CORRELATION ANALYSIS

The correlation functions  $R_{\alpha\alpha}(\tau)$  and  $R_{\alpha\alpha}(\xi)$  have already been compared previously in connection with testing Taylor's hypothesis. The present correlation analysis is concerned specifically with the form of  $R_{\alpha\alpha}(\tau)$  and with the correlation function of two arguments,  $R_{\alpha\alpha}(\tau, \xi)$ , which is given by

$$R_{\alpha\alpha}(\tau, \xi) = \overline{u_{\alpha}(t, x_0) u_{\alpha}(t+\tau, x_0+\xi)} \quad , \quad \alpha = 1, 2, 3 \quad . \quad (7.8)$$

The expectation indicated by the overscore is a time average. The data for the computation are for parallel wind components measured at two fixed locations separated by distance  $\xi$ . In the logarithmic array only one set of two towers are separated by a given space lag,  $\xi$ .

## Correlation Forms

Skelton (Reference 2.7) has proposed that the autocorrelation function for each of the three velocity components can be represented by a function such as

$$R_{\alpha\alpha}(\xi) = e^{-|\xi|/L_0} \cos(\kappa_0 \xi) \quad . \quad (7.9)$$



At this point, it seems appropriate to explain, even if heuristically, why the autocorrelation function for atmospheric wind components might approximate this form and also indicate how the final form may be the result of both general atmospheric behavior and deviations therefrom associated with winds at a particular location.

Intuitively, one would expect the autocorrelation function of a boundary layer velocity component time series to decay exponentially, while the reasons for the cosine factor are less obvious. To begin, one can observe that when

$$R_{\alpha\alpha}(\xi) = e^{-|\xi|/L_0} \quad , \quad (7.10)$$

the power spectral density from the Fourier transform relationship is

$$S_{\alpha\alpha}^*(\kappa) = 2u_{\alpha}u_{\alpha} \int_0^{\infty} e^{-\xi/L_0} \cos \kappa\xi \, d\xi = \frac{2L_0}{1+(\kappa L_0)^2} \quad . \quad (7.11)$$

This spectral function, commonly known as the Dryden spectrum, decreases proportionally to the second power of  $\kappa$  for large  $\kappa$  and approaches a 0 slope asymptotically for small  $\kappa$ . In other words, a plot of this spectral function on log-log paper would be a curve changing slope from two asymptotic slopes; 0 for small  $\kappa$ , and -2 for large  $\kappa$ . This differs from  $S_w(n)$  in Equation 7.6, which follows the -5/3 power for large  $n$ , as required by the Kolmogoroff theory for the inertial subrange. Therefore, although both the autocorrelation function and the spectral function in Equations 7.10 and 7.11 may be good engineering approximations, it is clear that neither fundamentally relate to atmospheric physics. The manner in which the exponential curve will compare with an experimental curve yielding a spectrum with a -5/3 slope will be shown later in this section when the experimental curves are discussed.

# Contrails

The  $L_0$  is a characteristic length associated with the decay of the autocorrelation function. The cosine factor in Equation 7.9 suggests the presence of another characteristic length in the turbulence — this time associated with the maximum eddy dimensions themselves, rather than with the decay of the autocorrelation function. It is possible that insight may be gained into the physical relevance of the cosine factor if the observation is first made that characteristic length scales are a property of filters as well as the turbulence and that the connection with the former is more fundamental than with the latter. To argue this point, one can first observe that turbulence, by its very definition as a process of nonlinear interaction between eddy sizes, is fundamentally antagonistic to characteristic lengths. In other words, the nonlinear interaction tends to spread the turbulence over a continuum of eddy sizes and to keep all these eddy sizes uncharacteristic or equally characteristic.

Therefore, when autocorrelation functions are found that follow a cosine curve, the presence of some kind of natural filter in the atmosphere is suggested. In order to associate the cosine term with a filter, one can suggest that the appearance of a damped cosine wave in an autocorrelation function is similar to the function  $(\sin \xi)/\xi$ , which differs only by a scale factor from the Fourier transform of a high pass block filter of length  $2\xi$ .

If the autocorrelation function for only the vertical component exhibits,  $(\sin \xi)/\xi$  factor, the height above the boundary would be a candidate for the characteristic length. On the other hand, if the  $(\sin \xi)/\xi$  factor is found chiefly in the two lateral components, a different interpretation is suggested in view of the turbulence energy equations for  $\overline{u'^2}$ ,  $\overline{v'^2}$ , and  $\overline{w'^2}$ . These equations show that turbulence energy created by interaction between the turbulent stress and the vertical shear of the mean horizontal wind enters directly into  $\overline{u'^2}$  only, and that the turbulence energy in the two lateral components is transferred from the longitudinal turbulence energy by means of a physical mechanism known as pressure-velocity correlations. If

this transfer mechanism is of the nature of a high pass filter, the influence of the  $(\sin \xi)/\xi$  factor should be evident primarily in the autocorrelation functions of the two lateral components. In this manner the apparent cosine wave in the autocorrelation function may be related to general atmospheric behavior, if future research bears out the connection.

On the other hand, the appearance of cosine waves in the autocorrelation function that damp out more slowly is associated with a local peak or spike in the spectrum, which would, of course, be connected with particular circumstances at the site of measurement. When wind passes over singular features of the lower boundary, eddies roughly of the dimensions of the singular feature are generated on the leeward side and propagate downwind. These could cause a peak in the spectrum and a cosine wave in the autocorrelation function that are associated with winds at the particular site when the wind is from a given direction.

To tie in all this discussion with turbulence as seen by aircraft, it can be pointed out that the band-pass nature of the aircraft in motion could very likely induce a stronger  $(\sin \xi)/\xi$  factor into the autocorrelation function of the turbulence as seen by the aircraft than any that pertain to the atmospheric turbulence locally. If so, the  $\kappa_0$  in Equation 7.9 for turbulence as seen by the aircraft may depend principally on the response characteristics of the aircraft flying at a particular speed.

### Effect of Nonstationarity on Correlation Values

When the same field velocity component data were analyzed both in raw form and then with the best fitting second order polynomial removed, it was demonstrated that the spectra and the autocorrelation functions are affected quite differently. The removal of energy was noticeable only up to about the eighth harmonic of the spectra, while the entire autocorrelation function was modified.

## Autocorrelation Analysis of Time Series, $R_{\alpha\alpha}(\tau)$

Autocorrelation functions for four of the tests were plotted, and periodic structure was definitely recognizable in the vertical component for all four tests. An example of this can be seen in Figures 7.39, 7.40, and 7.41 in which autocorrelation functions for the three components  $u'_a$ ,  $v'_a$ , and  $w'$  are shown with fitted curves of the form of Equation 7.10. (Since the angle made by the mean wind with the tower line was only  $9^\circ$ , the horizontal components can be considered as essentially equivalent to  $u'$  and  $v'$ .) The function for  $u'_a$  shows the least periodic structure; that for  $v'_a$  shows somewhat more; and that for  $w'$  shows considerably more. It is interesting to note that the first three local minima in the autocorrelation function for  $w'$  occur at 23, 40, and 57 seconds. Although the ratios between these numbers are not the ratios for minima of either  $\cos \tau$  or  $(\sin \tau)/\tau$ , they approach more closely those for the latter function, suggesting a natural filter effect rather than waves. Since the autocorrelation function for  $v'_a$  does not exhibit waves of the same period, it is suggested that the dominating natural filter working on each lateral velocity component is different — the height above the boundary being the principal factor for  $w'$  and the pressure-velocity correlations being a weak factor for  $v'_a$ , if a factor at all.

The autocorrelation functions from the other tests yield similar analyses. For Test E508, the autocorrelation function for  $v'$  did show stronger periodic organization, but still at a lower frequency than was the case for  $w'$  in the same test. Again this indicates that different natural filters dominate the transfer of turbulent energy to the separate lateral components.

The exponential curves fitted to the experimental curves are made to coincide at the point where  $R_{\alpha\alpha}(\tau)$  is equal to  $e^{-1}$ , or 0.368. Since the spectra for the exponential and experimental curves decrease according to the -2 and -5/3 power of the frequency, respectively, the experimental curve

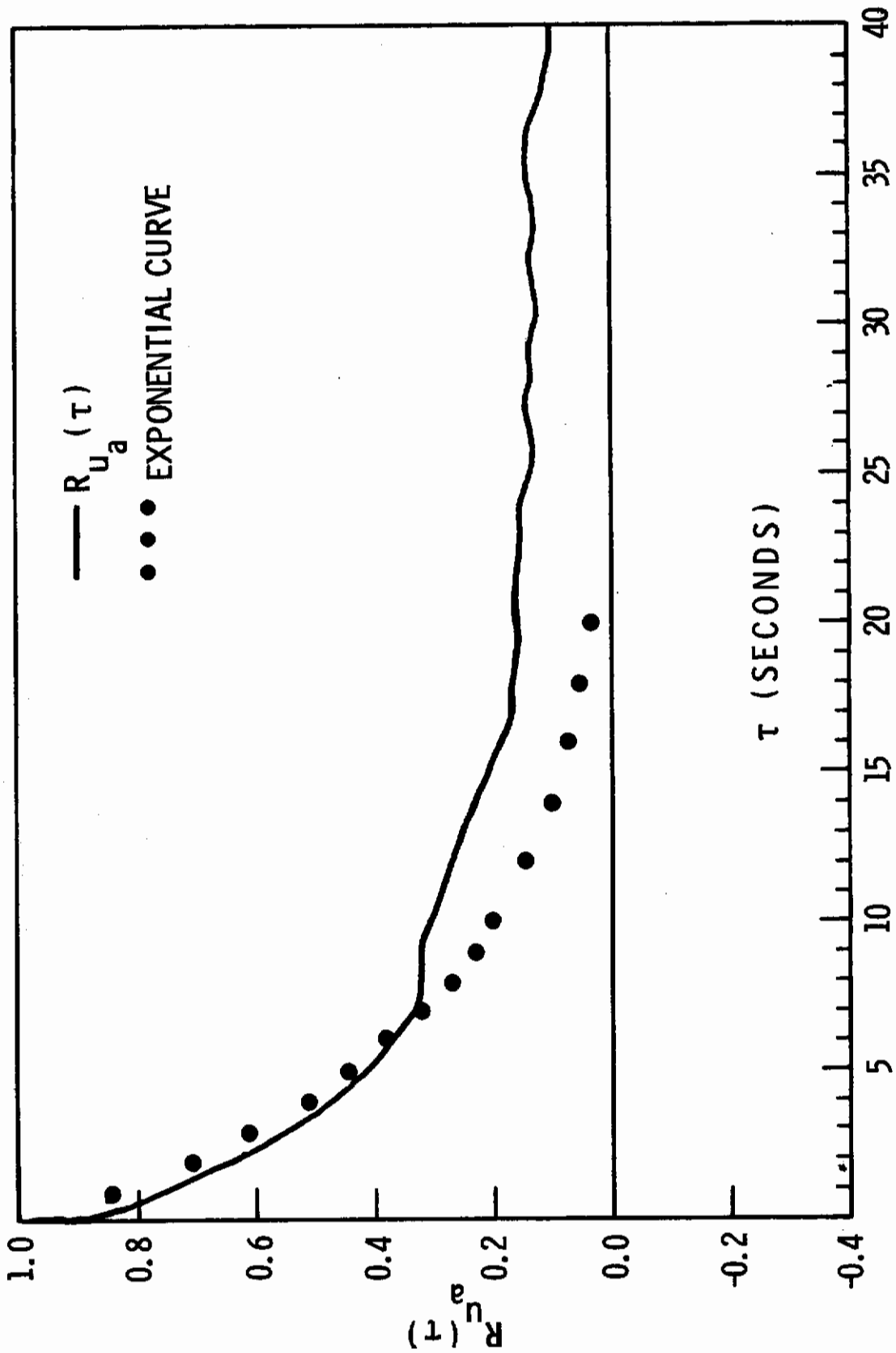


Figure 7.39 Autocorrelation Functions for  $u'_a$ , Test T603

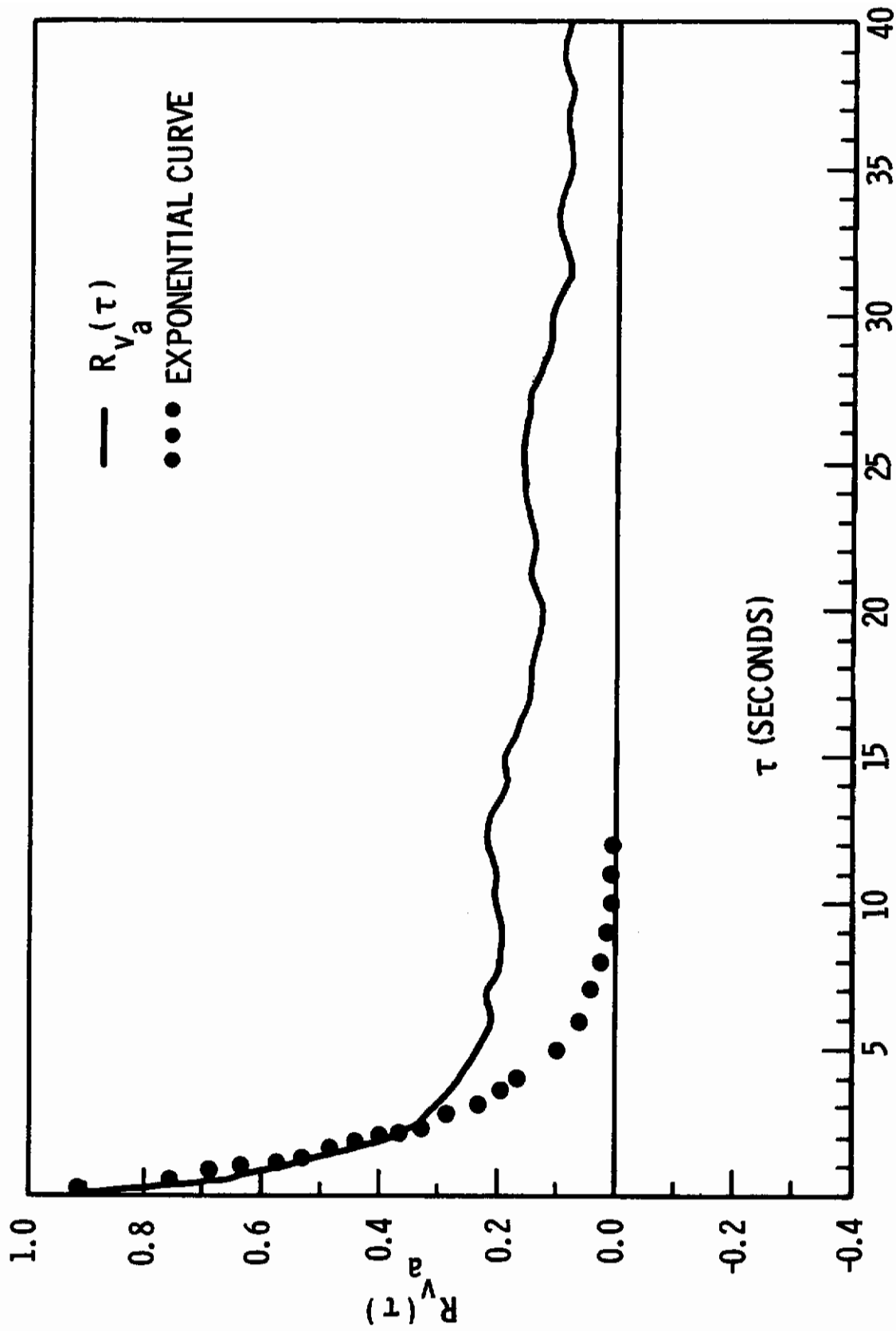


Figure 7.40 Autocorrelation Functions for  $v'_a$ , Test T603



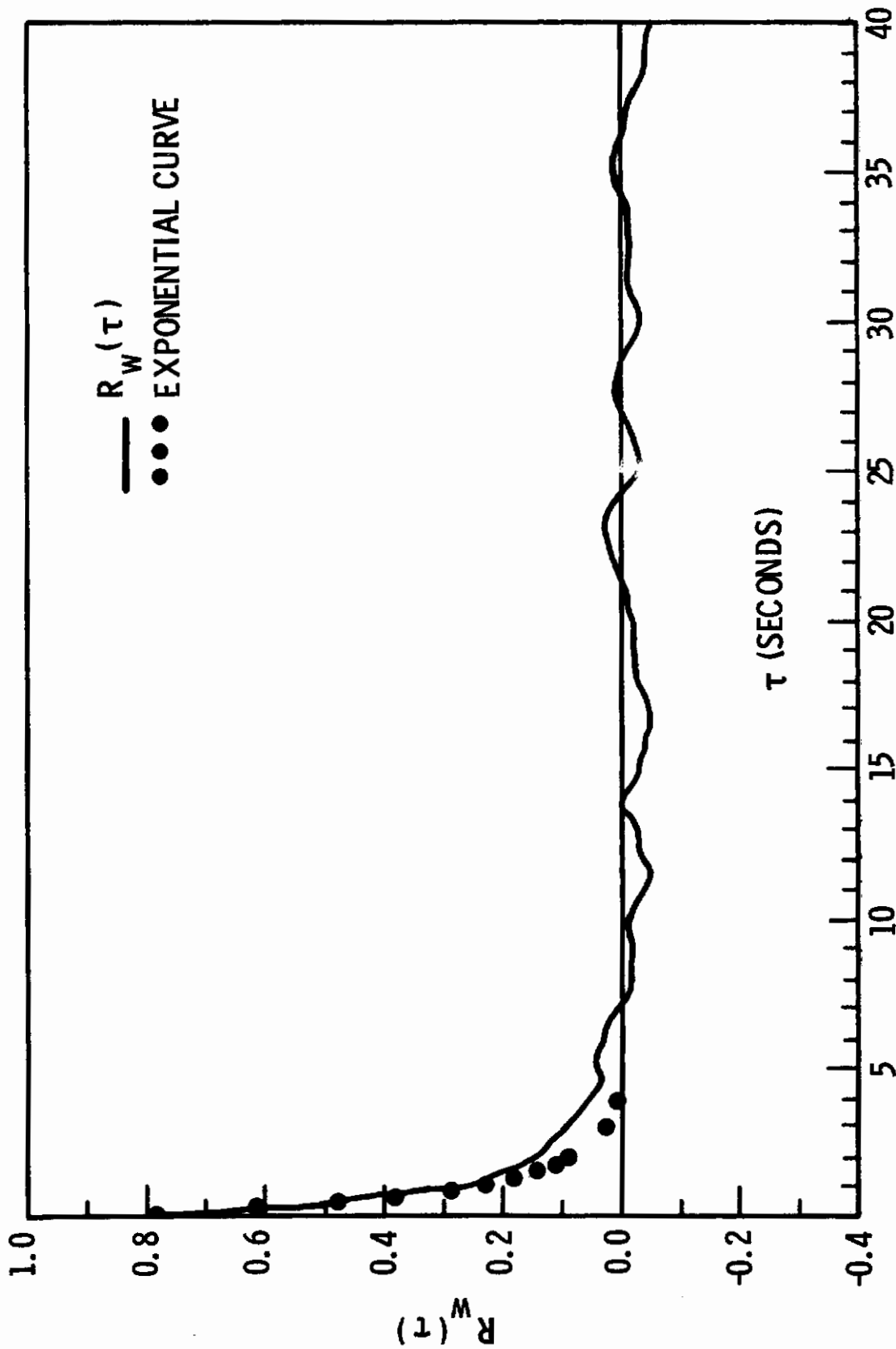


Figure 7.41 Autocorrelation Functions for  $w'$ , Test T603

represents turbulence with relatively more high frequency content and less low frequency content. Accordingly one would expect the experimental curve to descend more sharply from the origin and intersect the exponential curve from below, continuing above it at higher time lags, which is exactly what is seen in Figure 7.36, particularly for the two horizontal components.

The values of  $T_o$  and the length,  $L_o$ , obtained by multiplying  $T_o$  by  $\bar{U}$ , for the four tests considered, are given in Table 7.12. Again it is emphasized that these values are functions of sampling time and the interval,  $\Delta t$ , between successive data points.

TABLE 7.12

CHARACTERISTIC TIME AND LENGTH VALUES FROM AUTOCORRELATION FUNCTIONS

<u>Number</u>	<u>Height</u> (m)	<u><math>\Delta t</math></u>	<u><math>u'</math></u>		<u><math>v'</math></u>		<u><math>w'</math></u>	
			<u><math>T_o</math></u> (sec)	<u><math>L_o</math></u> (m)	<u><math>T_o</math></u> (sec)	<u><math>L_o</math></u> (m)	<u><math>T_o</math></u> (sec)	<u><math>L_o</math></u> (m)
E508	7.5	0.4	19.0	139	4.5	33	1.8	13
T603	15	0.2	6.2	40	2.2	14	0.82	5
T703	30	0.2	24.2	325	12.2	163	1.3	17
T805	131	0.4	73.6	262	81.2	292	31.6	114

### Correlations in Space and Time

By cross correlating at different time lags the parallel components measured at different sensors on the logarithmic line, examples of turbulence correlations in time and space, as expressed by Equation 7.8, may be obtained. This correlation is expected to be a function of stability, wind speed, wind direction, and height. It has been proposed by Skelton (Reference 2.7) that such graphs could provide one means of determining an estimate of the correlation functions experienced by aircraft flying at

different speeds and different azimuth angles with respect to the mean wind. Analysis of this type is also of interest for other concepts relating turbulence to diffusion and has been conducted on the TOLCAT data for these purposes in AEC sponsored research (Reference 7.7). These analyses are presented here and considered in connection with aircraft applications. Graphs for the three components for two tests, Test T603 and T704, are shown in Figures 7.42 through 7.47. In each case the two axes are scaled so that equal distances represent  $\tau$  and  $\xi$  when  $\xi = \bar{U}\tau$ . Therefore, when the wind direction is in the direction of or makes a small angle with the tower-line direction the isopleths should be approximately elliptical with their major axes along the line,  $\xi = \bar{U}\tau$ , which makes a  $45^\circ$  angle with the positive  $\tau$  and  $\xi$  axes.

During Test T603 the azimuth angle between the tower-line direction and the mean wind direction was only  $9^\circ$ ; therefore this test essentially represents the zero azimuth case. The graphs for  $u'_a$ ,  $v'_a$ , and  $w'$  are given in Figures 7.42, 7.43, and 7.44, respectively. All show elliptical contours with their major axes approximating the line  $\xi = \bar{U}\tau$ . The slope of major axes, especially for the higher correlations, is slightly greater than unity, indicating an effective eddy translation speed slightly greater than  $\bar{U}$ , as was earlier discussed in the section on Taylor's hypothesis. The eccentricity of the contours appears to be less for  $u'_a$  than for either of the other components.

Because of the mixture of sonic and Gill correlations some smoothing was done to remove features of the isopleths that were clearly due to this difference. Therefore, little can be said about the departures of the isopleths from elliptical shape.

The same data for T704 are shown in Figures 7.45, 7.46, and 7.47. Since the azimuth angle is approximately  $90^\circ$  ( $88.7^\circ$ ), the line  $\xi = \bar{U}\tau$  does not appear on these graphs since no elongation is expected except parallel to the time axis. The figures show that even the small departure of the

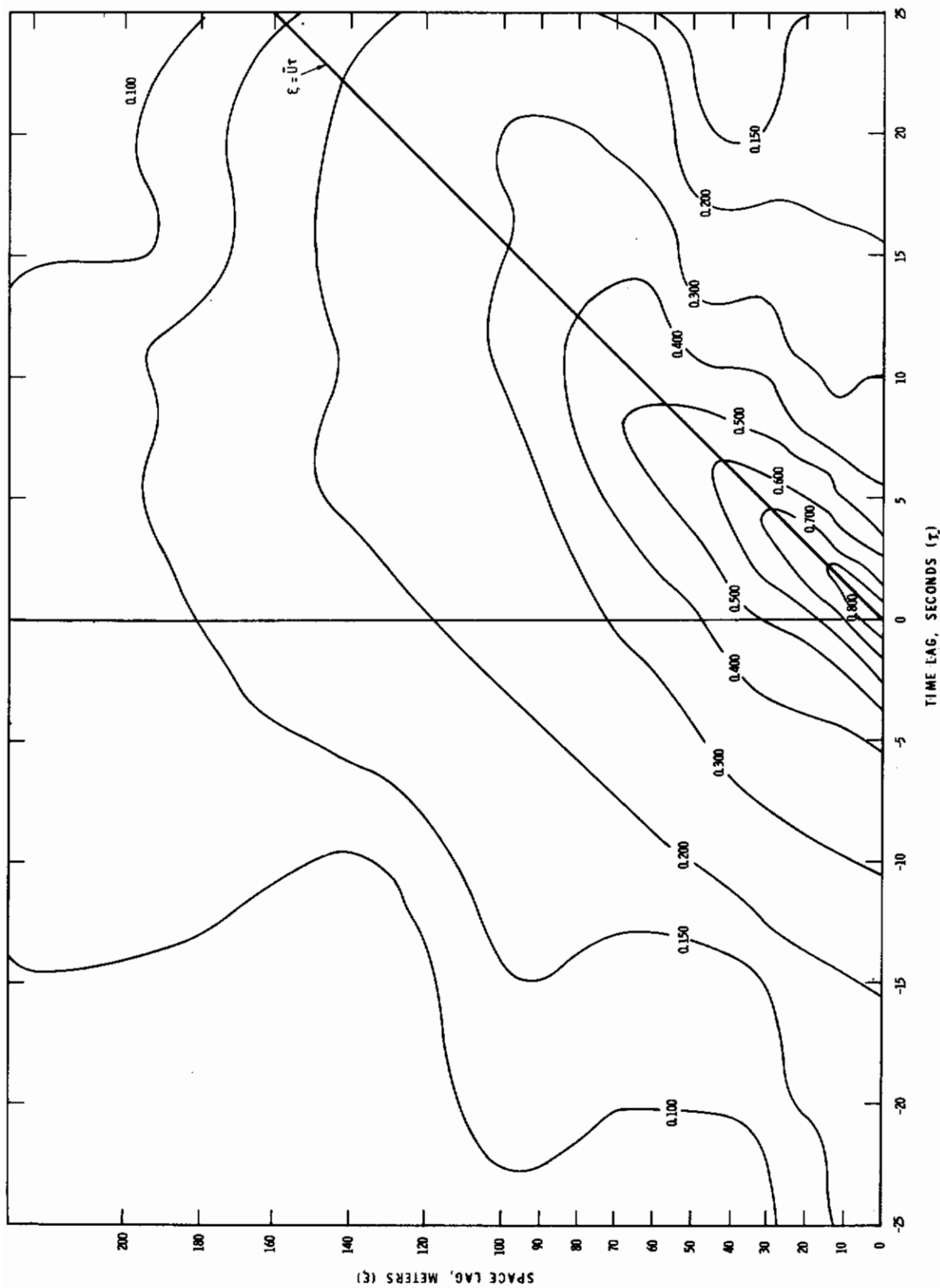


Figure 7.42 Two-Argument Autocorrelation Function of  $u'$  in Time and Space, Test T603

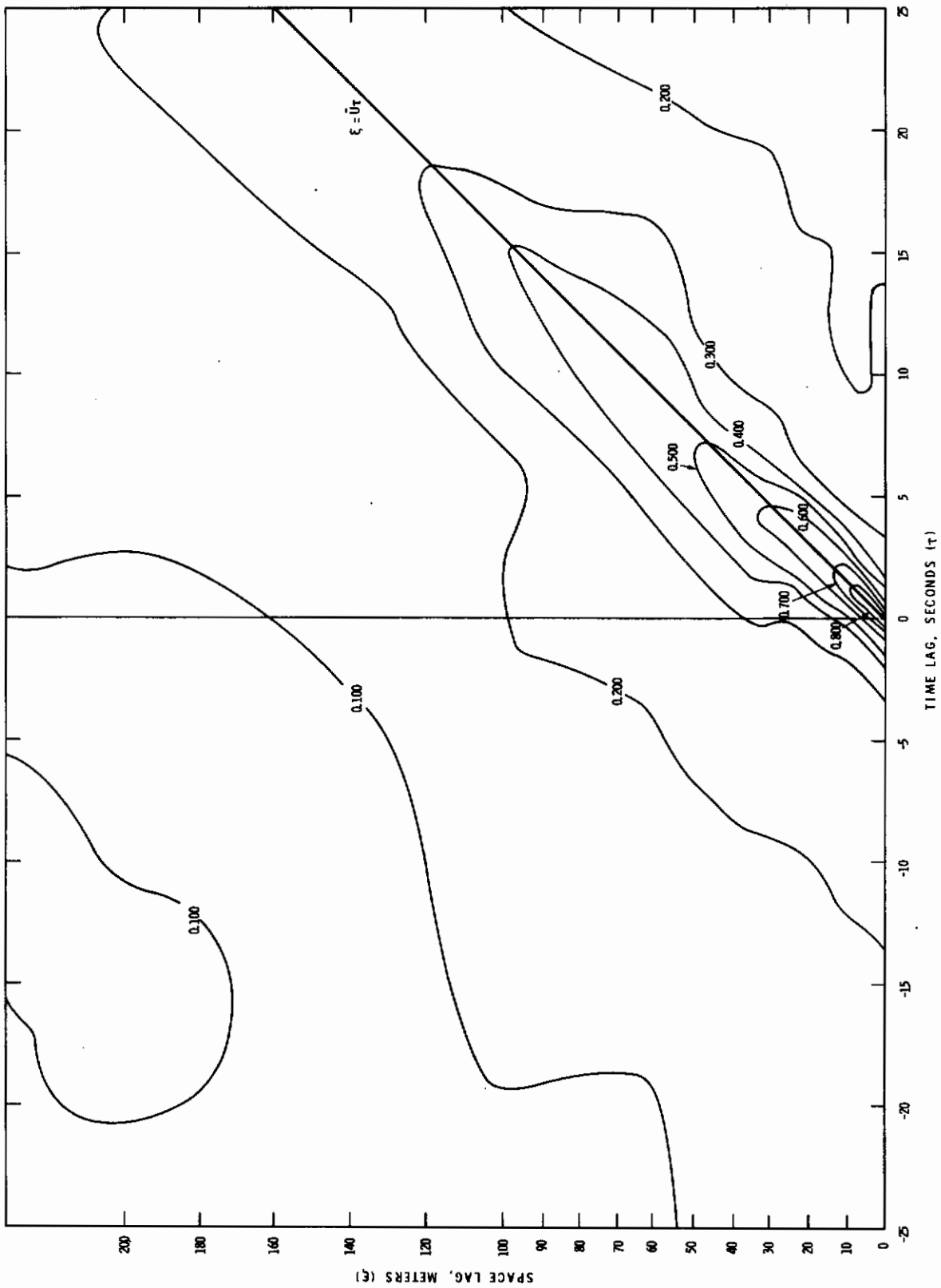


Figure 7.43 Two-Argument Autocorrelation Function of  $v'_a$  in Time and Space, Test T603

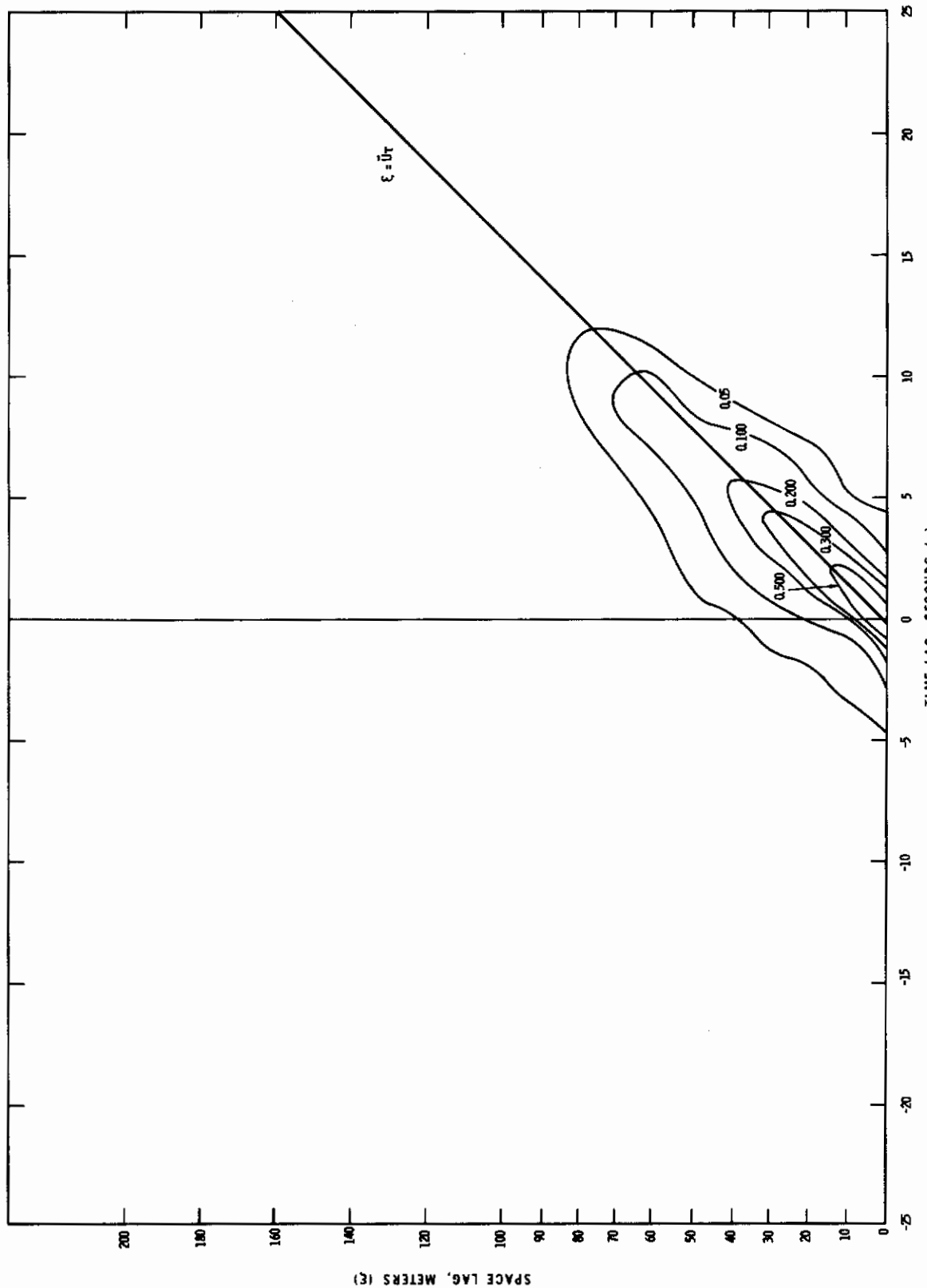


Figure 7.44 Two-Argument Autocorrelation Function of  $w'$  in Time and Space, Test T603



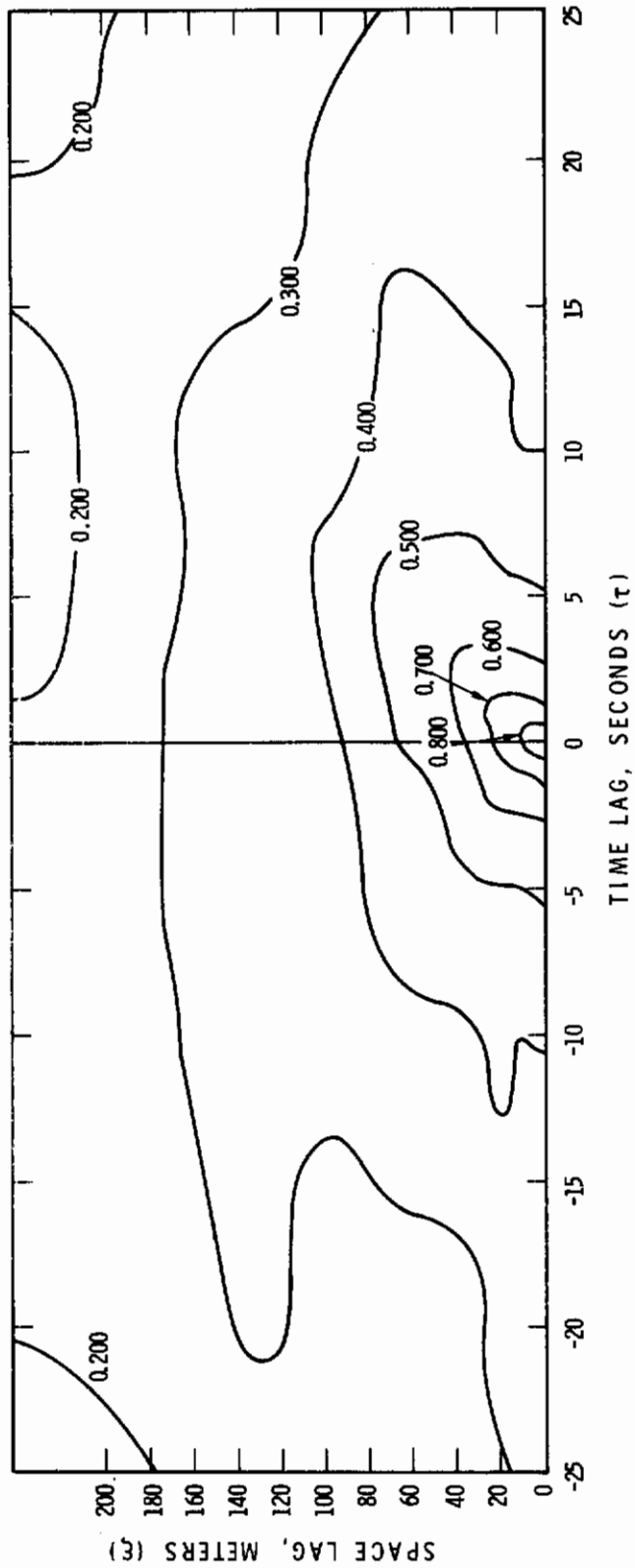


Figure 7.45 Two-Argument Autocorrelation Function of  $u'_a$  in Time and Space, Test T704

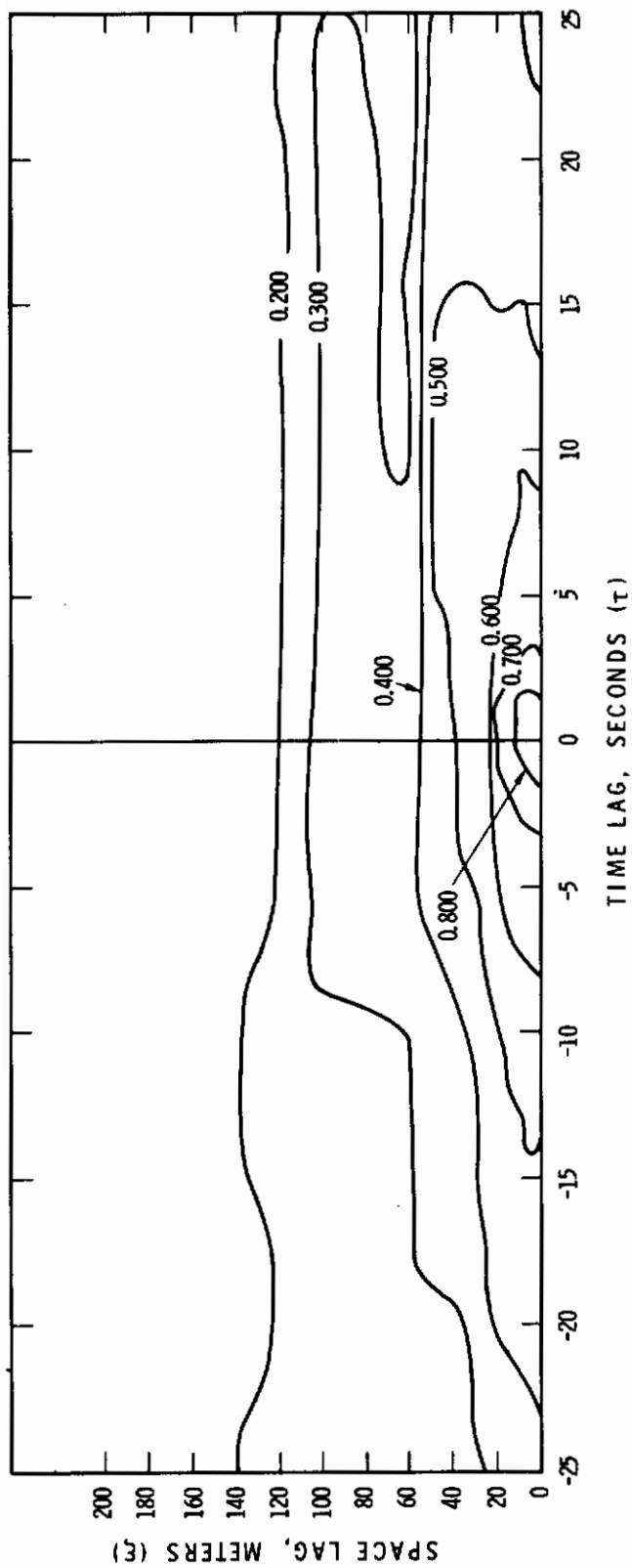


Figure 7.46 Two-Argument Autocorrelation Function of  $v'_a$  in Time and Space, Test T704

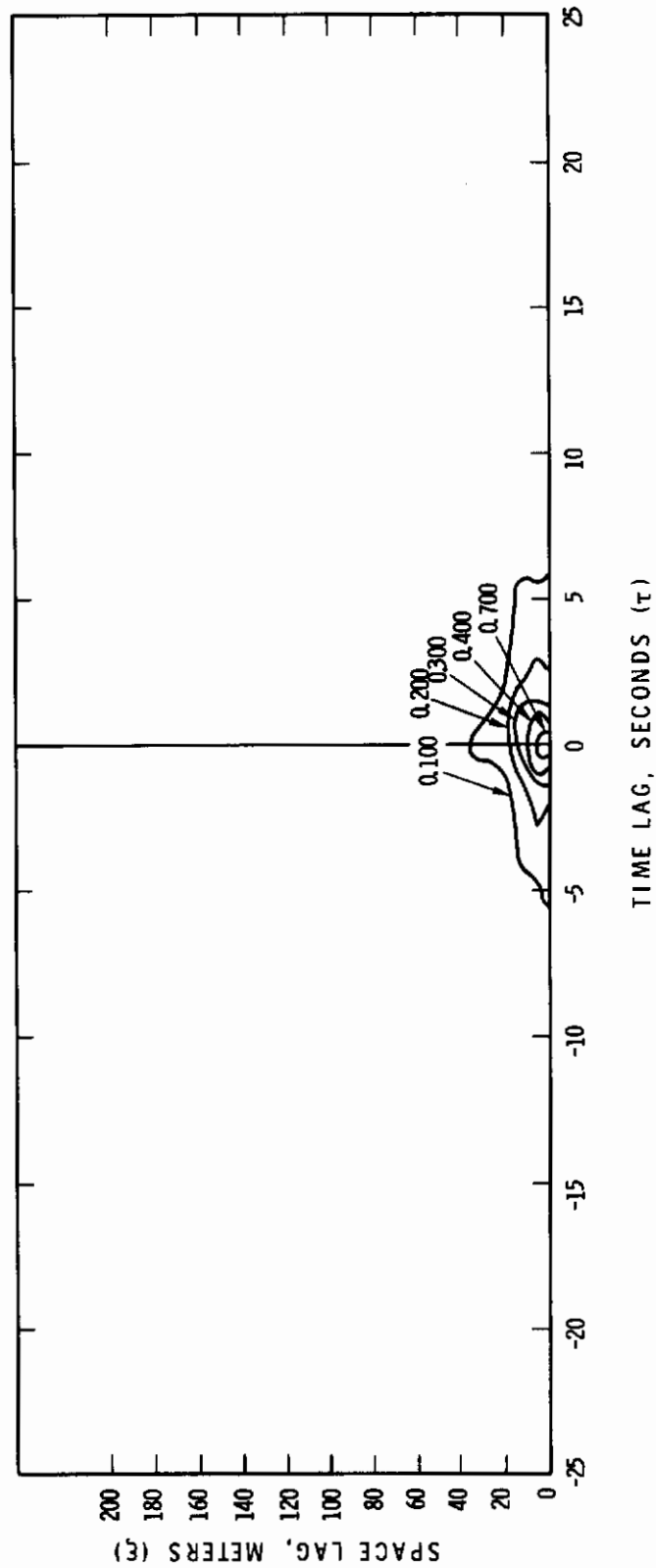


Figure 7.47 Two-Argument Autocorrelation Function of  $w'$  in Time and Space, Test T704

azimuth angle from  $90^\circ$  is apparently enough to bend the isopleths slightly toward the positive  $\xi$  side. These graphs, along the two axes, also give measures of the crosswind versus alongwind eddy dimensions.

One interesting feature is the higher correlation values for  $v'_a$ , which is the alongwind component in this case, at 128 meters rather than 96 meters. Both distances were instrumented by Gills eliminating any sensor difference effects. No comparable feature is found in the graphs for the other two components. Since instability prevailed, it is quite possible that some characteristic length associated with the convection could be involved. Future measurements including measurement of heat and momentum fluxes at a standard level, are recommended to determine whether or not there is any dependable relationship between characteristic lengths evident from humps in the correlation function and the Monin-Obukov L.

## SHEAR INTENSITIES

The analysis results on shears available at this time are from the data of the T-array test, Test T202. In the T configuration the two wing points, A and B, were 9 meters apart and the tail position, C, was located 6 meters from the intersection of the fuselage and wing lines. A detailed analysis of the data from Test T202 is found in the Interim Report. One item of interest not covered in the Interim Report is the cross covariances between various gusts and shears. With reference to positions A, B, and C, in the T-array, the following gusts or shears are of interest:

$$\begin{aligned}u_s &= (u'_a)_A + (u'_a)_B \\u_d &= (u'_a)_A - (u'_a)_B \\w_s &= w'_A + w'_B \\w_d &= w'_A - w'_B \\v_t &= (v'_a)_C \\v_t &= (w')_C\end{aligned}$$

From analysis of the 55-minute period, Table 7.13, the cross-correlation values are found. The cross covariances are normalized with the variances listed.

TABLE 7.13

CROSS-CORRELATIONS FROM T-ARRAY DATA

<u>Gust or Shear</u>	<u>Variances</u>	<u>Gust or Shear</u>	<u>Cross Correlations</u>
$u_s$	4.38	$u_s, v_t$	0.14
$u_d$	1.01	$u_d, v_t$	-0.39
$w_s$	0.97	$w_s, v_t$	0.01
$w_d$	0.28	$w_d, v_t$	-0.08
$v_t$	0.81	$u_s, w_t$	-0.30
$w_t$	0.42	$u_d, w_t$	-0.03
		$u_d, w_d$	-0.01

According to Skelton's lower limit of 0.28 for cross-correlations significant to aeronautical applications there appear to be only two of the above cross-correlations of concern. The first,  $u_d$  cross-correlated with  $v_t$ , is most likely a function of the azimuth angle. The second, the cross-correlation between the longitudinal gust sums on the wings with the vertical gusts on the tail, reflects the inherent transfer of momentum in the boundary layer and infers a pitching effect on the aircraft. Power spectra for the shear functions are given in the Interim Report.

TOLCAT Test T704 provides a data source for additional crosswind shear analyses. In this case, winds were at a 90° azimuth to the tower line. From these data it is possible, using one of the options in the analysis program, to compute shears for any of the three components at all the separation distances provided by the logarithmic line and to analyze them in the same way the gusts have been analyzed. This extended analysis should be made as an early part of any continuation or extension of the TOLCAT work.

BISPECTRAL ANALYSIS

Although initial bispectral analysis has yielded information of interest, the character of the results obtained thus far indicate that the development stage has not really been completed. The most serious problem is the lack of estimation theory for the estimator as defined in Section VI, (Equation 6.8),

$$B(n_1, n_2) = C(n_1) C(n_2) C^*(n_1+n_2) \quad .$$

Perhaps this gap could be filled by continued search of the literature. On the basis of presently available information, it appears that at least three times as much data are required for good third-moment analysis than are required for good second-moment analysis.

As indicated in Section VI, the bispectral results from the computer program cover one octant of the double frequency plane. The parameter given in the analysis is  $n_1 n_2 B(n_1, n_2)$ , with real and imaginary parts separately listed.

In the computer printout the power spectral estimates are given in 32-banded estimates spaced at 10 per frequency decade. When using 8192 data points per series, the bands are formed from raw estimates for the Fourier coefficients,  $C_1(n)$ , for 4096 wave numbers in core. In analogous fashion the bispectral computer output for the second octant is derived from the same Fourier coefficients — the difference being that the output is two dimensional rather than one dimensional, as in the case of the power spectra. In other words the computer printout consists of entries of  $n_1 n_2 B(n_1, n_2)$  into the upper left half of a 32 by 32 square of the double frequency plane,  $n_1, n_2$ . The entries are logarithmically spaced at 10 per frequency decade in each dimension, as shown in Figure 7.48. The area cut off by the heavy line at the upper right has no estimates because the sum of the two frequencies,  $n_1$  and  $n_2$ , is greater than the folding frequency for all  $n_1$  and  $n_2$  that would fall in these squares and therefore, as can be seen from



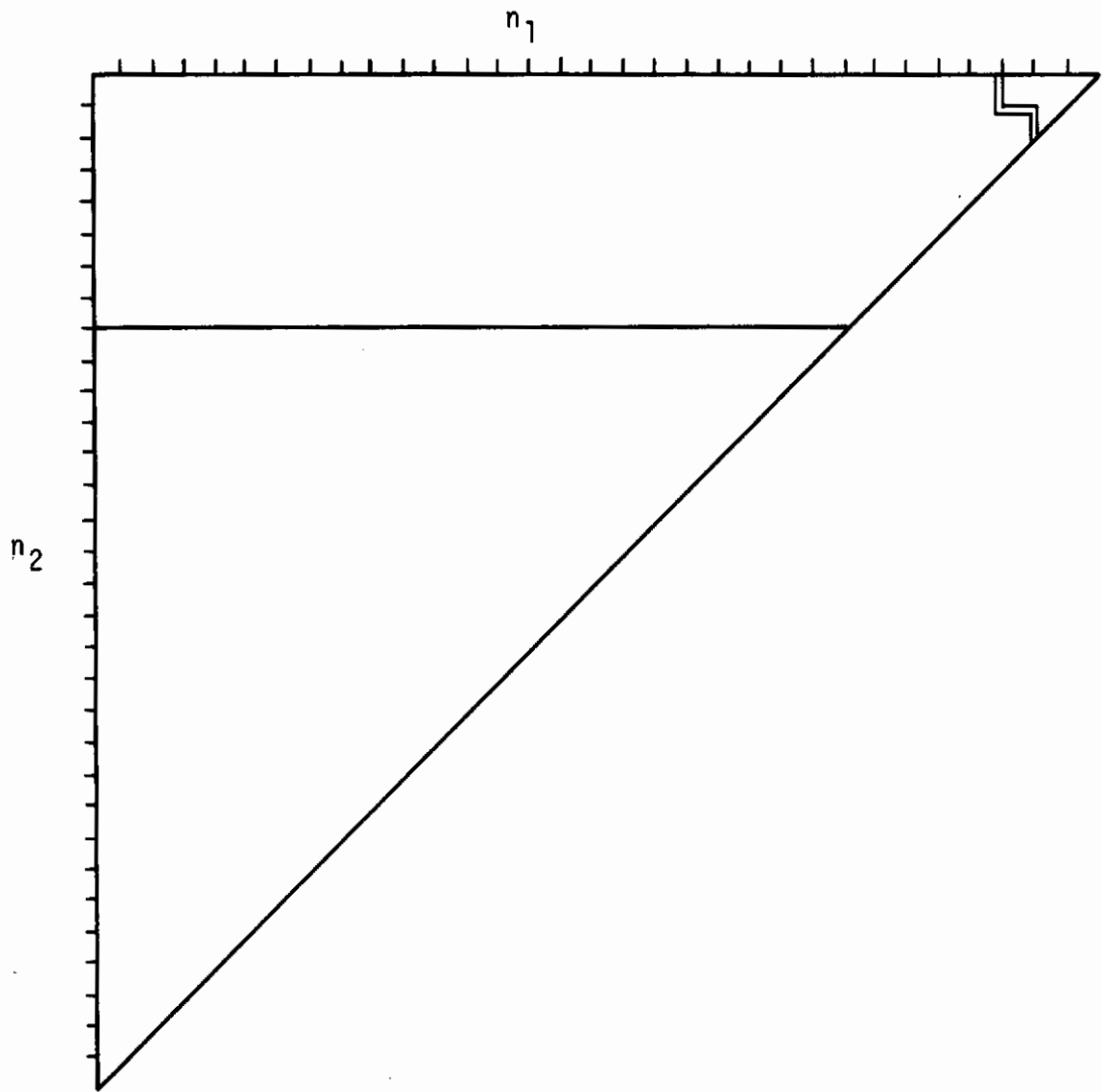


Figure 7.48 Display of 2nd Octant of Bispectral Computations

# Contrails

Equation 6.8, calculations are not available. The dashed line shows the limit arbitrarily placed on the computer computations, making the final array half of a 24 by 24 square. This limitation was exercised for reasons of economy and was considered partially justified since beyond this limit the turbulence is mostly isotropic, as was indicated by the small random numbers appearing toward the upper margin of the 24 by 24 output.

Lacking any precise notion of what to expect for bispectral estimates as a function of  $n_1$  and  $n_2$ , the most encouraging numerical result would have been one showing considerable positive correlation between adjacent banded values in the  $n_1, n_2$  plane. Initial examination revealed some pattern of organization of bispectral data for 60 and 131-meter height but not as much as is found for power spectral estimates. Little or no correlation between adjacent estimates was evident in bispectra from data taken at 7.5 or 15 meters under neutral conditions demonstrating that no identifiable third-moment characteristics occur over the frequency range considered in these cases.

The best illustration of the bispectral results thus far are from Test T805. The largest areas of exclusively positive or exclusively negative estimates for both the real and imaginary parts of the bispectrum for  $w'$  are shown in Figure 7.49. In the real part the most interesting feature is the large positive area roughly between 0.0016 Hz and 0.0032 Hz. This is consistent with the positive third moment found for  $w'$ , which is  $0.38 \text{ m}^3/\text{sec}^3$ . The negative area in the lower left has little significance because the number of degrees of freedom in each banded estimate in this area is insufficient for confidence.

The pattern for the imaginary part is even more striking, showing better defined negative and positive area, the negative area clearly occupying lower frequencies. The negative area is smaller on the graph than the positive area, but the greater absolute value of the negative numbers far more than compensates.

# Contrails

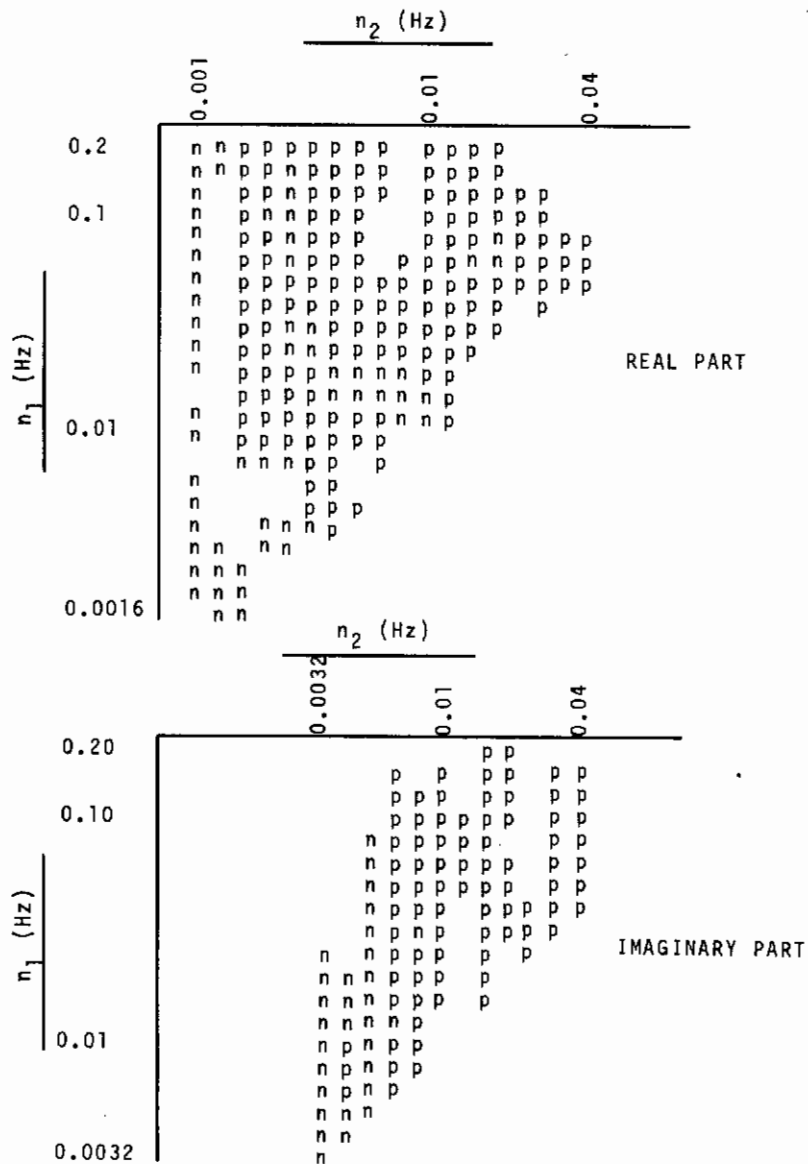


Figure 7.49 Positive and Negative Areas for Real and Imaginary Parts of  $B_w(n_1, n_2)$  for Test T805

As explained in Appendix II, the negative area in the imaginary part indicates that the original data function has long segments of small negative slope and short segments of greater positive slope. This can be seen in the original W data, as shown in Figure 7.50. The bispectral results, in this case, can then provide a measure, for aircraft application, of how much sharper upward gusts are than downward gusts. Some of the numbers in the bispectrum are of insignificant magnitude. When one of these occurred in an area of large numbers of opposite sign, the difference was ignored in preparing Figure 7.49. The numbers of largest absolute values are found near and on the diagonal.

By consideration of Equation 6.8, it is easily seen that even one octant of bispectral estimates contains more apparent degrees of freedom than are in the original data. Therefore, the estimates for different frequencies are not statistically independent as is the case for power spectral estimates. This can also be seen directly from Equation 6.8.

Mathematically a set of statistically independent pairs could be selected by using Equation 6.8. For example, the bispectrum could be calculated for all pairs such that  $n_1 = n_2$  and such that no value of  $n$  is twice that of another  $n$ . Such a list of harmonics would consist of every odd number. However, this has not been done, and physically the idea does not seem very relevant.

Another way of displaying bispectral estimations is to integrate over one of the frequency arguments,

$$\beta_1(n_1) = \int_{-\infty}^{\infty} B_1(n_1, n_2) dn_2 \quad . \quad (7.12)$$

When the mapping properties of the bispectrum are considered, as shown in Appendix II, Figure II.5, it becomes evident that any path of integration crosses six segments that can all be mapped into the first octant. This

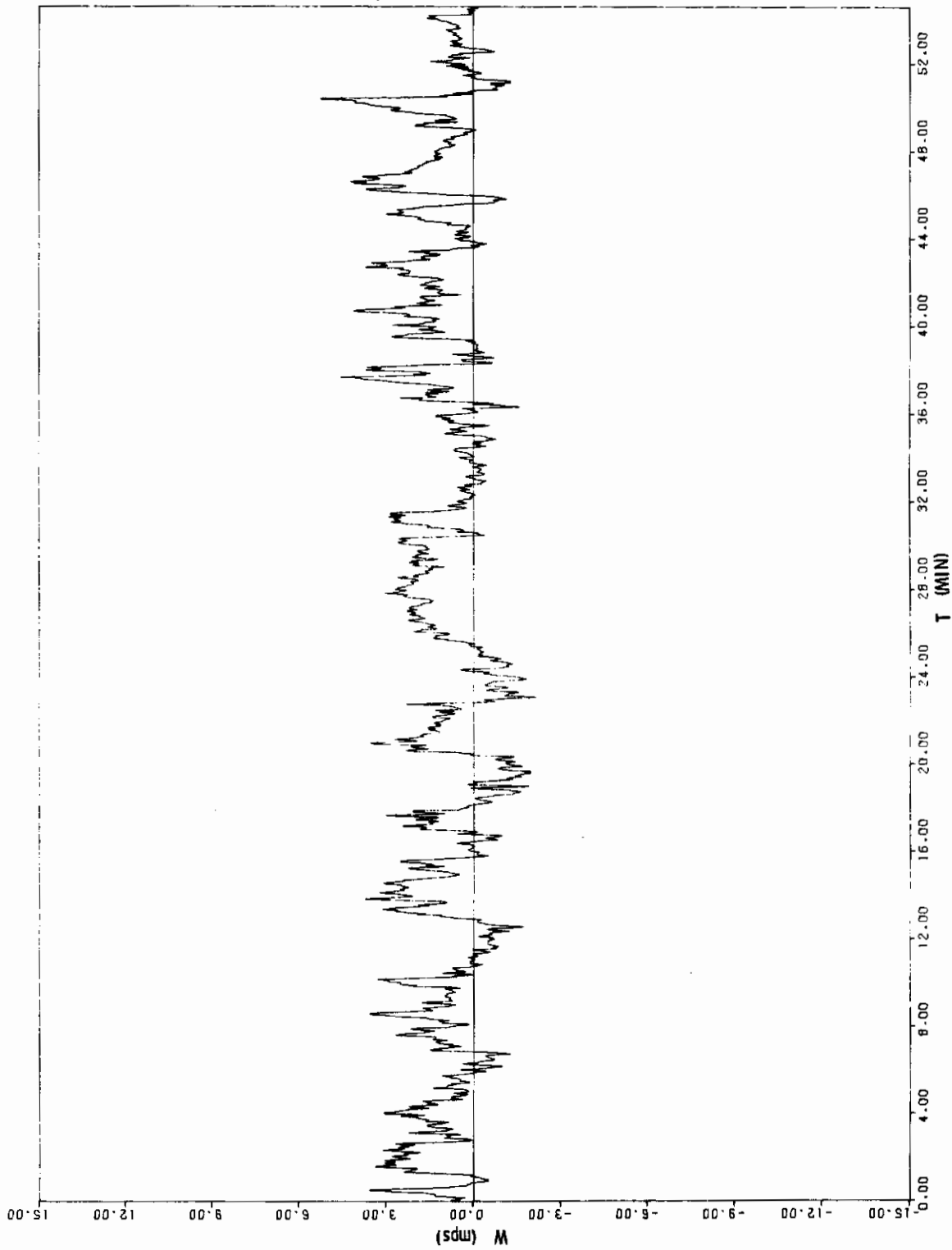


Figure 7.50 Vertical Component, W, Test T805

result suggests that an equivalent path of integration in the first octant would consist of six segments joined end to end and leading in a variety of directions. When the paths of integration are actually deduced, it is found that three paths on the single octant printout are each traversed in opposite directions, as shown in Figure 7.51.

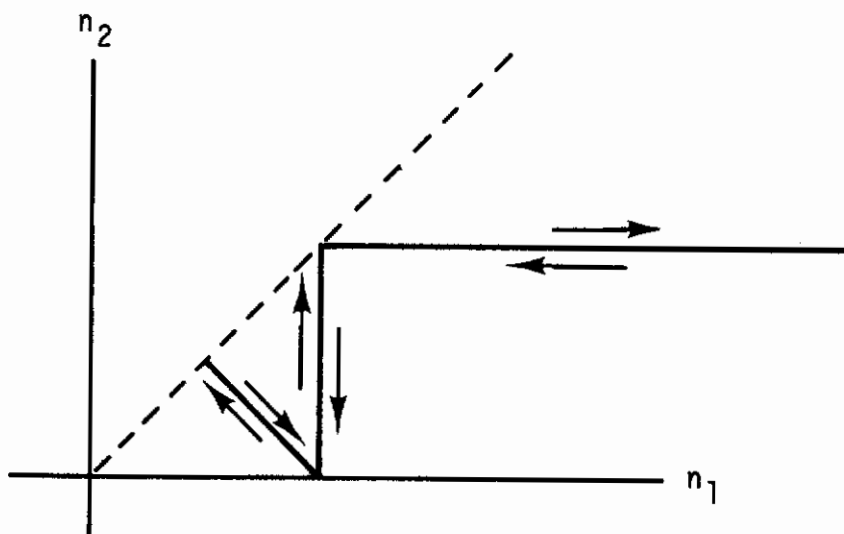


Figure 7.51 Equivalent Path of Integration for Horizontal Line when Mapped into First Octant

Of course, the integration does not cancel as it may appear from the graph since the differential of the integration is not the discontinuous function of the path mapped into the first octant.

The computer program has not yet been programmed to perform this integration, and since the bispectrum was not computed for the entire frequency



range available, accurate computation could not be made by hand either. Nevertheless, in order to get some idea of what kind of a function would be produced, the printed computer output was summed in the manner indicated by the horizontal and vertical lines in Figure 7.51. This is equivalent to the following integration,

$$\tilde{\beta}_1 = \int_0^{F_m} B_1(n_1, n_2) dn_2 \quad (7.13)$$

The results of this integration (or summation of printed computer output) for the vertical component over the 55-minute duration of Test T805 are shown in Figure 7.52. For this run the folding frequency is 1.25 Hz, and  $F_m$  (in Equation 7.13) is 0.225 Hz. The real part of the bispectrum is shown by the solid line, and the imaginary part by the dashed line. In the real part, the principal peak is shown at 0.005 Hz, and secondary peaks of descending magnitude are seen at frequencies that are roughly octaves of 0.005 Hz. In other words, the frequency locations of successive peaks are about 2 to 1 or 2-1/3 to 1. If this feature were found in a power spectrum, it would suggest a sharp second-order disturbance occurring periodically at about every 200 seconds. Whether or not third-order disturbances in the atmosphere have this property would have to be ascertained by examining more bispectra.

The imaginary part has one outstanding negative peak at 0.0025 Hz. This indicates at low frequencies a tendency toward slow decrease of  $w'$  followed by rapid increase. The positive peak at 0.008 to 0.010 Hz indicates just the opposite tendency at higher frequencies.

The vertical organization apparent in the bispectrum,  $B_w(n_1, n_2)$  from Figure 7.49 suggests that an integration of the kind

$$\tilde{\beta}_1(n_1) = \int_{n_1}^{F_m} B_1(n_1, n_2) dn_2 \quad (7.14)$$

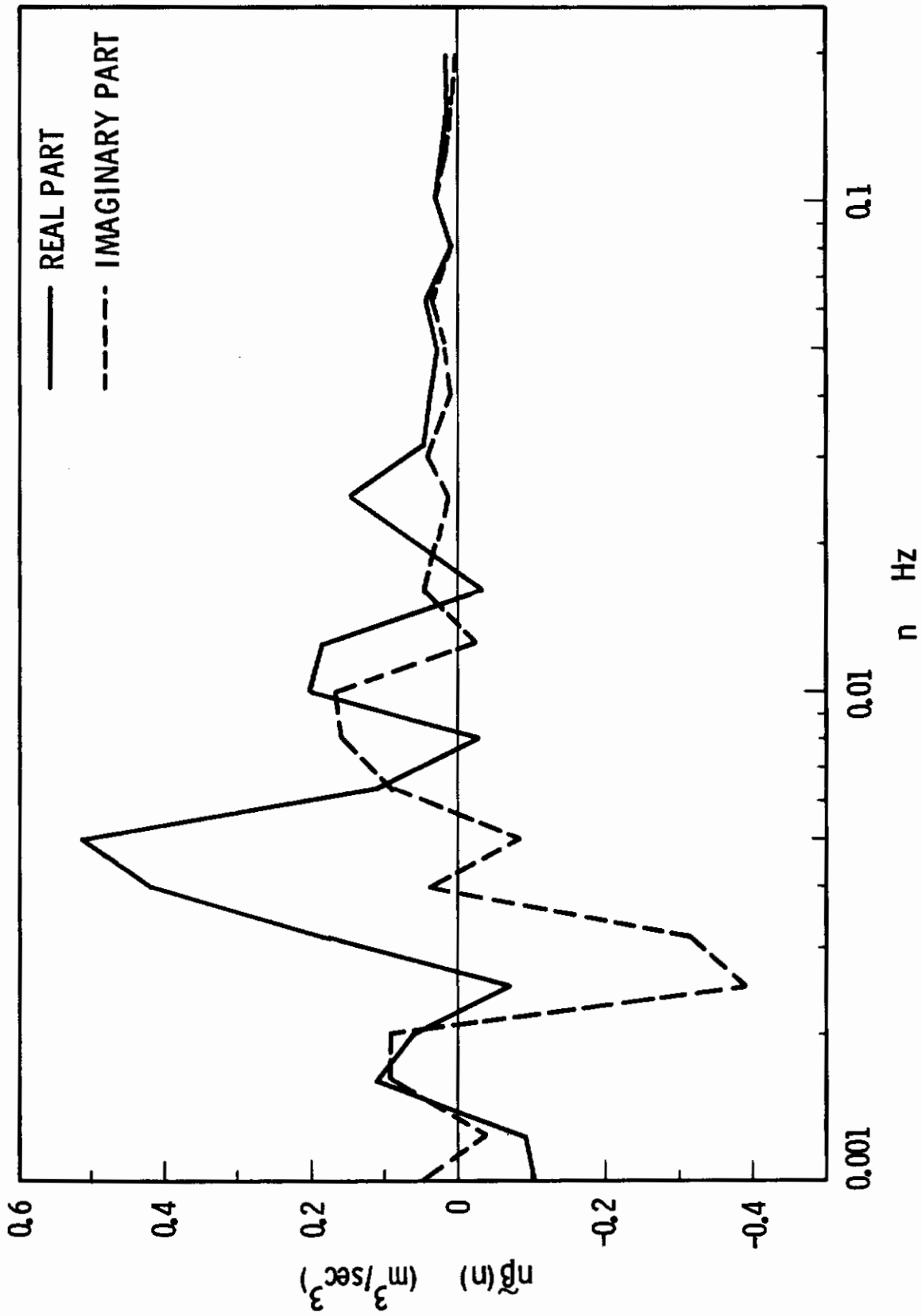


Figure 7.52 Bispectrum of One Argument - Integration of  $B_1(n_1, n_2)$  over One Quadrant

should produce a more organized function than the integration according to Equation 7.13. When this function was plotted from the same data, as shown in Figure 7.53, the large positive area in the real part and the large negative area in the imaginary part were both defined, and both were centered at about 0.004 Hz. Also, the peaks at higher harmonics in the real part were missing. At this stage there is difficulty in saying which result is physically more significant.

## PROBABILITY DENSITIES

In the Interim Report extensive collections of figures illustrated both individual and joint probability densities of various gust and shear combinations. Since these techniques have already been well illustrated, and since establishing and illustrating techniques rather than extensive application is the emphasis of the study up to this time, the probability density material in this report is minimal.

In their article on exceedance modeling, Pritchard et al (Reference 7.8) refer to two types of turbulence, storm turbulence and nonstorm turbulence. The former is distinguished from the latter by the much greater probability of large gusts. Therefore, although adequate sampling of both are needed to describe atmospheric behavior in probabilistic terms, most turbulence data collected by meteorologists (and this includes all the data analyzed in this report) are of the nonstorm type. There are two reasons for this preference. The theoretical reason is that the other descriptors of turbulence, spectra, correlation functions, etc., are defined only for statistically stationary processes. Therefore, the tendency is to measure when the same condition is expected to prevail for a period of time. The practical reason is that good storm data are much more difficult to obtain. Sonics have to be oriented to receive winds from a limited sector that may be exceeded directionally by strong gusts and by change of direction with a frontal passage. Therefore, sonic representation of storm winds is quite likely to be somewhat distorted. The trouble with Gills in storm conditions is that the propellers frequently become disengaged from the remainder of

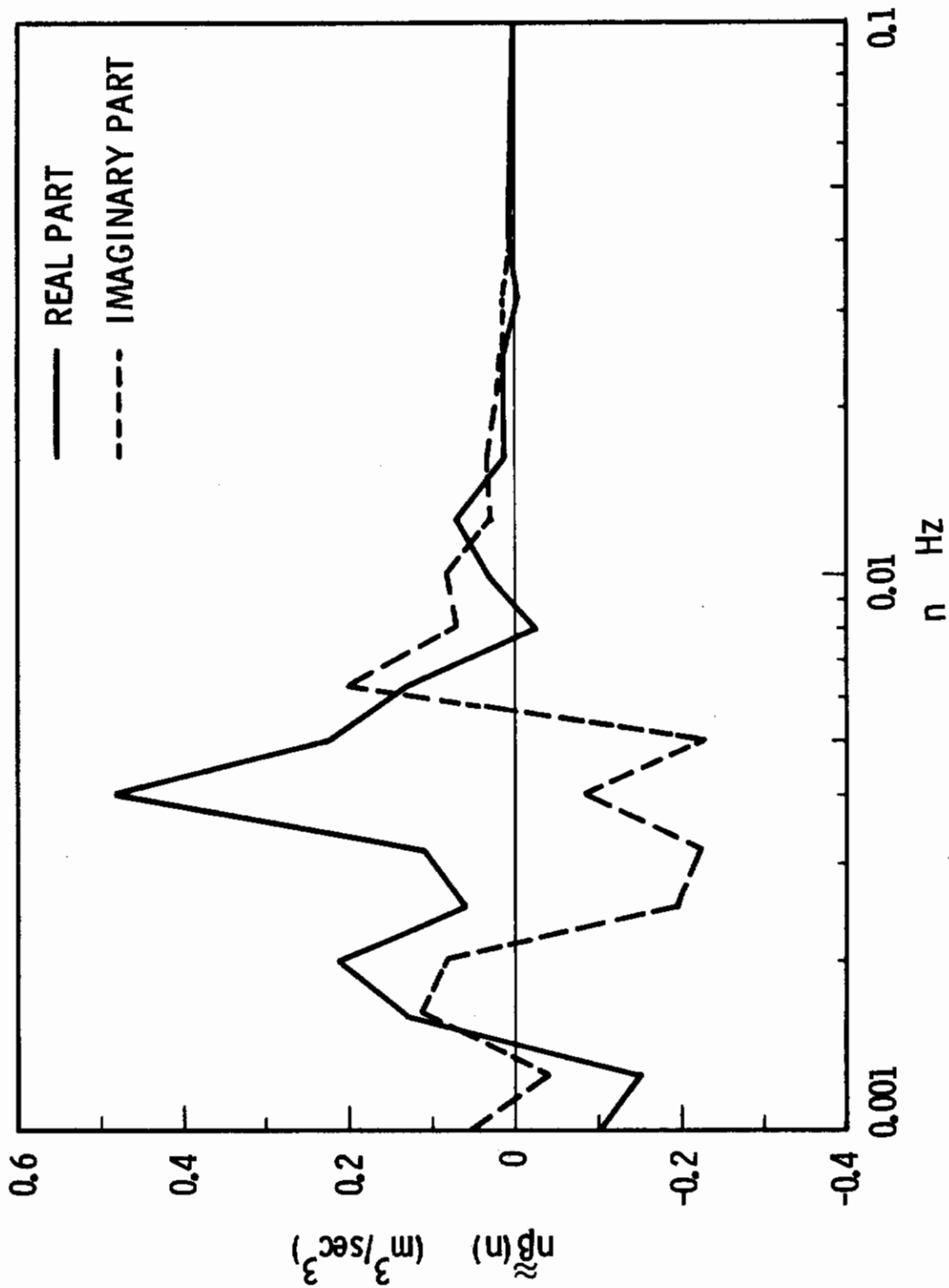


Figure 7.53 Bispectrum of One Argument - Integration of  $B_i(n_1, n_2)$  over One Octant

the instrument when winds exceed 30 mps. However, gust probabilities during storms must be known if an adequate exceedance model (as well as models of other descriptors) of gust behavior is to be constructed — therefore, storm measurements must be taken and analyzed in future measuring programs.

Because it makes considerable difference to aircraft whether the amplitude shown by the probability distributions is due to quick or slow changes, the probability distributions are given not only for the original data but also for three high-pass filtered versions. The original analysis is generally of 8192 data points for each component with  $\Delta t$  equal to anywhere from 0.05 to 0.4 second. Subsequent probability analyses of the same data are made after running means of 1501, 301, and 61 points have been subtracted out. Obviously, amplitude of the probability distribution from the final filtering must be due to the wind variations that take place over a short time interval. When  $\Delta t$  is 0.2 second, as it is in the data analyzed in this report, the total time is about 28 minutes, and the high-pass filter averaging times are 5 minutes, 1 minute and 12 seconds.

### Individual Probability Distributions

The probability analyses included in this report are of two unstable tests, Tests T701 and T704, at 30 meter-height, during which the highest mean wind speeds and variances prevailed. Both samples are 28 minutes long, (Table 7.2). The figures for the individual probability distributions are given in Appendix IV as Figures IV.5 to IV.12.

These data appear to be more Gaussian than those described in the Interim Report, however, the real difference is probably in the editing procedures. The shortcomings of the editing used before the Interim Report were chiefly responsible for the exaggerated kurtosis figures calculated for some of those data, which reached as high as 11 and 13 in two cases. The kurtosis figures for the Tests T701 and T704 do not exceed 4.6 — the highest values being for horizontal component data from the 12-second high-pass filter.

The vertical component does not show a strong positive skewness such as was associated with cases in the Interim Report. The reason may be in the lower height for the data analyzed here.

Variances obviously decrease with high-pass filtering, and kurtosis figures increase. The increase of kurtosis shown for Test T704 is very slight, in contrast to other data analyzed.

The data seem to infer that turbulence at the 30-meter level generated by winds of 10 to 15 mps under unstable conditions departs little from a Gaussian model.

## Joint Probability Densities

There are many gust and shear combinations that may be selected for joint probability analysis for data from a logarithmic array of towers. In the Interim Report extensive results were shown of joint probability density functions (jpdf's) for orthogonal gusts at the same point and for various shear and gust combinations available from the T-array, using the same filtering technique as described above. For further illustration a limited selection of jpdf's for parallel gusts taken at different locations on the logarithmic array are shown in Figures 7.54 through 7.57 and also in Appendix IV, Figures IV.13 through IV.20. Obviously, these graphs can be plotted for a variety of separation distances, and for a variety of gust and shear combinations. Also, the probability density can be renormalized across any horizontal or vertical line to obtain conditional probability densities (i.e., the probability of B given A); and also the joint probability density can be integrated on one side to give a marginal probability density.

The jpdf's in Figures 7.54 through 7.57 are for Test T704. During this test the mean wind at the height of measurement (30-meters) was 13.5 mps, and the mean wind direction was perpendicular to the tower line.



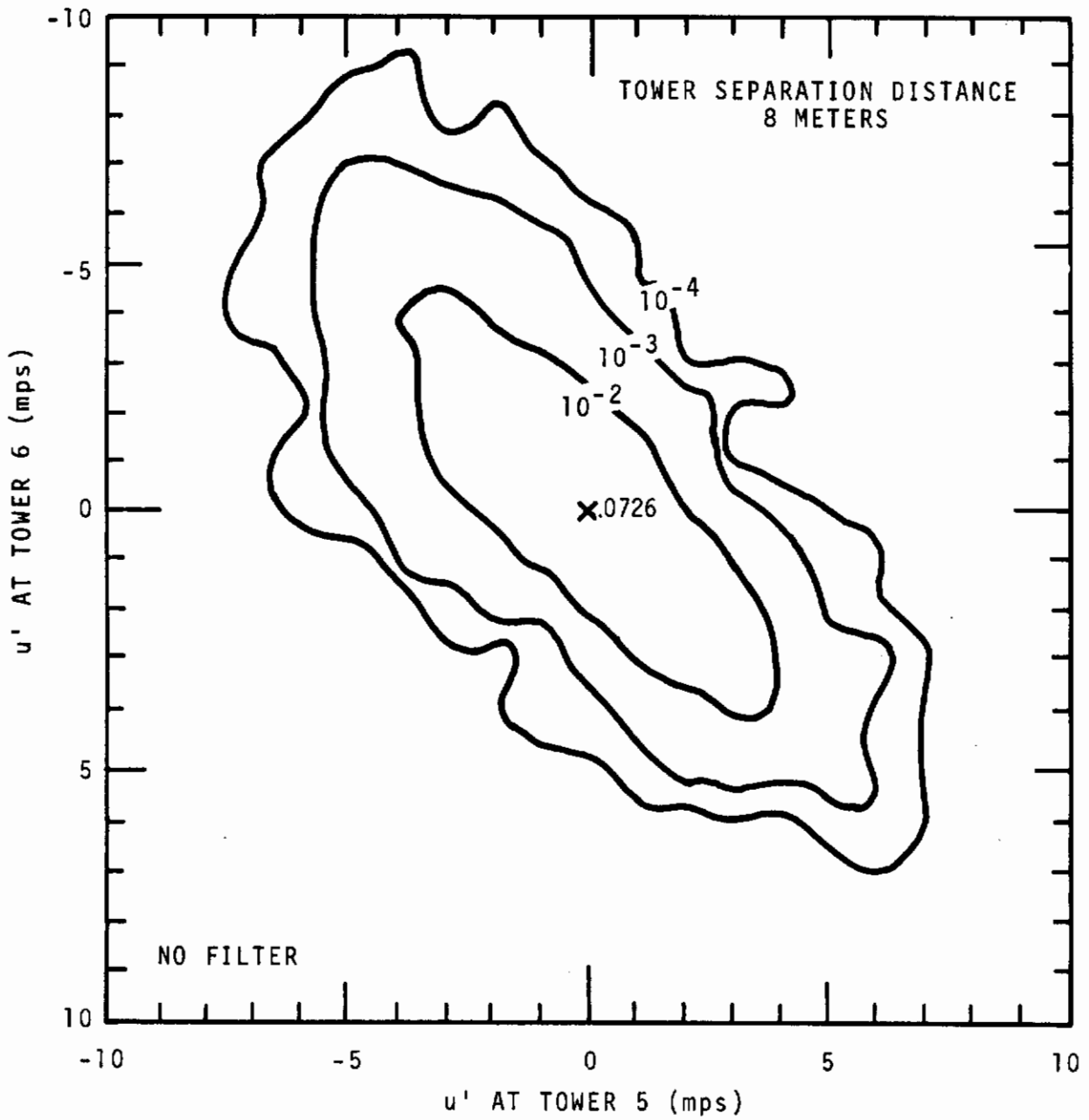


Figure 7.54 Joint Probability Density Function for  $u'$  -- No Filter  
Test T704

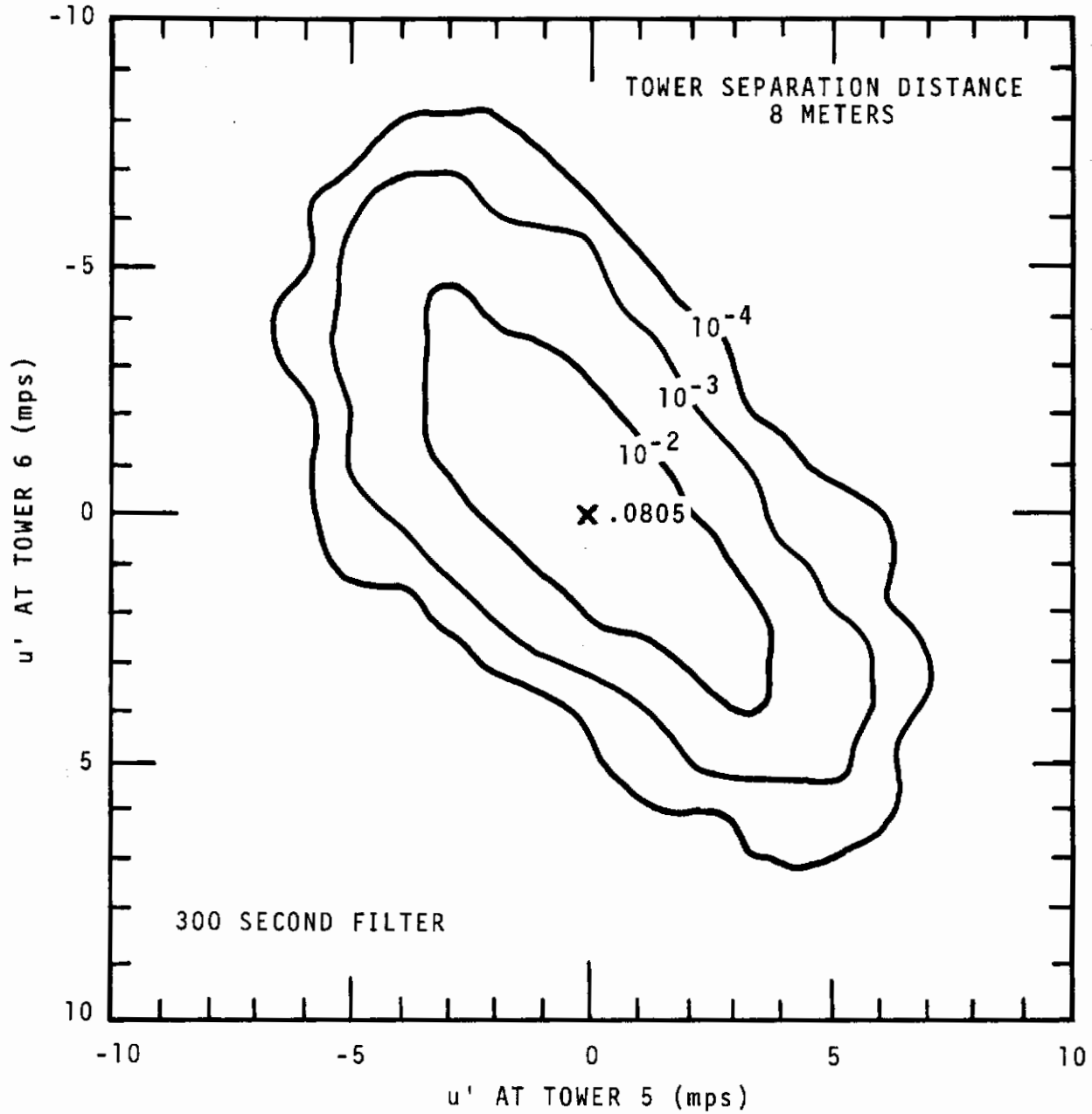


Figure 7.55 Joint Probability Density Function for  $u'$  -  
300-Second High-Pass Filter  
Test T704

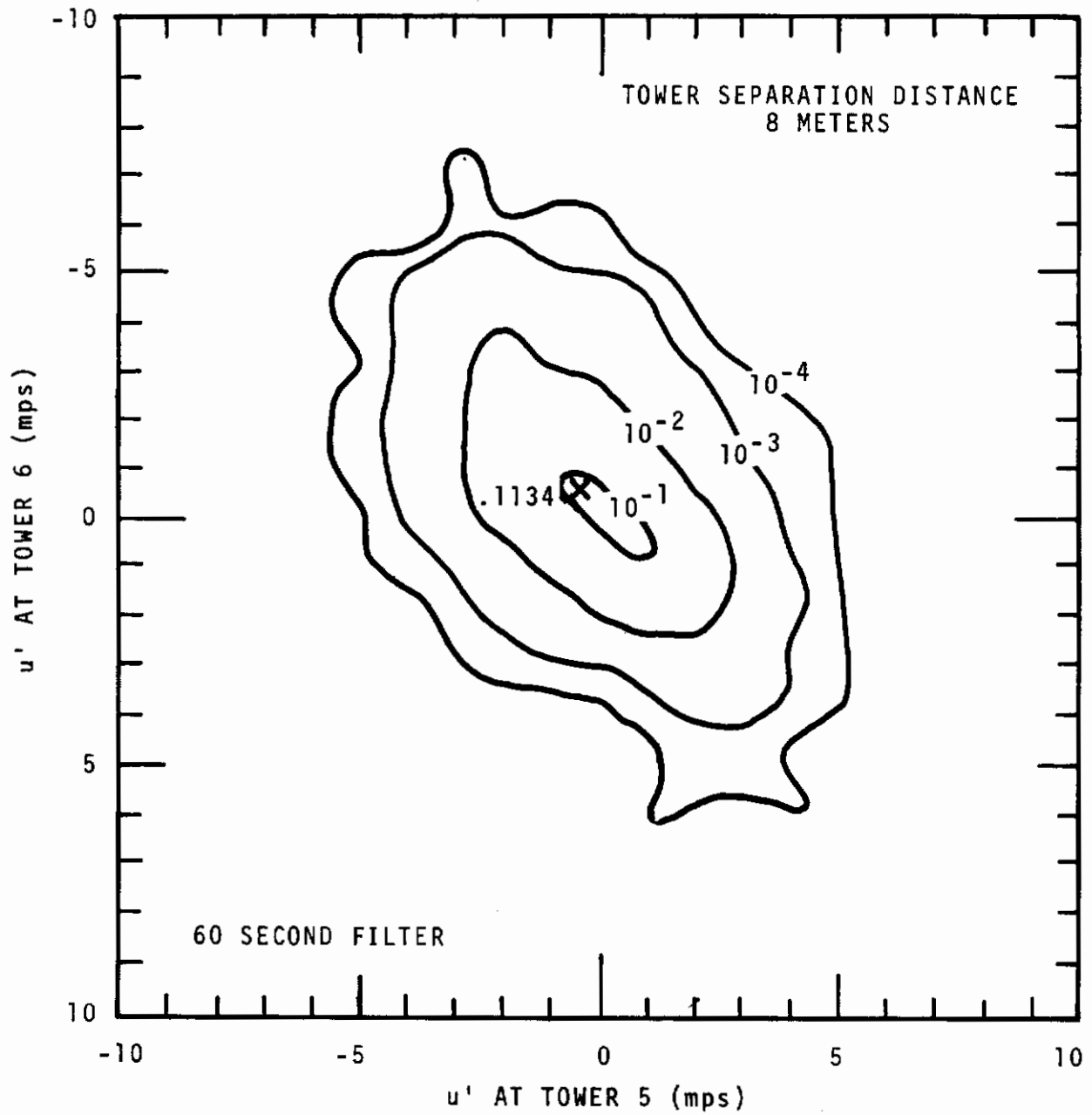


Figure 7.56 Joint Probability Density Function for  $u'$  —  
60-Second High-Pass Filter  
Test T704

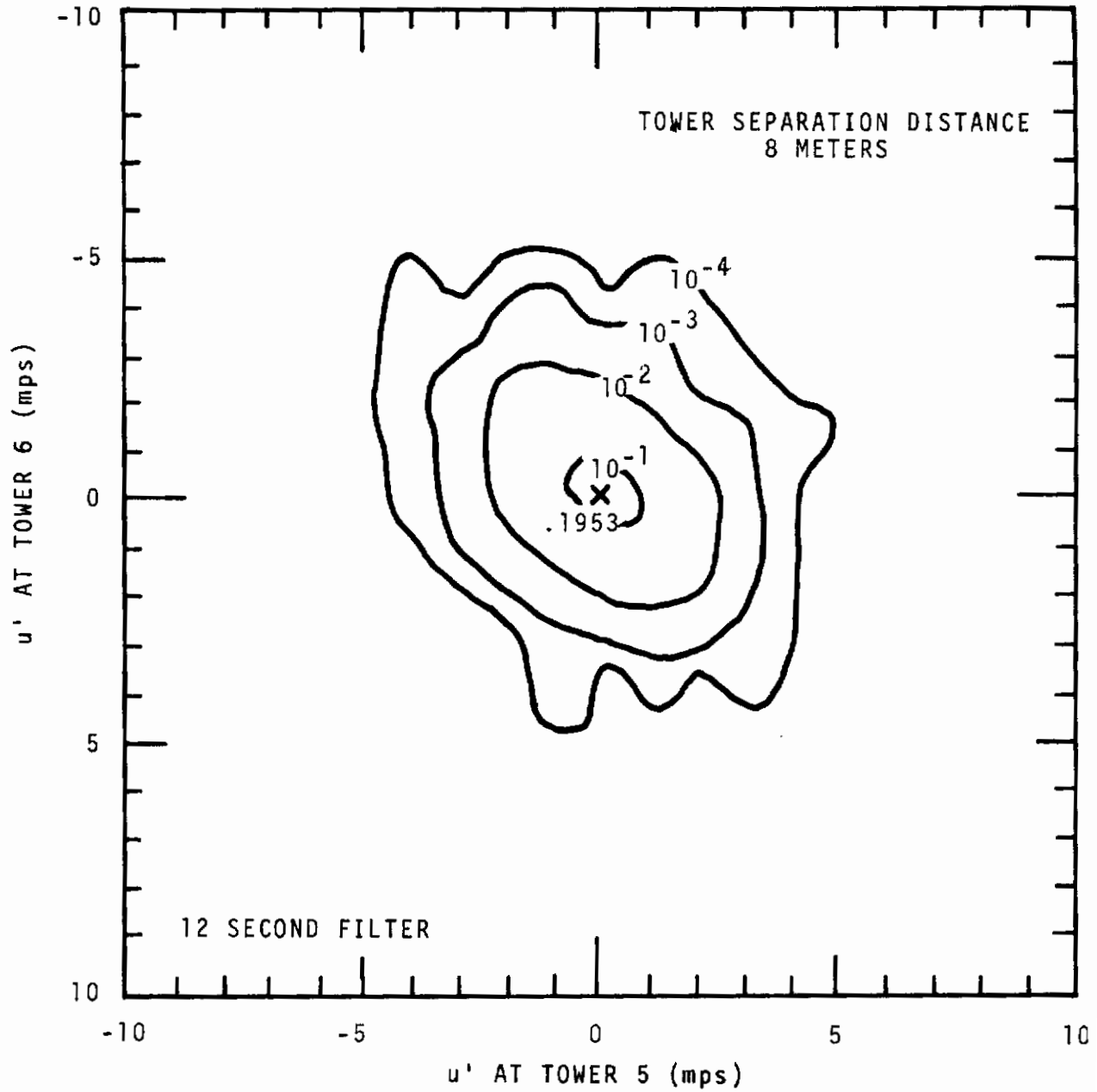


Figure 7.57 Joint Probability Density Function for  $u'$  -  
12-Second High-Pass Filter  
Test T704

# Contrails

For the probability analysis (and nowhere else in the report), the tower line is used to simulate the wing span, or the y-axis. Therefore, the winds called  $u'$ , i.e., the longitudinal component, in this discussion are identical with those called  $v'_a$ , i.e., the cross sampling line component, in other analyses of this test.

The analysis simulates the joint probabilities for each of  $u'$ ,  $v'$ , and  $w'$ , one at a time at two wing locations 8 meters apart when the mean wind direction as seen by the aircraft is head-on. From the same test, similar analyses can be obtained for 20 other separation distances varying from 4 to 252 meters. It will be noticed that the domain of the function is from -10 to 10 mps, on each side, which is twice the linear dimension used for the graphs in the Interim Report. Perhaps, the most striking feature of the sequence is the disappearing correlation between the two gusts as the high-pass filters are applied. The two gusts are highly correlated when all the long wave structure is left intact. But when a 12-second running mean is subtracted out of the data, the resulting two-gust series appear essentially independent.

This type of analysis should definitely be exploited in the future to a far greater extent than has been possible for the present report. The relative de-emphasis of probability analysis compared to spectral analysis is not to be construed as indicating a recommendation that future analyses of turbulence for aeronautical purposes be of the same proportions. Quite to the contrary, it is believed that a descriptor which emphasises the intermittency of atmospheric turbulence is indispensable for aeronautical purposes.

## SECTION VIII

### SUMMARY AND CONCLUSIONS

#### RESULTS

The TOLCAT system was developed for measurement and analysis of turbulence in the lowest few hundred feet of the atmosphere. Both temporal and spatial descriptions of turbulence resulting from this system are pertinent to take-off and landing problems encountered by aircraft. The system utilizes sensors mounted on an array of towers for measurement of turbulence fluctuations in the three components of the wind at various heights and horizontal spacings, and under various meteorological conditions. The data are collected in the field on analog or field digital tape recorders, played back into a medium-range computer for preprocessing and are re-recorded on industry standard tapes for later detailed processing and analysis on a UNIVAC 1108 computer.

Two types of turbulence sensors are utilized: fast response sonic anemometers for the most accurate determinations of momentum and heat fluxes used in characterizing the stability of the atmosphere and for spatial correlations over small separation distances; and less expensive Gill three-propeller anemometers for the greater number of measurements at large separation distances where their slower response is adequate. Noise initially found frequently in the signals from the sonic anemometers was eventually overcome by improving the insulation and grounding within the transducers and upon replacing internal cables within the sensing heads. A threshold in the response of the vertical component propeller of the Gill was overcome by tilting the vertical arm into the wind, so that the propeller always turned in one direction, thus removing the contribution of the horizontal wind components with the signals from the other two propellers. However, except where low velocity single gust details are required, the modification to the instrument does not presently appear to



# *Contrails*

be justified since there is no noticeable improvement in the more commonly used first and second moment statistics. Therefore, this modification to the Gill has not been adapted for standard use. A correction for the lack of true cosine response of the propeller does significantly improve the accuracy of all statistics from the Gill, however, and has been added to routine data processing for this sensor.

The mounting of both types of instruments has been improved to assure true sensor leveling and optimum orientation into the wind at inaccessible remote locations on tower tops and on the ends of tower booms. This has been accomplished by utilizing remotely monitored electrolytic levelers on each sensor and an antenna rotor base on each sensor for remote reorientation from a centrally located control trailer.

The sensors are mounted on four permanently erected, 62-meter towers and eight 30-meter collapsible, portable towers which can be repositioned for various measurement configurations to meet different experimental requirements. The sensor booms can be moved to various heights on the 62-meter towers and the sensors on the tops of the 30-meter towers can be raised and lowered to measure the turbulence at selected heights.

Two trailers downwind of the tower array contain the signal conditioning and data recording equipment. Two 14-channel analog magnetic tape recorders are generally used to record the three wind component signals from eight of the four sonics and six Gills available, and two of the temperature signals from the sonics. One channel on each recorder is used for a coordination timing signal. An inexpensive field digital recorder has also been added to the system. Its use has demonstrated the opportunity for simple and inexpensive expansion of the system with additional similar units while at the same time offering improvements over the signal to noise ratio limitations and calibration accuracy limitations inherent in the analog tape recorders.

# Contrails

After each experiment, tape recordings of the field data are taken to a computer laboratory where data are played back from one of the analog tape units into an analog-to-digital converter, interfaced to an SEL 840A medium-range computer. A tape reader designed to retrieve data from the field digital recorder is also interfaced to the SEL 840A. The computer is programmed to test the data for reasonableness and perform preliminary editing, average a selectable number (usually five) of the 100 to 200 basic samples per second together to minimize aliasing and provide a range of optional digitizing rates, make instrument corrections such as conversion of sonic nonorthogonal measured components to cartesian wind components, perform scaling functions to account for gains and offsets used during measurements, and finally to record digital values of the three orthogonal wind components and temperature on an industry standard digital tape recorder interfaced with the SEL 840A. The SEL 840A is also programmed to accept the field digital recorder data and to perform the above operations, leading to re-recording it in a form suitable for detailed analysis on the UNIVAC 1108 computer.

The UNIVAC 1108 programs perform more refined editing and correct Gill anemometer data for deviations of the propellers from a true cosine response before re-recording the true wind components in cm/sec and temperature in °C on "master tapes." Generally, two master tapes, corresponding to the two analog recordings in the field, are produced for each experiment with 13 separate channels of the three wind components and temperature from several instruments recorded on each tape. When an experiment is to be analyzed, one or both of the master tapes are read into drum storage. From the total number of variables stored, the first selection of 2 or 3 variables is made and placed in "principal drum files" for joint analysis. These are then processed by the probability program which, for selectable time periods within the total data segment in the principal drum files, calculates and removes means for each of the variables, reorients the coordinate system in the direction of the mean wind if desired, provides up to three different high-pass filterings of the data and the probability

# Contrails

density functions — individual and joint — for each when requested, and calculates variances for each component and covariances between them as well as the third and fourth moments. An option to plot any of the time series in the data segment being analyzed, also is available. These unfiltered turbulence variables are then selected, two at a time, for analysis by the spectral program. Here, the data are optionally detrended with the best fitting first or second order polynomial for each time series and tapered to prevent ringing oscillations in the fast Fourier transform calculated from which banded power spectral and cross-spectral estimates are formed. The auto- and cross-correlation function can, in turn, be transformed from these estimates if required. Variances and covariances for the detrended time series are also available from this program. Finally, bispectral estimates are optionally calculated from the detrended, tapered time series.

The sensing, data logging, processing and analyzing capabilities were demonstrated through the evaluation of 2 tests conducted during the first experimental phase and 10 tests during the second experimental phase. As well as illustrating the adequacy of the experimental and analytical techniques required for TOLCAT, some useful meteorological conclusions were reached. The turbulent gusts, as they affect aircraft, were found to exhibit some unexpected characteristics, both in their magnitude and their scale.

The magnitudes of the gusts are most generally described by the variances of the three wind components which in turn are usually characterized by two covariances:  $\overline{u'w'}$ , reflecting the momentum flux, and  $\overline{w'T'}$ , reflecting the heat flux. These two terms, along with bouyancy,  $g/T$ , provide a measure of stability. The momentum flux, by itself, provides the characteristic velocity,  $u^*$ , generally used in modeling the wind component variances. Initially, it was expected that the fluxes would be reasonably constant through the 60-meter range of measurement heights. However, it was found later in AEC studies at Hanford, concurrent with the TOLCAT experiments, that particularly during very unstable conditions the momentum fluxes at

# Contrails

30 and 60 meters fell sharply below that closest to the ground. However, the TOLCAT averaged results showed that the local fluxes at the upper measurement levels gave results reasonably consistent with the constant flux concept. Wind speeds from 15-meter height which are representative of the near surface flux, provided more consistent individual ratios with the variances from 30 and 60 meters than did the the directly measured fluxes at those heights. The variances from 15 meters, however, formed reasonably consistent ratios with  $\overline{u'w'}$  at that height. In addition, when lower frequencies which do not affect aircraft are filtered out, the ratios of the three wind component variances to  $\overline{u'w'}$  are smaller than those used by Skelton from previous variance ratios from Hanford measurements nearer to the surface. It is clear that further measurements of variances of the three wind components at all heights of interest for TOLCAT must be made in the future for adequate determination of the appropriate ratios to be used in predicting gust intensities for aircraft applications. The near surface momentum flux should be determined in all cases to provide more consistent ratios and the heat flux should also be determined for a number of tests in each of several stability classes so that stability dependence of the variances can be modeled.

The size of the turbulent eddies encountered by aircraft is also important. Information on energy associated with various eddy sizes is most generally presented in the form of power spectra of the three individual wind components from time series measurements at a fixed point. TOLCAT measurements and analysis of this type demonstrated reasonable agreement with other recent measurements and modeling of spectra at Hanford, conducted by Battelle in research programs for the AEC. In the inertial subrange the Kolmogoroff minus 5/3 power dependence was consistently demonstrated and the 4/3 ratio of the longitudinal component spectrum with the lateral and and with the vertical component spectrum was found to be closely approximated in 60 percent of the cases. The spectra for the vertical component and for the longitudinal component were found to be modeled from the micro-meteorological peak through the inertial subrange by normalizing the



spectral energy,  $nS(n)$ , with the square of the friction velocity,  $u_*^2$ , and plotting it as a function of  $nz/\bar{U}\phi_m$ . Here, the wave number (or reciprocal of the eddy size) is estimated by  $n/\bar{U}$ , the frequency divided by the mean wind speed, and is normalized with the height, reflecting the increase in eddy size with height, and further normalized with  $\phi_m$ , the dimensionless shear, reflecting the effect of stability shifting the spectrum to smaller eddy sizes for stable conditions and to larger eddy sizes for unstable conditions.

At frequencies below that for the micrometeorological peak in the turbulent energy, additional peaks occur. For the vertical component, distinct low frequency peaks occurred below the micrometeorological peak, which occurs at  $nz/\bar{U}\phi_m = 0.46$  in a number of unstable tests, apparently produced by convective activity, which does not conform to any models of turbulence spectra yet proposed. Likewise, for the longitudinal component additional peaks and considerable energy are present at frequencies below that of the micrometeorological peak, which occurs at about  $nz/\bar{U}\phi_m = 0.056$ . From the first TOLCAT measurement phase, spectra at 58 meters showed a low frequency peak occurring in several tests at  $n = 0.003$  Hz, corresponding to a secondary peak appearing at a fixed frequency for all 5 heights of measurement from 3.75 meters to 60 meters in an AEC experiment in neutral conditions. This peak which apparently reflected surges in the wind profile simultaneously at all heights, was not consistently found at the same frequency in the second phase of TOLCAT measurements, although separate low frequency peaks were found. It is clear that further measurements and analyses are required for a thorough definition of the time series spectral turbulence structure. At 30 meters and above there is yet some improvement needed throughout the entire frequency range during diabatic conditions where the fluxes are no longer constant. The less readily organized lateral wind component spectra also need further efforts in modeling. However, for applications to take-off and landing problems, the aircraft responds primarily to those wavelengths smaller than 600 meters where the time series spectra are quite well defined through the micrometeorological peak into the inertial subrange.

# Contrails

While considerable gains have been made in describing time series spectra from a fixed point, an aircraft feels the distribution of turbulence through space as well as in time. An understanding of both aspects is necessary. The simultaneous measurement of turbulence from multiple towers provides the opportunity for investigating both its spatial and temporal characteristics and the relation between them. Verification of Taylor's hypothesis would demonstrate that the time series analysis, in either autocorrelation function form or spectral form, can be translated through the mean wind speed directly to a spatial description. This in turn can be translated through the aircraft speed to the time series characteristics experienced by the aircraft.

Initial studies of Taylor's hypothesis showed that autocorrelation functions scaled by the mean wind speed to the expected spatial functions agreed quite well (least of all for the lateral wind component) with the measured spatial correlations except where the responses of different instruments caused small deviations. The characteristic lengths determined from exponential functions fit to the spatial correlation data show some tendency to increase with height and are generally greatest for the longitudinal component. These correlation function characteristic lengths are not necessarily those significant to aircraft applications, however. This is because large eddies, which are not critical as turbulence to the aircraft, are sampled in the tower measurements and dominate the scale of the correlation function. Therefore, it is also important to consider the spectral form of the spatial distribution of turbulence. Taylor's hypothesis should again be evaluated for application to the reasonably good understanding of temporal spectra. It is recognized that in the shear flow of the atmospheric boundary layer only eddy sizes smaller than some critical value, controlled by the shear, should follow Taylor's hypothesis.

Phase and coherency spectra were calculated for various pairs of tower-based measurements to determine what range of frequencies were advected with the mean wind speed over each separation distance. It was tentatively



# Contrails

concluded that the lower frequency limit for Taylor's hypothesis,  $n_0$ , varies approximately inversely with the height for a given stability. For a more unstable atmosphere a larger value of  $n_0$  is indicated. For stable conditions,  $n_0$  was found to be about  $2/3$  of  $u^*/kz$ , a measure of the shear. For unstable conditions, the ratio between  $n_0$  and  $u^*/kz$  was found to be 1.0 or larger. Another way of viewing this limitation is that eddy sizes smaller than 8 to 12 times the height of measurement follow Taylor's hypothesis.

It was also found in the phase spectral analysis that the eddies were not advected exactly with the mean wind speed but with a translation speed of about 10 percent higher. It was also observed that eddies were advected coherently over a maximum distance of about  $2/3$  their alongwind dimension.

Some conclusions can now be reached regarding the understanding of spatial spectra of interest to aircraft application during take-off and landing. First, since the largest wave length of interest is about 600 meters, the nondimensional frequency lower limit of interest is  $nz/\bar{U} = 0.1$  at a height of 60 meters which decreases to  $nz/\bar{U} = 0.01$  as the aircraft descends to 6 meters. But one can be confident in translating temporal spectra to spatial spectra through Taylor's hypothesis for eddy sizes smaller than about 10 times the height, or equivalently for  $nz/\bar{U} = 0.01$  and greater. Thus at 60 meters the turbulence spectra encountered by aircraft flying in the direction of the mean wind can be reasonably well described but as the aircraft descends to the surface an increasing range of eddy sizes is introduced at low frequencies, extending to  $nz/\bar{U} = 0.01$  at 6 meters, for which the energy content is uncertain. Uncertainty above 60 meters again increases because of the lack of time series data and analysis reflecting dominant convective features as well as the lack of understanding of the spatial characteristics.

The translation of time series spectra to that experienced by an aircraft holds only for the case where the aircraft flies in the direction of the wind. A more general approach for presenting the turbulence data from

multiple towers is to plot the correlation function jointly in space and time for various wind directions to the line of towers, simulating different directions of flight relative to the mean wind. Such diagrams (Figures 7.42 through 7.47) showing contours of equal correlation as a function of both time lag and space lag, can be used to estimate the correlation function experienced by an aircraft moving through different points in space at different times, determined by its speed. Diagrams presented for the two limiting extremes in wind direction conditions, i.e., along the line of towers and normal to the line of towers, show correlation contours of approximately elliptical shape. The major axis is oriented along a diagonal with a slope approximately equal to the mean wind speed for the case with the wind along the line of towers. For the wind normal to the line the major axis is along the time lag axis, demonstrating that the alongwind dimension of the eddies (utilizing Taylor's hypothesis) is larger than the crosswind dimension.

The results discussed so far relate to average conditions encountered by an aircraft. Since critical turbulence conditions can occur in single gusts or over short nonstationary periods, the necessity for individual and joint probability distribution analyses must not be forgotten. The extreme individual gusts or combinations of gusts exceeding permissible limits can be determined from them for various high-pass filterings of the data, appropriate to various aircraft response characteristics and various aircraft speeds. The bispectral analyses may also be useful in identifying nonsymmetrical characteristics of the gusts which are hazardous to the aircraft and which are not evident in averaged lower moment analysis.

#### RECOMMENDED MEASUREMENTS AND OPTIMIZED ARRAY

The primary purpose of the TOLCAT investigation to date has been to develop and demonstrate the capability for turbulence measurements from multiple towers and the approach used to analyze and organize the turbulence data. Modeling of the turbulence, appropriate to take-off and landing problems,

can only result from an extensive measurement and analysis effort to follow the development phase.

## Dual System Operation

A continued experimental program should be conducted with two similar measurement systems. The first system would be permanently installed at a reference measurement site where influences of terrain and unusual flow features would be minimized and where a wide range of pertinent meteorological variables would be encountered. Experiments would be conducted in all seasons and over the full wind and temperature ranges of interest for modeling the turbulence as a function of the controlling effects of mechanical and convective turbulence. Modeling the temporal and spatial characteristics of the turbulence as a function of meteorological variables, excluding other influences, would eliminate the need for extensive testing in various climatological regimes.

The second system would be utilized in a semi-portable mode intermittently at sites where extraordinary terrain or flow features are expected to seriously alter the turbulence structure from that described by the general model developed at the primary site. The semi-portable system would be moved between various locations where different turbulence situations would be encountered. The sensors, mounting booms, 40-meter towers, cables and recording system would be completely portable for moving between sites while 80-meter towers would be permanently installed at each of the locations of interest. Such intermittent experimentation should include measurements at a location in the lee of a large mountain range such as the Rocky Mountains where waves generated in the large scale flow can cause unusual and extreme gust characteristics already evident in clear air turbulence aloft and which are undoubtedly propagated into the surface layer. Terrain features of a smaller scale, such as small mountains or large hills and canyons, can cause wakes and channeling of the flow which might significantly alter the turbulence structure from a general model. Large building complexes

could cause similar effects. Another common situation where a general turbulence model would most likely be significantly altered is the land-sea breeze circulations in coastal regions. Here, different turbulence characteristics advected from over land and over water can cause sharp nonstationarities and inhomogeneities in the turbulence field. Of equal significance in this situation are the wind direction and speed shears within the scale of the measurement system.

## Sensor Array Description

The measurement system configuration utilized at the primary and secondary sites would simply be an extension of that used to date in TOLCAT studies. The basic "L" array discussed previously would be utilized with the measurement capability being extended from one to three levels of simultaneously operated instrumentation and the sensing location at a given level held to the minimum necessary, as determined from analysis to date. The sensors would be supported by 6 permanent towers, 80 meters tall, and 4 portable towers expandable to 40-meter height, as shown in Figure 8.1.

As shown, the top measurement level at 80 meters would consist of sensors on 6 towers: 4 in the direction of the prevailing wind and 3 normal to that direction, forming the "L." The bottom measurement level would be at 10-meter height with the sensors, again, mounted on the 80-meter permanent towers. The intermediate level would be adjustable to various heights. A traveling dolly and instrument support boom (Figure 8.2) would be installed on each of the 6 permanent towers and would move the sensors between the top and bottom sensor locations for spatial turbulence definition at various heights in different experiments. Also, the 4 expandable towers could be cranked up to the traveling boom level to give more detailed spatial definition in the lowest 40 meters where it is most critically needed.

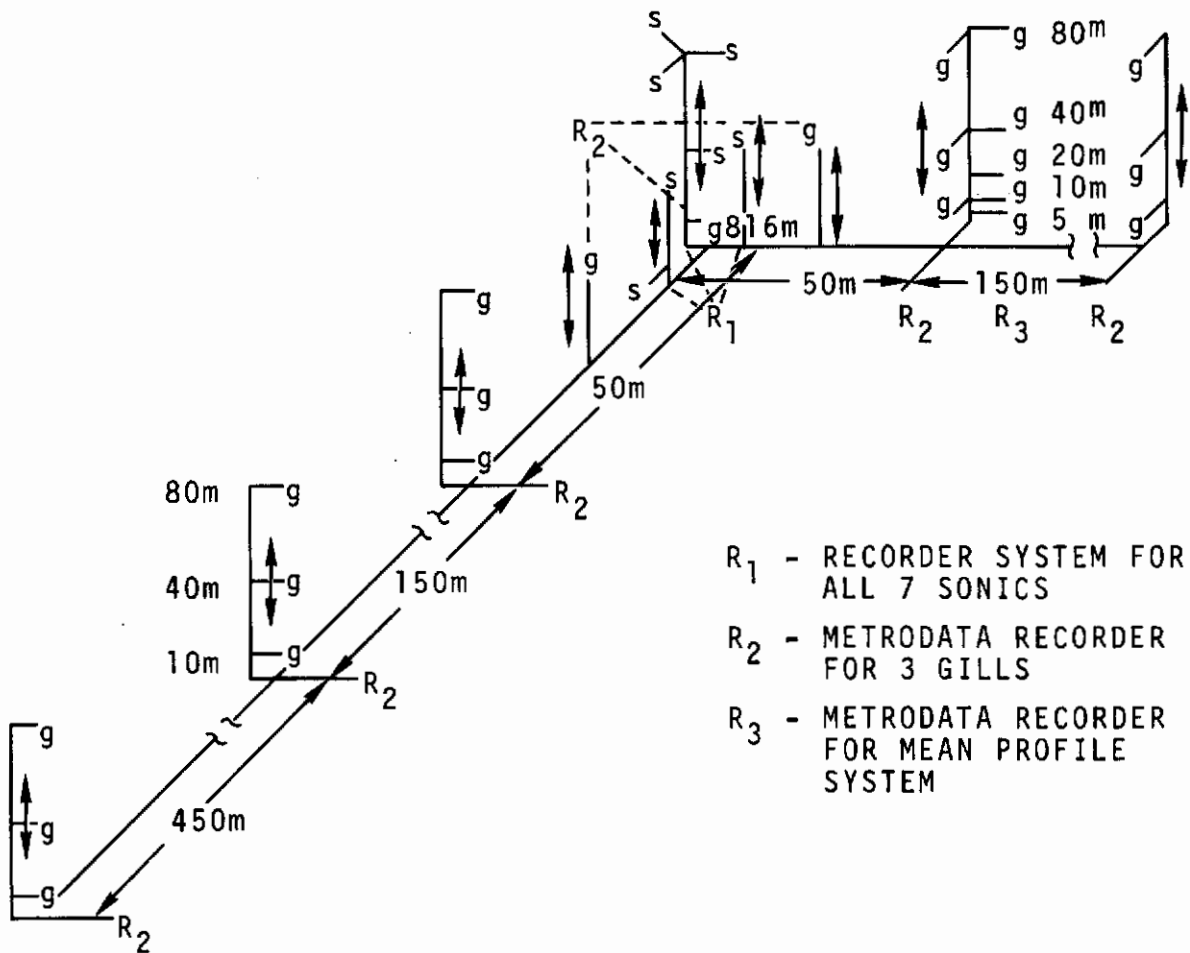


Figure 8.1 Optimized TOLCAT Array



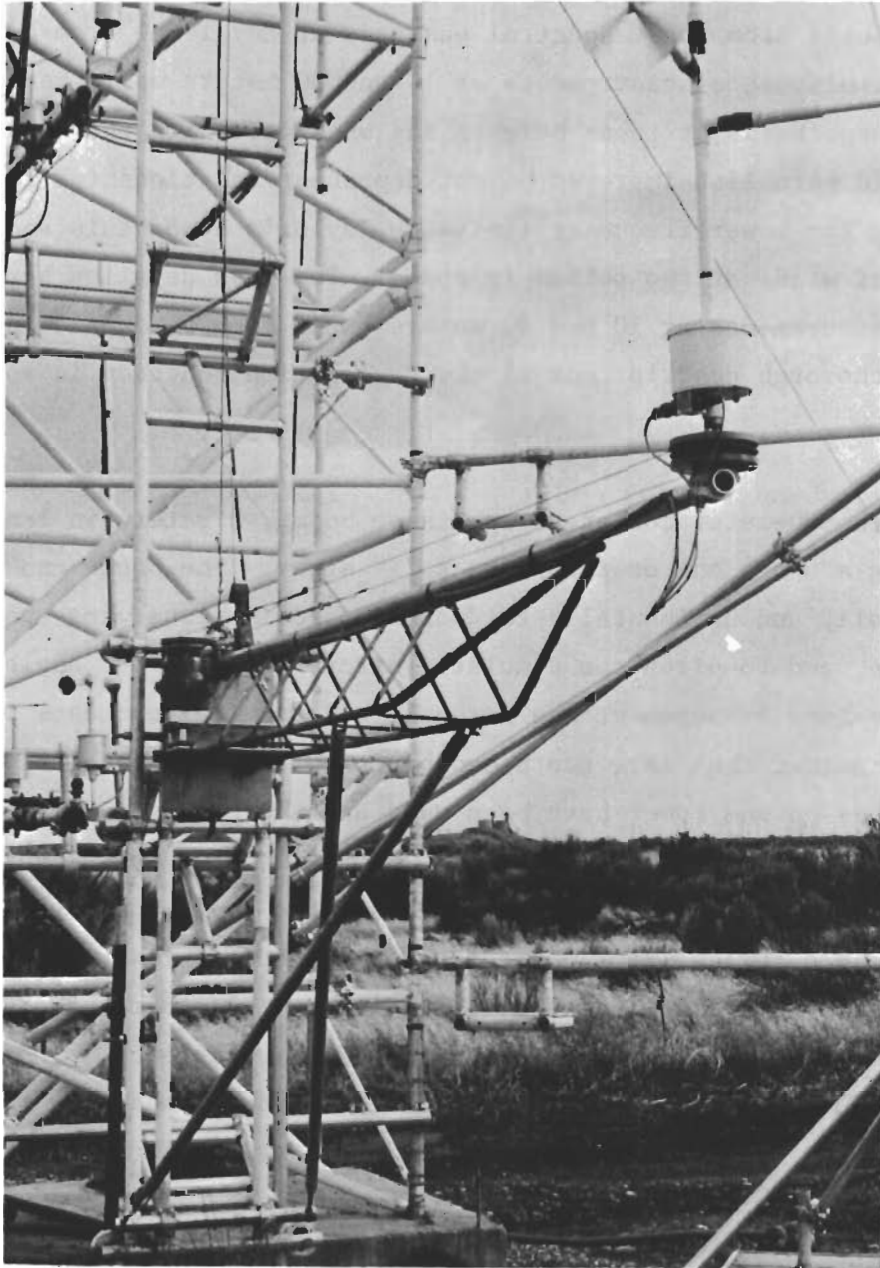


Figure 8.2 Traveling Instrument Boom



# Contrails

From analyses performed to date, instrument locations at the intermediate level were determined to be sufficiently dense to enable detailed space-time correlation function analysis as well as a thorough evaluation of Taylor's hypothesis from phase spectral analysis at any level from 10 to 40 meters. The simultaneous measurements at 10 and 80 meters would be used to test Taylor's hypothesis at those heights and when used with the mobile level data would establish improved height dependent relationships for time series spectra, for lower frequency limits to Taylor's hypothesis and for cross-spectra of winds at two points in space. The less detailed horizontally spaced measurements at 10 and 80 meters could then be supplemented to also yield thorough descriptions of the correlation function in space and time.

At the top of the 80-meter corner tower, three booms, 5 meters in length, each supporting a sonic anemometer, form a "T" array. The booms can be pivoted vertically and horizontally to decrease and increase wing span and tail separation, and to pitch the simulated aircraft at various angles. While the three-boom arrangement was not utilized for T-array tests in experiments performed thus far, two booms pivoting at their respective attachment plates on one tower have been used and the extension to the three-boom arrangement is straightforward. At the intermediate level, the sonic on the mobile boom of the corner tower and the sonics on top of the 40-meter expandable towers, each 8 meters from the corner tower at right angles, also form a "T" allowing adjustable pitch. All other sensors are Gills except for a sonic at 10 meters for providing surface flux characteristics recognized as being necessary in the discussion of analysis results in Section VII. An additional T-array of interest at the intermediate level is formed with Gills at 24 meters from the corner sonic.

The second 80-meter tower in the short sampling leg would be equipped with 5 Gills at 5, 10, 20, 40, and 80-meter heights for wind micrometeorological profile definition in addition to the other sensors previously mentioned for horizontal spatial turbulence description. Such a profile system is shown

in Figure 8.3. (The previous cup and vane micrometeorological profile system discussed in the Interim Report is being replaced by the Gills as also seen in Figure 8.3.) Temperature and humidity profiles along with net radiation measurements will be added to the system.

All wind sensors would be oriented into the mean wind prior to an experiment with the remotely controlled rotor bases as utilized and demonstrated in the previous TOLCAT experiments. The remotely operated electrolytic sensor leveling method is available and would be particularly important for the three-boom T-array. Lead screw actuator motors are directly adaptable to the presently used lead screw adjusted boom leveling supports.

## Data Acquisition

The data acquisition systems for the permanent and the portable measurement systems would be the same except for the data from the sonic anemometers. Each 80-meter tower, with the exception of the corner tower, would utilize a cassette field digital recorder. A cassette digital recorder, Metrodata Model DL-620, though not used extensively in past TOLCAT experiments, was demonstrated in one experiment (Figure 8.4) to be suitable for recording the TOLCAT sensor outputs and for reading into the SEL 840A computer for data processing with the TOLCAT programs. The nine signals from 3 Gill anemometers would each be sampled at a rate of approximately 6 samples per second. Another cassette digital recorder would be used for the 3 Gills near the corner of the array: one at the 10-meter level on the corner tower and one on each of the two 40-meter towers at 24-meter distance from the corner tower along each leg of the array. A cassette digital recorder would also be utilized for recording the micrometeorological profile data from the 5 levels at a slower repetitive sampling rate.

At the reference site the two Ampex FR-1300, 14-channel, analog tape recorders, used for most of the recording in the past, would be used in the primary system to record the signals from the 7 sonics at the center of the

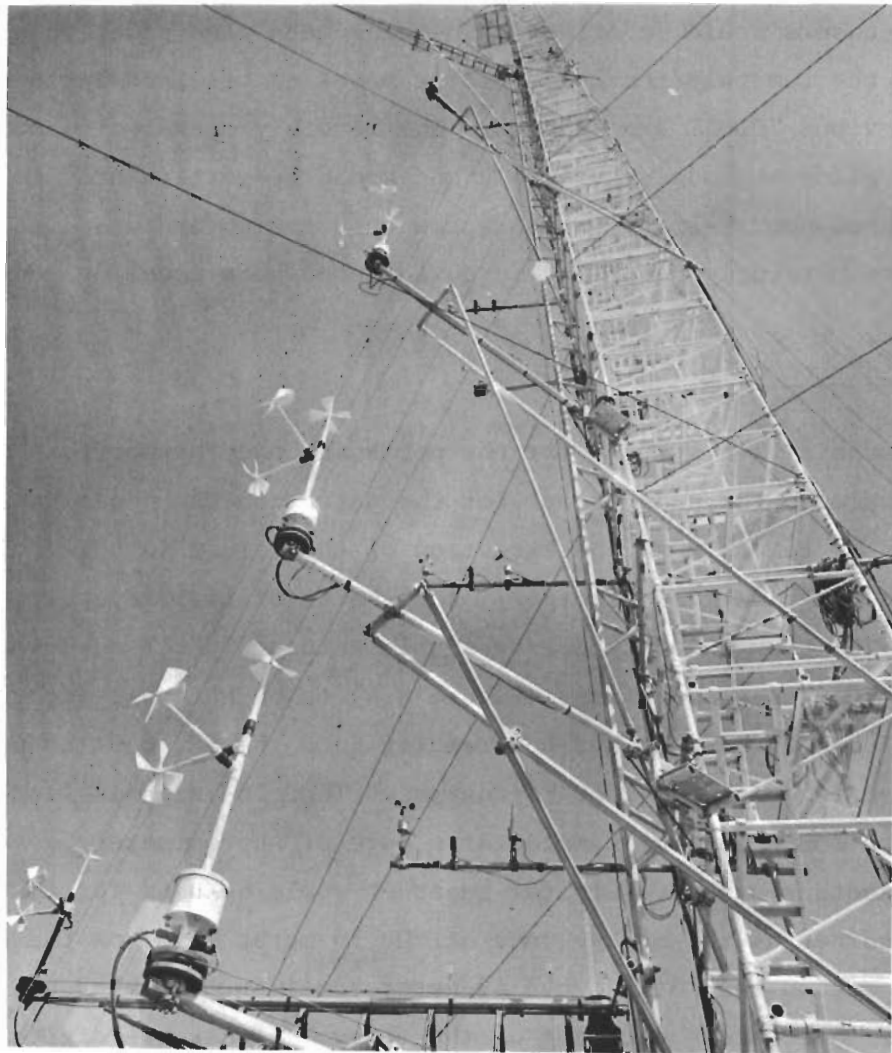


Figure 8.3 Micrometeorological Profile System Utilizing Gill Anemometers

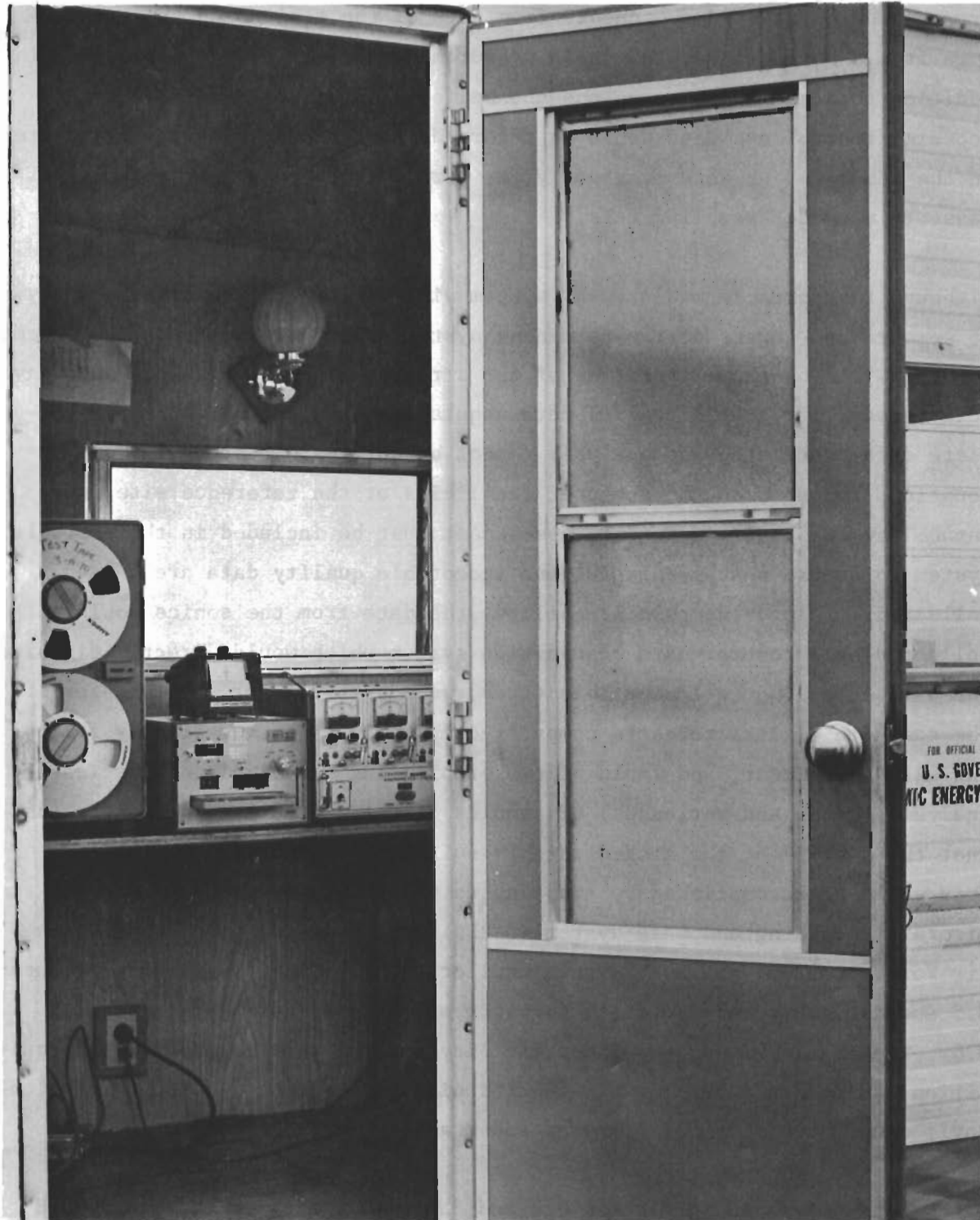


Figure 8.4 Field Digital Recorder, Metrodata DL-620 in TOLCAT System



array. The three wind components from each of the sonics and the temperature from a sonic at each of the 3 measurement heights would be recorded in addition to a timing pulse on one channel of each of the recorders for coordination. These data would be recorded continuously and digitized later in the SEL 840A, as done previously, at a rate equal to a multiple of the cassette recorder sampling rate.

Although the portable measurement system will utilize the same basic array of sensors and towers as the permanent system, and the same recording scheme for the Gills on the extremities of the array, the portable system must have more versatility in the central data acquisition system. Because the complete data processing and analysis cannot be carried out promptly for locations remote from the computer facilities at the reference site, some capability for preliminary data assessment must be included in the portable system to assure that meaningful and acceptable quality data are being collected. To provide this capability, the data from the sonics would be collected by a central data acquisition system which would directly digitize the data onto computer compatible tapes, would provide for the transfer of the cassette digital tapes to computer compatible tapes immediately following each experiment, and would allow for plotting and simple statistical analyses (means and variances) of samples of the stored data demonstrating that the quality of the stored data is suitable for detailed analysis. This would be accomplished by adapting to the TOLCAT system, the Combat Aircraft Recording and Data System (CARDS) made available from a previous Air Force program. The semi-truck trailer housing CARDS is shown in Figure 8.5 and the equipment contained in the trailer is illustrated in Figure 8.6. The trailer is an excellent facility for the transportable data acquisition equipment, providing air conditioning and heating for the controlled environment necessary for computer and magnetic tape equipment.

Block diagrams shown in Figures 8.7 and 8.8 illustrate the existing CARDS equipment housed in the trailer and the optimized data acquisition, processing, and quality monitoring system.



Figure 8.5 CARDS Trailer



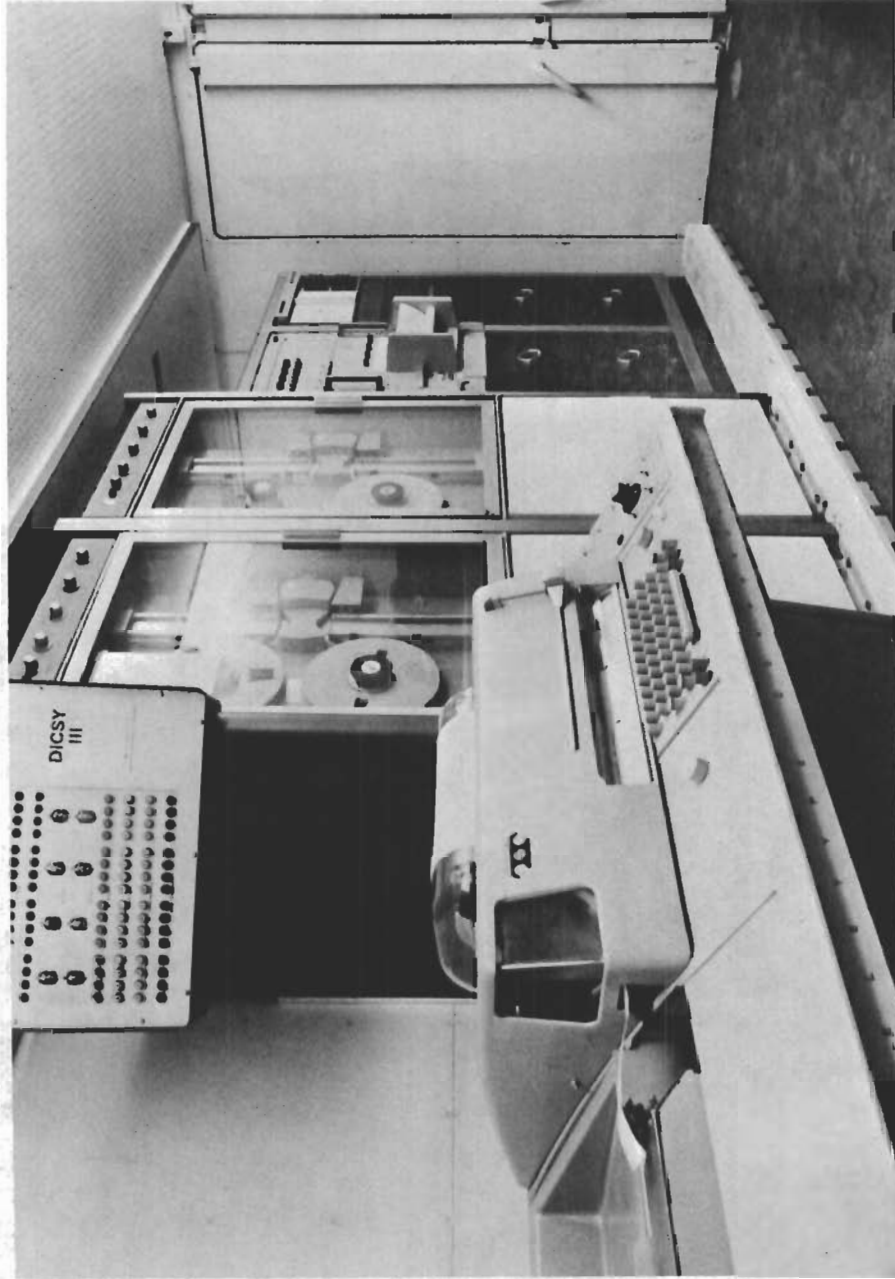


Figure 8.6 CARDS Equipment

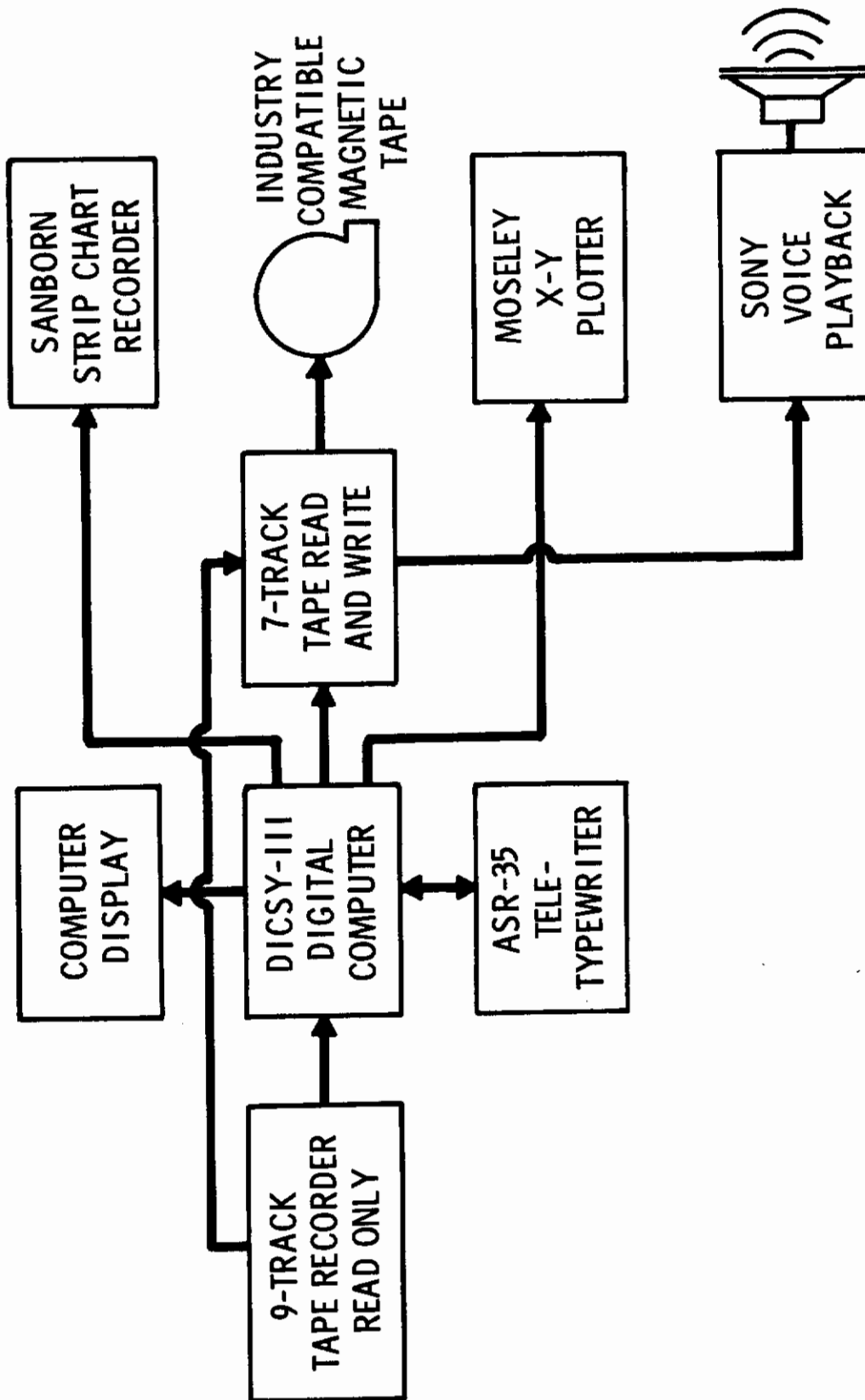


Figure 8.7 CARDS Digital Data Processing System - Major Assemblies

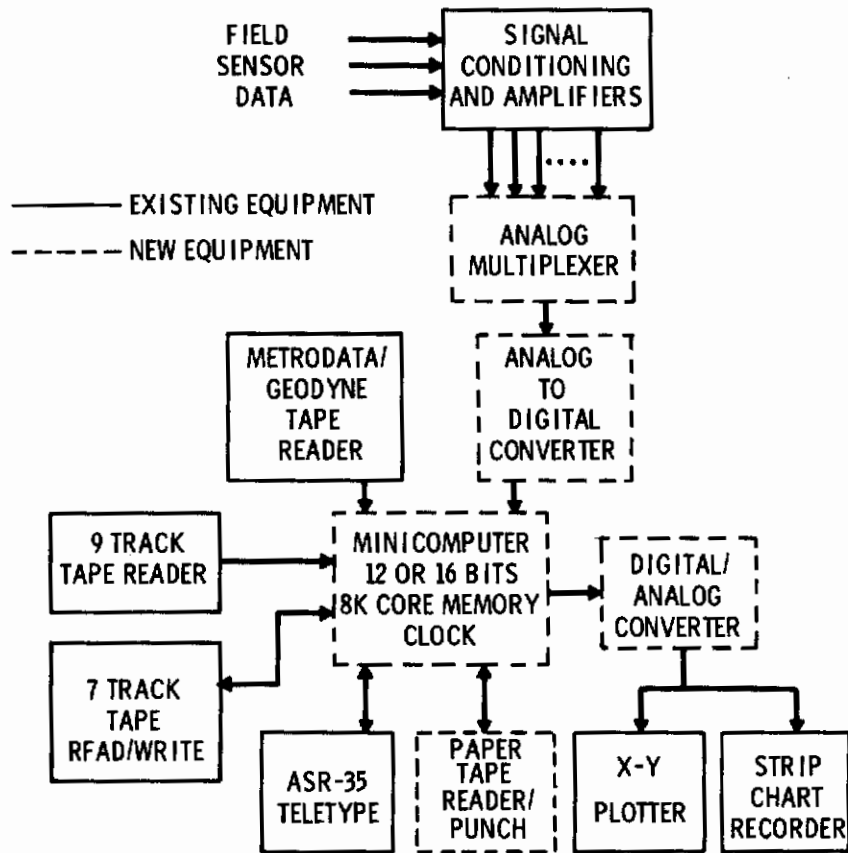


Figure 8.8 Optimized Configuration for Portable Wind Turbulence Data Acquisition System

# *Contrails*

The CARD's system computer (DISCY-III) is a hybrid specialized computer utilizing a hexadecimal word format system with no reasonable data programming capability. Therefore, to accomplish the necessary data management functions prior to data storage and the minimal statistical analysis for verification of data quality, a general purpose, mini-computer would replace the DISCY and allow effective utilization of the existing CARD's system peripheral equipment for TOLCAT applications.

The measurement systems described would provide for the most efficient utilization of data for modeling purposes. Applying the analysis programs utilized to date, the height dependent features of the turbulence, the horizontal spatial characteristics, and the dependence on average meteorological parameters as well as unusual flow and terrain features would be determined with a minimum of data collection.

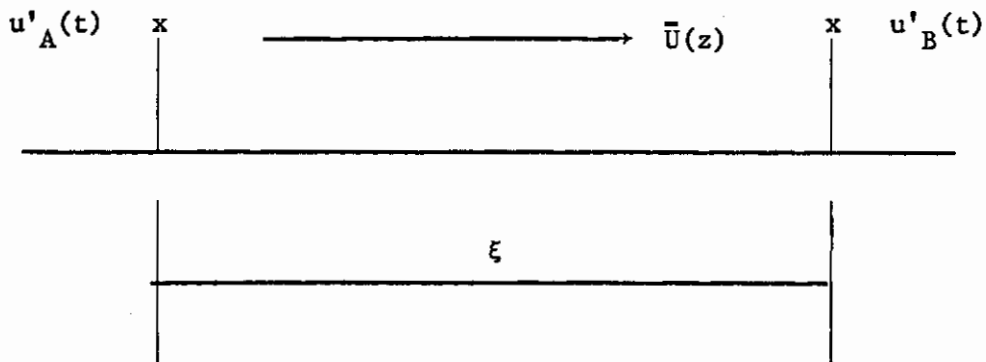
# *Contrails*

(Intentionally Blank)

APPENDIX I

PHASE SPECTRUM IN RELATION TO TAYLOR'S HYPOTHESIS

Derivation of the phase spectrum for data from 2 points using Taylor's hypothesis.



If Taylor's hypothesis hold such that  $u'_B(t)$  is the same process as  $u'_A(t)$  but lagging by time  $t' = \xi/\bar{U}$

then

$$u'_B(t) = u'_A(t-t') \quad . \quad (I.1)$$

$u'_A(t)$  and  $u'_B(t)$  both have the same complex Fourier expansion,  $dZ(\omega)$ . These increments are orthogonal for different values of  $\omega$  so that

$$dZ^*(\omega_1) dZ(\omega_2) = 0 \quad \omega_1 \neq \omega_2 \quad (I.2)$$

$$dZ^*(\omega) dZ(\omega) = S(\omega) d\omega \quad (I.3)$$

where  $S(\omega)$  is the power spectrum of  $u'(t)$ .



# Contrails

Therefore,

$$u'_A(t) = \int_{-\infty}^{\infty} e^{i\omega t} dZ(\omega) \quad (I.4)$$

$$u'_B(t) = \int_{-\infty}^{\infty} e^{i\omega(t-t')} dZ(\omega) \quad (I.5)$$

The covariance between  $u'_A$  and  $u'_B$  at time lag  $\tau$  may be written

$$\begin{aligned} \text{Cov}[u'_A(t), u'_B(t+\tau)] &= \overline{u'_A(t) u'_B(t+\tau)} = \overline{u'(t) u'(t+\tau-t)} \\ &= \overline{u'^*(t) u'(t+\tau-t')} = \overline{\int_{-\infty}^{\infty} e^{-i\omega_1 t} dZ^*(\omega_1) \int_{-\infty}^{\infty} e^{i\omega_2(t+\tau-t')} dZ(\omega_2)} \\ &= \int_{-\infty}^{\infty} \int_{-\infty}^{\infty} e^{i[(\omega_2-\omega_1)t+\omega_2(\tau-t')]} \overline{dZ^*(\omega_1) dZ(\omega_2)} = \int_{-\infty}^{\infty} e^{-i\omega t'} S(\omega) e^{i\omega\tau} d\omega. \end{aligned} \quad (I.6)$$

Define the cross spectrum between  $u'_A$  and  $u'_B$  as

$$S_{AB}(\omega) = \text{Co}_{AB}(\omega) - i \text{Qu}_{AB}(\omega) \quad (I.7)$$

Then

$$\overline{u'(t) u'(t+\tau-t')} = \int_{-\infty}^{\infty} S_{AB}(\omega) e^{i\omega\tau} d\omega = \int_{-\infty}^{\infty} e^{-i\omega t'} S(\omega) e^{i\omega\tau} d\omega \quad (I.8)$$

# Contrails

Therefore,

$$S_{AB}(\omega) = e^{-i\omega t'} S(\omega) = \cos \omega t' S(\omega) - i \sin \omega t' S(\omega) , \quad (I.9)$$

$$\text{Co}_{AB}(\omega) = \cos \omega t' S(\omega) , \quad (I.10)$$

$$\text{Qu}_{AB}(\omega) = \sin \omega t' S(\omega) , \quad (I.11)$$

and

$$\text{phase spectrum} = \phi(\omega) = \tan^{-1} \frac{\text{Qu}_{AB}(\omega)}{\text{Co}_{AB}(\omega)} = \tan^{-1} \tan \omega t' = \omega t' . \quad (I.12)$$

Since

$$t' = \xi / \bar{U}$$

and

$$\omega = 2\pi n ,$$

we have

$$\phi(n) = \frac{2\pi n \xi}{\bar{U}} . \quad (I.13)$$

APPENDIX II

BISPECTRAL ANALYSIS

DEFINITIONS

If a time series possesses third-order stationarity, a covariance tensor of two lags may be defined as the following expectation function of the wind turbulence components,  $u_i$ ,  $i = 1, 2, 3$ ,

$$Q_{ijk}(\tau_1, \tau_2) = \overline{u_i(t) u_j(t+\tau_1) u_k(t+\tau_2)} \quad (II.1)$$

The bispectral tensor is defined as follows:

$$B_{ijk}(\omega_1, \omega_2) \equiv \iint_{-\infty}^{\infty} Q_{ijk}(\tau_1, \tau_2) e^{-i(\omega_1 \tau_1 + \omega_2 \tau_2)} d\tau_1 d\tau_2 \quad (II.2)$$

where

$$Q_{ijk}(\tau_1, \tau_2) = \frac{1}{4\pi^2} \iint_{-\infty}^{\infty} B_{ijk}(\omega_1, \omega_2) e^{+i(\omega_1 \tau_1 + \omega_2 \tau_2)} d\omega_1 d\omega_2 \quad (II.3)$$

$B_{ijk}(\omega_1, \omega_2)$  is a complex valued function on the real  $\omega_1, \omega_2$  plane.

$Q_{ijk}(\tau_1, \tau_2)$  is a real valued function on the real  $\tau_1, \tau_2$  plane.

In the following discussion and in the analysis section the only third-order covariance functions and bispectra considered are those for which all tensor letters are the same. Hence the notation from here on for these two functions will include one subscript only.

## PROPERTIES OF $Q_1(\tau_1, \tau_2)$

### Comparisons with Second-Order Covariance Function

The liability of covariance or spectral analysis for applied purposes is that different original data functions are mapped into the same covariance or spectral function. Therefore, it seems reasonable to assume that the same covariance function can represent two velocity histories that would have quite different effects on aircraft encountering these velocities. This is true of third-order covariances as well as second-order covariances. However, interest in the third-order covariance function can be motivated by illustrating different time series that the third-order covariance function distinguishes between while the second-order covariance functions do not.

The essential time series property to be considered is lack of symmetry with respect to either the  $u_i$  axis or the  $t$  axis and with respect to any translation of either axis. Nonsymmetry with respect to the  $t$  axis may be illustrated by Figure II.1

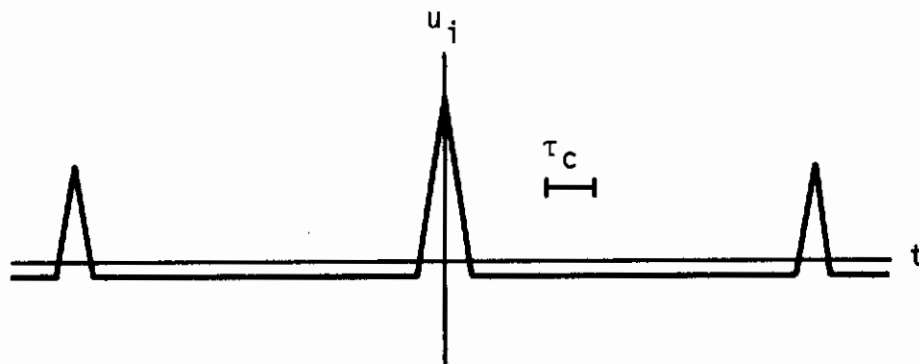


Figure II.1 Even Function, Skewed with Respect to Horizontal Axis

Figure II.1 illustrates a time series that is an even function for which  $\overline{u_1}$  is zero and for which  $u_1$  is positively skewed. It is easy to see that when the time lags  $\tau_1$  and  $\tau_2$  of  $Q(\tau_1, \tau_2)$  are small compared to  $\tau_c$ , the covariance value will be positive, since the covariance function is continuous and since as  $\tau_1$  and  $\tau_2$  approach zero  $Q(\tau_1, \tau_2)$  approached  $\overline{u_1^3}$ , which is greater than zero. Now if the time series is inverted with respect to the  $t$  axis, the skewness is of opposite sign, and the values for all the third-order covariances change sign while the values for all the second-order covariances (autocovariances) remain unchanged. If  $u_1$  is  $w$  for an aircraft flying near the ground, this difference could be important.

Nonsymmetry with respect to the  $u_1$  axis may be illustrated as shown in Figure II.2.

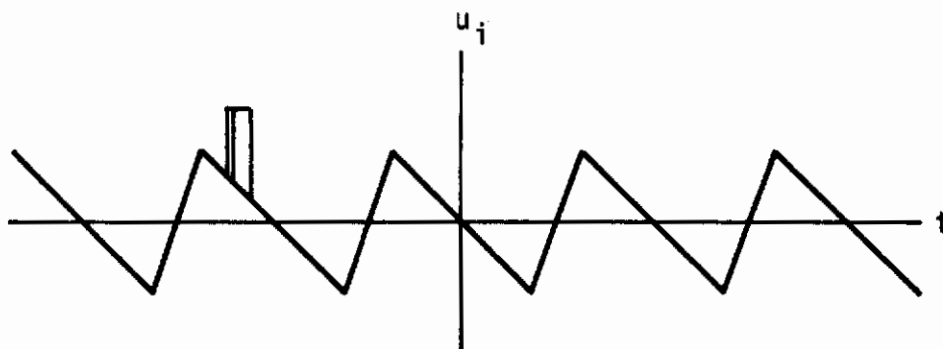


Figure II.2 Odd Function, Skewed with Respect to Vertical Axis

Figure II.2 illustrates time series for which both  $\overline{u_1}$  and  $\overline{u_1^3}$  are zero, but which is an odd function and nonsymmetrical with respect to any placing of the  $u_1$  axis.

The three short vertical lines illustrate  $\tau_1$  (lines 1 and 2) and  $\tau_2$  (lines 1 and 3). In the case where  $\tau_1 \ll \tau_2$ , by inventing an appropriate numerical example and calculating, it is evident that

$$Q_1(\tau_1, \tau_2) > 0 \quad , \quad (II.4)$$

$$Q_1(\tau_2 - \tau_1, \tau_2) < 0 \quad , \quad (II.5)$$

and

$$Q_1(\tau_1, \tau_2) + Q_1(\tau_2 - \tau_1, \tau_2) = 0 \quad . \quad (II.6)$$

If the time series of Figure II.2 is reflected with respect to the  $u_1$  axis, the descriptions in Equations II.4 and II.5 would have the inequalities reversed. In fact  $Q_1(\tau_2 - \tau_1, \tau_2)$  in the reflection is identical to  $Q_1(\tau_1, \tau_2)$  for the figure drawn. However, the second-order covariance makes no distinction between the two.

The third-order covariance function also has its "blind spots." Starting with any truncated data sample, a sample four times as long may be generated by adding first a reflection of the original sample with respect to one axis and then adding a reflection of the doubled sample with respect to the other axis. The resulting time series function maps into the null third-order covariance function, i.e., the value of  $Q_1(\tau_1, \tau_2)$  is zero for all values of the arguments.

### Redundancy in the Third-Order Covariance Function

The second-order covariance function (autocovariance) is the same for negative as for positive arguments. For the third-order covariance function, one octant maps into the remainder of the  $\tau_1, \tau_2$  plane, if the octant is any of the 1st, 2nd, 5th, or 6th octants. One of these octants also maps into the entire 2nd quadrant and into the entire 4th quadrant.



# Contrails

This is an immediate result of interchanging the arguments and of various substitutions of the type,  $t = t' - \tau_1$ , in Equation II.1, which are permissible for a third-order stationary process. If  $\tau_2 > \tau_1 > 0$ , then

$$Q_1(\tau_1, \tau_2) = Q_1(\tau_2, \tau_1) \quad , \quad (II.7)$$

$$Q_1(\tau_1, \tau_2) = Q_1(-\tau_1, \tau_2 - \tau_1) = Q_1(\tau_2 - \tau_1, -\tau_1) \quad , \quad (II.8)$$

and

$$Q_1(\tau_1, \tau_2) = Q_1(-\tau_2, -\tau_1 - \tau_2) = Q_1(\tau_1 - \tau_2, -\tau_2) \quad . \quad (II.9)$$

Equation II.7 shows the mapping of the 2nd octant into the 1st octant; Equation II.8 shows the mapping of the same octant into the 2nd and 4th quadrants; Equation II.9 shows the mapping of the same octant into each octant of the third quadrant. The mapping may be illustrated by Figure II.3. The letters a, b, c, and d represent different values of the covariance function.

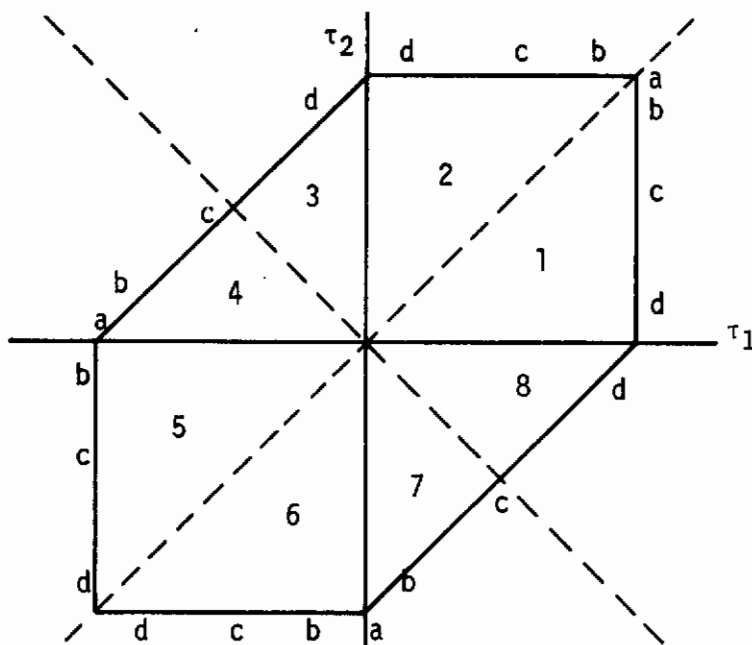


Figure II.3 Mapping of  $Q_1(\tau_1, \tau_2)$  from First Octant into Remainder of  $\tau_1, \tau_2$  Plane

If  $u_1(t)$  is symmetrical with respect to the  $u_1$  axis, as shown in Figure II.1, the additional relation

$$Q_1(\tau_1, \tau_2) = Q_1(\tau_2 - \tau_1, \tau_2) \quad (\text{II.10})$$

holds, as can be seen from inspection. By using Equation II.9 for this case,

$$Q_1(-\tau_1, -\tau_2) = Q_1(\tau_1, \tau_2) \quad (\text{II.11})$$

which simply states that  $u_1(t)$  is an even function of  $t$ .

Figure II.2 illustrates the opposite case, where  $u_1(t)$  is an odd function and

$$Q_1(-\tau_1, -\tau_2) = -Q_1(\tau_1, \tau_2) \quad (\text{II.12})$$

## COMPUTATION OF $B_1(\omega_1, \omega_2)$ FOR FAST FOURIER TECHNIQUES

Computation of  $B_1(\omega_1, \omega_2)$  according to Equation II.2 requires first computing  $Q_1(\tau_1, \tau_2)$  according to Equation II.1, and this procedure is economically unfeasible. The way around the trouble is to compute the bispectrum from the fast Fourier coefficients while these are all in the computer core according to

$$B_1(\omega_1, \omega_2) = C_1(\omega_1) C_1(\omega_2) C_1^*(\omega_1 + \omega_2) \quad (\text{II.13})$$

where

$$C_1(\omega) = \int_{-\infty}^{\infty} u_1(t) e^{-i\omega t} dt \quad (\text{II.14})$$

# Contrails

and where  $C^*$  is the complex conjugate of  $C$ .

The derivation of the relationship is as follows.

$$\begin{aligned}
 & C_1^*(\omega_1 + \omega_2) C_1(\omega_1) C_1(\omega_2) \\
 &= \int_{-\infty}^{\infty} u_1(t) e^{i(\omega_1 + \omega_2)t} dt \int_{-\infty}^{\infty} u_1(s) e^{-i\omega_1 s} ds \int_{-\infty}^{\infty} u_1(r) e^{-i\omega_2 r} dr \\
 &= \int_{-\infty}^{\infty} \int_{-\infty}^{\infty} \int_{-\infty}^{\infty} u_1(r) u_1(s) u_1(t) e^{-i\omega_1(r-t) - i\omega_2(s-t)} dt ds dr \quad . \quad (II.15)
 \end{aligned}$$

Let

$$r - t = \tau_1; \quad dr = d\tau_1; \quad s - t = \tau_2; \quad ds = d\tau_2 \quad , \quad (II.16)$$

then the last expression becomes

$$\begin{aligned}
 & \int_{-\infty}^{\infty} \int_{-\infty}^{\infty} \int_{-\infty}^{\infty} u_1(t + \tau_1) u_1(t + \tau_2) u_1(t) e^{-i(\omega_1 \tau_1 + \omega_2 \tau_2)} dt d\tau_1 d\tau_2 \\
 &= \int_{-\infty}^{\infty} \int_{-\infty}^{\infty} e^{-i(\omega_1 \tau_1 + \omega_2 \tau_2)} \int_{-\infty}^{\infty} u_1(t) u_1(t + \tau_1) u_1(t + \tau_2) dt d\tau_1 d\tau_2 \\
 & \int_{-\infty}^{\infty} \int_{-\infty}^{\infty} e^{-i(\omega_1 \tau_1 + \omega_2 \tau_2)} Q_1(\tau_1, \tau_2) d\tau_1 d\tau_2 = B_1(\omega_1, \omega_2) \quad . \quad (II.17)
 \end{aligned}$$

PROPERTIES OF  $B_1(\omega_1, \omega_2)$

First of all it can be easily shown that if Equation II.11 holds, the entire content of  $Q_1(\tau_1, \tau_2)$  is transformed into the real part of  $B_1(\omega_1, \omega_2)$ . Likewise if Equation II.12 holds, the entire content of  $Q_1(\tau_1, \tau_2)$  is transformed into the imaginary part of  $B_1(\omega_1, \omega_2)$ .

$B_1(\omega_1, \omega_2)$  for the entire  $\omega_1, \omega_2$  plane can be obtained from any one octant, but the mapping is quite different from that shown for  $Q_1(\tau_1, \tau_2)$ . For convenience, the first octant will be chosen as the octant to be mapped into the other octants. Then the first octant is trivially mapped into the second octant by

$$B_1(\omega_1, \omega_2) = C_1(\omega_1) C_1(\omega_2) C_1^*(\omega_1 + \omega_2) = B_1(\omega_2, \omega_1) \quad . \quad (II.18)$$

The first octant maps conjugately into the fifth octant by

$$\begin{aligned} B_1(\omega_1, \omega_2) &= C_1(\omega_1) C_1(\omega_2) C_1^*(\omega_1 + \omega_2) = C_1^*(-\omega_1) C_1^*(-\omega_2) C_1(-\omega_1 - \omega_2) \\ &= B_1^*(-\omega_1, -\omega_2) \quad . \end{aligned} \quad (II.19)$$

By using Equation II.19, the fifth octant maps into the sixth as the conjugate of the first octant.

The equation mapping the first octant into the eighth octant maps only into the upper portion of the eighth octant, i.e., that part between the  $\omega_1$  axis and a line from the origin to the right with  $-0.5$  slope. For  $\omega_2 - \omega_1 \geq \omega_2 \geq 0$ ,  $B_1(\omega_1 - \omega_2, \omega_2)$  is in the first octant, or on its border, and

$$\begin{aligned} B_1(\omega_1 - \omega_2, \omega_2) &= C_1(\omega_1 - \omega_2) C_1(\omega_2) C_1^*(\omega_1) \\ &= C_1^*(\omega_1) C_1^*(-\omega_2) C_1(\omega_1 - \omega_2) = B_1^*(\omega_1 - \omega_2) \quad . \end{aligned} \quad (II.20)$$

Provided that the above inequalities are met,  $\omega_2$  will not be more than half as great as  $\omega_1$ , and the argument will be in the upper portion of the eighth octant. By using Equations II.18 and II.19 the half octant maps into the upper half of the third octant as the conjugate of the first octant, and into the lower halves of the fourth and seventh octants exactly as the first octant. The mapping of Equation II.20 can be graphically illustrated by Figure II.4.

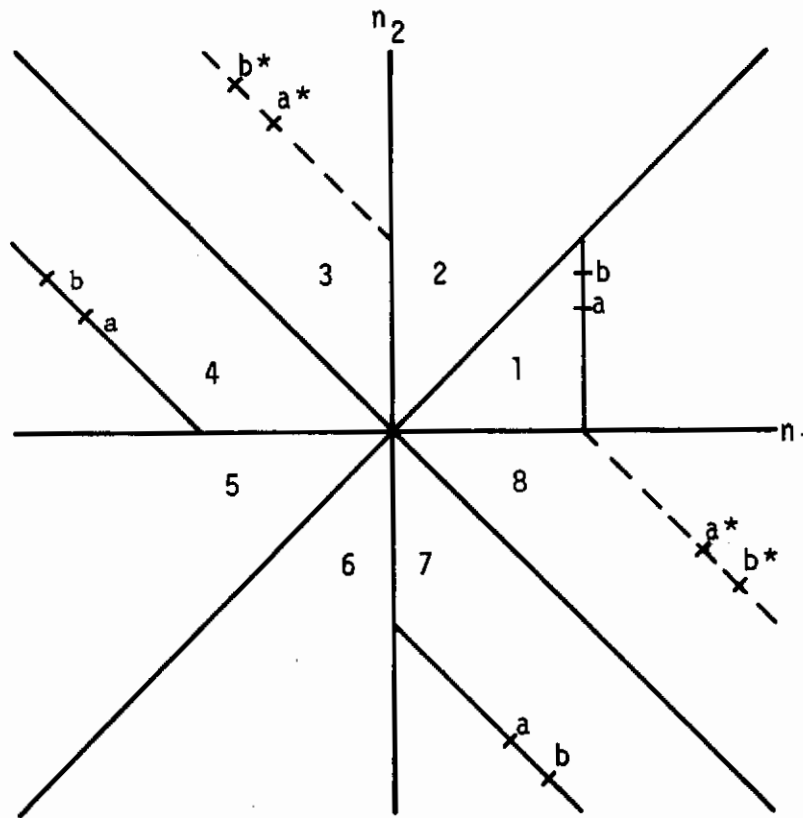


Figure II.4 Direct Mapping of  $B_1(\omega_1, \omega_2)$  from First Octant into Third, Fourth, Seventh, and Eighth Octant

# Contrails

Here the bispectral function along the vertical line in the first octant is mapped by Equation II.2 into the other areas shown. Conjugate mapping is indicated by the dashed line.

All that is required to map the first octant into the remainder of the eighth octant is to first map the first octant into the second, Equation II.18, and then use Equation II.20 to map the second octant into the lower portion of the eighth octant. Then by further use of Equation II.10 and Equation II.19, the mapping into the entire  $\omega_1, \omega_2$  plane may be completed.

The complete mapping of the same segment by the entire set of Equations II.18, II.19, and II.20 is shown in Figure II.5.

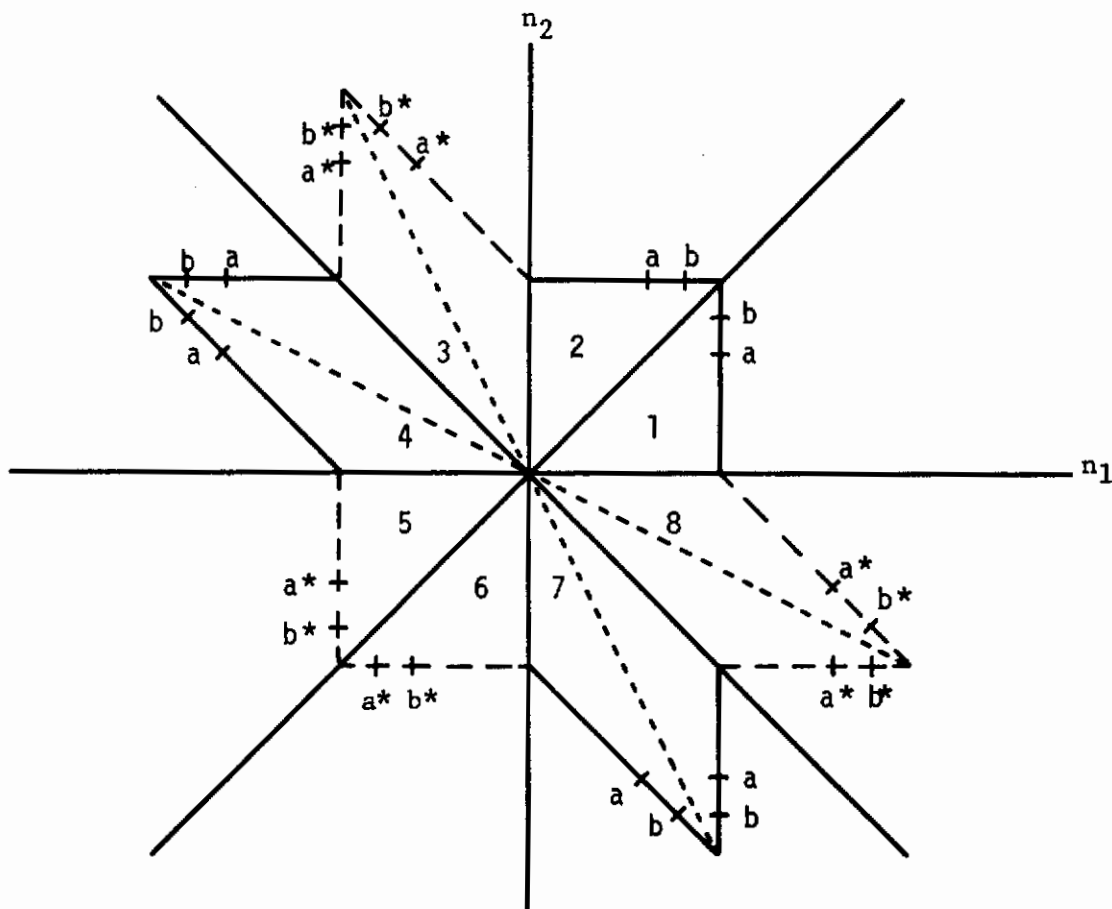


Figure II.5 Complete Mapping of  $B_1(\omega_1, \omega_2)$  from First Octant Into Remainder of  $\omega_1, \omega_2$  Plane



The mapping by Equation II.18, II.19, and II.20 can be conveniently expressed by linear transformation matrices,  $L$ , of rank 2. The matrices necessarily have the common property,  $L^2 = I$ , where  $I$  is the identity matrix.

TABLE II.1

LINEAR TRANSFORMATION MATRICES OF MAPPING EQUATIONS FOR THE BISPECTRUM

<u>Equation II.18</u>	<u>Equation II.19</u>	<u>Equation II.20</u>
$L_1 = \begin{matrix} 0 & 1 \\ 1 & 0 \end{matrix}$	$L_2 = \begin{matrix} -1 & 0 \\ 0 & -1 \end{matrix}$	$L_3 = \begin{matrix} 1 & 1 \\ 0 & -1 \end{matrix}$

The fourth procedure, the one for mapping the first octant into the second and then into the lower half of the eighth, corresponds to the linear operator

$$L_3 L_1 = \begin{matrix} 1 & 1 \\ -1 & 0 \end{matrix} .$$

Similar matrices apply to Equation II.7, Equation II.8 and Equation II.9 for  $Q_1(\tau_1, \tau_2)$ .

The skewness of  $u_1$  with respect to the  $t$  axis (commonly called simply the skewness of  $u_1$ ) is the double integral of the bispectrum over all frequencies,

$$\overline{u_1^3} = Q_1(0,0) = \int_{-\infty}^{\infty} \int_{-\infty}^{\infty} B_1(\omega_1, \omega_2) d\omega_1 d\omega_2. \quad (\text{II.21})$$

# Contrails

Because of the conjugate mapping, it is possible to obtain a purely imaginary integral by changing the sign of  $B_1$  in the above integral in all octants of conjugate mapping, namely, the third, fifth, sixth, and eighth octants. This integral is evidently a measure of the skewness with respect to the  $u_1$  axis. The integral of the imaginary part is negative when short upward ramps are mixed with long downward ramps as shown in Figure II.2. When the reverse is true, i.e., the long ramps are in the upward direction, the integral is positive.

APPENDIX III

SENSOR LEVELING AND ORIENTATION DETAILS

Appendix III depicts details and functional calibrations of equipment used in remotely controlling and leveling TOLCAT sensors. Sensor platform leveler details are illustrated in schematics along with leveler calibration as a function of monitor indication. The sensor direction heading calibration of preset heading with deviation meter indication versus real heading for a single control system and a mutichannel (10) control system is graphically presented.

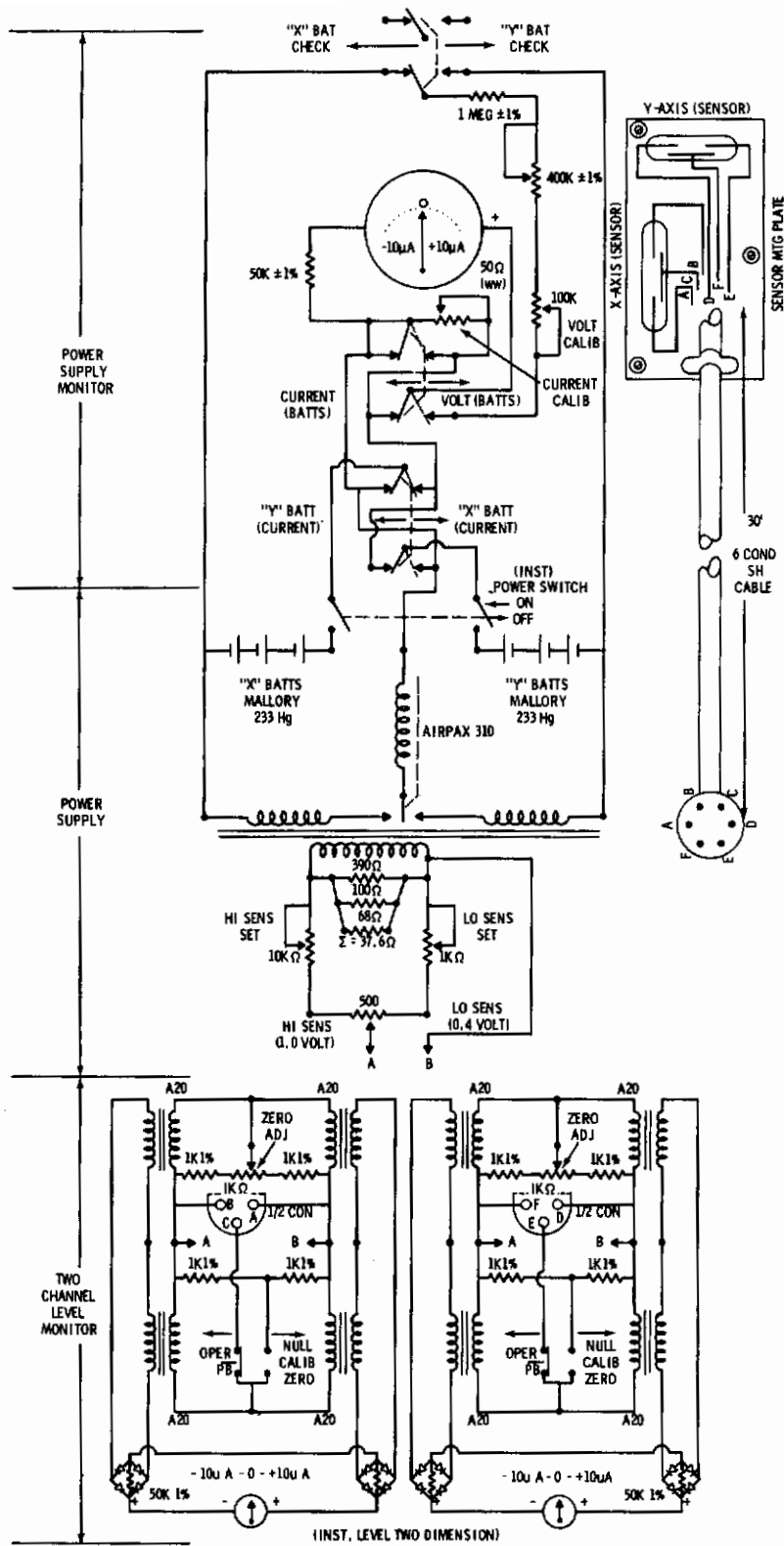


Figure III.1 Two Dimensional X-Axis and Y-Axis Leveler Schematic

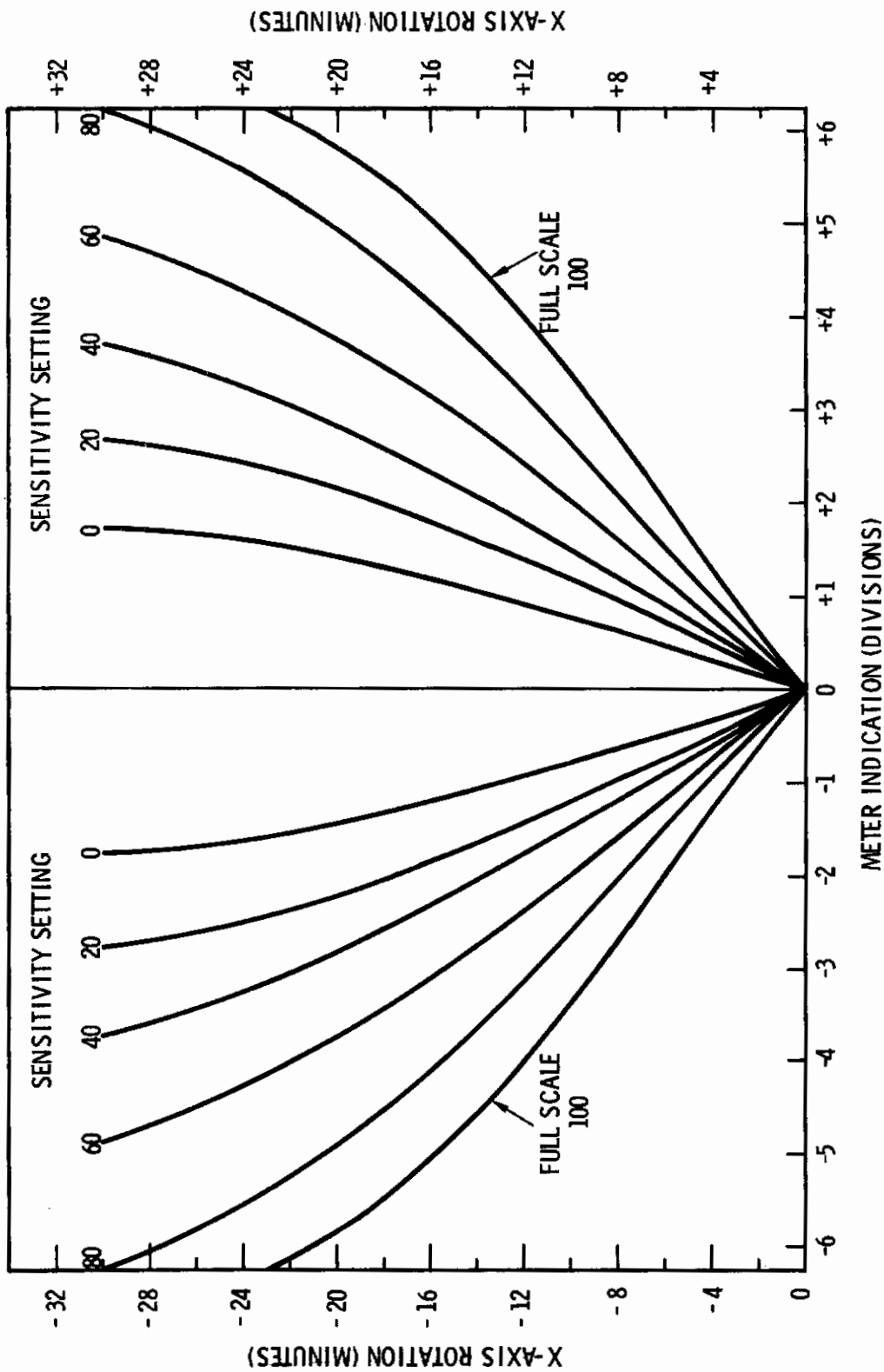


Figure III.2 Level Monitor Calibration - X-Axis Versus Meter Indication

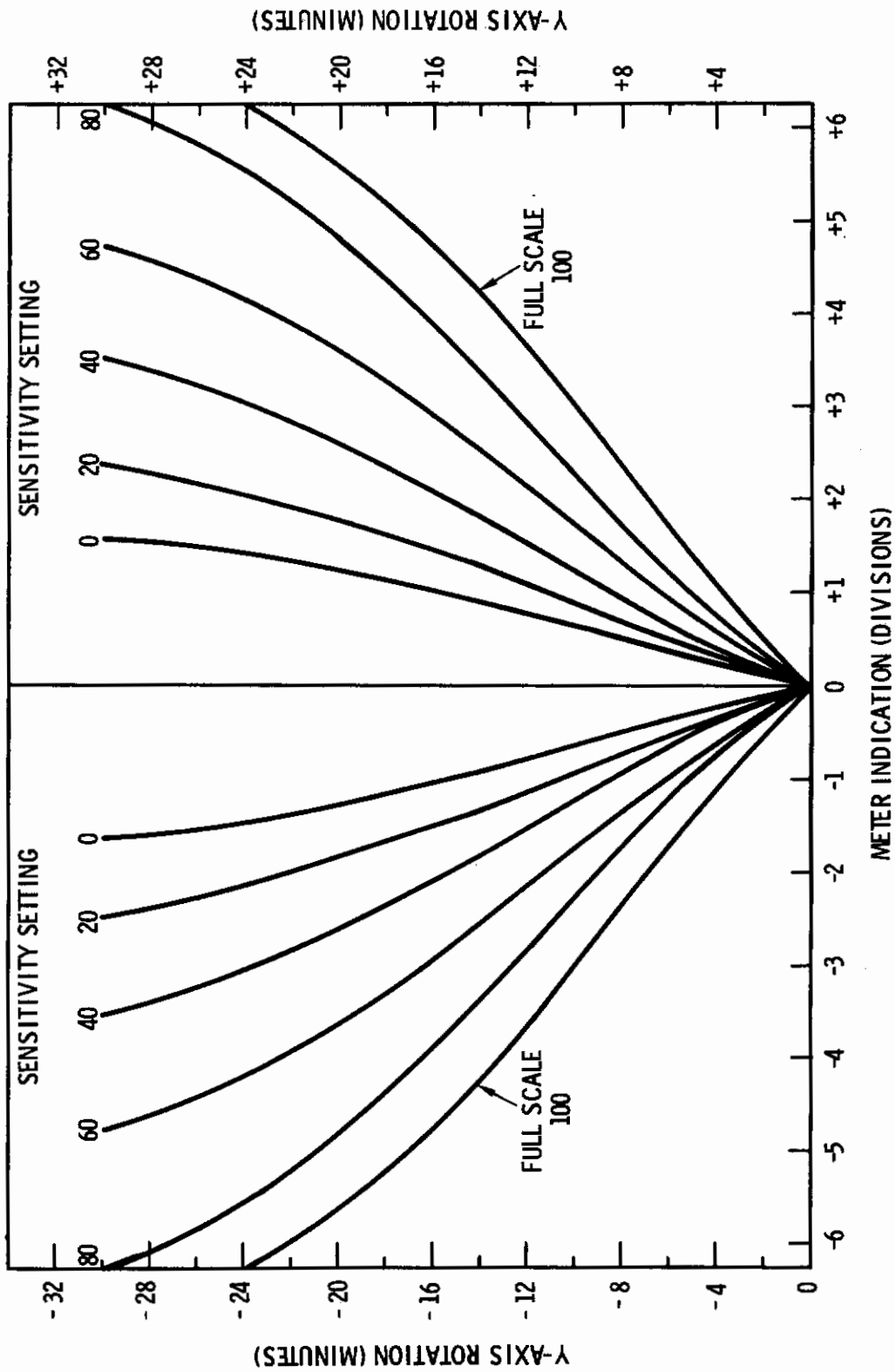


Figure III.3 Level Monitor Calibration - Y-Axis Versus Meter Indication



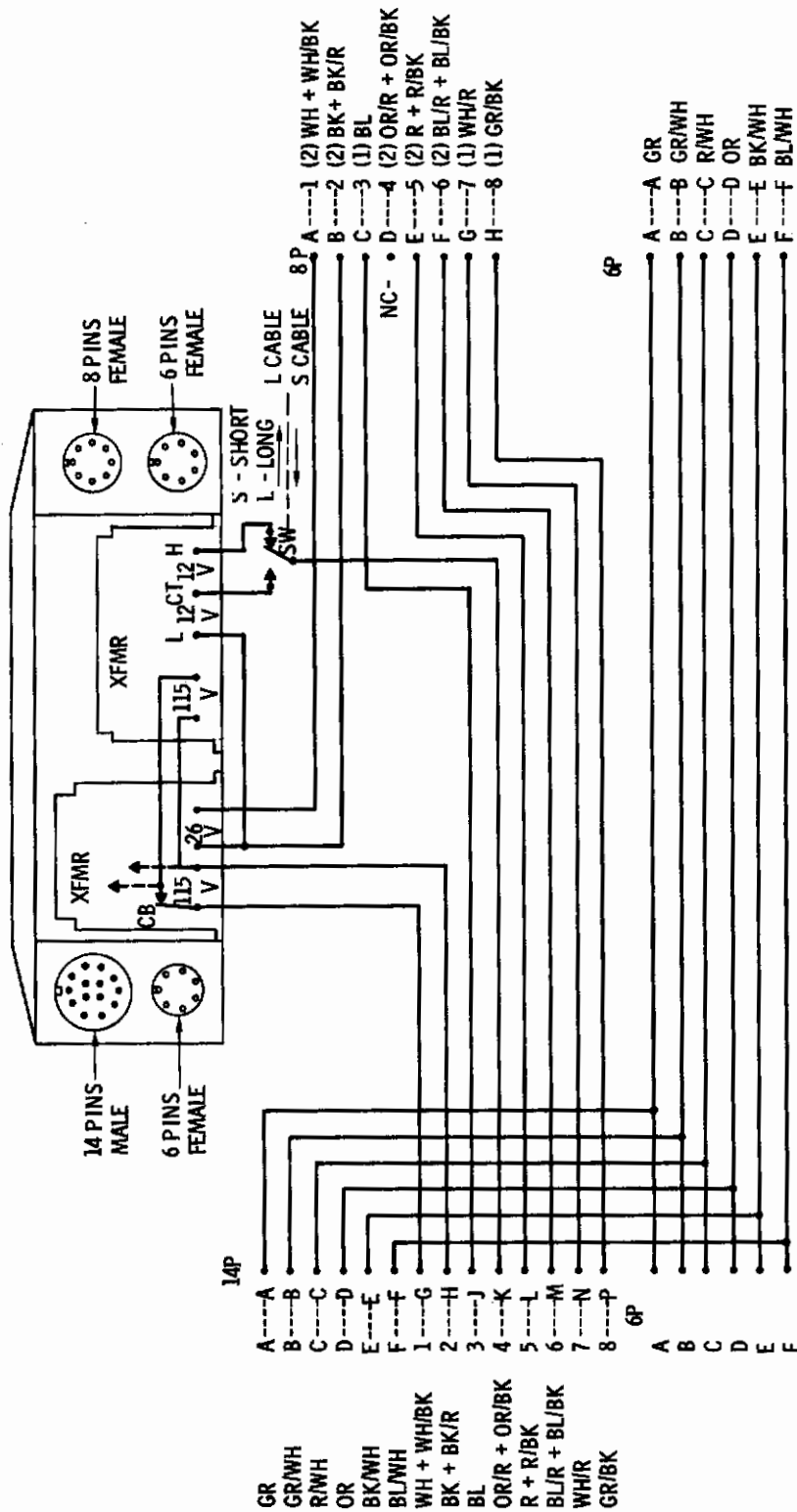


Figure III.4 Remote Long Line Rotor Control Junction Box

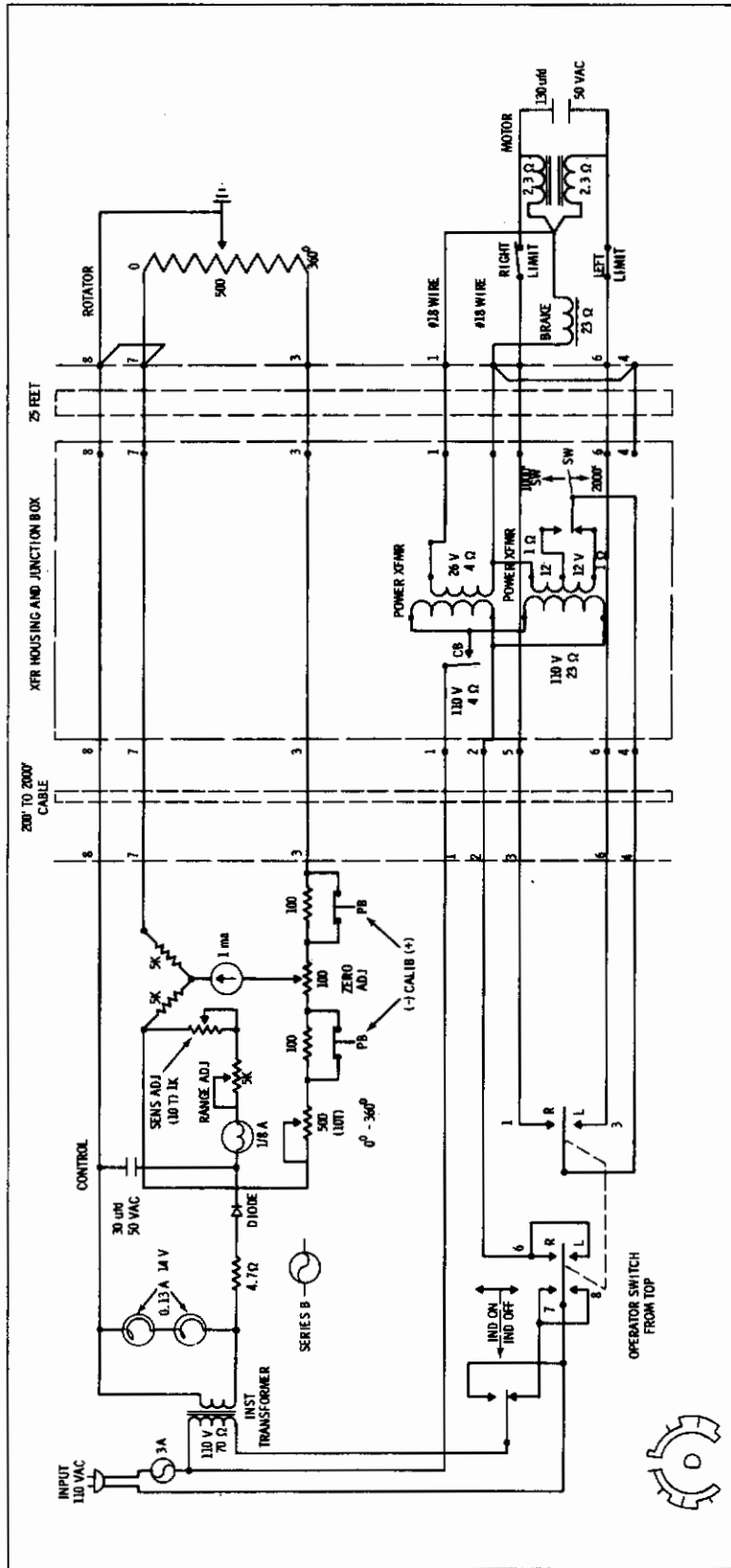


Figure III.5 Rotor Control and Direction Heading System Schematic

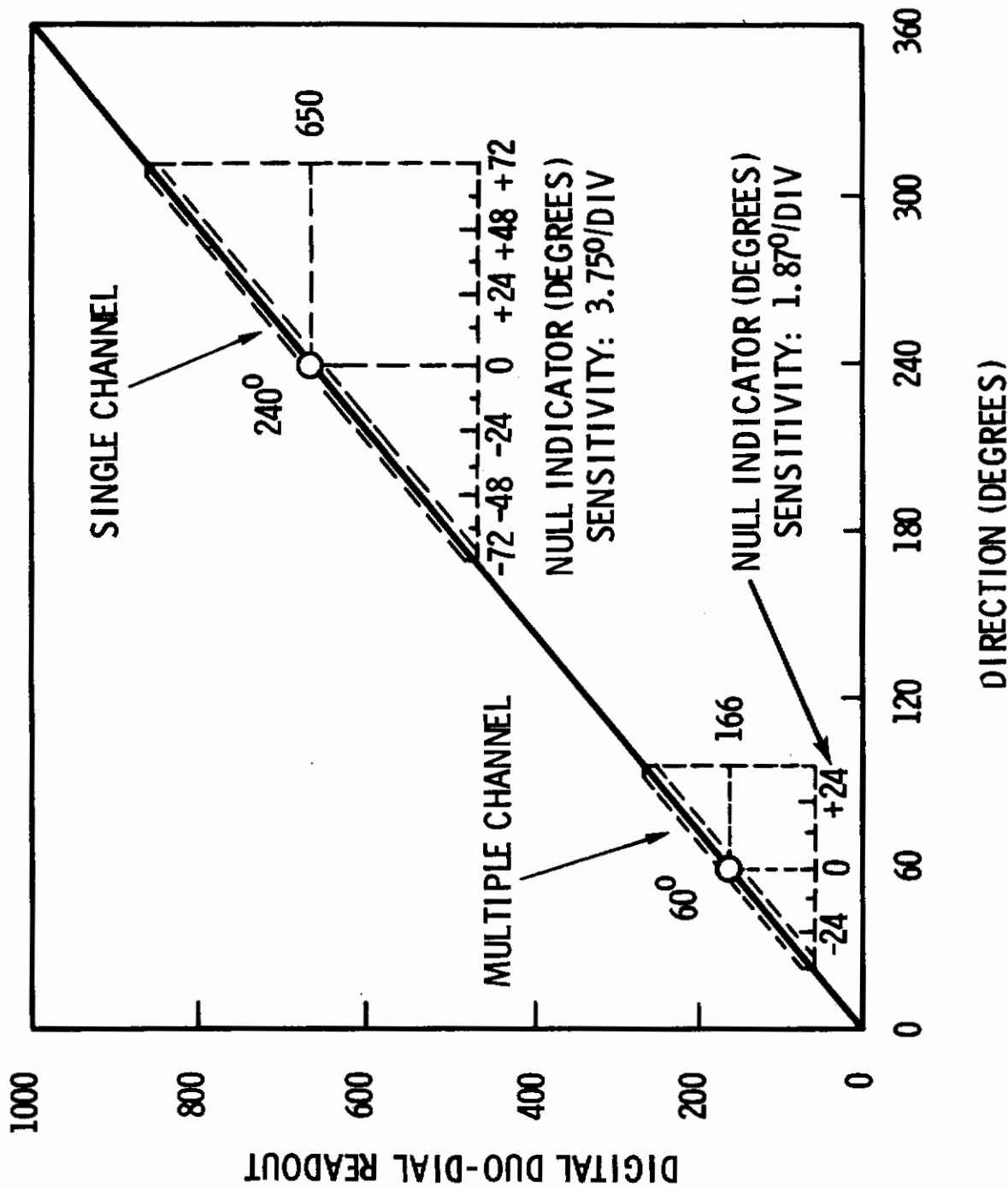


Figure III.6 Rotor and Instrument Direction Heading Calibration - Duo-Dial and Null Indicator Readout Versus Direction Heading



APPENDIX IV

SUPPLEMENTARY ANALYSIS FIGURES

The figures in this Appendix, referred to in various parts of Section VII, constitute supplementary illustrations of the ideas discussed in that Section.

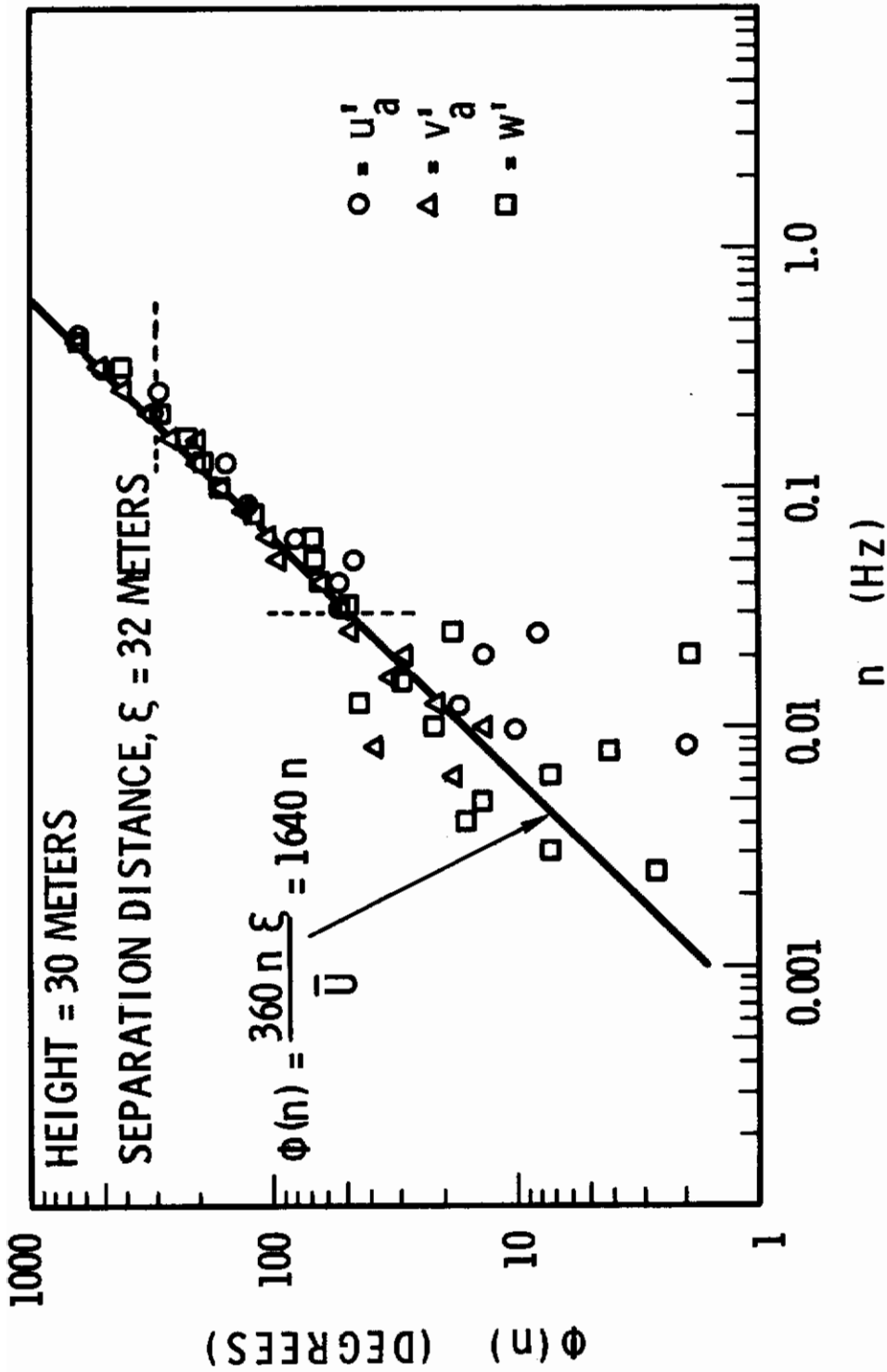


Figure IV.1 Phase Spectra - Separation Distance 32 Meters, Test T703



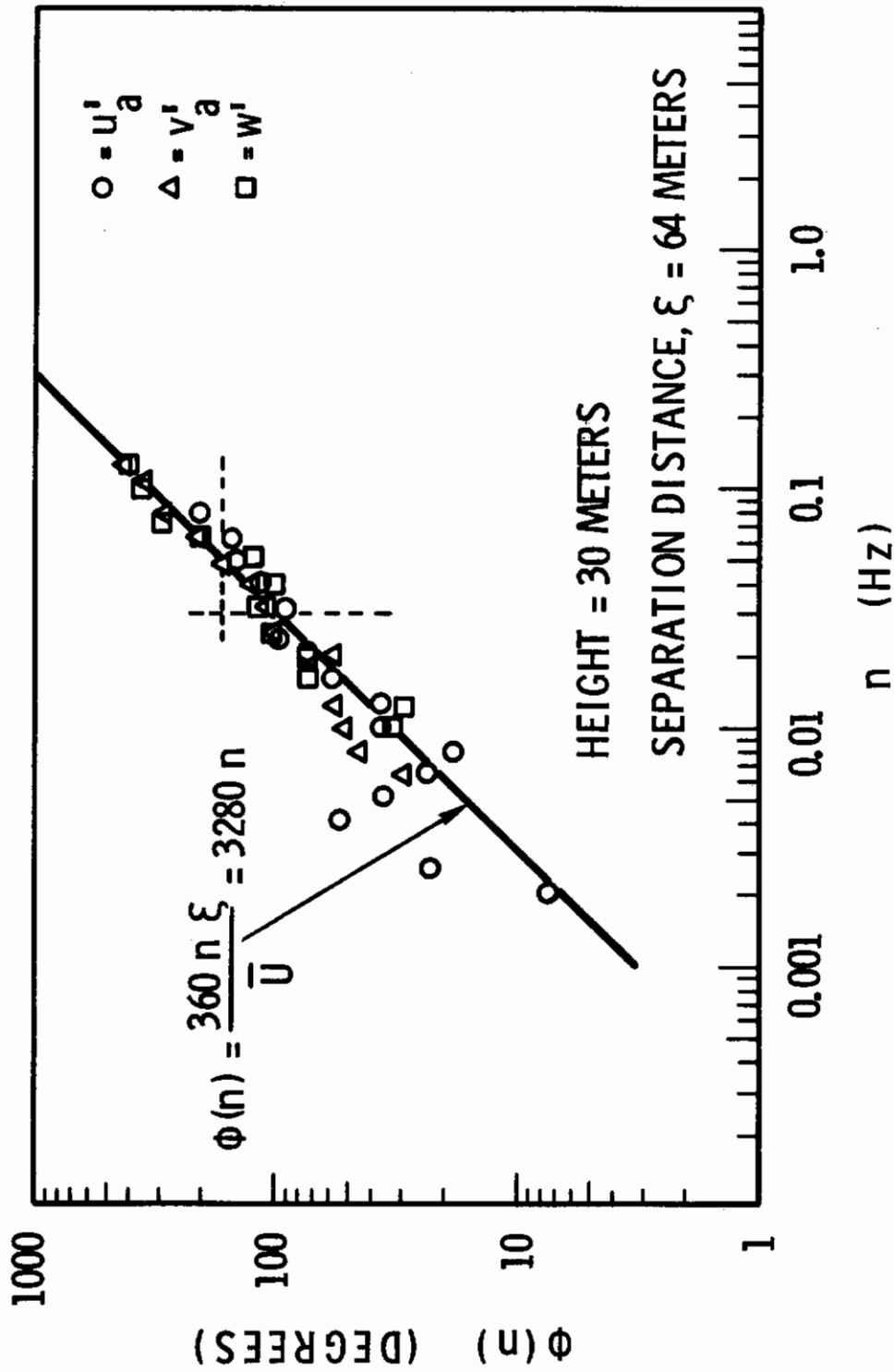


Figure IV.2 Phase Spectra - Separation Distance 64 Meters, Test T703

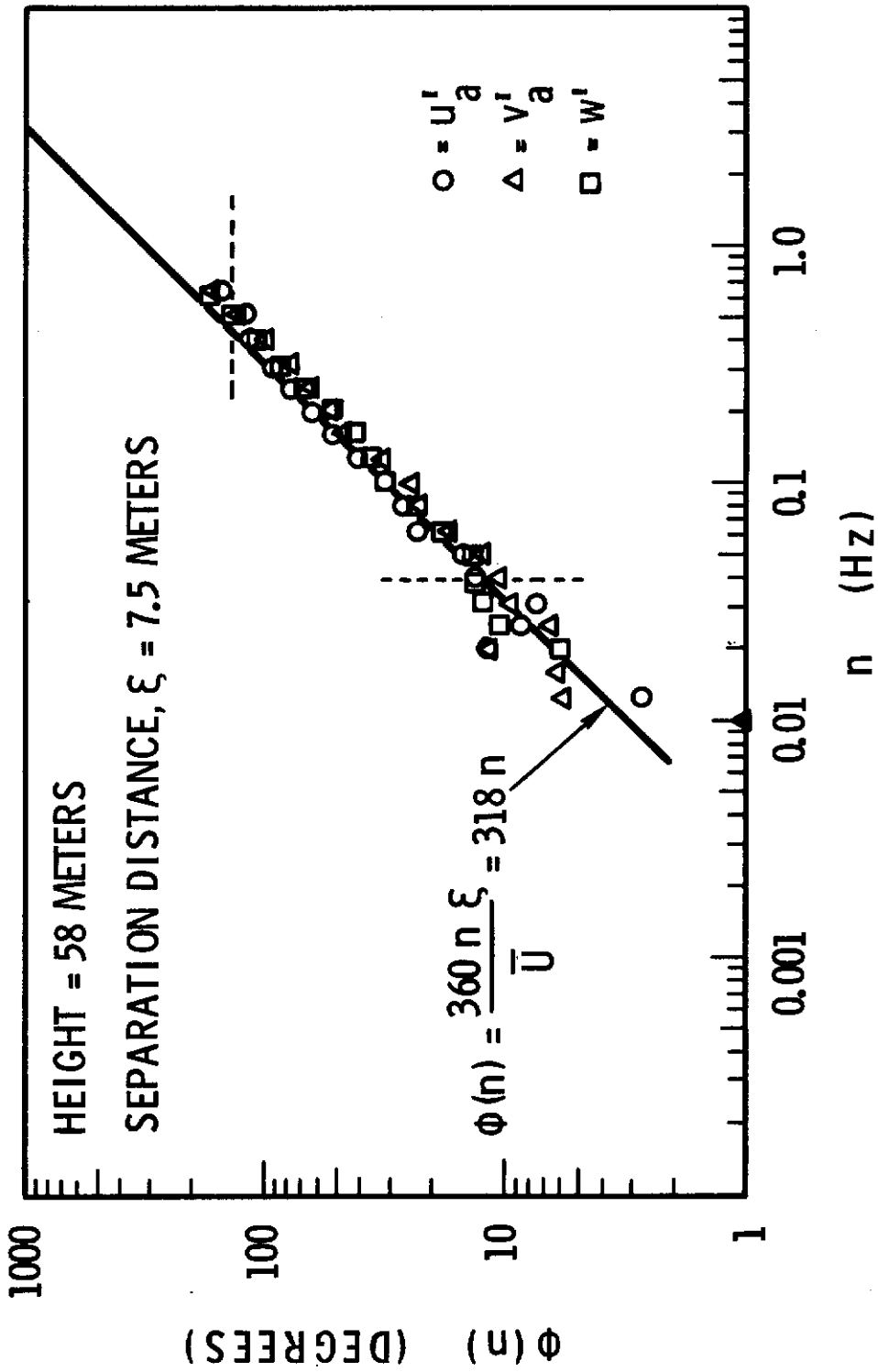


Figure IV.3 Phase Spectra - Separation Distance 7.5 Meters, Test T202

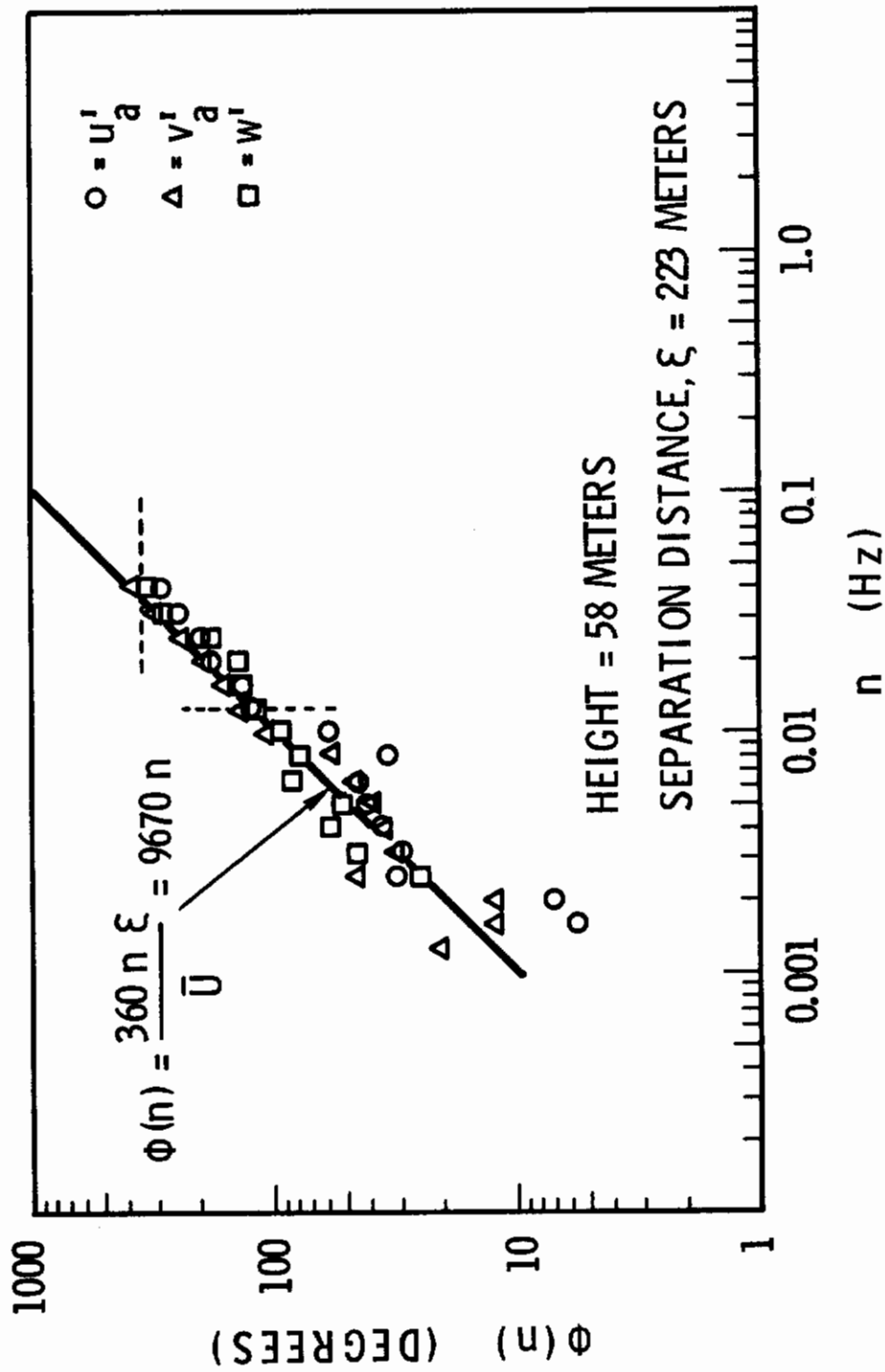


Figure IV.4 Phase Spectra - Separation Distance 223 Meters, Test T105

# Contrails

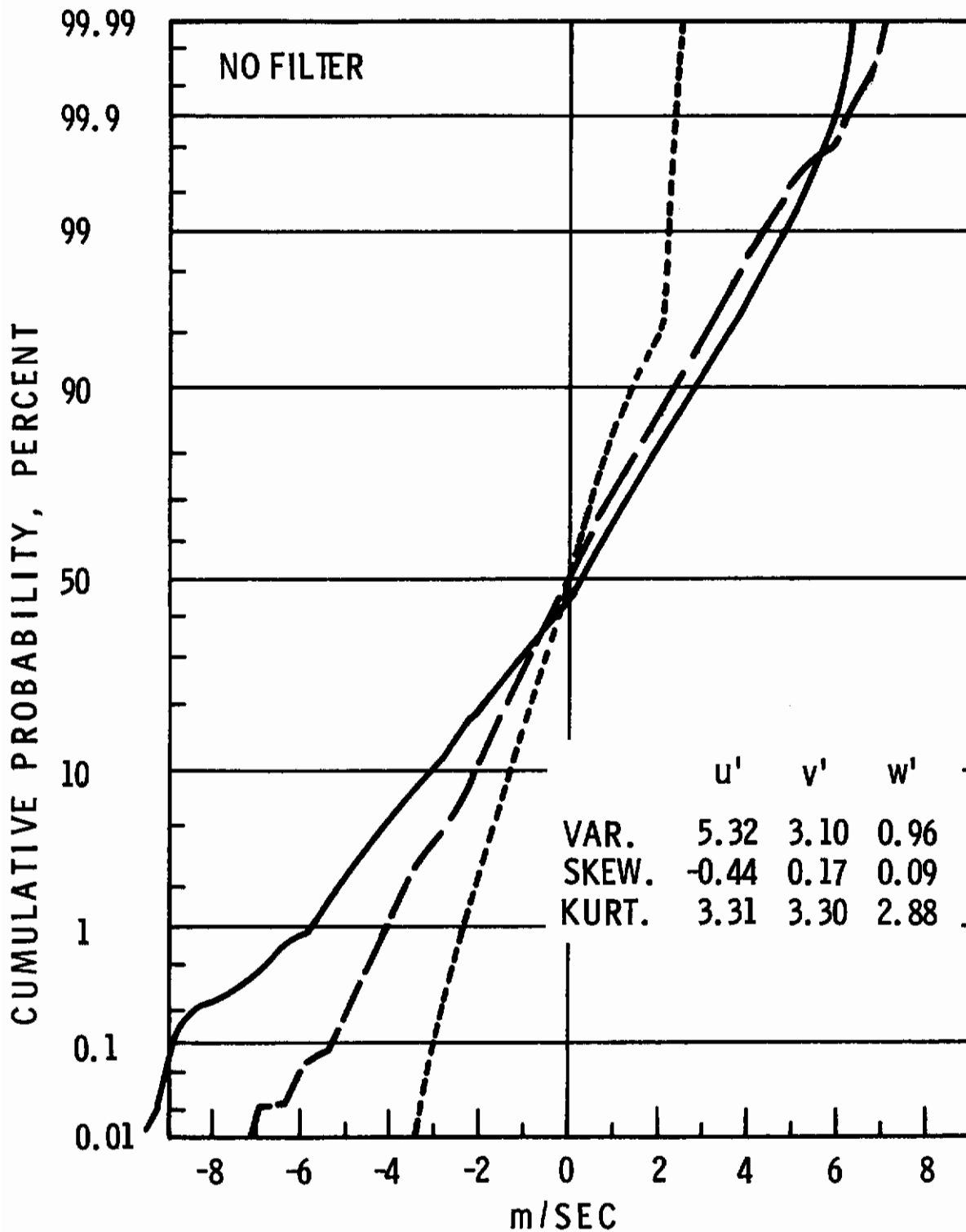


Figure IV.5 Probability Density Function for  $u'$ ,  $v'$ ,  $w'$ ,  
Test T701, No Filter

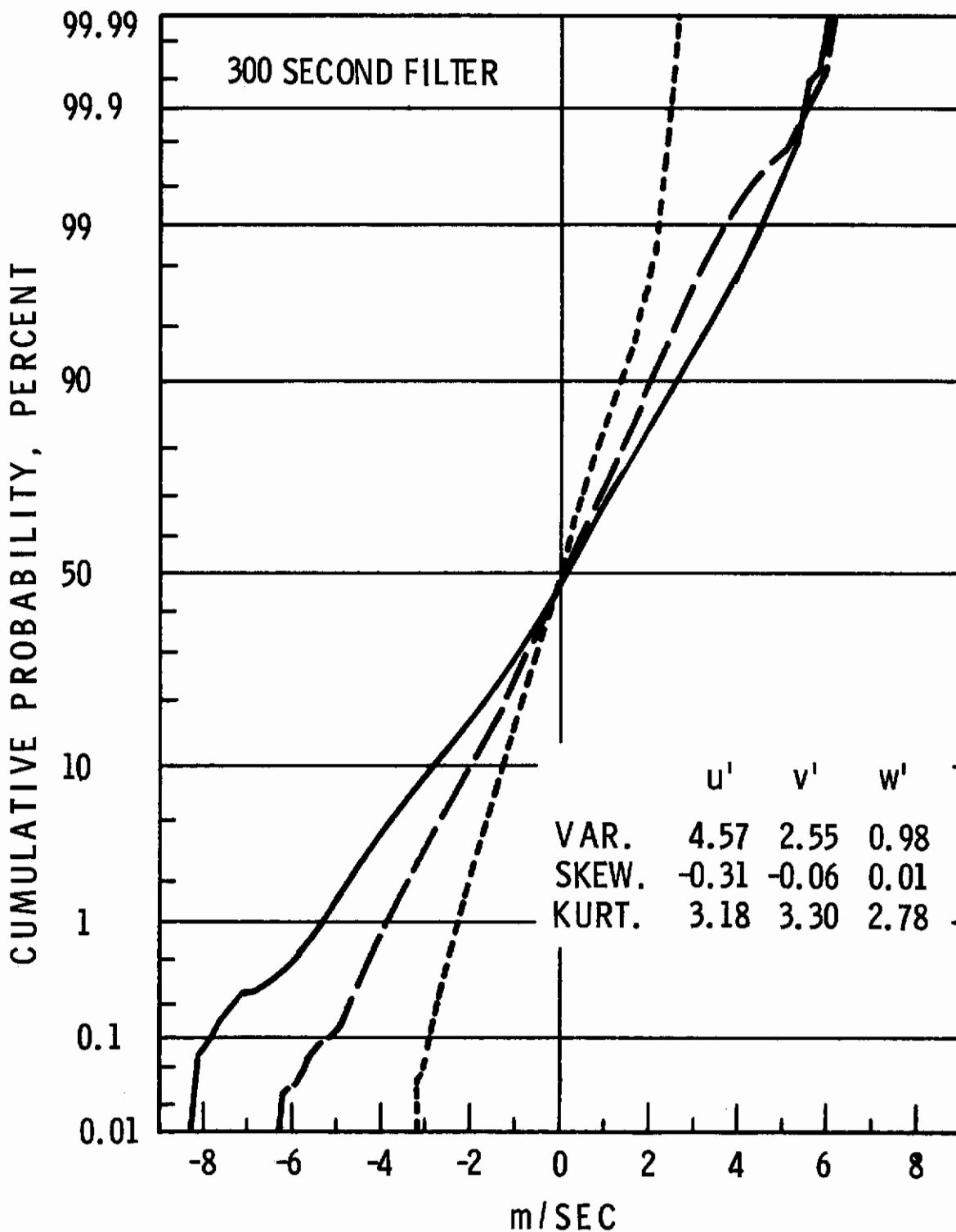


Figure IV.6 Probability Density Function for  $u'$ ,  $v'$ ,  $w'$ , Test T701, 300-Second High-Pass Filter

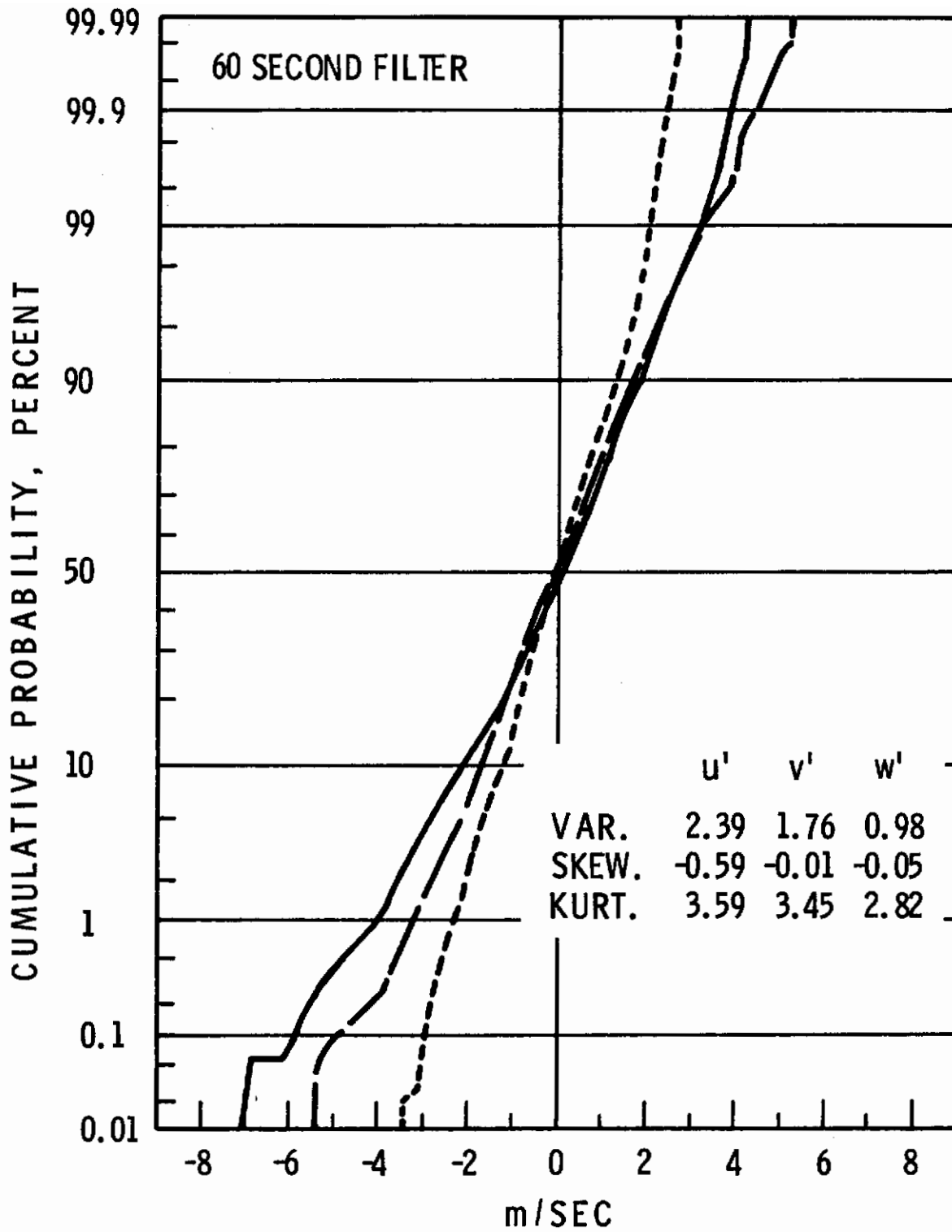


Figure IV.7 Probability Density Function for  $u'$ ,  $v'$ ,  $w'$ ,  
Test T701, 60-Second High-Pass Filter



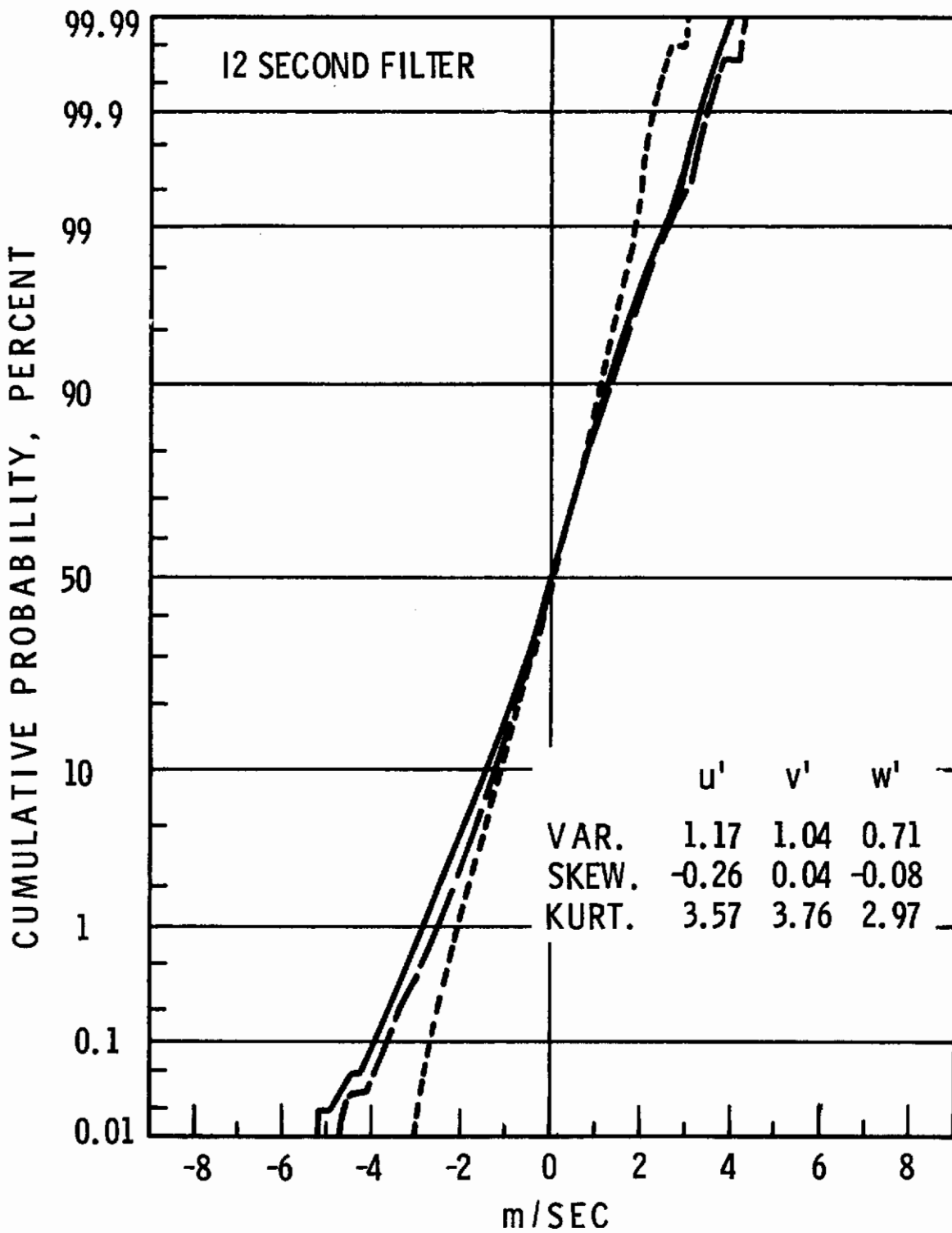


Figure IV.8 Probability Density Function for  $u'$ ,  $v'$ ,  $w'$ , Test T701, 12-Second High-Pass Filter

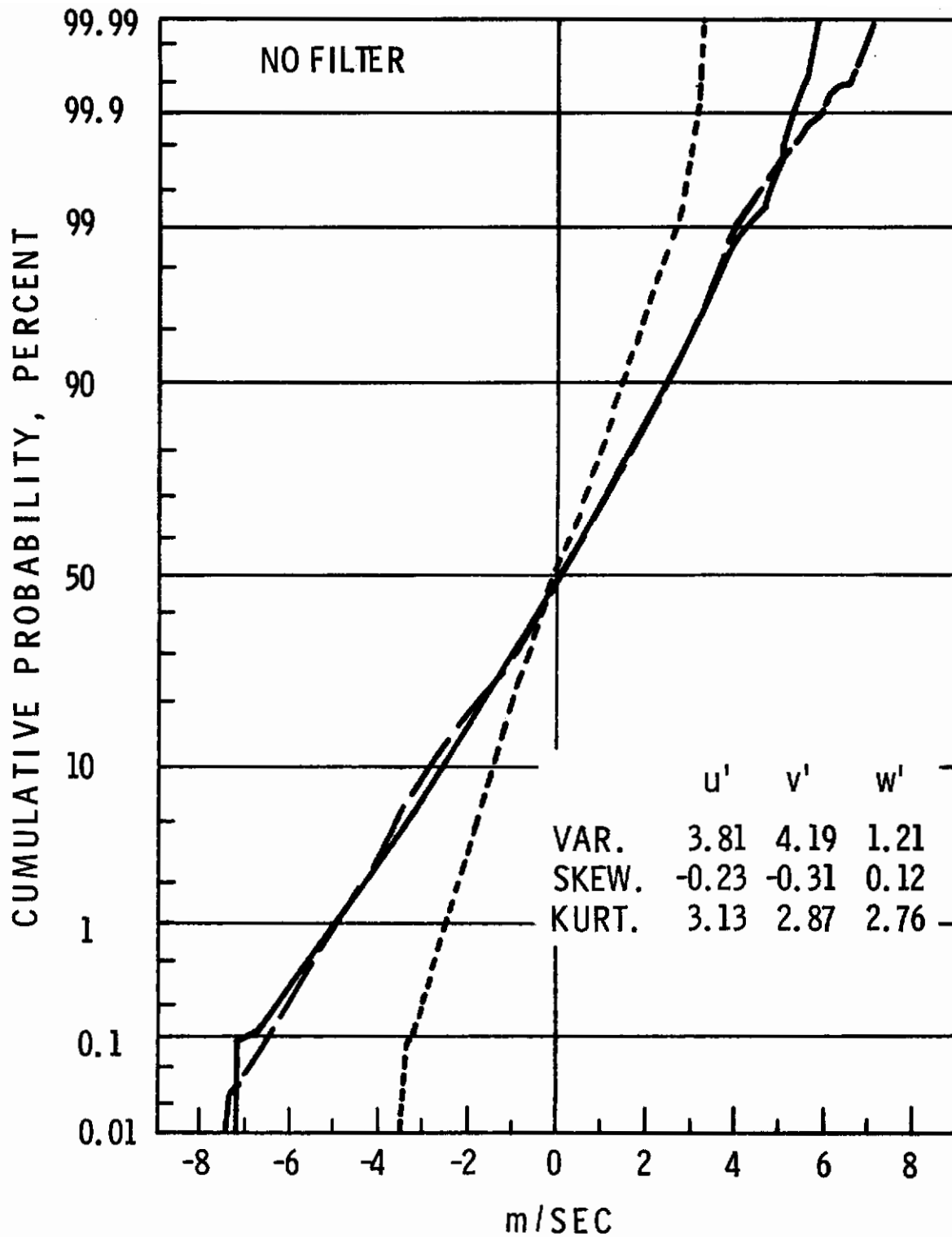


Figure IV.9 Probability Density Function for  $u'$ ,  $v'$ ,  $w'$ , Test T704, No Filter

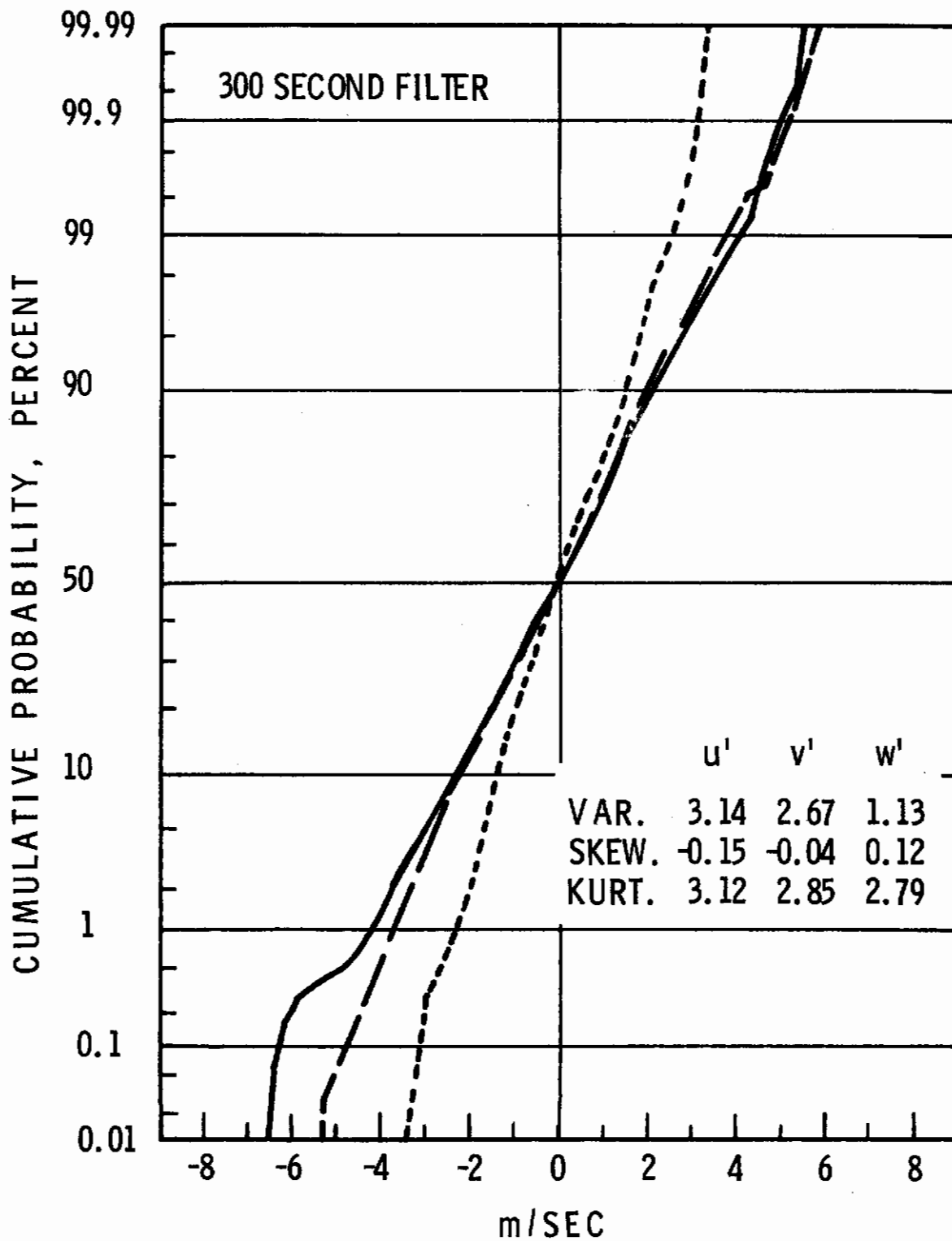


Figure IV.10 Probability Density Function for  $u'$ ,  $v'$ ,  $w'$ ,  
Test T704, 300-Second High-Pass Filter

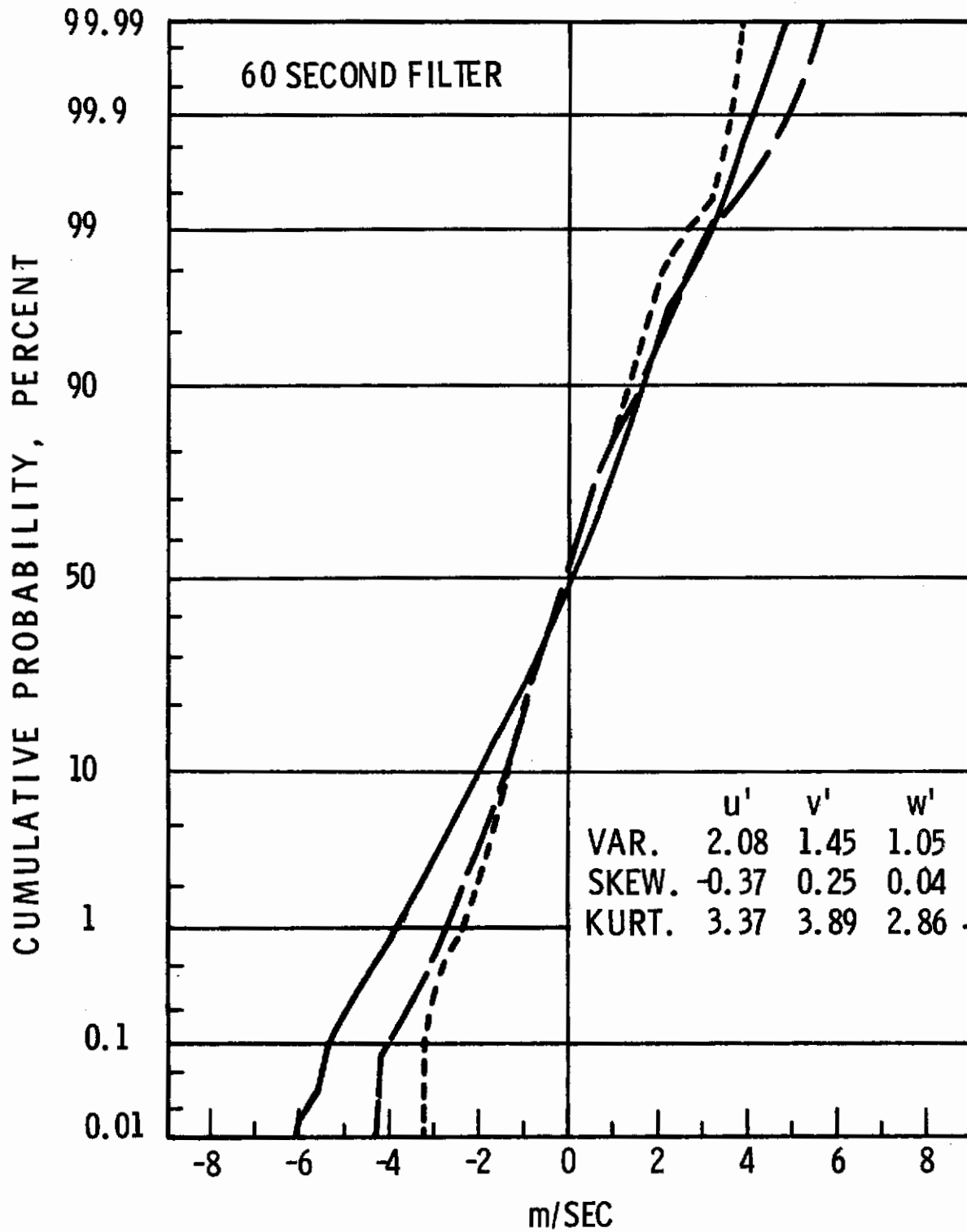


Figure IV.11 Probability Density Function for  $u'$ ,  $v'$ ,  $w'$ ,  
Test T704, 60-Second High-Pass Filter

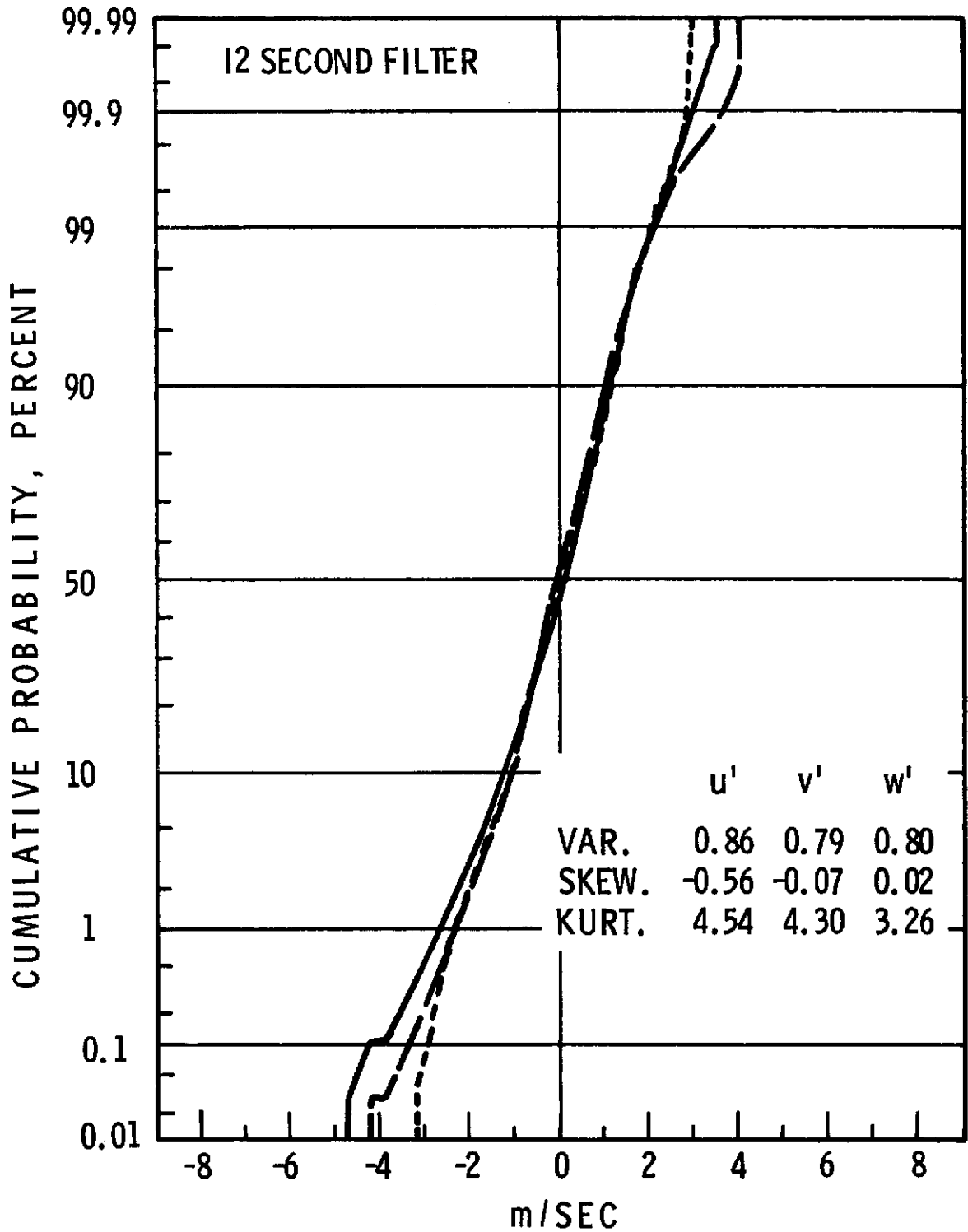


Figure IV.12 Probability Density Function for  $u'$ ,  $v'$ ,  $w'$ ,  
Test T704, 12-Second High-Pass Filter

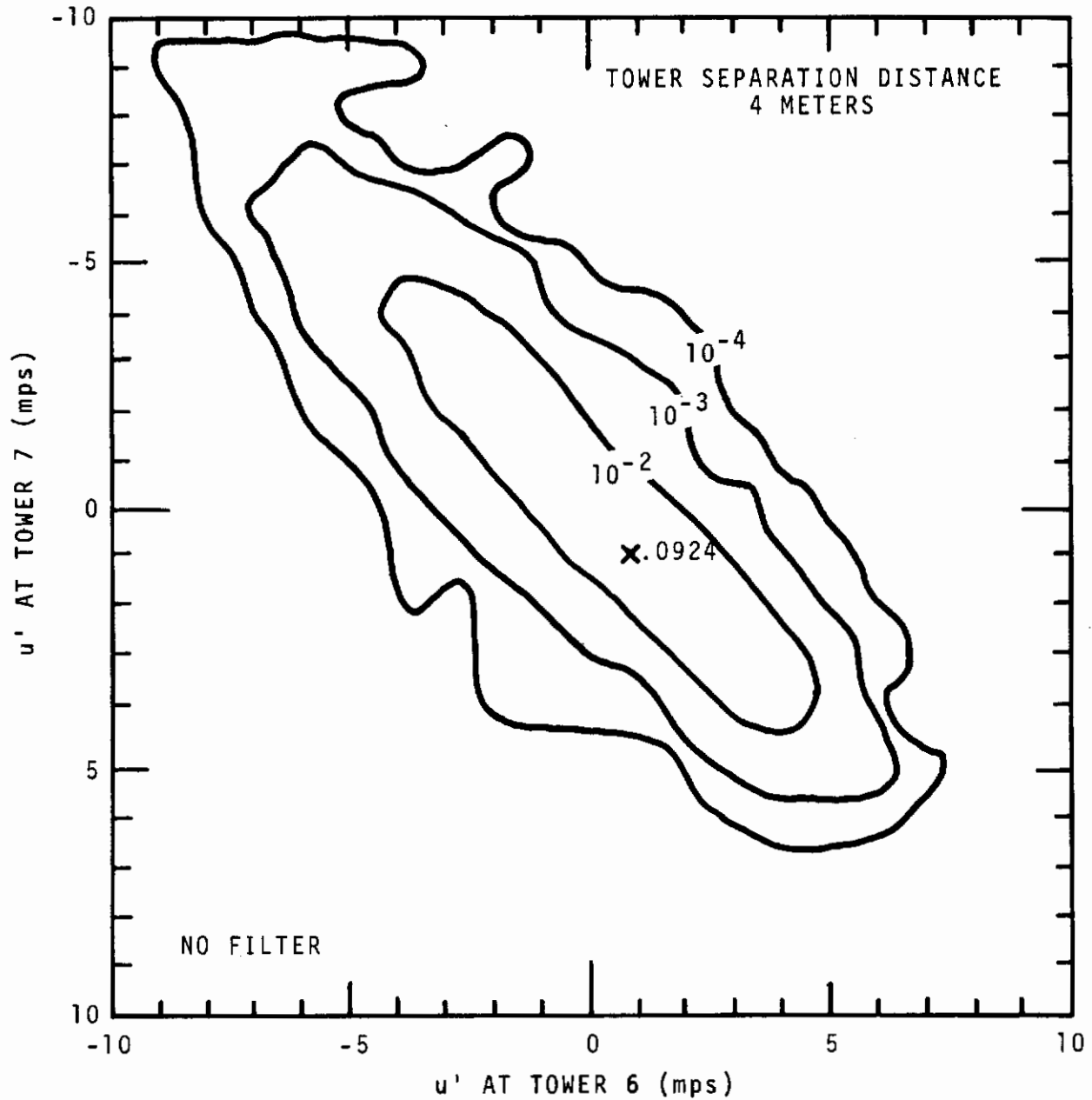


Figure IV.13 Joint Probability Density Function for  $u'$ ,  
Test T704, Separation Distance 4 Meters



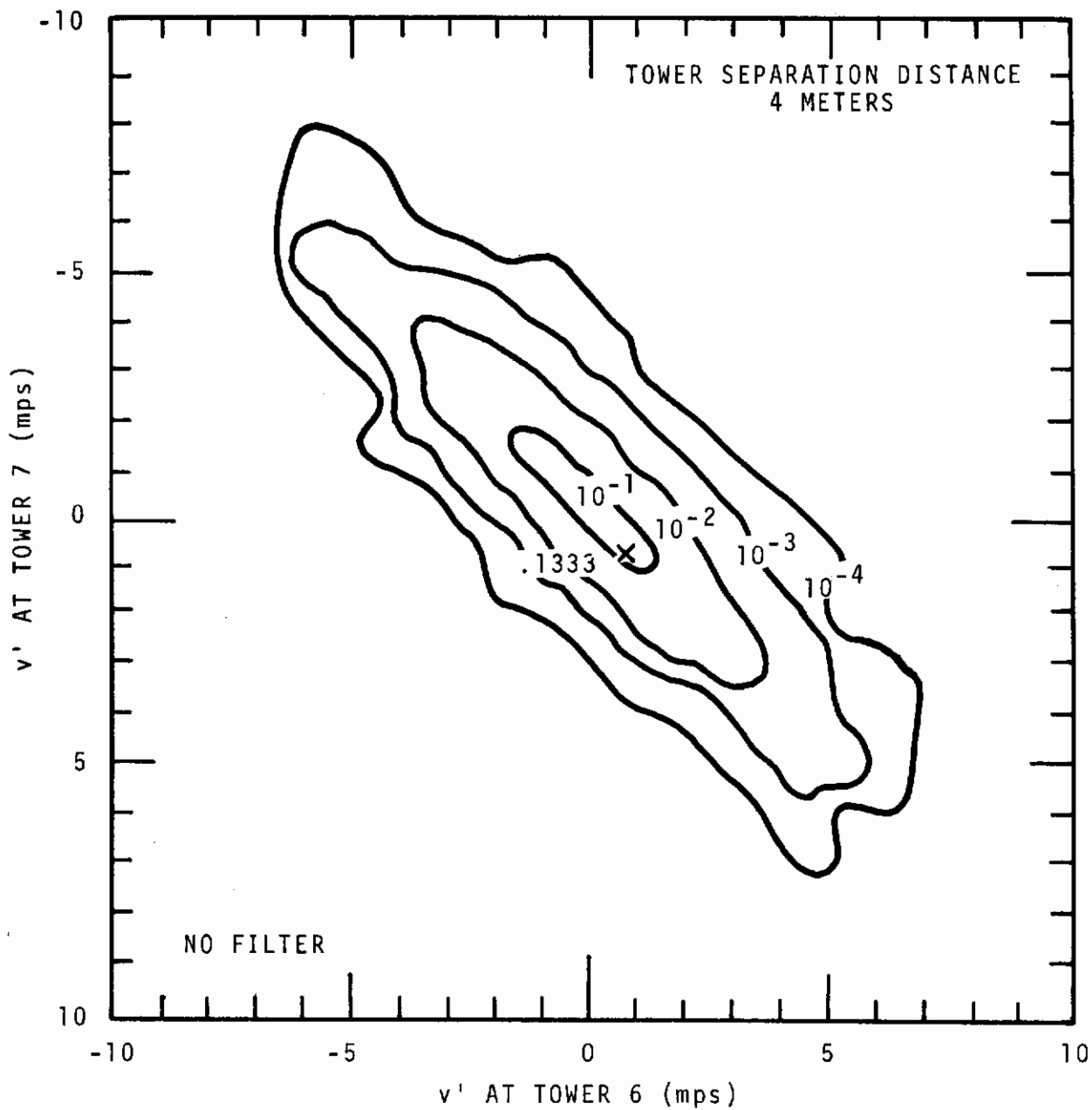


Figure IV.14 Joint Probability Density Function for  $v'$ , Test T704, Separation Distance 4 Meters

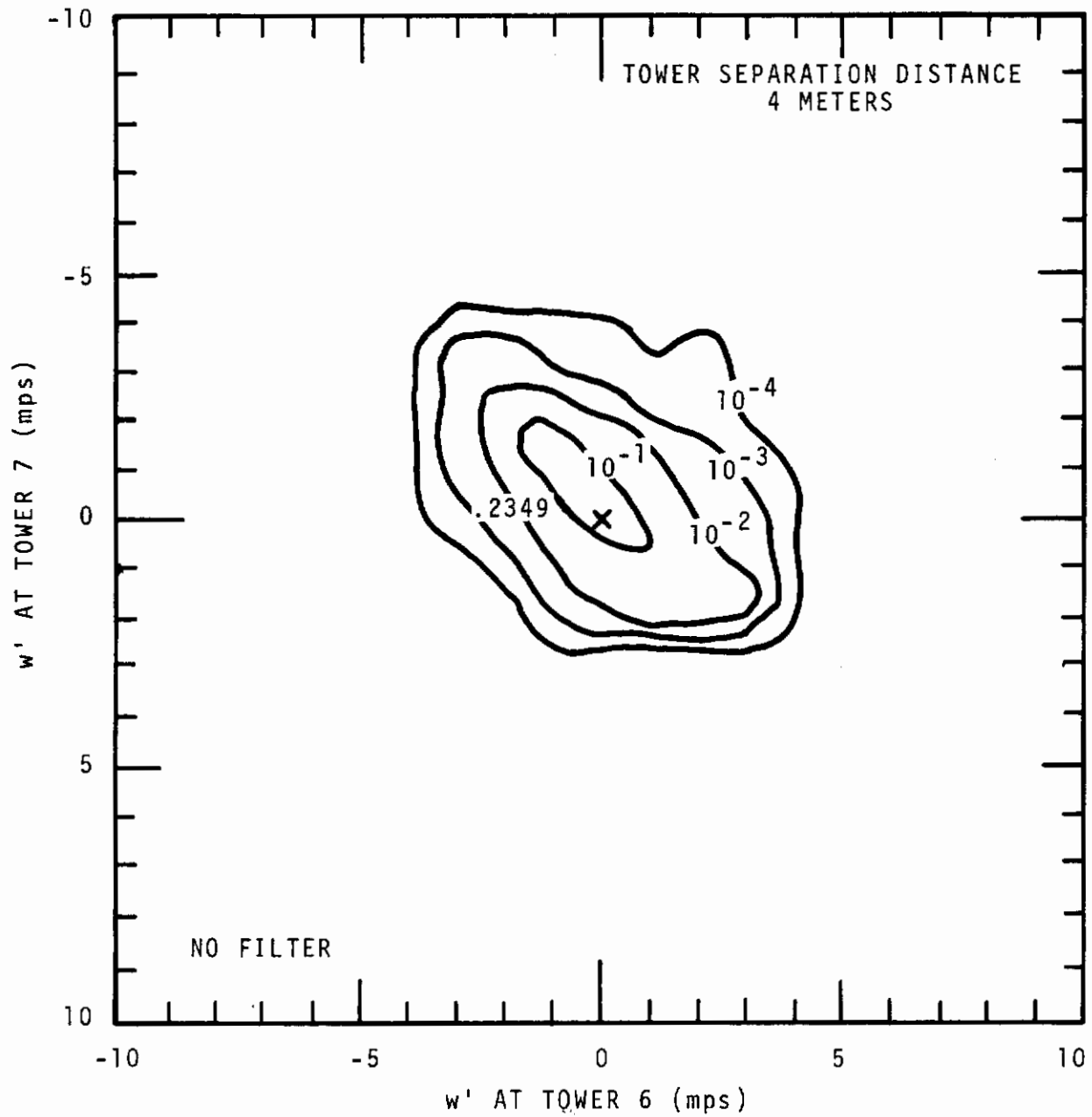


Figure IV.15 Joint Probability Density Function for  $w'$ ,  
Test T704, Separation Distance 4 Meters

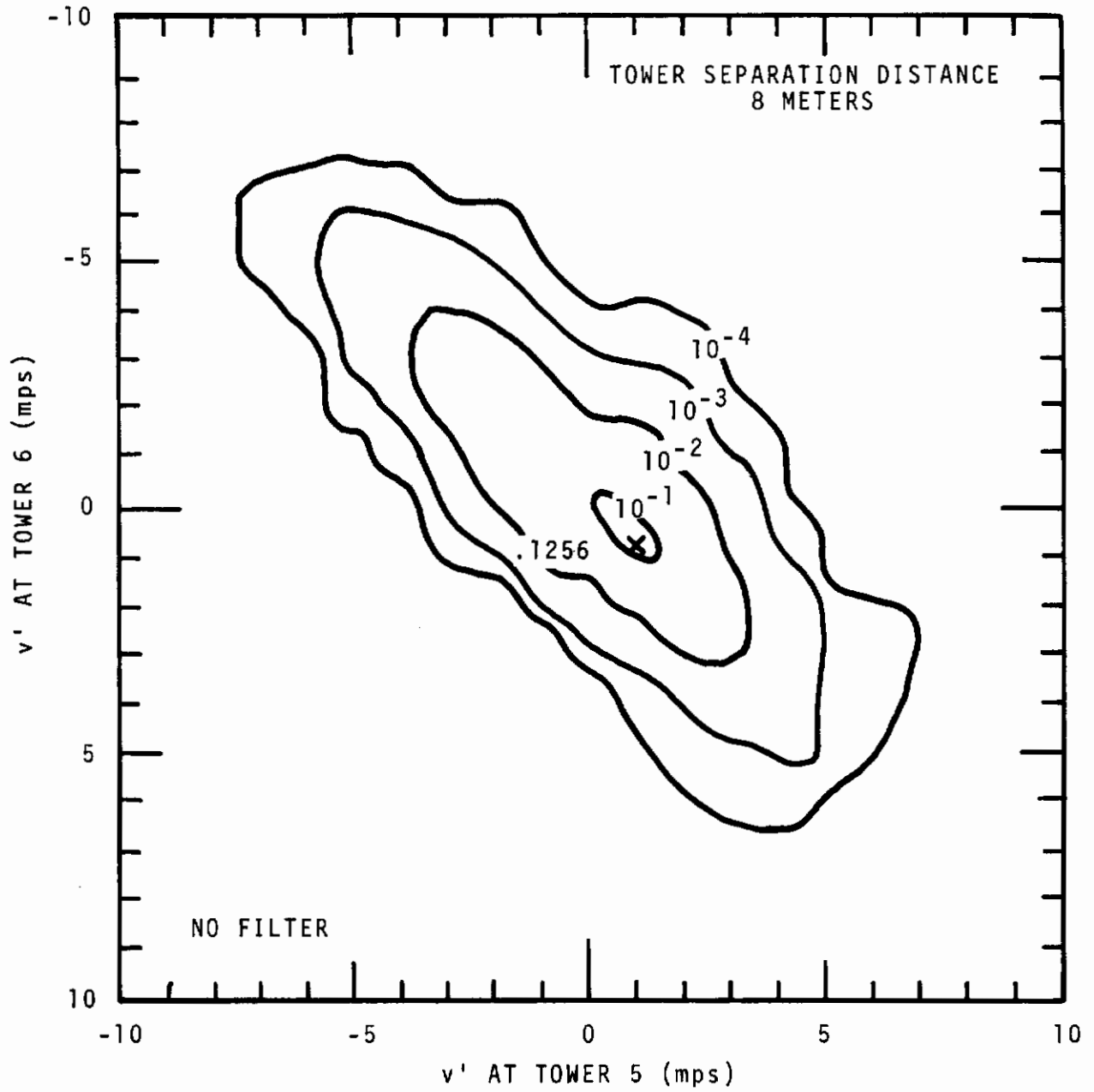


Figure IV.16 Joint Probability Density Function for  $v'$ ,  
Test T704, Separation Distance 8 Meters

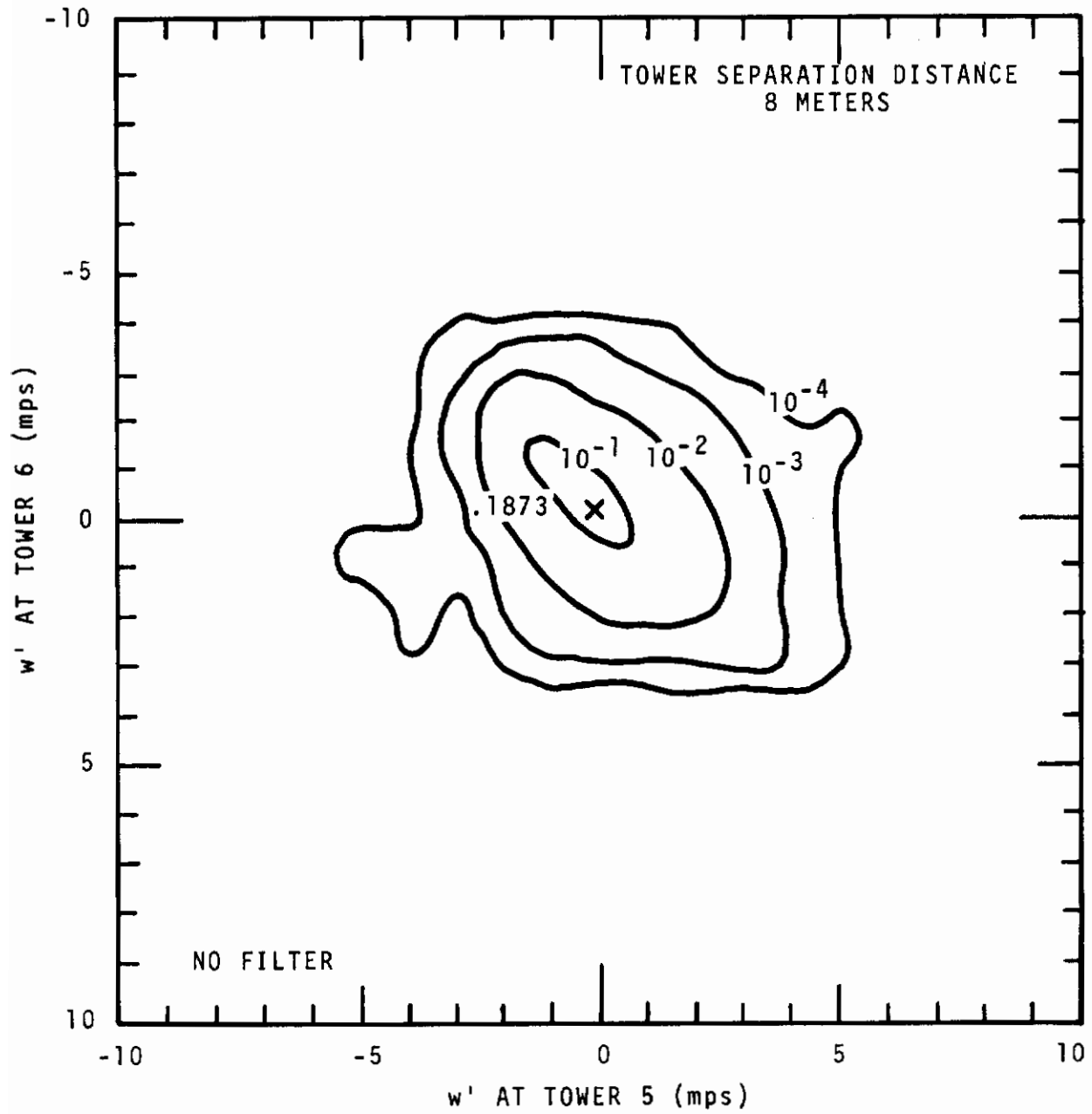


Figure IV.17 Joint Probability Density Function for  $w'$ ,  
Test T704, Separation Distance 8 Meters

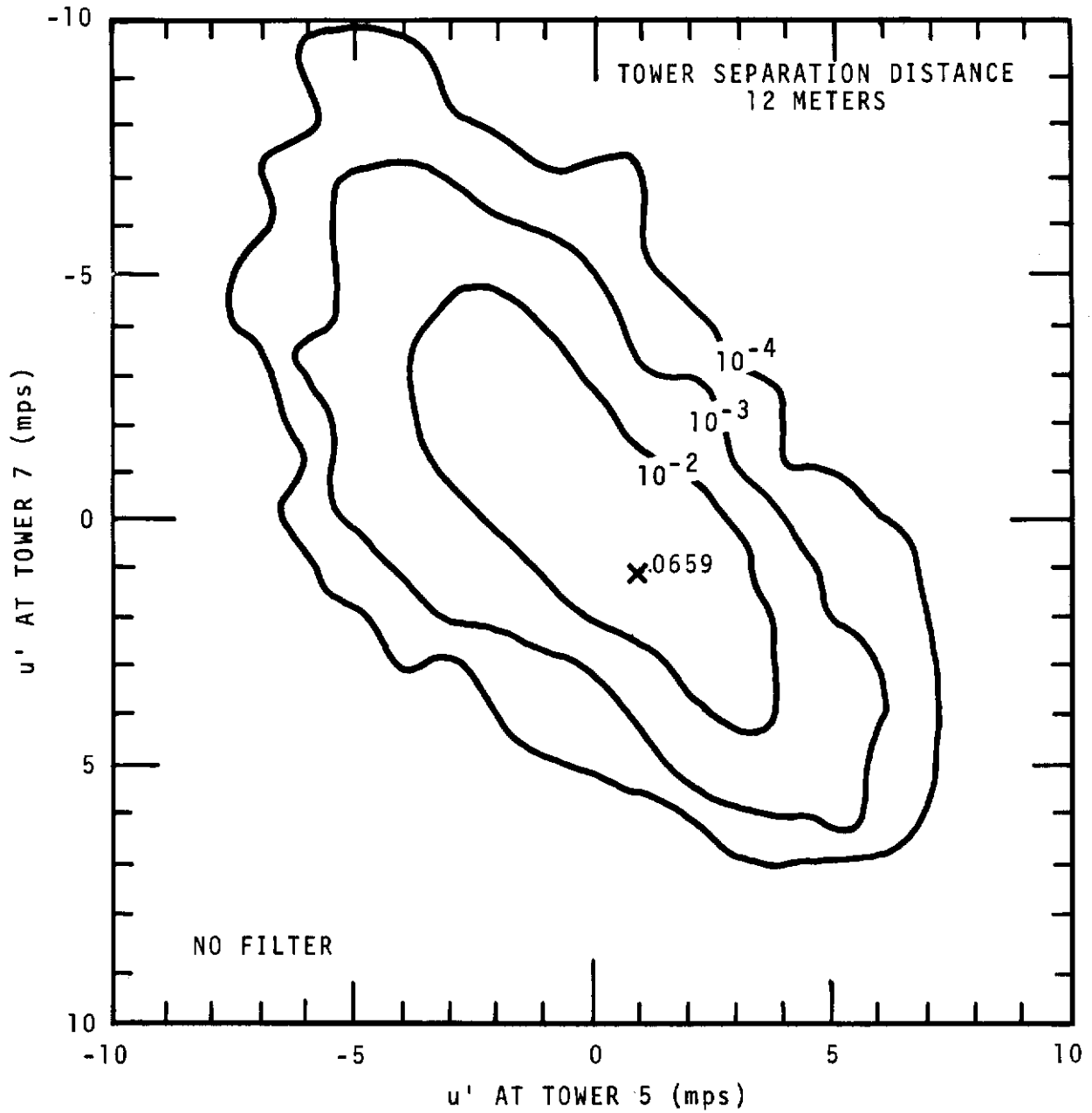


Figure IV.18 Joint Probability Density Function for  $u'$ ,  
Test T704, Separation Distance 12 Meters

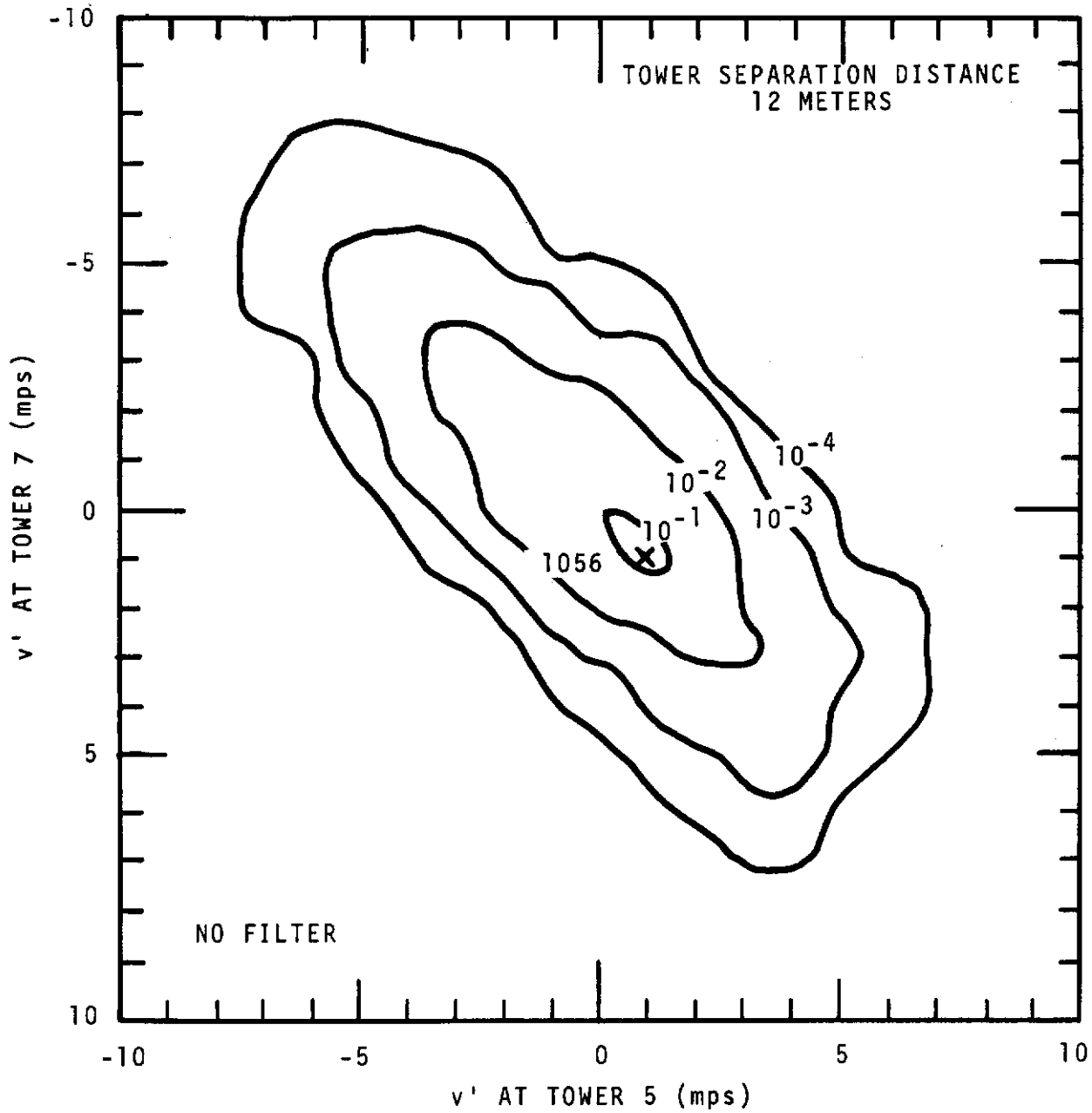


Figure IV.19 Joint Probability Density Function for  $v'$ ,  
Test T704, Separation Distance 12 Meters



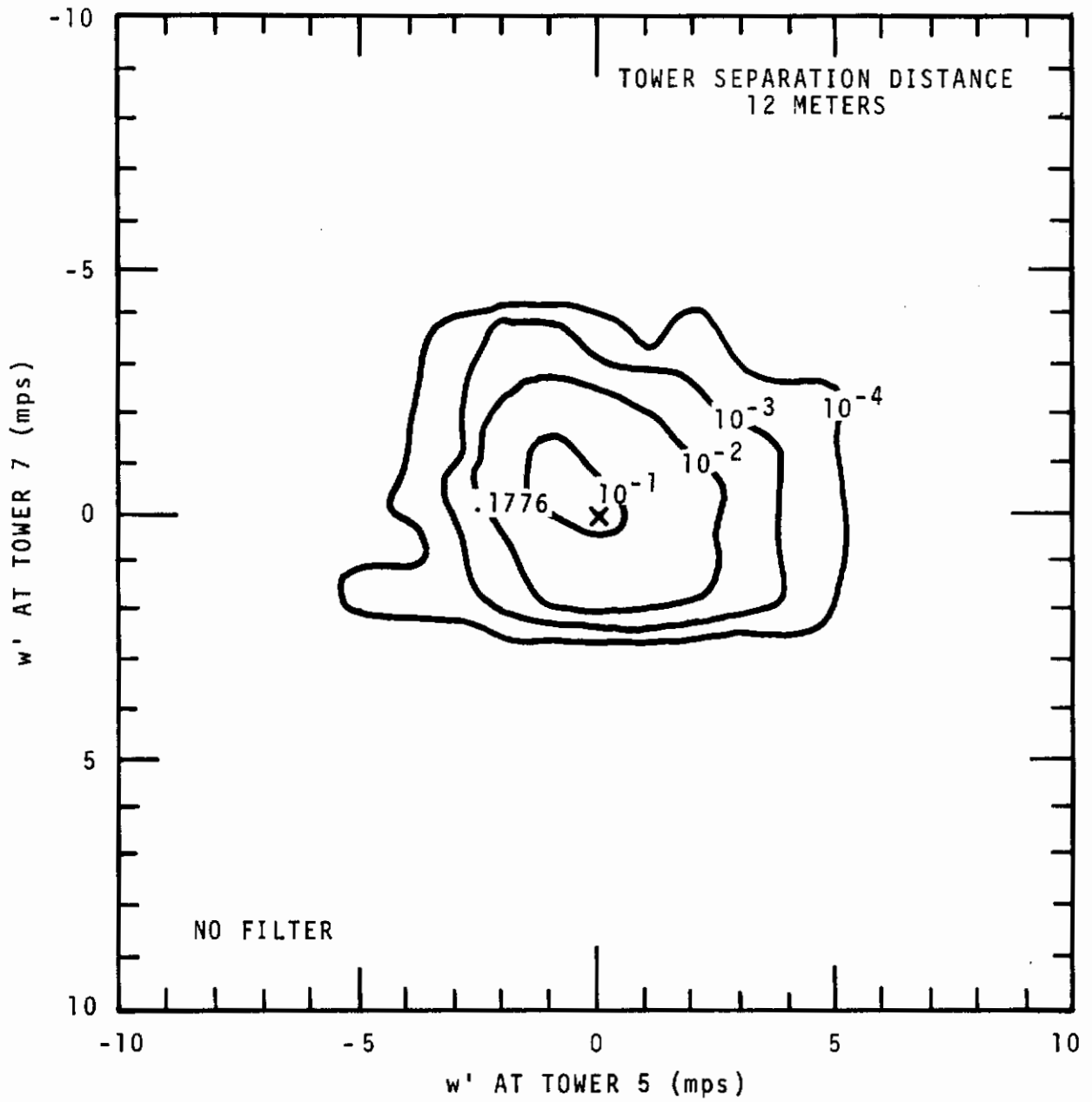


Figure IV.20 Joint Probability Density Function for  $w'$ ,  
Test T704, Separation Distance 12 Meters

## REFERENCES

- 1.1 C. E. Elderkin, D. C. Powell, A. G. Dunbar and T. W. Horst. Take-Off and Landing Critical Atmospheric Turbulence (TOLCAT) Experimental Investigation, Technical Report AFFDL-TR-70-117, Wright-Patterson Air Force Base, Ohio, May, 1971.
- 2.1 J. C. Wyngaard, O. R. Cote, and Y. Izumi. "Local Free Convection, Similarity, and the Budgets of Shear Stress and Heat Flux," Air Force Cambridge Research Laboratory, Bedford, Mass., March, 1971, (unpublished).
- 2.2 Y. H. Pao. "Undulance and Turbulence in Stably Stratified Media," Symposium on Clear Air Turbulence and Its Detection, Seattle, Washington, August 14-16, 1969, Science Research Laboratories, DL-82-0740, 1969.
- 2.3 J. O. Hinze. Turbulence, and Introduction to Its Mechanisms and Theory, McGraw-Hill Book Co., Inc., New York, N.Y., 1959.
- 2.4 J. L. Lumley and H. A. Panofsky. The Structure of Atmospheric Turbulence, Interscience Publishers, John Wiley Co., New York, N.Y., 1964.
- 2.5 C. C. Lin. "On Taylor's Hypothesis and the Acceleration Terms in the Navier-Stokes Equation," Quarterly of Applied Mathematics, Vol. 10, No. 4, pp. 295-306, 1952.
- 2.6 N. E. Busch and H. A. Panofsky. "Recent Spectra of Atmospheric Turbulence," Royal Met. Society Qtrly. Journ., Vol. 94, 1968.
- 2.7 G. B. Skelton. Investigation of the Effects of Gusts on V/STOL Craft in Transition and Hover, Technical Report AFFDL-TR-68-85, Wright-Patterson Air Force Base, Ohio, October, 1968.
- 3.1 C. E. Elderkin. Experimental Investigation of the Turbulence Structure in the Lower Atmosphere, BNWL-329, Battelle-Northwest, Richland, Washington, December, 1964.
- 3.2 J. C. Kaimal, J. C. Wyngaard and D. A. Haugen. "Deriving Power Spectra from a Three-Component Sonic Anemometer," J. Applied Meteorology, Vol. 7, No. 5, pp. 827-837, October, 1968.
- 3.3 J. C. Kaimal and J. A. Businger. "A Continuous Wave Sonic Anemometer-Thermometer," J. Applied Meteorology, Vol. 2, No. 1, pp. 156-164, February, 1963.

# Contrails

- 3.4 P. B. MacCready, Jr. and H. R. Rex. "Response Characteristics and Meteorological Utilization of Propeller and Vane Wind Sensors," J. Applied Meteorology, Vol. 3, No. 2, pp. 182-193, April 1964.
- 3.5 R. M. Young. R. M. Young Company, Ann Arbor, Michigan, Personal Communication. March, 1970.
- 4.1 D. C. Powell. "Diabatic Effects on Profiles of the Shear Stress," Pacific Northwest Laboratory Annual Report for 1970 to the USAEC Division of Biology and Medicine, BNWL-1551, Vol. II, Part 1, pp. 148-153, Battelle, Pacific Northwest Laboratories, Richland, Washington, June, 1971.
- 4.2 C. E. Elderkin. "Diabatic Effects on Atmospheric Turbulence Spectra," Pacific Northwest Laboratory Annual Report for 1970 to the USAEC Division of Biology and Medicine, BNWL-1551, Vol. II, Part 1, pp. 143-147, Battelle, Pacific Northwest Laboratories, Richland, Washington, June, 1971.
- 4.3 C. E. Elderkin, D. C. Powell and T. W. Horst. "Modeling of Wind Component Spectra," Pacific Northwest Laboratory Annual Report for 1970 to the USAEC Division of Biology and Medicine, BNWL-1551, Vol. II, Part 1, pp. 148-153, Battelle, Pacific Northwest Laboratories, Richland, Washington, June, 1971.
- 7.1 I. Van der Hoven. "Power Spectrum of Horizontal Wind Speed in the Frequency Range from 0.0007 to 900 Cycles per Hour," J. of Meteorology, Vol. 14, pp. 160-164, April, 1957.
- 7.2 R. Roth. "Turbulence Spectra with Two Separated Regions of Production," J. of Applied Meteorology, Vol. 10, No. 3, pp. 430-432, June 1971.
- 7.3 W. M. Crooks, F. M. Hoblit, David T. Prophet, et al. Project HICAT and Investigation of High Altitude Clear Air Turbulence, Technical Report AFFDL-TR-67-123, VOL. II, Wright-Patterson Air Force Base, Ohio, November, 1967.
- 7.4 J. A. Businger, J. C. Wyngaard, Y. Izumi and E. F. Bradley. "Flux-Profile Relationships in the Atmospheric Surface Layer," J. of the Atmospheric Sciences, Vol. 28, pp. 181-189, 1971.
- 7.5 G. H. Fichtl and G. E. McVehil. "Longitudinal and Lateral Spectra of Turbulence in the Atmospheric Boundary Layer at the Kennedy Space Center," J. of Applied Meteorology, Vol. 9, No. 1, pp. 51-63, February, 1971.
- 7.6 G. M. Jenkins and D. G. Watts. Spectral Analysis and Its Applications, Holden-Day, Inc., San Francisco, California, 1968.

- 7.7 C. E. Elderkin. "Measurements and Graphs of Turbulence Autocorrelations in Space and in Time," BNWL-SA-4086, Presented at the Symposium on Air Pollution Turbulence and Diffusion, Las Cruces, New Mexico, December 7-9, 1971.
- 7.8 F. E. Pritchard, C. C. Easterbrook and G. E. McVehil. Spectral and Exceedance Probability Models of Atmospheric Turbulence for Use in Aircraft Design and Operation, Technical Report AFFDL-TR-65-122, Wright-Patterson Air Force Base, Ohio, 1965.

# *Contrails*

UNCLASSIFIED

Security Classification		
DOCUMENT CONTROL DATA - R & D		
<i>(Security classification of title, body of abstract and indexing annotation must be entered when the overall report is classified)</i>		
1. ORIGINATING ACTIVITY (Corporate author) Battelle, Pacific Northwest Laboratories Richland, Washington 99352		2a. REPORT SECURITY CLASSIFICATION UNCLASSIFIED
		2b. GROUP
3. REPORT TITLE Take-Off and Landing Critical Atmospheric Turbulence (TOLCAT) - Experiments and Analysis		
4. DESCRIPTIVE NOTES (Type of report and inclusive dates) Final Report/November 1969 to October 1971		
5. AUTHOR(S) (First name, middle initial, last name) C. E. Elderkin, D. C. Powell, A. G. Dunbar, and T. W. Horst		
6. REPORT DATE April 1972	7a. TOTAL NO. OF PAGES 283	7b. NO. OF REFS 24
8a. CONTRACT OR GRANT NO. F33615-68-M-5009	9a. ORIGINATOR'S REPORT NUMBER(S)	
b. PROJECT NO. c. ADP 682E d.	9b. OTHER REPORT NO(S) (Any other numbers that may be assigned this report) AFFDL-TR-71-172	
10. DISTRIBUTION STATEMENT Approved for public release; distribution unlimited.		
11. SUPPLEMENTARY NOTES	12. SPONSORING MILITARY ACTIVITY Air Force Flight Dynamics Laboratory Wright-Patterson AFB, Ohio 45433	
13. ABSTRACT Measurements of turbulence were made from various arrays of tower mounted sensors to demonstrate methods of describing the temporal and spatial character of turbulence. Measurement and data reduction techniques for sonic and three-propeller anemometers were optimized to assure true and accurate measurements of the vertical and two horizontal wind components. Both analog and digital magnetic tape field recording options were demonstrated to provide flexibility in measurement array configurations and to optimize recording capabilities for a variety of measurement requirements. Probability density functions, both individual and joint, were calculated for any pair of wind component variables, oriented in a preselected coordinate system, and optionally high pass filtered for various aircraft response applications. Power spectra of each time series and cross spectra for different wind components at the same point and for the same component at different points were calculated for time series optionally tapered or detrended. Plots of the space-time dependence of correlation functions were obtained from turbulence measurements taken from a logarithmically spaced line of towers, offering a means of determining the turbulence spectra for a given wind component encountered by an aircraft flying through a field of turbulence at a given wind speed. Such analyses were obtained for each wind component with the mean wind along the line of towers and with the wind normal to the line of towers.		

DD FORM 1 NOV 65 1473

UNCLASSIFIED

Security Classification

UNCLASSIFIED  
Security Classification

14. KEY WORDS	LINK A		LINK B		LINK C	
	ROLE	WT	ROLE	WT	ROLE	WT
Low Altitude Turbulence V/STOL Aircraft Micrometeorology Towers Instrumented Meteorology Towers Wind Components Turbulence Data Analysis Wind Vanes Anemometers						